Development of immuno and nano PET/SPECT probes: towards novel theranostics for EGFR positive solid tumors

by

Nasim Sarrami

A thesis submitted in partial fulfillment of the requirements for the degree of

Doctor of Philosophy

in
Pharmaceutical Sciences

Faculty of Pharmacy and Pharmaceutical Sciences
University of Alberta

Abstract

Cancer continues to be a significant global public health issue, and regrettably, it remains one of the leading causes of death. Statistics indicate that 1 in 5 men or women will be diagnosed with cancer during their lifetime, resulting in 1 in 12 women and 1 in 9 men succumbing to the disease. Therefore, improving the current methods for diagnosis and treatment of cancer is a must. Time to first diagnosis plays an important role when it comes to managing cancer cases since as the cancer progresses its management will become more difficult, and the treatment of advanced cancers are not as effective. One possible solution to mange cancer cases faster than current practice, is to combine diagnosis and treatment steps into one. These compounds, known as theranostics, have attracted significant attention for the management of cancer in recent years. In this context, development of nanotheranostics, nanomedicine entities that can be tracked in real time and carry a high payload of medication to cancer lesions is expected to provide additional opportunities for the targeted and optimized treatment of tumor burden in patients. The hypothesis of this research was that antibodies and actively targeted nanoparticles against epidermal growth factor receptors (EGFR) labeled with radioactive traceable elements to home on EGFR positive tumors and provide means for tumor imaging in real time. To assess this hypothesis, we initially developed ^{64}Cu labelled panitumumab, a clinically approved monoclonal antibody against EGFR. Further studies indicated that the ^{64}Cu labelled panitumumab can be taken up by EGFR+ non-small cell cancer (NSCLC) cell lines. The radiolabelled panitumumab was able to detect EGFR+ subcutaneous and metastatic NSCLC xenografts in mice as shown by positron emission tomography (PET) imaging. Moreover, to assess the capability of radiolabelled panitumumab to detect other type of EGFR+ cancers and assess the capability of radiolabeled Pb as a radioisotope for developing theranostics, we developed ^{203}Pb labeled panitumumab and assessed its capability on detecting EGFR^{+} patient

derived xenografts (PDX) of head and neck caner in mice using SPECT imaging. Our findings showed ^{203}Pb-panitumumab to be capable of detecting EGFR^{+} head and neck cancer subcutaneous PDX. Furthermore, it can persist in the tumors for up to 120 hours after injection. We then worked on developing nanotheranostics by using poly (ethylene oxide)-poly(ε-benzylcarboxylate-ε-caprolactone) nanoparticles (PEO-PBCL NPs) as the nano delivery system and the base of the intended nanotheranostic. The surface of PEO-PBCL NPs was modified with panitumumab and

1,4,7-Triazacyclononane-1,4-bis (acetic acid)-7-(3-azidopropylacetamide) (NO2A-azide) chelator accommodate ^{64}Cu. This modification was done on the Fc region of antibody, using glycan remodeling process. Despite preferential homing of panitumumab modified NPs on EGFR + NSCLC cell lines compared to plain NPs, the *in vivo* PET imaging and biodistribution studies did not indicate any advantage in terms of tumor homing and targeting for panitumumab modified NPs compared to plain NPs. In the final chapter of this thesis, we examined different cryoprotectants for long term storage of PEO-PBCL NPs using either freeze drying or freeze thaw methods. Our data showed the best condition for long-term storage of NPs to be provided by freeze-thawing method using polyethylene glycol (PEG)s at 3350 Da molecular weigh or higher leading to no aggregation of NPs upon storage. Sucrose was also found to be an effective cryoprotectant for this purpose.

In conclusion, our presented research indicated that radiolabeled panitumumab can detect EGFR+ cancer and can be used for developing theranostics. We have also successfully developed radiolabelled PEO-PBCL NPs that can be tracked by PET imaging in real time *in vivo*, providing valuable information on the pharmacokinetic and biodistribution of NPs in different animal models

of disease. Traceable NPs can be further developed for use in human patients to identify cancer patients who may benefit from NP drug delivery.

Preface

Chapter one of the thesis describes the background knowledge behind different aspects of this thesis in addition to the rationales, objective, hypotheses and specific aims of the thesis.

Chapter two of the presented thesis has been submitted for publication as Sarrami, N., Wuest, M., Paiva, I.M., Leier, S., Lavasanifar, A., Wuest, F. **Immuno-PET imaging of EGFR with ^{64}Cu-NOTA Panitumumab in subcutaneous and metastatic non-small cell lung cancer xenografts.** Most of the experiments were carried out by me, excepting the development of metastatic non-small cell lung cancer animal model (Paiva, I.M.) and animal PET imaging and biodistribution studies (Wuest, M.). Also, optimization of the radiolabeling reaction was done with the help of Leier,S. Dr.Lavasanifar and Dr.Wuest contributed to the supervision, edits and corrections of the manuscript. All animal experiments were conducted in accordance with the CCAC guidelines and received approval from the Cross Cancer Institute local animal care committee (protocol # AC21256).

Chapter three has been submitted for publication as Sarrami, N., Nelson, B., Leier, S., Wilson, J., Chan, C., Meens, J., Komal, T., Ailles, L., Wuest, M., Schultz, M., Lavasanifar, A., Reilly, R.M., Wuest, F. **SPECT/CT imaging of EGFR-positive head and neck squamous cell carcinoma patient derived xenografts with ^{203}Pb-PSC-panitumumab in NRG mice – potential application in a radiotheranostic approach with ^{212}Pb-PSC-panitumumab.** In this project, Nelson, B., Leier, S., Wilson, J. prepared the ^{203}Pb for the studies. Schultz, M. developed and characterized the PSC chelator. The animal models were developed in Dr. Ailles laboratory by Meens, J.; also, Komal, T. took care of SPECT/CT imaging. Chan, C. and Wuest, M. assisted with biodistribution and *in vitro* studies. All other experiments were conducted by me. The manuscript

was supervised, edited, and corrected by Dr. Lavasanifar, Dr. Wuest, and Dr. Reilly. A patient with HNSCC underwent surgery to obtain a primary tumor specimen (#391) in accordance with approved protocols from the Research Ethics Board and Animal Care Committee at the University Health Network (Protocol No. 12–5639). Animal studies followed the approved protocol (AUP 2843.14) by the Animal Care Committee at the University Health Network, in accordance with the Canadian Council on Animal Care guidelines.

Chapter four will be submitted as part of a publication as Sarrami, N et al. **Glycan remodeling of panitumumab for the development of PET traceable EGFR targeted nano-theranostics in non-small cell lung cancer.** In this project, Leier, S. and Wilson, J. produced 64Cu for the radiolabeling purposes. Also, Wuest, M. conducted PET imaging and biodistribution studies. I conducted all other experiments. Dr. Lavasanifar and Dr. Wuest played a role in supervising, editing, and correcting the manuscript. The Canadian Council on Animal Care (CCAC) guidelines were followed for all animal experiments, which were also approved by the Cross Cancer Institute local animal care committee (AC 21256).

Chapter five will be submitted for publication as Sarrami, N., Honary, S., Vakili, M.R., Lavasanifar, A. **Development of methods for long-term storage of poly(ethylene glycol)-poly(α-benzyl carboxylate-ε-caprolactone) nanoparticles: The effect of cryoprotectant and storage conditions on nanoparticle aggregation.** In this project, preliminary experiments on the effect of sugars as cryoprotectants for freeze-thawing and freeze-drying PEO-PBCL nanoparticles, were conducted by Dr. Honary with the help of Dr. Vakili conducted. All the other experiments were done by me. Dr. Lavasanifar supervised, edited and corrected the manuscript.

Dedication

To my beloved parents, Niloufar and Mahmood,

For their endless love, support and unwavering faith in me.

Acknowledgements

I would like to express my sincere gratitude towards my supervisor Dr. Afsaneh Lavasanifar. I'm truly thankful for her continuous support, care, and guidance during my PhD journey. She taught me not just science, but also valuable life lessons. Being her student has been an absolute pleasure, and I am forever grateful for this opportunity to gain experience from her.

I would like to express my sincere gratitude to my co-supervisor, Dr. Frank Wuest, for his invaluable support, guidance, and for introducing me to the fascinating world of radiochemistry. Also, I would like to sincerely thank Dr. Melinda Wuest for her support and assistance during this time. I appreciate all her valuable efforts in teaching me about nuclear imaging and helping with my projects. It has been a wonderful lifetime experience to work with her.

I would like to thank my supervisory committee members, Dr. Marianna Kulka and Dr. Frank Wuest for their valuable comments and suggestions throughout my journey as a graduate student.

I would like to thank Dr. Mohammad Reza Vakili for his valuable advice in the chemistry field. I would like to express my gratitude towards my lab mates in both teams for their assistance and support during all this time, especially, Samantha, Cody, Bryce, Jeniffer, Parnian, Munira, Sara and Ahmed. I learned a lot from each one of them and collaborating with them has been an incredible experience.

I would also like to thank Dr. John Wilson, David Clendening, Blake Lazurko, Lloyd Barker and Endrit Pllana from the Edmonton Radiopharmaceutical Center (ERC) for ^{18}F production at the cyclotron facility of the Cross Cancer Institute (CCI, Edmonton, AB, Canada) and the 64Cu production at the Medical Isotope and Cyclotron Facility (MICF, Edmonton, AB, Canada). The authors are also grateful to Cody Bergman (Dept. of Oncology, University of Alberta) for the synthesis of [18F]FLT, Dan McGinn (Vivarium of the Cross Cancer Institute, Edmonton, AB, Canada) for supporting the animal work and Dr. Hans-Soenke Jans (Dept. of Oncology, University of Alberta) for technical help and support of the PET imaging experiments. We also thank Jennifer Dufour for her help with the cell culture work. Moreover, Mr. Vishwanatha Somayaji's contribution with ^{1}H NMR experiments from FoPPS/UofA is greatly appreciated.

I would like to acknowledge the funding agencies for supporting me during my studies. I thank Alberta Innovates, the NSERC-CREATE grant for the Polymer Nanoparticles for Drug Delivery (PoND) program, the Nano Medicine Innovation Network (NMIN), Canadian Institutes of Health Research (CIHR) and the graduate scholarships from the Faculty of Pharmacy and Pharmaceutical Sciences of the University of Alberta.

Lastly, I would like to thank my family and friends, especially my parents. I genially appreciate all their support, encouragement and motivation throughout this journey.

Table of contents

List of tables

List of Figures

List of abbreviations

Abbreviation	Full description
^{18}F-FDG	2-deoxy-2-[18f]fluoro-d-glucose
1H-NMR	proton nuclear magnetic resonance
Ab	antibody
AgNP	silver nanoparticle
ANOVA	analysis of variance
ATC	anaplastic thyroid carcinoma
ATCC	american type culture collection
AuNP	gold nanoparticle
BCA	bicinchoninic acid
BCL	benzyl carboxylate-ε-caprolactone
BCN	bicyclononyne
Bq	becquerel
CCAC	canadian council on animal care
CD	cluster of differentiation
$CDCl_3$	deuterated chloroform
CL	cross linked
CRC	colorectal cancer
CT	computed tomography
Cy5	cyanine 5
DLS	dynamic light scattering
DMEM	dulbecco's modified eagle medium
DMEM/F12	dulbecco's modified eagle medium/nutrient mixture f-12
DMSO	dimethylsulfoxide
DOTA	1,4,7,10-tetraazacyclo-dodecane-1,4,7,10-tetraacetic acid
DP	degree of polymerization

DSC	differential scanning calorimetry
DSPE	1,2-distearoyl-sn-glycero-3-phosphoethanolamine
DTPA	diethylenetriamine pentaacetate
EDTA	ethylenediaminetetraacetic acid
EGFR	epideral growth factor receptor
EPR	enhanced permeability and retention
Fab	antigen-binding fragment
FBS	fetal bovine serum
Fc	crystallisable fragment
Fcγ	crystallisable fragment gamma
FDA	food and drug administration
g	gram
GRP78	glucose-regulated protein 78
HER2	human epidermal growth factor receptor 2
HNCC	head and neck cancer carcinoma
ID	injected dose
IgG	immunoglobulin class g
KCPS	kilo counts per second
KDa	kilodaltons
L	liter
LET	linear energy transfer
m	milli
mAb	monoclonal antibody
MALDI-TOF	matrix-assisted laser desorption ionization time-of-flight
MAP	maximum a posteriori
Mn	number average molecular weight
mol	mole

mPEO	methoxy poly(ethylene oxide)
mRNA	messenger rna
MSNP	mesoporous silica nanoparticle
MWt	weight average molecular weight
NaOAc	sodium acetate
NH_2-Bn-DOTA	s-2-(4-aminobenzyl)-1,4,7,10-tetraazacyclododecane tetraacetic acid
NO2A-azide	1,4,7-triazacyclononane-1,4-bis (acetic acid)-7-(3-azidopropylacetamide)
NOTA-NCS	2-*s*-(4-isothiocyanatobenzyl)-1,4,7-triazacyclononane-1,4,7-triacetic acid
NP	nanoparticle
NRG	NOD rag2 γc
NSCLC	non-small cell lung cancer
Pan	panitumumab
PBCA	poly (butyl cyanoacrylate)
PBCL	poly(ε-benzylcarboxylate-ε-caprolactone)
PBS	phosphate-buffered saline
PCL	poly (caprolactone)
PD-1	programmed cell death protein 1
PDI	polydispersity index
PEG	polyethylene glycol
PEO	polyethylene oxide
PEO-PBCL	poly(ethylene oxide)-block-poly(α-benzyl carboxylate ε-caprolactone)
p.i	post injection
PET	positron emission tomography
PLGA	poly(lactic-co-glycolic acid)
PNKP	polynucleotide kinase-phosphatase
PPy	polypyrrole
PSC-NCS	2,2'-(4-(2-amino-2-oxoethyl)-10-(2-((4-isothiocyanatobenzyl)amino)-2-oxoethyl)-1,4,7,10 tetraazacyclododecane-1,7-diyl) diacetic acid

PSMA	prostate-specific membrane antigen
PVA	poly vinyl alcohol
RES	reticuloendothelial systems
RIPA	radioimmunoprecipitation assay buffer
ROI	regions of interest
RTX	rituximab
SD	standard deviation
SDS-PAGE	sodium dodecyl-sulfate polyacrylamide gel electrophoresis
SEM	standard error of measure
SNA	spherical nucleic acid
SPECT	single photon emission computed tomography
SUV	standardized uptake values
T/B	tumor to blood ratio
T/M	tumor to muscle ratio
TBS	tris-buffered saline
TEM	transmission electron microscopy
THF	tetrahydrofuran
TLC	thin layer chromatography
TRT	targeted radionuclide therapy
w	weight

Chapter 1

Introduction

1.1. Theranostics: A general overview

Radiopharmaceuticals are a group of biologically active compounds that have been labeled with radioisotopes. The purpose of the radioisotope can be to provide a probe for imaging and diagnosis of the disease or its treatment(1). The radioisotope used in radiopharmaceuticals for diagnostic purposes should emit rays that could be detected by gamma or positron devices such as single photon emission computed tomography (SPECT) and PET imaging, respectively. For therapeutical purposes, the radiolabeled element should emit high energy radiation so that the radiopharmaceuticals be toxic to the target site (2). Some commonly used radioisotopes for diagnostic and therapeutical purposes are mentioned in Table 1.1.

Table 1.1.Examples of different radioisotopes used for imaging and therapy

Radioisotope	Half-life (minutes)	β− MeV (%)	β+ MeV (%)	EC (%)	γ MeV (%)	Use	Reference
Carbon-11	20.3	-	0.968 (100%)	-	-	PET imaging	(3–6)
Fluorine-18	110	-	0.635 (97%)	3	-		
Copper-64	762	0.573 (38.4)	0.655 (17.8%)	43.8	0.511 (35.6)		
Technetium-99m	360	-	-	-	0.140 (100)	SPECT imaging	(7–12)
Indium-111	4032	-	-	100	0.173 (89)		
Lead-203	3114	-	-	100	0.279 (81)		
Lutetium-177	9648	0.497 (78.6) 0.384 (9.1) 0.176 (12.2)	-	-	0.113 (6.6) 0.208(11)	radiotherapy	(13–22)
Lead-212	638.4	0.57 (100)	-	-	-		
Iodine-131	11520	0.606 (89.6) 0.334 (7.23) 0.807 (0.39)	-	-	-		
Yttrium-90	3840	2.28 (100)	-	-	-		
Copper-67	3715.2	0.141 (100)	-	-	184.5 (48.7)		

Radiopharmaceuticals usually contain biologically active components, such as a monoclonal antibody (mAb), a peptide, or a small molecule that covalently conjugates radioisotopes directly or a chelators that can host radioisotopes. The choice of the biologically active components of radiopharmaceuticals is usually made based on the cells and/or organelles of interest for treatment or diagnosis purposes (11, 12).

The radiolabeling of peptides requires a different approach from radiolabeling mAb due to their difference in the radiolabeling process, for example, the reaction conditions that peptides can endure are rough such as non-aqueous solvents, temperature above 40°C or pH that is significantly different from biological pH. However, these conditions can affect the protein structure causing the protein to lose its biological activity. Therefore, the most performed condition for protein (e.g., mAb) reactions is mild and aqueous (25).

Compared to peptides, mAbs show higher affinity for the target protein. They are also larger in size, which can limit their permeation inside the cells by non-active mechanisms of cell transport. Due to their larger molecular weight, they cannot pass the glomeruli filtration by kidneys and usually show long half-lives. mAbs are also prone to aggregation upon storage during their shelf life. Nevertheless, for decades mAbs have been in use for diagnosis and treatment of different diseases particularly cancer (24,26).

The term theranostic refers to a compound that has both diagnostic and therapeutical features (27). In nuclear medicine, theranostics refers to the same compound being labeled with diagnostic and therapeutic radioisotopes such as labeling prostate-specific membrane antigen-617 (PSMA-617) with gallium-68 (^{68}Ga) and lutetium-177(^{177}Lu) for imaging and treatment, respectively (28). In an alternative approach the same radiolabeled compound can be used at different doses for imaging

and treatment such as the ^{131}I which is used for imaging thyroid tissue and its disorders which is used in higher doses for treating thyroid cancer (29,30). The aim of using theranostics is to have an opportunity for real-time monitoring of treatment efficiency by imaging changes in the expression of certain biomarkers in the disease sites. Theranostics can also be used to track the fate of drugs in the biological system ensuring delivery of medication at the right location and time in patients (31,32).

The goal in nuclear medicine is to maximize the concentration of radiopharmaceuticals in the specific tissue being targeted while minimizing the concentration in healthy non-target tissues. This ensures that the treatment or diagnostic procedure is effective and specific for the diseased site. Targeting of radiopharmaceuticals to the disease site minimizes their potential side effects on healthy tissues at the same time (33). The biologically active component of radiopharmaceuticals composed of mAbs, peptides or small molecules targeting specific receptors on the diseased cells can provide an efficient tool for selective delivery of these agents. To further advance the tissue targeting capabilities of theranostics and at the same time make them amendable for delivery of high drug payloads as well as effective drug cocktails, nanotheranostics were developed (34).

Nanotechnology based products have been used to diagnose, treat, or prevent diseases at cellular and subcellular levels (34). Particles in the nanometer size range 10-100 nm termed nanoparticles (NPs) cannot be easily eliminated through kidneys because of their size being above kidney filtration threshold. They show a high surface-to-volume ratio, providing opportunities for better interaction with cells of interest at their surface, as well as capacity to attach multiple targeting ligands on one NP. If engineered properly for their size and surface properties, they can accumulate into organs harboring leaky and/or angiogenic vasculature, as well (35).

Nanotheranostics, can be developed from different materials at nanometer size range; including lipid based, polymer based or inorganic NPs (36). Nanotheranostics, can take advantage of unique features of nanotechnology, imaging probes, and therapeutical agents together (37).

1.2. Antibody as imaging and therapeutic entities

Antibodies (Abs) are Y shaped glycoprotein structures from the immunoglobulin (Ig) family that can recognize and neutralize foreign antigens and lead to an immune response. Each Ab is comprised of two heavy and light chains. Furthermore, the portion of the Ab that attaches to antigens is named fragment antigen-binding (Fab) and the base of the antibody which interacts with the other immune systems member, is named fragment crystallizable (Fc) (38) . There're five different types of Ig in humans: IgM, IgG, IgA, IgE and IgD (39) with the IgG subtype being the most approved antibody for use in clinic (40).

Upon the discovery of antibodies, Sir Gustav Nossal proved that each B cell clone produces a unique type of Ab that targets a specific segment of the antigens and were named monoclonal Ab (mAb) (38). Then after, mAb have found their way for treatment of different diseases such as cancer, autoimmunity and chronic inflammatory diseases (40).

Initially the developed mAb had murine origins which led to immunogenic responses in humans and limited their use in the clinic (38). However, advancements in mAb productions resulted in production of humanized mAb leading to approval of more than 100 Ab-based treatments for use in the clinic nowadays (38,40).

The use of mAb for cancer treatment has seen substantial progress, making it one of the leading therapies for cancer (26,29). mAb against tumor biomarkers has been utilized for precise diagnosis

and treatment of cancers (42). The most common biomarkers targeted in cancers by mAbs are: growth factor receptors such as epidermal growth factor receptor (EGFR) and human epidermal growth factor receptor 2 (HER2), B cell markers CD19 and 20, immune check point inhibitors such as programmed cell death protein 1 (PD-1) and vascular endothelial growth factor (VEGF) which is an angiogenic growth factor (40).

mAbs have the ability to eliminate cancer in multiple ways (38). One mechanism is by inhibiting certain functions, like blocking the dimerization of receptors such as epidermal growth factor receptor (EGFR) (43,44). Additionally, mAbs can play a role in immune-mediated cell destruction like antibody-dependent cell-mediated phagocytosis. mAb can also interact with secreted growth factors and interfere with their function, for instance mAbs that inhibit tumor vascularization can attach to vascular endothelial growth factor (43).

Various subtypes of IgG mAb can be utilized based on their intended purpose. IgG is categorized into four subtypes - IgG1, IgG2, IgG3, and IgG4 - based on their Fc region, which affects their binding affinity to Fcγ receptors on immune cells (45,46). IgG1 has the highest binding affinity, followed by IgG3, IgG2, and IgG4. Therefore, for immune-mediated cell destruction aims IgG1 and for antigen targeting aims IgG2 and IgG4 subtypes are good candidates (46). Table 1.2. compares IgG four subtypes (47,48).

Table 1.2. Comparison of different IgG subtypes. In the presented structures, blue represents antibodies heavy chain and purple represents light chains. Red arrow indicating the the Fc and green arrow indicating the Fab segment of Ab.

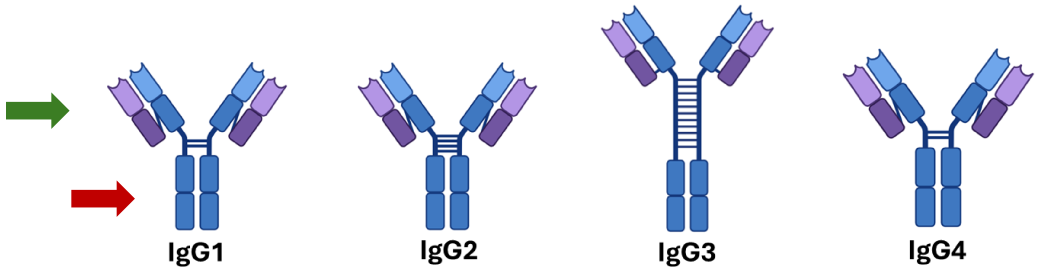

	IgG1	IgG2	IgG3	IgG4
Molecular weight (KDa)	146	146	170	146
Disulfide bonds within heavy chains	2	4	11*	2
Amino acids in hinged reign	15	12	62*	12
Half-life (Days)	21	21	7/~21*	21

** Depends on the antibodies allotype*

Chemotherapeutics can covalently be attached to mAb making antibody dug conjugates (ADC)s for precise drug delivery to cancer cells. Since mAb have high specificity toward target recognition, a decrease in the side effects and an increase in drug activity is resulted from the use of ADCs (49).

Other than chemotherapy drugs, radioisotopes could be attached to mAb. Depending on the type of radioisotope attached; the developed radioimmunoconjugate could be used for diagnosis and therapeutical purposes for example 89-zirconium labeled panitumumab and ^{131}-iodine labeled 3F8 are in clinical trials for diagnosis of colorectal cancer and treatment of brain tumors respectively (50).

1.2.1. EGFR and Anti-EGFR monoclonal antibodies

EGFR is trans-membrane receptor from the ErbB family of receptor tyrosine kinases (51) over-expressed in many solid tumors, such as head and neck squamous cell carcinoma (HNSCC) with 90-95% and non-small cell lung cancer (NSCLC) with 50-90% of cases overexpressing EGFR (52,53). Furthermore, several studies indicated that the expression of EGFR to have a negative association with survival of patients with solid tumors (54). These factors make EGFR a good target for solid tumors. Among $EGFR^{+}$ solid tumors, HNSCC shows the highest EGFR expression (53). The overall prevalence of lung cancer and relatively high expression of EGFR in these patients makes this cancer type another good candidate for investigations concerning EGFR targeting (55–57). Anti-EGFR mAbs attach to the extracellular part of the EGFR and block the activation of downstream cascade associated with EGFR. (58).

Currently all anti-EGFR approved mAbs are IgG isotype (59). Cetuximab and panitumumab are examples of anti-EGFR Abs approved by US Food and Drug Administration (FDA) for the treatment of HNSCC and metastatic colorectal cancer (CRC) respectively (60). However, resistance to anti-EGFR Ab has been reported in clinic due to multiple reasons such as reduction in Ab-receptor interaction, activation of alternative pathways for activating tyrosine kinase, and constant activation of downstream cascades (58). Yet, this does not mean that anti-EGFR Abs cannot be used as targeting agents, as a matter of fact, they can be used for targeted delivery of chemotherapies and radionuclides (61).

Panitumumab is an IgG mAb against EGFR and the first member of anti-EGFR Ab family that is fully humanized. There is no reports on the development of Abs against panitumumab (62,63).

Furthermore, less hypersensitivity from panitumumab has been reported in comparison to other members of the anti-EGFR Ab family including cetuximab (63).

In the literature there has been many reports on radiolabelling panitumumab for targeting $EGFR^+$ tumors with different isotopes such as labeling with ^{89}Zr for use as an immune-PET probe (64), ^{111}In for use as an immune-SPECT probe (65) , ^{212}Pb as an therapeutic agent (66) and labeling with ^{111}In and ^{177}Lu as a theranostic (67).

1.3. Nanoparticles

NPs are defined as particles with 10-1000 nm range size. These particles can be used to encapsulate different drugs for improving their water solubilized levels, modifying drugs' pharmacokinetic and pharmacodynamic properties, increasing drugs circulation half-life and delivering the drug to the site of interest (68). NPs ranging from 10-100 nm in size have potential applications in cancer therapy as they can enhance drug accumulation in solid tumors by the enhanced retention and permeation effect (EPR) (69).

1.3.1. Passive and active targeting of NPs in cancer

The abnormal blood vessel permeability and impaired lymphatic drainage in cancerous tumors offer a window to transport and retain particles larger than the pores of the tumor's blood vessels (70). The phenomenon known as EPR allows NPs to passively target cancer cells (19,20). This method of targeting known as passive targeting can deliver NPs to the tumor site but it can not selectively deliver the NPs to the cancer cells (71). Furthermore, this targeting method does not have an impact on NP uptake or bypassing multidrug resistance by cancer cells. Another level of

targeting can be achieved through modification of NPs with ligands that interact with overexpressed receptors on cancer cells. This is known as active targeting (71,72) (Figure 1.1.).

Active targeting enhances tumor specificity, and binding affinity and decreases the required drug amount for therapeutical effect (73,74). Different ligands such as peptides and nucleic acids that bind to the overexpressed receptors on cancer cells could be considered as targeting agents(75). Among different targeting ligands, antibodies have proven to be highly selective and possess a strong binding affinity towards their target receptors. This is primarily because of antibodies having two epitopes per molecule, making them an excellent choice for targeting agents. Large size of antibodies, however, may be considered as a roadblock as far as modification of NPs with such targeting ligands is concerned. This may limit the efficiency of NP modification with the targeting ligand due to steric hindrance caused by larger size of antibodies compared to peptides. Besides, the larger size and hydrophobicity of antibodies may mark the NPs for uptake by the mononuclear phagocytic cells, *in vivo*, leading to a reduction in targeting ability of NPs. The need for the use of aqueous media during the conjugation process is another limiting factor when antibodies are compared to peptides.

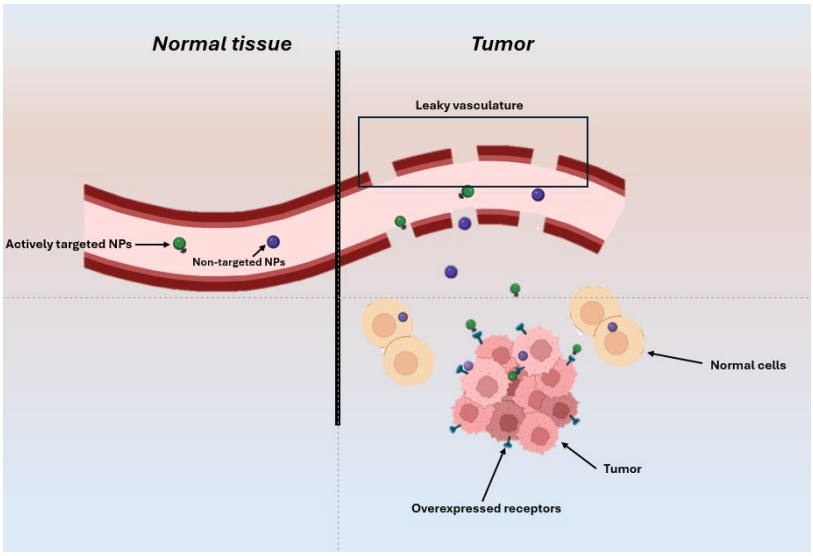

Figure 1.1. Passive and active targeting of nanoparticles in tumors Vs normal tissue

1.4. Development of Antibody Modified Nanoparticles

In general, the Ab binding strategies to NPs can be divided into three major groups: physical adsorption, covalent bond formation, and employment of adaptor molecules (76,77). Each strategy has its advantages and disadvantages depending on the features of each component and their final application. For instance there is a high chance of antibody release from the surface of NP when attached via physical adsorption although Ab modification is not required via this method (78,79). Nevertheless, it is crucial that the binding method does not alter the structure, conformation, and orientation of the antibody (80). The binding methods are described in more detail below (77). Figure 1.2. provides a general scheme of attachment methods and Table 1.3.

provides examples for each described method:

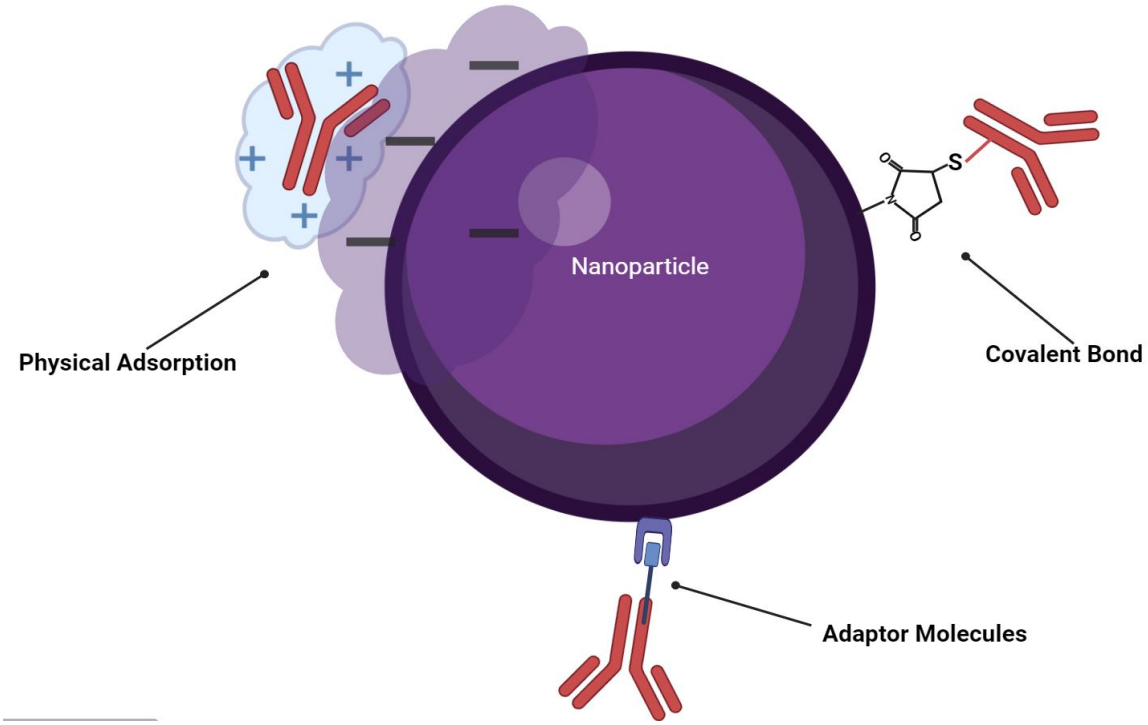

Figure 1.2. General scheme of attachment methods of mAb to NPs

1.4.1. Physical Adsorption of Ab to NPs

This method of NP modification is simple with no requirement for chemical modification on either Ab or the NPs' surface. Ab and NPs are mixed together, resulting in the formation of van der Waals and/or hydrogen bonds, hydrophobic and/or electrostatic attractions (79). In this method, there's no control over the orientation of the Ab on the surface of the NP and there is no guarantee that the Ab stays with NPs, *in vivo* (81).

1.4.2. Covalent bond formation

The attachment of the Ab to the surface of NPs via covalent bonds produces a more stable conjugation of Ab to the NPs (80). However, in this method modification of the NP with functional groups prior to the conjugation is required (80,82). Also, depending on the type of the reaction, chemical modifications of the Ab may be needed (80).

1.4.2.1. Amide bond formation

The Ab can be conjugated to the NPs surface by utilizing the high density of primary amines that can react with different functional groups on the NPs surface. In a typical reaction, NPs with carboxyl groups on their surface can be activated via 1-ethyl-3-(-3-dimethylaminopropyl) carbodiimide and form an amide bond with Ab (77,80).

1.4.2.2. Disulfide /maleimide-thiol bond formation

The free or generated sulfhydryl on Ab has the ability to create a disulfide bond with thiol modified NPs or interact with thiol-reactive functional groups such as maleimide, iodoacetyl, and 2-pyridyl disulfide on the NPs (83,84). However, if the disulfide bonds present in the Abs' hinge segment are cleaved by reducing compounds such as 2-mercaptoethanol, to form free sulfhydryl groups, Abs will get fragmented as the presence of disulfide bond is essential for the tertiary structure and function of antibodies (77). It is worth noting that the reaction condition for the maleimides to react with thiol is pH 6.5-7.5, in which amines are protonated and unwanted side reactions will not occur (85).

1.4.2.3. Bond formation via sugar moieties

Oxidation of polysaccharides present in the Fc region of antibodies can be utilized to selectively attach Abs to NPs through the Fc section of the Ab and preserve their Fab regions. Compounds

such as boronic acid derivatives can oxidize sugar moieties. Although this strategy resolves many issues of amide or disulfide conjugation methods, several steps are needed for conjugation also attachment to nanoparticles is random across the Fc segment of the Abs (77).

1.4.2.4. Click chemistry

The conjugation via click chemistry is the most reliable method with a high conjugation outcome which can occur under mild aqueous reaction conditions (86,87). Click chemistry conjugation can occur alongside other conjugation methods simultaneously. Modifying proteins with click-reactive groups is essential for click chemistry, such as modifying the Ab with azide and the NPs with alkyne groups (87).

1.4.3. Conjugation via adaptor molecules

An alternative conjugation method is to use a non-covalent approach which is strong yet reversible (88). One of the most common examples of this conjugation approach is the attachment of biotinylated Ab to NPs modified with structures that can rapidly bind to biotin with high specificity such as tetramers namely avidin, streptavidin, and NeutrAvidin with avidin being the most used compound in bio and nanotechnology field (89,90).

These conjugations are stable at a variety of conditions such as temperature and pH. The efficiency of this method is reliable on the amount of biotinylated Abs (88).

In this conjugation method, adaptor proteins can be conjugated to the Fc region of Abs while leaving the Fab part of Ab untouched and providing control over the orientation of the Ab (88). Moreover, in this method of conjugation, Abs can be substituted with each other. In addition, the orientation of Abs can be controlled via this method of conjugation (77).

Other than biotin and avidin binding, the NPs and Abs can be decorated via nucleic acids, both Ab and NPs are required to be modified with single-strand nucleic acids that are complementary to each other. As this method relies on base-pairing chemistry, the specificity of this strategy is high (91).

Another method of conjugation that needs to be considered is the conjugation of Ab to NPs via enzymes. Enzyme activity enables more specific conjugation compared to covalent bond formation in milder conditions. However, due to the multiple-step preparation, the outcome of the procedure could be inefficient (77).

Table 1.3. Example Ab modified NPs prepared by different methods of antibody conjugation

STRATEGY	METHOD	NANOCARRIER	ANTIBODY	THE OBJECTIVE OF THE STUDY	REF.
Physical Adsorption	Change of pH	Gold nanoparticles	Goat polyclonal IgG	Development of an improved method for preparing Ab-Au NPs by physical adsorption method	(92)
Covalent Bond Formation	Amide bond formation	Mesoporous silica nanoparticle	Anti-HER 2 scFv	Preparation of pH/temperature-responsive and HER2 targeting delivery system	(93)
		Fe3O4-based PLGA nanoparticles	Anti-CD206	Prepare NPs that target M2 macrophages and convert them to M1 phenotype	(94)
		Iron nanoparticles Silica nanoparticles	polyclonal antibody IgG *B. abortus*	Design of immuno-nano-biosensor with high sensitivity to detect *B.abortus*	(95)
		Magnetic nanoparticle	Goat anti-mouse/rabbit IgG	Synthesis and determination of magnetic NPs for biomedical applications	(96)
		Mixed micelles of PEO-PCL or PEO-PBCL with RTX- PEG-DSPE	Rituximab	Development of mixed polymeric micelles modified with rituximab for targeting B-cell lymphoma cells.	(97)
		Gold nanoparticles	Anti-PD-L1	chemo-photothermal targeting therapy for CRC treatment by the development of DOX and anti-PD-L1 conjugated gold NP	(98)
		Fluorescent silica nanoparticles	Goat anti-human IgG	Development of Polycarboxylated dextran, multivalent linker, for attachment of Ab to NPs	(99)
	Disulfide functional groups	MSNP	Cetuximab	Development of targeted therapeutics to enhance radiation sensitivity	(100)
		PBCA nanoparticles	Cetuximab and Nimotuzumab	Development of polymeric micelle targeted with mAb for glioblastoma treatment	(101)
		Gold Liposomes	R17217	Impact of TfR Ab density on the uptake and transport of nanoparticles into the brain	(102)
	Sugar moieties	Magnetic nanoparticles	Anti-serum amyloid P	Development of optimal oriented Ab	(103)
		Silver nanoparticles	IgG of Anti-NT-proBNP	assessment of heterobifunctional cross-linker on Ab orientation and activity	(104)
	Click chemistry	Quantum dots	Anti-human EGFR mAb	Conjugation of antibodies to Quantum dots using copper-free click chemistry	(105)

		Superparamagnetic iron oxide	Anti-CD 20 (RTX)	Comparison of click chemistry and carbodiimide Ab conjugates	(106)
Conjugation via adaptor molecules	Biotin binding protein	Gelatin nanoparticles	Anti-CD3	Targeting CD3 positive T-cells by modifying the surface of gelatin nanoparticles	(107)
		Self-assembled hexameric protein barrel	Rabbit IgG	Delivering enough functional antibody to the cytosol	(108)
	Fc binding proteins	Quantum dots	Anti-HER2 (Herceptin)	Preparation of antibody-conjugated quantum dots with facile strategy	(109)
		Lipid modified Quantum dots	Anti claudin-4,Anti-mesothelin, Anti-cadherin-11 Anti-mucin-4	Development of a method to conjugate Ab to lipid-coated NPs using Fc-gamma receptor 1	(110)
	Nucleic acid hybridization	Spherical Nucleic acid (SNA) with gold core	HER2	Synthesis of novel SNA-nucleic acid-antibody conjugate	(91)

1.5. Methods for the development of radiolabeled Ab-NP

The choice of an appropriate radionuclide for radiolabeling a system requires consideration of factors such as linear energy transfer (LET), half-life, and the affected area by the radioisotope (111). Among the radiation emitters, α particles have the highest LET, followed by auger electrons then β particles (112). The range affected by auger electrons is about 10 μm (113); also, the range for α particles is 50-100 μm (114). The high energy of α particles and short range make them well-suited for targeting micrometastasis and malignancies in the blood and bone as their short range will not effect the surrounding cells. On the other hand, β particles, with a range of 2-10 mm (112), are well-suited for targeting larger tumors due to their impact on multicellular dimensions. Radionuclides that emit γ rays other than the mentioned rays could be used for theranostic purposes as the γ rays could be detected via SPECT imaging such as ^{131}I (115,116).

Radiolabeling of NPs that are modified with a protein or peptide as their targeting ligand can follow to different pathways: 1. Radiolabeling the NPs 2. Radiolabeling the protein or peptide on the NPs.

1.4.4. Radiolabeling Ab-NP by labeling NPs

Different delivery systems such as polymeric micelles and liposomes loaded with different cargos have been radiolabelled for *in vivo* tracking using different methods such as directly attaching the radiometal to NPs structure, or while preparing the NPs such as liposome development, the lipid film can be hydrated with radionuclides added to aqueous solution or by using chelators to trap the radionuclides (117–119). Yang et al. (120) designed theranostic micelles labeled with ^{125}I acting as an imaging moiety as well as an oncolytic due to their photothermal activity. In this study, to poly(ethylene glycol)–poly(l-tyrosine) an amphiphilic diblock polymer indocyanine green (ICG)

was added and after that ^{125}I to the polymers followed by preparation of polymeric NPs from dye and radiolabelled polymers. In this study, since ICG can convert to absorbed optical energy to heat, the developed NPs had photothermal and photoacoustic properties. Furthermore, since the NPs were labeled with ^{125}I, they were detected via SPECT imaging.

NPs can be radiolabeled by adding chelators to NPs, encapsulating the radioisotope in the NPs or in the case of liposomes, incorporating it into the phospholipid bilayer (119). The choice of radiolabeling method is dictated by NP and radionuclide properties (121). For instance Lamichhane et al. (122) reported on radiolabeling of liposome and the encapsulated drug both. The liposomes were labeled by ^{111}In complexation with diethylenetriamine pentaacetic acid (DTPA) which was then detected by SPECT imaging and the drug cargo, a derivative of carboplatin, was labeled with ^{18}F which was detected via PET. This system allowed the investigators to track the biodistribution of liposome/drug complex *in vivo* with exquisite detail (122,123)

By considering the type of delivery system such as gold, silica, and magnetic NPs, the radionuclide conjugation method can be chosen. For example, Glaus et al. (124) iron oxide NPs were labeled with ^{64}Cu through the attachment of 1,4,7,10-tetraazacyclo-dodecane-1,4,7,10-tetraacetic acid (DOTA) chelator to the PEGylated phospholipids which were covering the iron oxide core leading to the development of a dual imaging probe. Another example is liposomes, due to their hydrophilic core, radioisotopes such as ^{99m}Tc and ^{111}In have been encapsulated to develop imaging probes (125).

1.4.5. Radiolabeling Ab-NP by labeling antibodies

The attachment of radiolabeled Ab to NP can be used for 2 different approaches: 1. Simultaneous radiolabeling and active targeting of the NPs (126). 2. Providing means for delivering radiolabeled Ab to the tissue of interest. There are several advantages to this method; first the NPs presumably provide a more efficient delivery method throughout the circulation and into the tissues, second, multiple antibodies can be attached to each nanoparticle, and third, the entire structure is less likely to be degraded by proteases leading to an increase in Ab half-life i*n vivo* (127) For example, in a study cetuximab was initially labeled with ^{89}Zr via complexation with desferal followed by attachment to AuNPs. This study assessed the difference in the biodistribution of ^{89}Zr labeled cetuximab alone and attached to AuNPs which indicated that attaching ^{89}Zr labeled cetuximab to AuNPs will not alter the EGFR recognition properties and tumor accumulation of ^{89}Zr labeled cetuximab (128).

In another study, silver NPs (AgNPs) were decorated with ^{131}I labeled isatuximab, which is an anti-CD38 mAb used for treatment of multiple myeloma. In this study, isatuximab was radiolabeled with ^{131}I via Chloramine-T method and for preparing radiolabeled AgNPs, isatuximab was initially added to the NPs then radiolabled with the same method. The results indicated that ^{131}I labeled isatuximab AgNPS show higher toxicity, apoptotic effect than ^{131}I labeled isatuximab (129).

1.5. Application of radiolabeled antibody-modified NPs in cancer diagnosis and/or therapy

One of the commonly used radioisotopes in nuclear medicine is ^{111}In. This radionuclide has a half-life of 2.8 days and emits γ rays which cause less damage to normal tissues in comparison to a β emitter such as ^{188}Re. Cheng et al. (130) conjugated ^{111}In to their delivery system and developed a

polymeric nano delivery system that targeted glucose-regulated protein 78 (GRP78) which is overexpressed in gastric cancer. The NPs were composed of poly(ethylene glycol)–poly(ε-caprolactone) polymeric micelles, (diethylenetriamine pentaacetate) DTPA-^{111}In complex, and GRP78 binding peptide. *In vivo* study of nude mice bearing MKN45 tumors showed that ^{111}In labeled GRP78BP NPs accumulated two-fold higher in tumors in comparison to ^{111}In labeled NPs.

The decay half-life of ^{111}In makes it a suitable candidate for SPECT imaging of long-circulating delivery systems such as the study done by Makhlouf et al. (131). In this study, DOTA was used as the chelator since it could be attached to both ^{111}In (γ ray emitter) and ^{225} Ac (α particle emitter). *In vitro* cell uptake results showed ^{111}In-Fab-DOTA-NPs were internalized by the RPMI-7951 melanoma cells more significantly than the ^{111}In-DOTA-NPs. However, in mice bearing G361 melanoma tumor, ^{111}In-DOTA-NPs were internalized by the tumor significantly more than ^{111}In-Fab-DOTA-NPs as shown by SPECT/CT imaging which could be a result of high spleen uptake of actively targeted NPs.

NPs were developed by Werner et al. (132) using poly(D,L-lactide-co-glycolide)-lecithin-PEG, which were targeted against folate receptors by adding folate onto the NPs. These NPs were then loaded with paclitaxel and radiolabeled using yttrium-90 (^{90}Y). Their *in vitro* assessments on OVCAR-3, SW626 and SKOV-3cell lines indicated that actively targeted radio chemotherapy NPs are the most effective NPs in comparison to actively targeted NP that have either paclitaxel or ^{90}Y or any of non-targeted NPs. *In vivo* outcomes on murine-bearing SKOV-3 tumors agents were in line with *in vitro* results that indicated folate-targeted NPs had more effect than non-targeted NPs.

Another therapy combination that has been studied is a combination of photothermal therapy with internal radiotherapy (133,134). For example, polypyrrole (PPy) nanoparticles were actively

targeted against transferrin receptors by using transferrin. In this development, transferrin not only acts as the targeting agent but also helps to stabilize the PPy NPs. By radiolabeling transferrin with ^{131}I, the developed system had the capability for simultaneous photothermal and radio therapy due to presence of PPy and ^{131}I. This delivery system showed significant higher internalized by U87MG and accumulation in the U87MG tumor of tumor-bearing nude mice three fold more than PPy nanoparticles which were not actively targeted (135).

Gold NPs have been an attractive nanodelivery system due to their versatile size, the capability of delivering small drug molecules, and lack of toxicity and this delivery system has been used to target EGFR in breast cancer cells (136). This design uses DTPA as a chelator whereby EGF is radiolabeled with ^{111}In and then attached to the surface of Au NPs. The size of these particles was 14 nm and about 78 EGF molecules were attached to each particle. These nanoparticles were internalized by MDA-MB-468 (high expression of EGFR) cells more than by MCF-7 cells that do not express EGFR. Both cell lines incorporated very small amount of $^{111}InCl_3$. A colony forming cell assay demonstrated that these EGF-Au NPs were toxic to MDA-MB-468 cells. The therapeutic efficiency of the nanoparticles was improved greatly when they were radiolabeled (136).

Furthermore, radiolabeled and actively targeted NPs can be loaded with compounds that make up for tumor mutations such as the p53 oncogene. By this delivery, cancers such as anaplastic thyroid carcinoma (ATC) may become sensitive to radiation. Huang et al. (137) worked on a compound namely Prima-1 that restores p-53 mutation. They initially confirmed that CD44 receptor is over-expressed in samples from ATC patients then prepared NPs using a tyrosine–hyaluronic acid-polyethyleneimine conjugate and Prima-1 was loaded through the self assembly of NPs. Hyaluronic acid served as the CD44 targeting agent and tyrosine was added so that it could attach

to ^{131}I and radiolabel the NPs. *In vitro* and *in vivo* experiments indicated that actively targeted NPs loaded with prime-1 and radiolabeled with ^{131}I can result in cytotoxicity in $CD44^{+}$ ATC with p53 mutation.

1.6. Rationale, hypothesis, and objectives

1.6.1. Rationale

Cancer remains a major public health problem worldwide, and unfortunately, it still ranks among the top causes of death from diseases (138,139). The estimation suggests that 1 out of 5 individuals, either male or female, will experience a cancer diagnosis in their lifetime, resulting in 1 in 12 women and 1 in 9 men losing their lives to the illness (139). Moreover, estimates suggest that there will be more than 28 million cancer cases by 2040 and approximately 35 million cases by 2050 (139,140). These findings led to attempts to diagnose and treat cancer at early stages of the disease, aiming to improve survival rates and reduce invasiveness, side effects, and costs since current limitations in cancer diagnosis and treatment is the reason for the deaths caused (31,140). To improve cancer management, development and application of theronostics are suggested. Theranostics can track the fate of treatment in real time in patients, be used to monitor treatment effectiveness using less invasive options compared to biopsy, reduce time to first diagnosis and help in choosing the best treatment option for cancer patients towards a personalized treatment (31).

Nanocarriers have the potential to encapsulate poorly soluble drugs effetely and direct them towards solid tumors by passive targeting. This is shown to lead to lowered side effects and increased therapeutic activity for several anticancer agents.

Among different materials that NPs have been prepared from, polymeric NPs are one of the most studied organic NPs as their flexibility in design allows for customization based on the desired function (141). Moreover, polymeric NPs are simple to develop and can be made biocompatible which makes them a good candidate for cancer therapy (142).

Nanoparticles based on poly(ethylene oxide)-poly(ε-benzylcarboxylate-ε-caprolactone) (PEO-PBCL) have been under investigation for the delivery of different anticancer agents by our research groups in the past decade (97,143,144). This includes delivery of an inhibitor of DNA repair, known as A83B4C63, by PEO-PBCL NPs. The NP formulation of this drug was shown to enhance the sensitivity of CRC tumor xenografts to radiation therapy. This contrasted with free A83B4C63 which was proved to be ineffective. The superior activity of NP formulation of A83B4C63 as a radio-sensitizer was attributed to enhanced accumulation of drug by its NPs in tumor tissue (145).

To further enhance the activity and targeting ability of PEO-PBCL NP formulations of A83B4C63, we have recently reported on the modification of PEO-PBCL NPs with EGFR targeting peptide, GE11. (146). Our data, using fluorescent as well as PET imaging showed a modest advantage for GE11 in increasing the homing of PEO-PBCL NPs in subcutaneous CRC models, but no correlation was found between GE modification and homing of PEO-PBCL NPs in metastatic tumor lesions.

1.6.2. Objective

The long-term objective of this research was to develop new theranostics for detection and therapy of EGFR positive solid tumors. Towards this goal we first pursued radiolabeling of a clinically approve mAb against EGFR and validated their activity in imaging of cancer lesions in different models of $EGFR^+$ NSCLC and HNC. Moreover, to combine the advantages of PET imaging in

tracing the fate of cancer treatment, the capacity of NPs in delivery of a high payload of anticancer drugs (e.g., A83B4C63) and that of EGFR antibodies in targeting EGFR positive tumors, we developed PET traceable plain and panitumumab modified NPs. The potential of developed systems in tracking the fate of NPs in an animal model of NSCLC was then assessed.

1.6.3. Hypothesis

The hypothesis of this research was that PET and SPECT traceable EGFR mAbs can image EGFR positive tumors in primary and metastatic site, in real time. Our second hypothesis was that PET traceable plain and mAb modified NPs can be developed and used to track the fate of NPs in real time, in tumor bearing animal models.

1.6.4. Specific objectives

1. To develop a metastatic EGFR+ non-small cell lung cancer animal models and assess the potential of ^{64}Cu labeled panitumumab on detecting metastatic tumors as well as studying the biodistribution of ^{64}Cu labeled panitumumab in metastatic animal model.

2. To develop ^{203}Pb labeled panitumumab and assessing its potential on detecting EGFR+ head and neck cancer animal models up to 120h after injection of immune-SPECT probe. Also, to study the biodistribution of ^{203}Pb labeled panitumumab in these animal models

3. to prepare positron emission tomography (PET) traceable panitumumab modified nanoparticles and assess their capability in recognition of EGFR overexpressing cancer cells, *in vitro* and *in vivo*

4. To assess different storage conditions for PEO-PBCL NPs with the use of different cryoprotectants

Chapter 2

Immuno-PET imaging of EGFR with ^{64}Cu-NOTA Panitumumab in subcutaneous and metastatic non-small cell lung cancer xenografts

A version of this chapter has been submitted for publication

2.1. Introduction

Lung cancer is the leading cause of cancer deaths worldwide, with a 5-year survival rate of ~15%. Around 50% of diagnosed cases are at the metastatic stage (1,2). In the USA alone, it is estimated that in 2024, lung cancer will cause the death of about 340 people per day, which is 2.5 times higher than deaths caused by the second most common cancer, colorectal cancer (3). About 87% of lung cancer cases are non-small cell lung cancer (NSCLC). For this phenotype, 40% of all cases are at the metastatic stage when first diagnosed (4). Advanced NSCLC has a poor prognosis with average survival rates of only 8-10 months (2). NSCLC metastases are primarily detected in the brain, bone, liver, and adrenal glands (1). Survival rates of lung cancer patients with liver and bone metastasis are worse compared to the ones with only nervous system metastasis (5). Patients with liver metastasis have the lowest overall median survival of 3-4 months (6). Poor prognosis and high incidences highlight the importance of early detection and precision treatment of metastatic NSCLC (7).

Epidermal growth factor receptor (EGFR) was the first identified oncogenic target in NSCLC, which is overexpressed in 40-89% of all NSCLC cases, depending on the patient cohort (8,9). Elevated protein expression of EGFR in NSCLC is associated with cancer metastasis, proliferation and apoptosis suppression, playing a significant role in cancer relapse following therapy and poor patient outcome (10–12).

For imaging and diagnosis of NSCLC, computed tomography (CT) was initially used. However, CT was not adequate to detect all cancer lesions in patients, especially at the advanced and

metastatic disease stage. In contrast to CT, positron emission tomography (PET) allows for functional imaging of NSCLC, leading to more accurate diagnosis and staging (13). PET radioligand 2-deoxy-2-[18F]fluoro-D-glucose (18F-FDG), a radiolabeled analogue of glucose, is frequently used for the detection of NSCLC lesions in patients (14,15). However, 18F-FDG also shows false-positive signals at inflammation and infection sites due to the high uptake of 18F-FDG by immune cells, including neutrophils, lymphocytes, and activated macrophages (14,16,17). Another radioligand clinically used for PET/CT imaging of NSCLC is 3'-deoxy-3'-18F-fluorothymidine (^{18}F-FLT), measuring cell proliferation independent of metabolic changes and inflammatory processes (20).

An alternative for PET imaging of NSCLC is immuno-PET with radiolabelled immunoconjugates. Radiolabelled immunoconjugates display high specificity and can provide opportunities for patient selection for targeted treatments by mapping the target protein expression in tumour cells in vivo (19). EGFR is involved in cell signalling pathways that control cell division and survival. Aberrant cell division is a typical cancer hallmark, and the reported high expression of EGFR in NSCLC lesions (12,13) makes EGFR a suitable NSCLC imaging biomarker for non-invasive diagnosis and drug target for targeted therapy.

Panitumumab is a recombinant, fully human monoclonal antibody that binds with high affinity to the extracellular portion of EGFR, preventing dimerization and, therefore, activation of the receptor associated with cell migration, adhesion, and proliferation. The U.S. Food and Drug Administration (FDA) approved panitumumab (Vectibix) for treating patients with EGFR-expressing, metastatic colorectal carcinoma (20). Panitumumab has a pharmacological half-life of 7.5 days (21), making it a suitable candidate for developing radiotheranostics for immuno-PET

detection and targeted therapy of NSCLC (22–24). Interest in radiotheranostics, compounds that can simultaneously diagnose and treat cancer using pairs of radioisotopes, has significantly increased over recent years (25,26). Matched radioisotope pairs like ^{64}Cu/^{67}Cu are suitable for PET imaging (^{64}Cu) and targeted beta-radiotherapy (^{67}Cu) (27). Paired with targeted ligands like panitumumab, radioisotopes from the same element do not change the radioligand's chemical properties and biodistribution profile, enabling accurate detection of a disease biomarker and targeted cancer treatment, including metastases (147). In addition, decorating nanoparticles with specific targeting units such as mAb panitumumab and radiolabelling with diagnostic radioisotopes such as ^{64}Cu would allow for monitoring of targeted delivery of chemotherapeutic drugs loaded into the core of these nanoparticles to enhance treatment efficacy (146).

The goal of the presented work was to analyze the potential of ^{64}Cu-NOTA panitumumab using immuno-PET for detecting EGFR^{+} NSCLC tumour models to visualize tumour burden, especially in the metastatic disease making comparisons with that for the subcutaneous tumor xenografts.

2.2. Materials and Methods

2.2.1. Materials

2-*S*-(4-isothiocyanatobenzyl)-1,4,7-triazacyclononane-1,4,7-triacetic acid (NOTA-NCS) was purchased from (Macrocyclics Inc ,USA). Panitumumab (Vectibix®) (Amgen Inc., USA) was gifted by the Cross Cancer Institute Pharmacy in Edmonton, Canada. LoBind Eppendorf tubes were purchased from Eppendorf, USA. Bio-Rad 10DG desalting column, Chelex 100 Resin, Laemmili buffer and SDS-PAGE Mini-PROTEAN® TGX™ Precast Protein Gels were purchased from Bio-Rad, USA. Aquastain protein staining reagent from Bulldog Bio, USA, was used. The NanoDrop OneC from Thermo Scientific, USA and AR-2000 radio-thin layer chromatography (radio-TLC) imaging scanner from Eckert and Ziegler, USA were used. Cell culture media DMEM/F12, fetal bovine serum (FBS), and penicillin−streptomycin-L-glutamine were purchased from GIBCO, Life Technologies Inc., Carlsbad, CA. $^{64}CuCl_2$ was produced via the $^{68}Zn(p,n\alpha)^{64}Cu$ nuclear reaction (148) at the Medical Isotope and Cyclotron Facility (MICF) at the University of Alberta, Edmonton, Canada.

2.2.2. NOTA conjugation to panitumumab

100 µg of 2-*S*-(4-isothiocyanatobenzyl)-1,4,7-triazacyclononane-1,4,7-triacetic acid (NOTA-NCS) was dissolved in 50 µL of chelex-treated 0.1 M sodium bicarbonate buffer (pH 9.0) in a LoBind tube. Then, an aliquot of 2 mg of panitumumab was added to the tube, and the pH was adjusted to pH 8.5. The mixture was incubated at room temperature for 1.5 hours at 700 rpm on a thermoshaker. The sample was passed through a size exclusion chromatography column (10DG desalting column) with chelex-treated 0.025 M NaOAc buffer pH 5.5 to purify the product. The

eluent was collected in LoBind tubes in 0.5 mL fractions. The amount of antibody in each fraction was determined by nanodrop at 280 nm. The samples with the highest amount of protein with a concentration of 5-10 mg/mL were submitted for matrix-assisted laser desorption/ionization (MALDI) mass spectroscopy (Agilent Technologies 6220 oaTOF; Agilent Inc., Santa Clara, CA, USA) at the University of Alberta, mass spectrometry facility for further analysis on the number of chelators per antibody (149).

2.2.3. ^{64}Cu labelling of NOTA-functionalized panitumumab

^{64}Cu was produced at the Medical Isotope and Cyclotron Facility (MICF, Edmonton, AB, Canada) according to a recently established procedure (148). [^{64}Cu]$CuCl_2$ (0.5 mL in 0.1 N HCl) was buffered by 10-15 µL of chelex-treated 2 M NaOAc buffer (pH 10) to pH 5.5. Then, ~100 µL of ^{64}Cu (200-300 MBq) was transferred to a LoBind Eppendorf tube containing 200 µg of NOTA-functionalized panitumumab. Radiolabeling with ^{64}Cu was performed by incubating the reaction at 37 °C for 60 min at 700 rpm on a thermoshaker. EDTA (1mM) was added to quench the reaction. ^{64}Cu-NOTA-panitumumab was purified on an Econo-Pac 10DG desalting column pre-equilibrated with 0.25 M NaOAc (pH 5.5) as the eluent. Elution fractions (400 mL) were collected from the column, and the radioactivity of collected fractions was measured using an Atomlab 400 dose calibrator. The incorporation efficiency of ^{64}Cu was measured using radio-TLC. For radio-TLC analysis, an EDTA (ethylenediaminetetraacetic acid) challenge was first done by adding 2 µL of 10 mM EDTA to 8 µL ^{64}Cu-NOTA-panitumumab from the reaction and incubating at room temperature for 10 min. Then, a 1.5 µL sample was spotted on a TLC plate and transferred to a TLC tank employing citric buffer as the mobile phase.

2.2.4. Analysis of ^{64}Cu-NOTA-panitumumab

Laemmili buffer was added to panitumumab, NOTA-panitumumab and ^{64}Cu-NOTA-panitumumab and the samples were incubated at 95 °C for 5 min. Then, the samples were loaded on SDS-PAGE gels under reductive conditions, and electrophoresis ran at 120 V for ~45 min. After electrophoresis, Aquastain® was added to the gel and incubated at room temperature for 30 min, and the gel was removed for further analysis. The gel was imprinted on film and scanned with a radio-scanner to analyze the radioactive bands on the gel.

2.2.5. Cell line

H1299 luciferase positive (H1299-luc+) cells were purchased from the American Type Culture Collection (ATCC) (Manassas, VA). H1299-luc+ cells were cultured in a 5% CO_2 incubator at 37 °C in DMEM/F12 media supplemented with 10% fetal bovine serum and 1% penicillin/streptomycin with media renewal 2-3 times per week.

2.2.6. Cell uptake studies

In vitro cell uptake studies were performed using H1299-luc+ cells and different incubation times. H1299-luc+ cells were initially seeded in each well of a 12-well plate and incubated overnight. The next day, after removing media in each well, 500 µL Krebs-Ringer buffer solution (120 mM NaCl, 4 mM KCl, 1.2 mM KH_2PO_4, 2.5 mM, $MgSO_4$, 25 mM $NaHCO_3$, 70 µM $CaCl_2$, pH 7.4) (29) was added. Then 0.2 MBq of ^{64}Cu-NOTA-panitumumab was added to each well, and the plate was kept at 5% CO_2 incubator at 37 °C for different time points. Radiotracer uptake was stopped

with 1 mL of ice-cold PBS, and the cells were washed twice with PBS and lysed in 0.4 mL radioimmunoprecipitation assay buffer (RIPA buffer). Radioactivity in 400 µL of cell lysates was determined as Becquerel [Bq] using a HIDEX automated gamma counter (Hidex Oy, Turku, Finland). Total protein concentration in the samples was determined by the bicinchoninic acid method (BCA 23227; Pierce, Thermo Scientific) using bovine serum albumin as protein standard. Data were calculated as percent of measured radioactivity per milligram of protein (%radioactivity/mg of protein). Graphs were constructed using GraphPad Prism 5.0 (GraphPad Software, San Diego, CA). Statistical differences were tested by one-way ANOVA and were considered significant for $p<0.05$. For the blocking experiments, plates with seeded H1299-luc+ were prepared as mentioned previously, and cells were co-incubated with different concentrations of unlabeled panitumumab (0.2 to 200 nM) and 0.2 MBq of ^{64}Cu-panitumumab. After 60 min, washing, lysing, and transferring samples to tubes were performed, as mentioned above.

2.2.7. Mice

Male 6-10 weeks old NSG mice were obtained from a breeding colony from Dr Lynne Postovit (Department of Oncology, University of Alberta, Edmonton, Canada). All animal experiments followed the Canadian Council on Animal Care (CCAC) guidelines and was approved by the Cross Cancer Institute local animal care committee (animal protocol # AC21256).

2.2.8. NSCLC animal models

The uptake and biodistribution of ^{64}Cu-NOTA-panitumumab was investigated in both subcutaneous and metastatic EGFR^{+} H1299-luc+ models in mice.

The subcutaneous mouse model was generated by subcutaneous injection of ~3×10^6 H1299-luc$^+$ cells in 100 mL of 50% Matrigel 50% PBS into the left shoulder of male NSG mice. After ~3-4 weeks, tumors reached a size of approximately 5x5 mm and were suitable for PET experiments. For the orthotopic metastatic mouse model, ~1×10^6 H1299luc$^+$ cells in 100 µL PBS were injected into the tail vein of male NSG mice.

After six weeks, these mice were analyzed with [^{18}F]FLT PET to determine if they had developed detectable metastatic lesions in their lungs or livers.

2.2.9. PET imaging experiments

Subcutaneous or metastatic H1299-luc$^+$ tumor-bearing NSG mice were anesthetized with isoflurane (100% O_2), and their body temperatures were kept constant at 37°C. Mice were injected intravenously with either 5-7 MBq [^{18}F]FLT in 100-150 µL 10% ethanol/saline (metastatic model only) or 7-9 MBq ^{64}Cu-NOTA-panitumumab in 100-150 µL 0.025 M sodium acetate through a tail vein catheter. Radioactivity in the injection solution (0.5 mL syringe) was determined using a dose calibrator (Atomlab^{TM} 500; Biodex Medical Systems, New York, NY, USA).

For blocking experiments, mice were injected intravenously with 1 mg panitumumab 48 h before injecting the ^{64}Cu-NOTA-panitumumab. Mice were positioned and immobilized in a prone position in the center of the field of view of an INVEON® PET/CT scanner (Siemens Preclinical Solutions, Knoxville, TN, USA). A transmission scan for attenuation correction was not acquired. Static PET scans were measured for 10 min at two h post-injection for [^{18}F]FLT and 10-30 min for ^{64}Cu-NOTA-panitumumab at two h, 24 h or 48 h post-injection. PET data were reconstructed using maximum a posteriori (MAP) reconstruction mode. No correction for partial volume effects was

performed. Image files were further processed using Rover v.2.0.51 software e (ABX GmbH, Radeberg, Germany). Masks defining 3-dimensional regions of interest (ROI) were set and defined by 50% thresholding. Mean standardized uptake values [SUV_{mean}=(activity/mL tissue)/(injected activity/body weight)] (mL/kg), were calculated for each ROI. Diagrams were constructed using GraphPad Prism 5.0 (GraphPad Software, San Diego, CA). All SUV PET data are presented as means ± SEM from n experiments. Statistical differences were tested by unpaired Student's *t*-test and considered significant for $p < 0.05$.

2.2.10. *Ex vivo* biodistribution experiments

For biodistribution studies using both tumour models, 3−5 MBq of ^{64}Cu-NOTA-panitumumab in 100-150 µL of 0.025 M sodium acetate was injected intravenously through a tail vein catheter of anesthetized tumour-bearing or control NSG mice. Radioactivity in the injection solution (0.5 mL syringe) was determined using a dose calibrator (AtomlabTM 500; Biodex Medical Systems, New York, NY, USA). For blocking experiments, mice were injected intravenously with 1 mg panitumumab 48 h before injecting the ^{64}Cu-radiolabeled antibody. The animals were allowed to regain consciousness until sacrifice. Animals were anesthetized again and euthanized by cervical dislocation after 48 h post injection. Organs of interest, including blood, heart, lung, liver, kidneys, spleen, stomach, duodenum, small and large intestines, pancreas, right femur, muscle, brain, fat, and tumours, were collected and weighed.

Radioactivity in all tissues was measured as becquerel in a HIDEX automated gamma counter (Hidex Oy, Turku, Finland), and results were analyzed as percentage of injected dose per gram of

tissue (% ID/g). Experiments were performed from n=4-5 mice. Data are represented as mean ± standard error of measure (SEM).

2.2.11. Statistical Analysis

All *in vitro*, *in vivo* and *ex vivo* data are expressed as means ± SEM from n experiments. Graphs were constructed using GraphPad Prism 5.04 (GraphPad Software, San Diego, CA). Statistical differences were tested by one-way ANOVA and unpaired Student's *t*-test and were considered significant for $p < 0.05$ (*), $p < 0.01$ (**) and $p < 0.001$ (***).

2.3. Results

2.3.1. ^{64}Cu labeling of NOTA-panitumumab

The bifunctional chelating agent NOTA-NCS was attached to panitumumab by thiourea formation using lysine residues. The number of NOTA chelators per antibody was determined by MALDI-TOF analysis. The m/z difference between NOTA-attached panitumumab (m/z = 147877) and panitumumab (m/z = 147185) revealed an average of 1.5 NOTA chelators conjugated per antibody. NOTA-functionalized panitumumab was used for radiolabelling with ^{64}Cu ($t_{1/2}$ 12.8 h). Radiolabelling of NOTA-panitumumab with [^{64}Cu]Cu(OAc)$_2$ (200-300 MBq) for 60 min at 37 ºC followed by size-exclusion (SEC) purification afforded ^{64}Cu-NOTA-panitumumab in isolated radiochemical yields of 47 ± 9 % (n=8) at an average molar activity of 0.65 GBq/mg (Figure 2.1. A and B). The radiochemical purity of isolated ^{64}Cu-NOTA-panitumumab exceeded 99%, as analyzed by radio-TLC (Figure 1C). SDS-PAGE analysis under reductive conditions revealed that panitumumab's light (25 kDa) and heavy chains (55 kDa) were decorated with NOTA and subsequently labelled with ^{64}Cu as analyzed by Coomassie staining and phosphor imaging (Figure 2.1. D and 1E). No other bands were observed, confirming the high radiochemical purity of ^{64}Cu-NOTA-panitumumab. Purified ^{64}Cu-NOTA-panitumumab was >95% stable in human serum over 48 h.

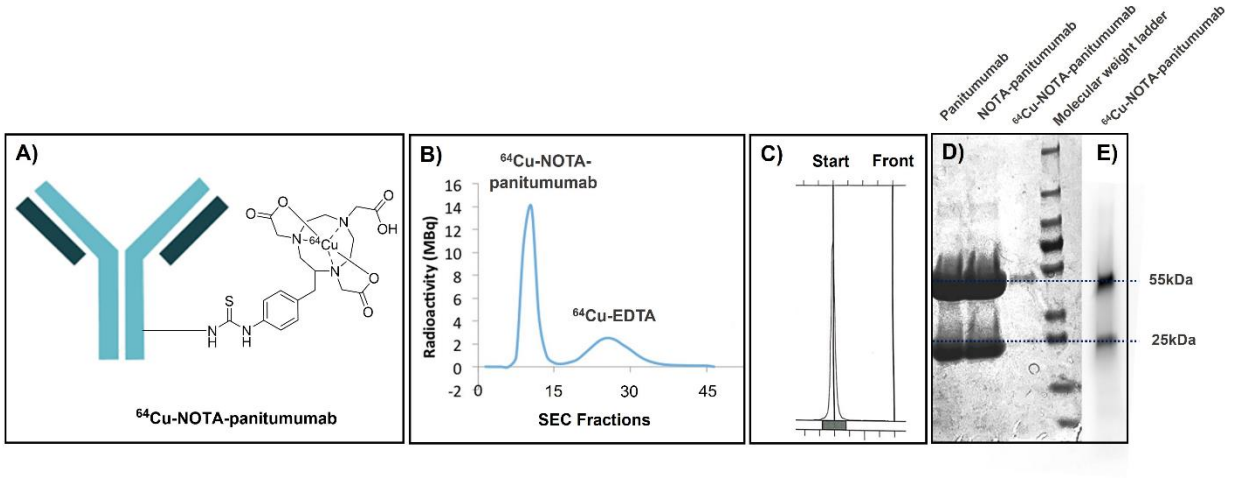

Figure 2.1. ^{64}Cu-NOTA-panitumumab (A); SEC purification histogram of ^{64}Cu-NOTA-panitumumab (B); Radio-TLC quality control of purified ^{64}Cu-NOTA-panitumumab (C); SDS-PAGE of panitumumab, NOTA-panitumumab, and ^{64}Cu-NOTA-panitumumab (Comassie staining (D) and (E) phosphor image of ^{64}Cu-NOTA-panitumumab.

2.3.2. *In vitro* cell uptake experiments

Non-small cell lung cancer H1299 cells were incubated with ^{64}Cu-NOTA-panitumumab at different time points, and cell uptake was monitored by measuring the amount of radioactivity present in the cell lysates (Figure 2.2. A). The results indicated that ^{64}Cu-NOTA panitumumab was increasingly bound and taken up by H1299-luc+ cells in a time-dependent manner, reaching 29.1±2.9% radioactivity/mg protein (n=3) at 90 min. Blocking studies with panitumumab confirmed EGFR-mediated uptake of radioligand ^{64}Cu-NOTA panitumumab in a concentration-dependent manner. Radioligand uptake was significantly reduced in the presence of 20 nM, 40 nM and 200 nM panitumumab (Figure 2.2. B).

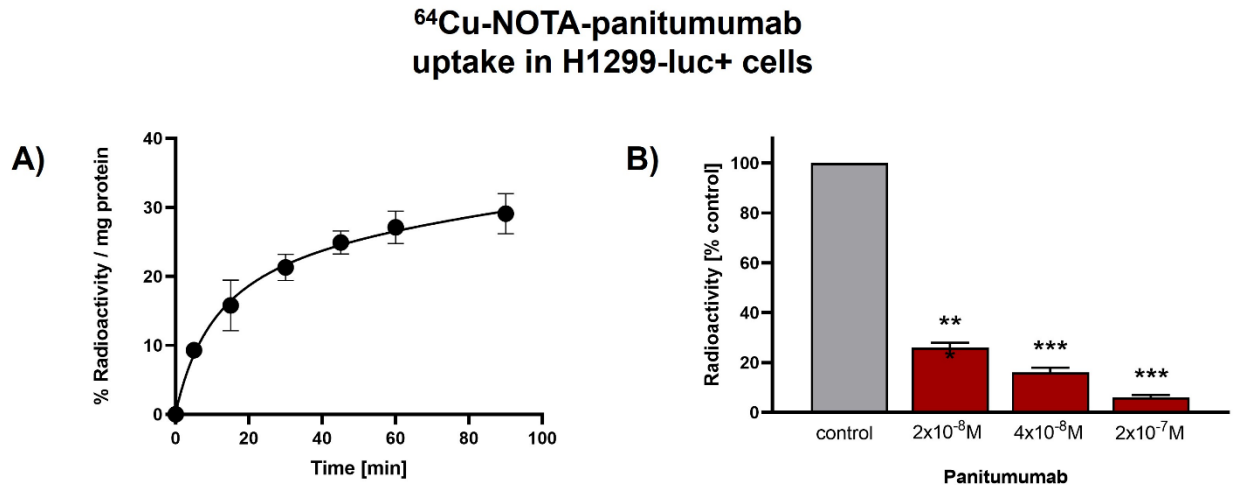

Figure 2.2. Cellular uptake of ^{64}Cu-NOTA-panitumumab in EGFR+ H1299-luc+ cells (A) and competitive inhibition studies of with panitumumab after 60 minutes of incubation with ^{64}Cu-NOTA-panitumumab and different concentrations of panitumumab (B). ** and * shows significant difference from control with no panitumumab pretreatment. P<0.01. P< 0.001, respectively, as indicated by One-way ANOVA test (n=3).**

2.3.3. PET imaging experiments

The subcutaneously injected tumors reached volumes of ~250 mm^3 after 28 days of H1299-luc+ cell injections. Figure 2.3. shows PET data at 2 h, 24 h and 48 h after administration of ^{64}Cu-NOTA panitumumab in this animal model.

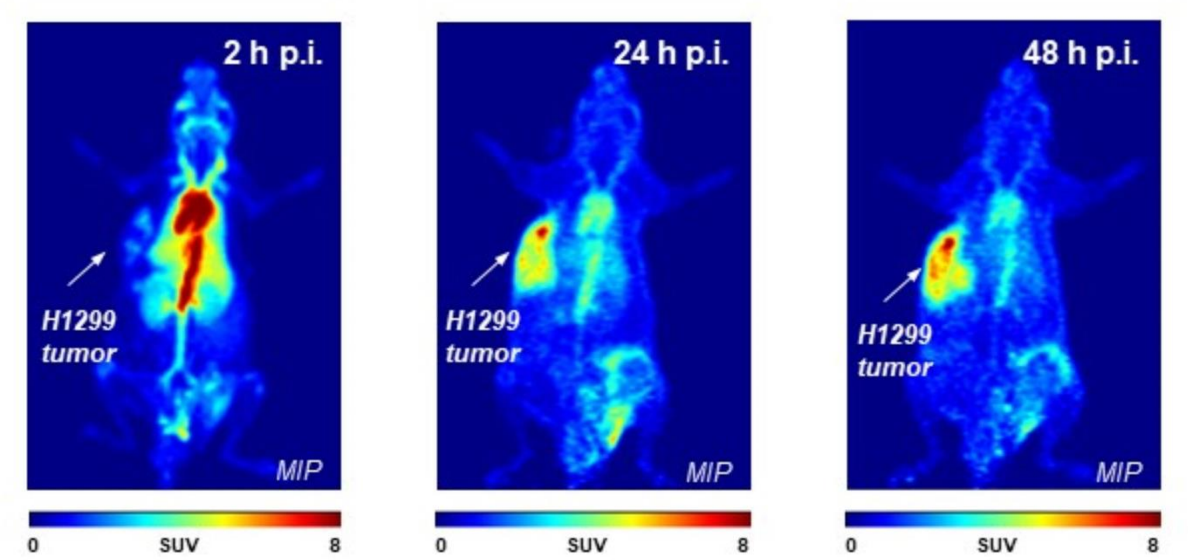

Figure 2.3.Representative PET images as maximum intensity (MIP) projections in H1299-luc+ subcutaneous tumor bearing NSG mice at 2h, 24h and 48 h after injection of ^{64}Cu-NOTA-Panitumumab.

PET images show the delayed blood pool clearance (visible over the heart region) typical for a larger compound such as the antibody panitumumab and the slower uptake into the target tumor tissue.

Figure 2.4. (top) presents PET images of ^{64}Cu-NOTA-panitumumab in the presence and absence of 1 mg cold pantitumumab. The diagrams in Figure 2.4. (bottom) summarize the mean standardized uptake values (SUV_{mean}) determined from regions of interest over the tumor area and the contralateral muscle. They revealed values of 1.92 ± 0.10 (n=5) after 2 h p.i., 4.70±0.42 (n=5) for 24 h p.i. and 5.37 ± 0.40 after 48 h p.i., respectively. Pretreatment of mice with 1 mg panitumumab 48 h before radiotracer injection significantly reduced binding of ^{64}Cu-NOTA-

panitumumab in H1299-luc+ tumors: $SUV_{mean,}$24h of 1.94±0.22 (n=4, t test $p<0.001$) corresponding to 59% inhibition of radiotracer uptake in the tumor tissue. At 48 h p.i., the blocking effect was slightly more pronounced, reaching 69% (bottom left). In contrast, the detected muscle uptake was low with SUV_{mean} 0.35 ± 0.05 at 2 h p.i., 0.56 ± 0.04 at 24 h p.i. and 0.66 ± 0.04 (all n=5) at 48 h p.i.. As shown in Figure 2.4. (bottom right), there was no significant change in muscle tissue uptake in the presence of 1 mg panitumumab.

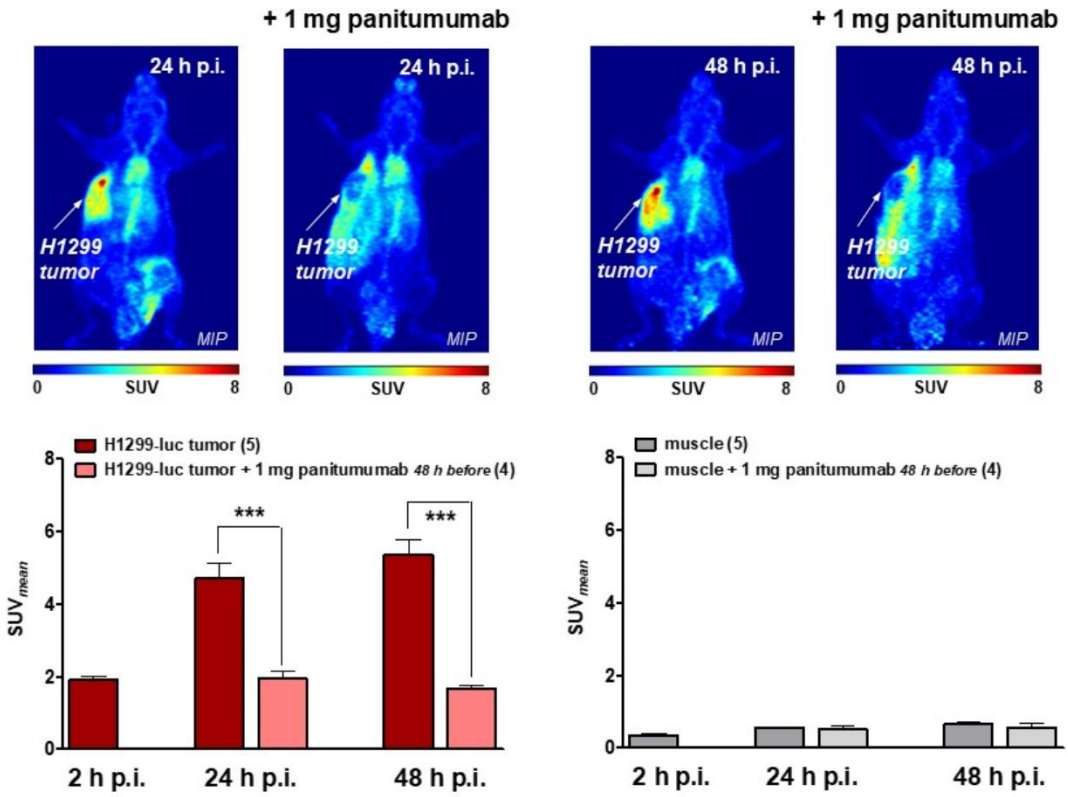

Figure 2.4. Top: Representative PET images as maximum intensity projections (MIP) of a H1299-luc+ subcutaneous tumour-bearing NSG mouse at 24 and 48 h after injection of ^{64}Cu-NOTA-panitumumab. Bottom: SUVmean values for radiotracer uptake into the tumour (left) and muscle tissue (right) and effects of administration of 1 mg panitumumab.

Data are shown as mean ± SEM. * considered significantly different between tumor uptake of ^{64}Cu-NOTA-panitumumab in the presence and absence of panitumumab p<0.001.**

The metastatic tumor model was generated by intravenous injection of H1299-luc+ cells into the tail vein of NSG mice. Six weeks after tumor cell injection, [^{18}F]FLT-PET scans were performed to analyze and confirm the presence of H1299-luc+ tumors. Figure 2.5. (top) displays PET images of two mice measured with [^{18}F]FLT at 2 h p.i. and subsequent ^{64}Cu-NOTA-panitumumab at 24 and 48 h p.i.. [^{18}F]FLT PET images revealed the presence of multiple tumor lesions in lung and liver tissue. Immuno-PET with ^{64}Cu-NOTA-panitumumab visualized the tumor lesions in more detail in these mice. In these metastatic H1299-luc+ tumor mice, all visible tumor lesions were analyzed for their uptake of ^{64}Cu-NOTA-panitumumab and mean SUV_{mean} values were calculated (Figure 2.5, bottom diagrams).

SUV_{mean} values in tumors reached 5.55 ± 0.34 after 24 h p.i. and 6.28 ± 0.46 after 48 h p.i. (both n=23 lesions from 6 mice). Pre-injection of 1 mg panitumumab (48 h before radiotracer injection) revealed SUV_{mean} values of 2.53 ± 0.10 after 24 h p.i. and 2.31 ± 0.15 after 48 h p.i. (both n=15 lesions from 4 mice) corresponding to a blocking effect of 54 and 63%, respectively (Figure 2.5).

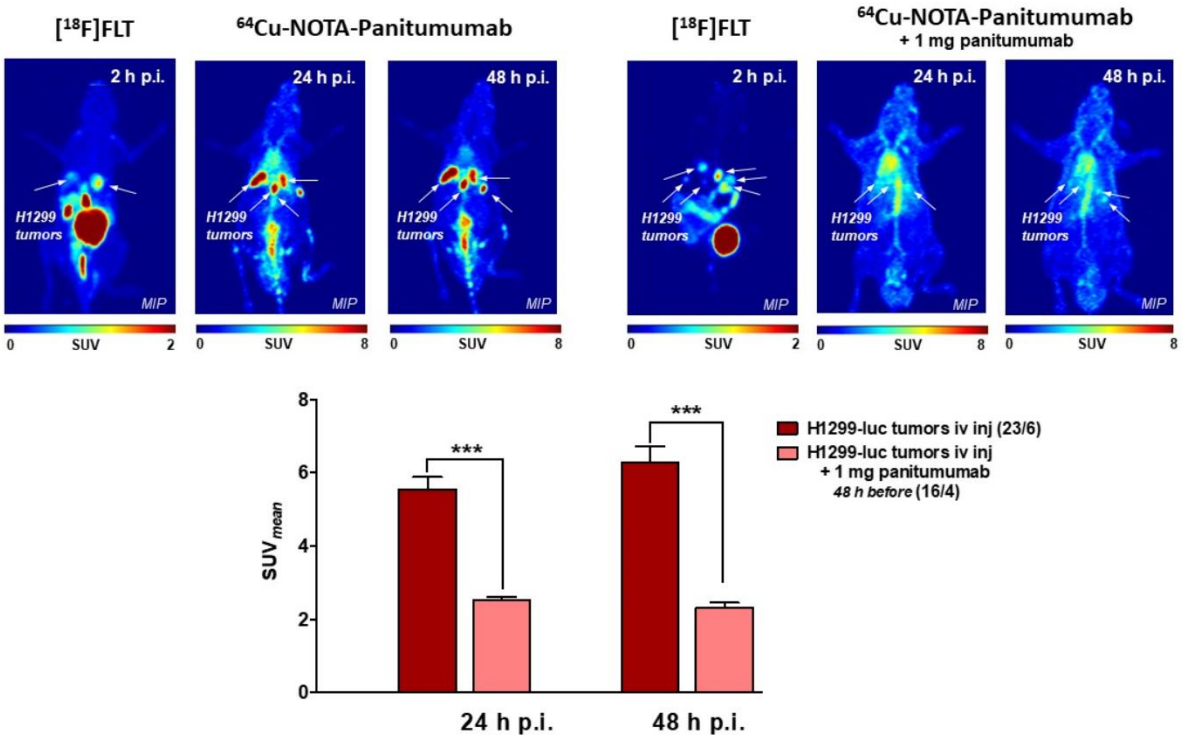

Figure 2.5. Top: Representative PET images as maximum intensity projections (MIP) at 2 h p.i. of [^{18}F]FLT and 24 h and 48 h p.i. of ^{64}Cu-NOTA-panitumumab in the absence (left) and presence (right) of 1 mg panitumumab in orthotopic metastatic H1299-luc+ tumour-bearing NSG mice. * considered significantly different between tumor uptake of ^{64}Cu-NOTA-panitumumab in the presence and absence of panitumumab $p<0.001$.**

2.3.4. *Ex vivo* biodistribution assessments

Biodistribution experiments using ^{64}Cu-NOTA-panitumumab were carried out in both the subcutaneous and the metastatic H1299-luc+ tumor models to verify and confirm PET imaging experiments, especially regarding the metastatic tumor model as well as for absolute quantification of the tumor uptake data. Table 2.1 summarizes all biodistribution data in both models in the presence and absence of 1 mg panitumumab and compares them to non-tumor-bearing control NSG mice.

Table 2.1.Biodistribution of ^{64}Cu-NOTA-panitumumab in control (non-tumor bearing mice), metastatic and subcutaneous (S.C.) H1299-luc+ tumor-bearing male NSG mice at 48 h p.i. with or without administration of panitumumab. Data are shown as means ± SEM from n=1-5 experiments.

	Control *non-tumor bearing mice*	Metastatic H1299-luc+	Metastatic H1299-luc+ *+1 mg panitumumab*	Subcutaneous H1299-luc+	Subcutaneous H1299-luc+ *+1 mg panitumumab*
n number	4	4	5	4	5
Organ					
Blood	14.83 ± 2.33	7.27 ± 2.55*	12.86 ± 1.57*	4.02 ± 0.15**	6.82 ± 0.63**
Heart	5.26 ± 0.88	4.08 ± 0.73	4.74 ± 0.45	2.19 ± 0.11	2.99 ± 0.23
Lung	6.87 ± 1.36	7.20 ± 1.49	8.35 ± 0.80	3.64 ± 0.14	4.48 ± 0.49
Liver	10.32 ± 0.99	11.23 ± 0.98*n.s.*	10.41 ± 0.45*n.s.*	16.60 ± 0.64	16.26 ± 0.79
kidney (right)	4.77 ± 0.99	4.93 ± 0.43	4.39 ± 1.15	3.74 ± 0.09	3.60 ± 0.24
kidney (left)	4.83 ± 1.15	4.61 ± 0.29	4.94 ± 0.12	3.98 ± 0.22	3.59 ± 0.22
spleen	4.83 ± 0.40	4.30 ± 0.97	4.37 ± 0.48	4.44 ± 0.28	5.13 ± 0.88
stomach	1.34 ± 0.34	1.45 ± 0.27	1.64 ± 0.16	1.39 ± 0.05	1.22 ± 0.04
duodenum	3.54 ± 0.84	2.85 ± 0.26	3.33 ± 0.08	2.40 ± 0.08	2.20 ± 0.18
small intestine	2.62 ± 0.34	2.70 ± 0.18	2.89 ± 0.14	2.38 ± 0.09	2.11 ± 0.14
large intestine	2.46 ± 0.45	3.16 ± 0.62	2.98 ± 0.13	2.57 ± 0.05	1.92 ± 0.08
pancreas	1.97 ± 0.58	1.74 ± 0.17	2.76 ± 0.34	1.13 ± 0.07	1.25 ± 0.08
bone	1.86 ± 0.38	0.99 ± 0.17	1.10 ± 0.12	0.68 ± 0.08	0.86 ± 0.23
muscle	0.92 ± 0.31	0.62 ± 0.13	0.79 ± 0.14	0.42 ± 0.04	0.60 ± 0.06
brain	0.60 ± 0.17	0.39 ± 0.09	0.68 ± 0.10	0.26 ± 0.02	0.37 ± 0.06
fat	1.27 ± 0.29	0.86 ± 0.12	1.91 ± 0.32	0.42 ± 0.03	0.59 ± 0.02
lung tumours		4.95 ± 9.41 *(n=3)*	3.20 *(n=1)*		
liver tumours		29.44 ± 8.14*	8.35 ± 1.30*		
S.C. tumour				11.01 ± 0.72***	3.67 ± 0.33***
lung tumours T/M[1]		20.58 ± 13.35	5.74 *(n=1)*		
lung tumours T/B[2]		2.42 ± 0.99 *(n=3)*	0.42 *(n=1)*		
liver tumours T/M		53.22 ± 35.18*	10.04 ± 7.46*		
liver tumours T/B		5.97 ± 3.84	0.66 ± 0.18		
S.C. Tumor T/M				26.33 ± 3.90***	6.31 ± 0.71***
S.C. Tumor T/B				2.75 ± 0.41	0.54 ± 0.02

[1]tumor to muscle ratio

[2] tumor to blood ratio

** $p < 0.05$, **$p < 0.01$, *** $p < 0.001$n.s. - not significant between with and without preinjection of panitumumab.*

Interestingly, blood pool uptake of ^{64}Cu-NOTA-panitumumab was significantly higher in the presence of 1 mg panitumumab, indicating longer blood pool retention and delayed blood clearance of the radiolabelled EGFR targeting antibody. In the metastatic model, visible and dissectible tumor lesions were removed from lung and liver tissue and analyzed separately as lung and liver tumors, as shown in Table 1.

Three of the four tumor bearing mice in this model developed lung lesions, but only 1 out of 5 mice from the blocking group had a dissectible lung tumor. The overall results indicated a similar biodistribution of ^{64}Cu-NOTA-panitumumab in both models, which was in line with the PET imaging results. The only noticeable difference was detected for liver tissue, as the metastatic model showed higher liver uptake, which could be blocked by the administration of panitumumab (1 mg). However, this blocking effect was not detected in the subcutaneous model, suggesting that the observed effect is specific to the metastatic model, including smaller and larger liver lesions. Blocking of the subcutaneous tumors reached a 67% blocking effect at 48 h p.i. (controls 11.01 ± 0.72 (n=4) *versus* blocked 3.67 ± 0.33 (n=5) % ID/g). Blocking of liver tumors in the metastatic model resulted in a 72% blocking effect (controls 29.44 ± 8.14 (n=4) *versus* blocked 8.35 ± 1.30 (n=5) % ID/g), respectively. The n=1 blocked lung tumor resulted in a 79% blocking effect. Taken together, blocking with 1 mg panitumumab proved the specificity of ^{64}Cu-NOTA-panitumumab uptake in metastatic and subcutaneous EGFR-expressing H1299-luc+ tumor lesions.

Figure 2.6 presents tumor-to-muscle (T/M) and tumor-to-blood (T/B) ratios for the uptake of ^{64}Cu-NOTA-panitumumab in both tumor models as determined from the *ex vivo* biodistributions. The blocking effect of 1 mg panitumumab per mouse administered 48 h before the radiotracer injection was significant ($p<0.05$) for T/M and T/B ratios in the subcutaneous and liver tumors in the

metastatic models. Only one mouse in the blocking group had a visible and dissectible lung lesion displaying a remarkably lower uptake.

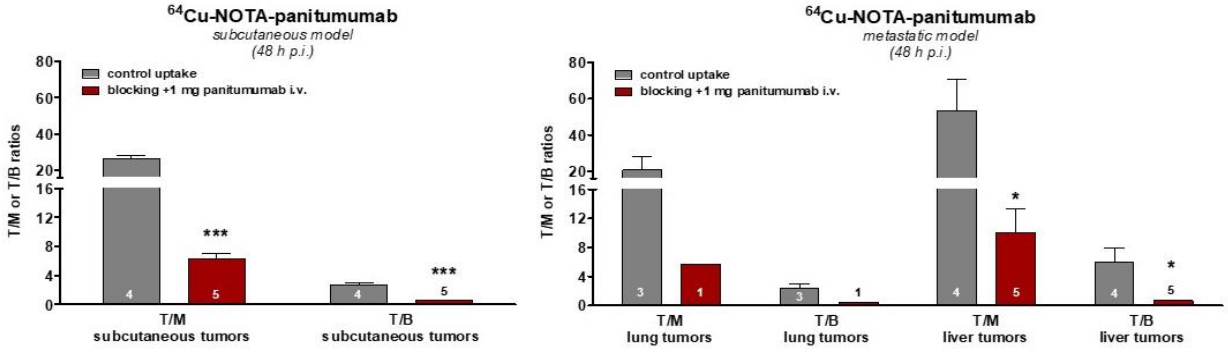

Figure 2.6. Tumor-to-muscle (T/M) and tumor-to-blood (T/B) ratios for uptake of ^{64}Cu-NOTA-panitumumab in H1299-luc+ tumor-bearing mice in the absence (control) or presence (blocking with 1 mg panitumumab) after 48h p.i. and determined from ex vivo biodistribution experiments. Left: subcutaneous tumor model; Right: metastatic tumor model. Data are shown as mean ± SEM from n animals (n numbers are shown in the diagrams).* $p<0.05$, *** $p<0.001$ as tested with unpaired student's t-test between control uptake and mice preinjected with 1mg panitumumab.

2.4. Discussion

In the presented work, metastatic and subcutaneous EGFR+ NSCLC mouse models were developed and analyzed with immunoPET and biodistribution studies using ^{64}Cu-labelled EGFR-targeting antibody ^{64}Cu-NOTA-panitumumab. Radioligand ^{64}Cu-NOTA-panitumumab uptake and retention were analyzed in NSCLC H1299-luc+ cells and tumors with and without pharmacological doses of panitumumab to demonstrate EGFR specificity. ^{64}Cu-NOTA-panitumumab provided PET images with high target-to-background ratios for detecting subcutaneous and metastatic tumors in both EGFR+ models. The results confirm that the EGFR-targeting antibody panitumumab is suitable for decorating nanoparticles such as Poly(ethylene oxide)-*b*-poly(α-benzyl-carboxylate-ε-caprolactone) (PEO-PBCL) (146) to deliver chemotherapeutic drugs also to metastatic EGFR expressing lesions.

Orthotopic NSCLC animal models reported in the literature were mainly developed by injecting NSCLC cancer cells into lung lubes or implanting tumors directly into lung tissue (150–155). Disadvantages of these models include that the cancer cells do not penetrate deeper into the lung tissue, only develop at the local injection site, and may only affect the immediate surrounding areas.

In contrast, the development of NSCLC models via direct intravenous injection leads to a more profound invasion of cancer cells, more comparable to that of metastatic lung cancer development in patients (156). The used mouse strain and cancer cells impact the development and growth of NSCLC tumor models through intravenous injection. The importance of cell lines and mouse strains for the development of orthotopic tumor models was extensively discussed by Jarry *et al.* (156), which helped us to successfully develop the metastatic tumor model using NSG mice and

EGFR+ H1299-luc+ cells. The absence of functional natural killer cells in NSG mice plays a crucial role in successful development of a metastatic lung cancer model (38).

Different immuno-PET radioligands have been used to detect NSCLC tumors by targeting various biomarkers, including CD8, activated T cells, PD1 and EGFR (157). Clinically used EGFR-binding monoclonal antibody panitumumab was previously radiolabeled with ^{89}Zr and used for diagnostic PET in EGFR-expressing tumors and monitoring therapeutic effects (64,158,159). ^{64}Cu was also used to prepare EGFR-targeting immuno-PET radioligands, including ^{64}Cu-DOTA-panitumab for PET imaging of head-and-neck cancer (160) and a ^{64}Cu-labelled panitumumab F(ab')$_2$ for PET imaging of pancreatic cancer (161) and monitoring response to radiotherapy (162).

We prepared ^{64}Cu-NOTA-panitumumab as a novel immuno-PET radioligand to systematically evaluate metastatic *versus* subcutaneous EGFR-expressing NSCLC models as a pre-requisite for the development of panitumumab-based radiotheranostics and panitumumab-decorated nanoparticles such as PEO-PBCL (146) for enhanced specific delivery of chemotherapeutic drugs to metastatic EGFR expressing lesions.

^{64}Cu-NOTA-panitumumab was able to detect EGFR+ tumors in both the subcutaneous and metastatic cancer models. Overall tumor uptake was ~20% (PET) and ~60% (biodistribution) higher in the metastatic lesions *versus* subcutaneous tumors. This observation can be explained by the dominant location of metastatic lesions in the liver, leading to a higher blood supply of liver metastases through better blood circulation in the liver. The determined tumor-to-muscle ratios from the PET and biodistribution studies further support that observation.

This observation also suggests that the tested metastatic liver model is suitable for evaluating EGFR-targeting radiolabeled immunoconjugates as immuno-PET and radiotheranostic

radiopharmaceuticals for imaging and therapy of cancer and for developing EGFR-targeting drug-loaded nanoparticles for directed and controlled drug delivery.

The specificity of ^{64}Cu-NOTA-panitumumab tumor uptake was confirmed by blocking experiments with panitumumab. In the PET experiments, blocking reached ~70 % in the subcutaneous and ~65% in the metastatic H1299-luc+ model at 48h p.i.. *Ex vivo* biodistribution experiments confirmed similar blocking effects, indicating a 30-35% tumor uptake of ^{64}Cu-NOTA-panitumumab by the enhanced permeability and retention (EPR) effect. The EPR effect is a crucial contributor to the overall tumor uptake using radiolabeled immunoconjugates in solid tumors, including radiotheranostics and antibody-decorated nanoparticles for targeted therapy and drug delivery (163).

Radioligand [^{18}F] FLT proved to be a valuable tool for detecting the presence of metastases in the intravenously injected NSCLC cells in mice. [^{18}F] FLT-PET was able to detect lesions in lung and liver tissue; however, ^{64}Cu-NOTA-panitumumab enabled more precise detection of lesions due to the EGFR-specific targeting capacity of the immuno-PET radioligand compared to radioligand [^{18}F] FLT measuring cell proliferation. [^{18}F] FLT-PET is suitable for detecting proliferating metastatic H1299-luc+ lesions. In contrast, immuno-PET with ^{64}Cu-NOTA-panitumumab allows for a more detailed analysis of EGFR expression in tumors as crucial biochemical information for targeted imaging and therapy of EGFR-expressing tumors like NSCLC using radiotheranostics and nanoparticles.

2.5. Conclusion

Our work describes a metastatic NSCLC mouse model generated by intravenous injection of EGFR+ H1299-luc+ cells in NSG mice. Immuno-PET radioligand ^{64}Cu-NOTA-panitumumab was used to analyze EFGR-expressing tumors in mouse subcutaneous and metastatic NSCLC tumor models. ^{64}Cu-NOTA-panitumumab was specifically accumulated and retained in EGFR+ NSCLC tumors, as confirmed by panitumumab blocking studies.

Ex vivo biodistribution experiments confirmed immuno-PET imaging data and the suitability of immuno-PET with ^{64}Cu-NOTA-panitumumab to detect metastatic NSCLC lesions in the liver and lung tissue. EGFR-specific antibody panitumumab is a suitable targeting vector for developing radiotheranostics and EGFR-targeting nanoparticles for directed and controlled drug delivery for targeted imaging and therapy of NSCLC.

Chapter 3

SPECT/CT imaging of EGFR-positive head and neck squamous cell carcinoma patient derived xenografts with ^{203}Pb-PSC-panitumumab in NRG mice – potential application in a radiotheranostic approach with ^{212}Pb-PSC-panitumumab

A version of this chapter has been submitted for publication

3.1. Introduction

Targeted radionuclide therapy (TRT) is a widely used cancer treatment option that employs radiopharmaceuticals to target and deliver ionizing radiation to kill cancer cells (1–3). TRTs have been used for cancer therapy demonstrating increased overall survival as exemplified in patients with thyroid cancer, prostate cancer, and neuroendocrine tumors (4). As a frontline type of current cancer therapy, TRT delivers a therapeutic dose of radiation to cancer cells using radioactive drugs (radiopharmaceuticals) labelled with alpha(α)- or beta(β-)-emitting radioisotopes (3,5). TRT with α emitters (α-TRT) offers several advantages compared to β- emitters, mainly due to the delivery of high-energy α-particles (5-9 MeV) to the tumor with a short pathlength (50-100 μm) and high linear energy transfer (LET) (80 keV/μm), causing less toxicity to neighboring healthy tissues (6). However, radiopharmaceuticals for α-TRT cannot directly be used for imaging applications *in vivo* to assess their biodistribution and target binding and retention profile as crucial criteria for patient selection and dose calculation in the clinical setting (7). The development and application of radiopharmaceuticals combining targeted imaging and therapy, also called radiotheranostics, represents a rapidly evolving field in oncologic nuclear medicine (8,9). Ideal radiotheranostics use different radioisotopes for imaging and therapy of the same chemical element to ensure similar pharmacokinetics, metabolism and biodistribution patterns (1,8). Typical examples of ideal radionuclide pairs in radiotheranostics include ^{64}Cu/^{67}Cu, ^{86}Y/^{90}Y, ^{124}I/^{131}I, ^{152}Tb/^{161}Tb, ^{133}La/^{135}La and ^{203}Pb/^{212}Pb (10–13). In addition, physical half-life, availability, and production costs also require special consideration in the design and development of radiotheranostics (14).

The ^{203}Pb/^{212}Pb radionuclide pair has recently gained much attention for developing radiotheranostics for TRT (11,12). ^{203}Pb emits γ-photons through electron capture, allowing

detection with single-photon emission computed tomography (SPECT) for diagnostic imaging, whereas ^{212}Pb decays by emitting β-particles and α-particles suitable for delivering therapeutic doses of radiation to cancer cells (12,13).

Targeting vectors in radiotheranostics for TRT encompass small molecules, peptides, antibodies, and nanoparticles (4). Among the targeting vector landscape, monoclonal antibodies (mAb) display exceptional target specificity, making mAb excellent candidates for TRT.

However, their relatively high molecular weight (~150 kDa) results in a long biological half-life (slow distribution and elimination profile), which must be matched with a compatible physical half-life of the radionuclide (15). Several radiolabeled mAb are on the frontline of radioimmunotherapy (RIT), demonstrating promising results in the clinic for targeting cancer biomarkers epidermal growth factor receptor (EGFR), prostate-specific membrane antigen (PSMA), and human epidermal growth factor receptor 2 (HER2) (16,17).

Panitumumab is an FDA-approved human monoclonal antibody specific to EGFR used as a single drug or in combination with other drugs to treat certain types of colorectal cancer (CRC), especially for the treatment of metastatic colorectal carcinoma with disease progression. Panitumumab binds to the extracellular domain of the EGFR, preventing EGFR dimerization and, thus, halting ligand-induced receptor autophosphorylation and intracellular signaling pathway activation (18). EGFR is overexpressed in many solid tumor cancers, including colorectal cancer (CRC), head and neck squamous cell carcinoma (HNSCC), non-small cell lung cancer (NSCLC) and breast cancer (19,20). Several studies demonstrated the relationship between EGFR overexpression and survival rate in these cancers: as EGFR expression increased, survival decreased (21), making EGFR a promising target for TRT of solid tumors.

Herein we describe the radiolabeling of panitumumab with ^{203}Pb using novel bifunctional chelating agent 2,2'-(4-(2-amino-2-oxoethyl)-10-(2-((4-isothiocyanatobenzyl)amino)-2-oxoethyl)-1,4,7,10 tetraazacyclododecane-1,7-diyl) diacetic acid (PSC-NCS) (11). Immuno-SPECT radioligand ^{203}Pb-PSC-panitumumab was evaluated using SPECT and biodistribution studies in NRG mice bearing subcutaneous (s.c.) HNSCC patient-derived xenografts (PDX). Our work using ^{203}Pb-PSC-panitumumab provides critical data for developing and testing ^{212}Pb-PSC-panitumumab for future TRT applications using $^{203/212}$Pb-PSC-panitumumab radiotheranostics.

3.2. Materials and Methods

3.2.1. Materials

Methoxy poly(ethylene oxide) (mPEO, 5 kDa) was purchased from Sigma (St. Louis, MO, USA) other used solvents such as Tetrahydrofuran (THF), all other chemicals were also purchased from Sigma (St. Louis, MO, USA) otherwise indicated. Maleimide polyethylene oxide (mal-PEO, 5 KDa) was obtained from JenKem Technology Inc. (Allen, USA). α-carbon modified-ε-caprolactone monomers (α-benzyl carboxylate-ε-caprolactone, BCL), that was synthesized based on previously reported methods (22), were obtained from Alberta Research Chemicals Inc. (Edmonton, Canada). Moreover, Stannous octoate was purchased from MP Biomedicals Inc. (Tuttlingen, Germany) and purified by vacuum distillation. Also, S-2-(4-Aminobenzyl)-1,4,7,10-tetraazacyclododecane tetraacetic acid (NH_2-Bn-DOTA) was purchased from Macrocyclics, USA. Panitumumab (Vectibix® 20mg/mL) was generously gifted by Edmonton's cross cancer institute pharmacy.

3.2.2. Production of ^{203}Pb

^{203}Pb was produced using a recently published procedure (11). Briefly, ^{205}Tl metal (99.9% isotopic enrichment) targets were irradiated at 23.3 MeV on a TR-24 cyclotron at currents up to 60 μA to produce ^{203}Pb via the ^{205}Tl(p,3n)^{203}Pb nuclear reaction. Following a cool-down period of >12 hours, targets were removed and irradiated 205Tl dissolved in 4 M HNO3. A NEPTIS Mosaic-LC synthesis unit performed automated separation using Eichrom Pb resin, and ^{203}Pb was eluted using 8 M HCl or 1 M NH4OAc. Purified ^{203}Pb yields of up to 12 GBq were attained (15.8 GBq at EOB). The [^{203}Pb]$PbCl_2$ and [^{203}Pb]$Pb(OAc)_2$ products contained no detectable radionuclides impurities besides ^{201}Pb (<0.1%), and <0.4 ppm stable Pb. ^{205}Tl metal was recovered with a 92% batch yield.

3.2.3. Preparation of ^{203}Pb-PSC-panitumumab radioimmunoconjugate

All glassware was rinsed with ultra-pure HCl (Fisherbrand, A508-P500). Trace metal-based ultra-pure chemicals for buffer preparations were purchased from Sigma Aldrich. All buffer solutions were treated with biotechnology-grade Chelex 100 (Bio-Rad, 143-2832).

3.2.4. PSC functionalization of panitumumab and radiolabeling with [^{203}Pb]Pb(OAc)2

2,2'-(4-(2-amino-2-oxoethyl)-10-(2-((4-isothiocyanatobenzyl)amino)-2-oxoethyl)-1,4,7,10-tetra-azacyclododecane-1,7-diyl) diacetic acid (PSC-NCS) chelator (200 µg) was dissolved in 50 µL of 0.1M NaHCO3 (pH = 9.0) and added to 400 µL panitumumab (Vectibex ® 20 mg/mL). The pH was adjusted to 8.0 and left on a thermoshaker set at 800 rpm and 30 °C for 2.5 hours.

The samples were purified via size exclusion chromatography (Bio-Rad 10DG desalting column, USA), which was pre-equilibrated and eluted with 0.025 M NaOAc buffer (pH=5.5). The antibody concentration of each fraction was measured using nanodrop (Thermo Scientific, NanoDrop OneC), and the fraction with the highest concentration was submitted for matrix-assisted laser desorption/ionization (MALDI) to assess the number of PCS chelators per antibody (~5 chelators per antibody). [^{203}Pb]Pb(OAc)$_2$ (150-200 MBq) was added to PSC-panitumumab (200 µg), and the reaction was kept at room temperature for 5-10 minutes at pH=5.

Radio-thin layer chromatography (radio-TLC) analysis (AR-2000, Eckert and Ziegler) was used to determine ^{203}Pb incorporation efficiency by spotting samples on silica plates and using 20 mM EDTA and 0.2 M NaOAc as the mobile phase; in this system, the Rf for [^{203}Pb]Pb(OAc)$_2$ will be 1.0 and for ^{203}Pb-PSC-panitumumab will be zero (13). ^{203}Pb-PSC-panitumumab was purified on

an Econo-Pac 10DG desalting column pre-equilibrated with 0.025 M sodium acetate, pH 5.5 used as the eluant.

Elution fractions (300 µL) were collected from the column, and the radioactivity was measured using an Atomlab 400 dose calibrator (Biodex, Shirley, NY, USA). Laemmli buffer (Bio-Rad, USA) was added to ^{203}Pb-PSC-panitumumab, and the samples (15 µL) were incubated at 95 °C for 5 minutes. Then, the samples were loaded on SDS-PAGE (Bio-Rad, Mini-PROTEAN® TGX™ Precast Protein Gels) and ran at 120 V. The gel was imprinted on film and evaluated by autoradiography on a BAS-5000 phosphor imager (Fujifilm).

3.2.5. Synthesization of poly(ethylene glycol)-block-poly(α-benzyl carboxylate-ε-caprolactone) and maleimide-Poly(ethylene glycol)-block-poly(α-benzyl carboxylate-ε-caprolactone) polymers

Poly(ethylene glycol) poly(α-benzyl carboxylate-ε-caprolactone) (PEO-PBCL) and maleimide-Poly(ethylene glycol)-block-poly(α-benzyl carboxylate-ε-caprolactone) (mal-PEO-PBCL) polymers were prepared based on the previously reported method (22).

In summary, either mPEO or mal-PEO and BCL were weighted in an ampule with the mol/mol ratio of 1:30 respectively. Following that, three drops of stannous octoate were added, and the ampule was sealed by flame after being connected to the vacuum line. The sealed ampule underwent a 4-hour heating process in a either 120°C or 140 °C oven for synthesization of mal-PEO-PBCL or PEO-PBCL respectively. The ampule contents were dissolved in dichloromethane and added to hexane to purify the polymers. A portion of the synthesized polymers were dissolved in deuterated chloroform and subjected to ^{1}H NMR analysis for characterization. The polymers

underwent evaluation using a 600-MHz Bruker spectrometer (Bruker Instruments, Inc., Billerica, MA, USA). On the ^{1}H NMR spectrum the peak intensity of PEO (-CH2CH2O-, δ 3.65 ppm) to that of BCL (-OCH2-, δ 4.1 ppm) were compared (22,23)

3.2.6. Preparing surface functionalized polymeric NPs using a mixture of PEO-PBCL and Mal-PEO-PBCL

PEO-PBCL block copolymers self-assemble into nanostructures by a co-solvent evaporation method using acetone as the organic co-solvent (24,25). In the present work, we prepared NPs using a mixture of PEO-PBCL and mal-PEO-PBCL polymers. Briefly, 10 mg of mixture of polymers were weighted in a manner that the final prepared NPs contain 30% maleimide on their surfaces. After weighing polymers with 1:1.32 w/w ratio of PEO-PBCL to mal-PEO-PBCL respectively. Polymers were dissolved in acetone at a concentration of 40 mg/mL and added dropwise to 5 mL aqueous media under stirring (25). Then, the sample was left overnight for the acetone to evaporate. The prepared NPs were analyzed using dynamic light scattering (DLS) Zeta-Sizer Nano (Malvern Instruments Ltd., Malvern, UK) set at 25 °C with a scattering angle of 173°.

3.2.7. Modification of surface functionalized PEO-PBCL NPs with panitumumab

The modification of PEO-PBCL NPs with panitumumab was done based on previously reported method (26). In summary, to 1.4 mg of panitumumab, 0.025mg 2-immunothiolane was added and incubated for 1 hour with surface functionalized NPs prepared as described above at room temperature while being stirred. The unreacted 2-immunothiolane was removed by dialyzing the sample against PBS for couple of hours. Then, the thiolated panitumumab was added to prepared

polymeric NPs with the 1:100 mol/mol ratio respectively and left overnight on stirrer. The following day β-mercaptoethanol was added to the sample with 1:1 mol/mol ratio to maleimide-PEO-PBCL for neutralizing the unreacted maleimide. The excess β-mercaptoethanol was then removed with dialysis for an hour against PBS.

The unattached panitumumabs were removed via a Sepharose CL-6B® size-exclusion chromatography column by eluting the column with PBS pH 7.4. The eluted fractions were characterized by (DLS) as mentioned above and absorption spectroscopy at 280 nm using a nanodrop (Thermo Scientific, NanoDrop OneC).

3.2.8. Radiolabeling panitumumab modified PEO-PBCL with with [^{203}Pb]Pb(OAc)$_2$

The radiolabeling process of panitumumab modified PEO-PBCL NPs was performed based on previously reported method (24). Briefly, to 20 µg of S-2-(4-Aminobenzyl)-1,4,7,10-tetraazacyclododecane tetraacetic acid (DOTA-Bn-NH2) dissolved in 2 µL of NH_4OAc (0.025mM, pH 5.5), [^{203}Pb]Pb(OAc)$_2$ was added and left for 15 minutes at room temperature. The chelation of 203Pb was monitored by reverse phase radio-TLC with using MeOH/1 M NH4OAc (9:1) as mobile phase with the ^{203}Pb labeled chelator having an Rf ≈ 0.3. Then, this mixture was cooled to 0 °C by placing in ice bath and set to pH of 1 by adding ~100 µL of 1 N HCl (tracemetal grade). Followed by addition of 10 µL of 2M sodium nitrate aqueous solution. After 5 minutes, the panitumumab decorated PEO-PBCL NPs were added to the solution with simultaneous increase in pH to ~8.5 by adding 1M NaOH. The reaction was left for 30 minutes on ice and the efficiency was monitored with reverse phase radio-TLC. The ^{203}Pb labeled panitumumab modified PEO-PBCL NPs (^{203}Pb-DOTA-panitumumab-NPs) were purified using size exclusion chromatography

(PD midiTrap® G-25, GE healthcare) eluting with PBS and collecting 300 µl fractions. The activity and purity of each fraction was measured using an Atomlab 400 dose calibrator and recerse phase radio-TLC.

3.2.9. Cell uptake studies

EGFR-expressing neck and neck cancer FaDu cells were cultured in a 5% CO_2 incubator at 37 °C in Gibco DMEM media supplemented with 10% fetal bovine serum (Gibco, USA) and 1% penicillin/streptomycin with media renewal 2-3 times per week. For cell uptake studies, the cells were seeded in 6-well plates and left in the incubator overnight. The media was removed, and 500 µL of Krebs-Ringer buffer solution (27) was added to each well, followed by the addition of 0.2 MBq of ^{203}Pb-PSC-panitumumab, and the plate was kept in the incubator at 37 °C at 5% CO_2. Cell uptake was terminated at 1, 5, 15, 30, 45, 60, and 90 min by adding ice-cold Krebs buffer and rinsing the wells twice to wash away unbound radioimmunoconjugates before lysing the cells with RIPA buffer. The cell lysates were transferred to scintillation vials and measured for radioactivity using a γ-counter (Wizard2® 2480 Automatic Gamma Counter, Perkin-Elmer, Canada). According to the manufacturer's recommendations, protein levels were quantified using a Pierce™ BCA protein assay kit. For blocking studies, the FaDu cells were co-treated with different amounts of unlabeled panitumumab (0.5-10 µg) and 0.2 MBq of ^{203}Pb-PSC-panitumumab. Cell uptake levels were normalized to percent of the total amount of radioactivity per milligram of protein (% radioactivity/mg protein) and plotted as a function of time. All experiments were performed in triplicates.

3.2.10. Immunoreactivity

The immunoreactivity of ^{203}Pb-PSC-panitumumab was assessed by a cell binding assay with EGFR-expressing FaDu cells using the Lindmo et al. method (28). FaDu cell concentrations of 0.25, 0.5, 1, 2, 3, 4, and 5 x10^6 were prepared in 500 µL of PBS and 1% bovine serum albumin (Sigma, USA). Then, 20,000 cpm of 203Pb-PSC-panitumumab was added to each cell concentration. The samples were placed on a rocker for one hour at room temperature. After triplicate PBS washes, the samples were transferred to 1.5mL LoBind® tubes (Eppendorf, USA), and by using a γ-counter (Wizard2® 2480 Automatic Gamma Counter, Perkin-Elmer, Canada), the counts of each sample were determined.

The radioactivity data obtained was corrected in the background and compared to counts from the total activity added to control samples in the experiments. The immunoreactive fraction was calculated by performing a linear regression analysis on a double-inverse plot of (total/bound) activity versus normalized cell concentration.

3.2.11. Xenograft models

A primary tumor specimen (#391) was surgically obtained from a patient with HNSCC under a protocol approved by the Research Ethics Board at the University Health Network (Protocol No. 12–5639). This tumor was dissected into small fragments (~ 1 mm^3) and engrafted subcutaneously (s.c.) on the right flank of NOD Rag2 γc (NRG) immunodeficient mice. These patient-derived tumor xenografts (PDX) were serially propagated in NRG mice following an animal care protocol (No. 1542.28) approved by the Animal Care Committee at the University Health Network and

following Canadian Council on Animal Care guidelines. The PDX used in this study was between the 3rd to 5th passage from the initial engraftment of the HNSCC tumor in NRG mice.

3.2.12. SPECT/CT imaging

NRG mice were anesthetized using 2% isoflurane in O_2, and microSPECT/CT images were acquired in a supine position at 48 h and 120 h on a NanoScan® SPECT/CT/PET system (Mediso). Either ^{203}Pb-PSC-panitumumab or ^{203}Pb-DOTA-panitumumab-NPs (~10 MBq; 140 μL) were injected into the tail vein of NRG mice engrafted with subcutaneous HNSCC PDX. Mice were divided into two study groups: A group of mice (n=3), was only injected with ^{203}Pb-PSC-panitumumab, and the other group (n=3) was injected with 1 mg of panitumumab 1 hour before administration of ^{203}Pb-PSC-panitumumab to block EGFR. SPECT/CT images were acquired 48 and 120 hours post-injection (p.i.) of the radioligand. Images were acquired in a 256 × 256 matrix.

A Mediso APT62 collimator (WB-HS standard) was affixed to each of the four detector NaI (TI) detector heads. Images were reconstructed by Monte Carlo methods with three subsets of data undergoing 48 iterations using the Mediso Nucline NanoScan acquisition and reconstruction software (version 3.00.020.0000). Before SPECT imaging, CT images were acquired with 50 kVp X-rays, 980 μA and a 300 msec exposure time. CT scans were reconstructed using the medium voxel and slice thickness settings, resulting in an isotropic voxel size of 250 μm. SPECT and CT were co-registered by the Mediso Nucline acquisition/reconstruction software. All animal studies were conducted under a protocol (AUP 2843.14) approved by the Animal Care Committee at the University Health Network following the Canadian Council on Animal Care guidelines.

3.2.13. Biodistribution studies

Mice were euthanized five days (120 h) after the injection of ^{203}Pb-PSC-panitumumab, and tissues and organs were collected, weighed, and radioactivity was counted in a γ-counter. The uptake was calculated as injected dose percentage per gram of each tissue (ID%/g). Two groups were studied for biodistribution experiments: 1) Mice (n=5) injected with ^{203}Pb-PSC-panitumumab, and 2) Mice (n=3) were injected with 1 mg of panitumumab one hour before the injection of ^{203}Pb-PSC-panitumumab to block EGFR.

3.2.14. Statistical analysis

All data are expressed as means ± SEM. Graphs were constructed using GraphPad Prism 4.0 (GraphPad Software). Where applicable, statistical differences were tested by unpaired Student's t-test and were considered significant for $p < 0.05$.

3.3. Results

3.3.1. Radiochemistry

MALDI analysis confirmed the conjugation of 4-5 PSC chelators per antibody by reacting the isothiocyanate group in PSC-NCS with lysine residues in panitumumab (Figure 3.1. A). PSC-conjugated panitumumab was used for radiolabeling with $[^{203}Pb]Pb(OAc)_2$, and the radiolabelling efficiency was measured with radio-TLC, indicating 99.2±0.7% incorporation of $^{203}Pb^{2+}$ (Figure 3.1. B and 1C) which is comparable to results obtained by Nelson *et al*. (164). SDS-PAGE analysis further confirmed incorporation of ^{203}Pb to panitumumab. Reductive SDS-PAGE conditions resulted in the formation of panitumumab light and heavy chains, which were visible at 25 and 50 kDa, respectively, indicating that both antibody portions were modified with the PSC chelator and labelled with ^{203}Pb (Figure 3.1. D).

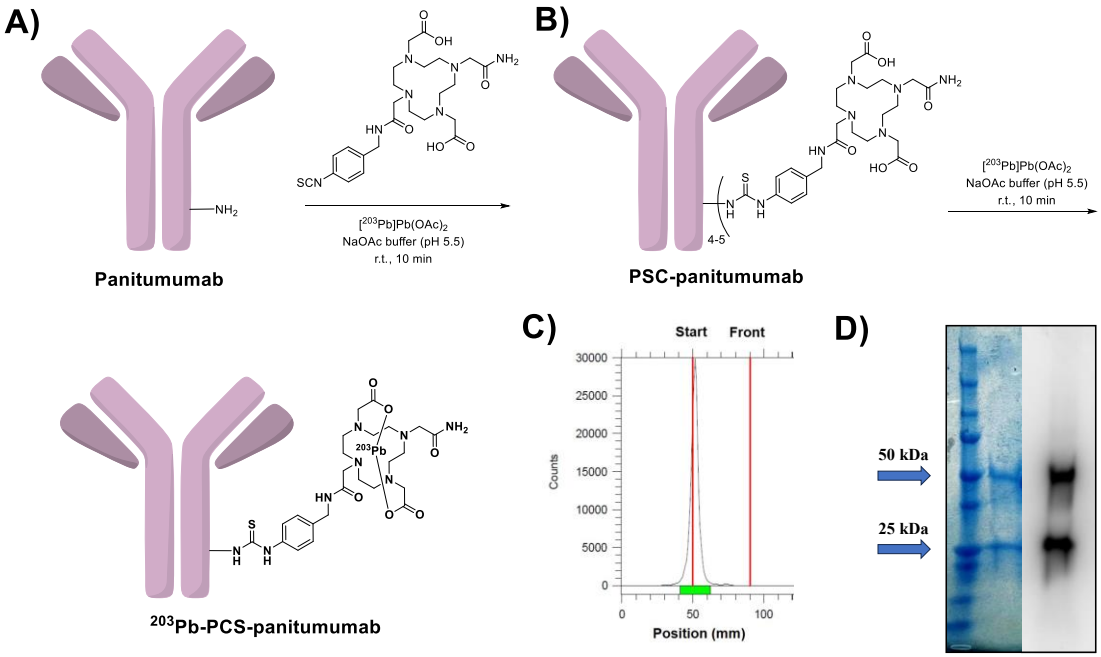

Figure 3.1. Synthesis and radiolabeling of PSC-conjugated panitumumab with ^{203}Pb (A and B) and measurement of $^{203}Pb^{2+}$ incorporation efficiency and radiochemical purity of purified ^{203}Pb-PSC-panitumumab by radio-TLC (C) and SDS-PAGE (D).

^{203}Pb-labeling and purification of radioimmunoconjugate ^{203}Pb-PSC-panitumumab provided isolated radiochemical yields of 41.5 ± 8 % (n = 5) at a molar activity of 1.2 ± 0.35 GBq/mg. The radiochemical purity of the isolated radioimmunoconjugates was greater than 99%, as analyzed by radio-TLC. Purified radioimmunoconjugates were >95% stable in human AB-type serum over 48 h.

3.3.2. Cellular uptake of ^{203}Pb-PSC-panitumumab

EGFR-expressing FaDu cells were incubated with ^{203}Pb-PSC-panitumumab, and cell uptake was measured at different time points. ^{203}Pb-PSC-panitumumab uptake in FaDu cells increased until it reached a plateau at 60 min (Figure 3.2. A). EGFR specificity of cellular uptake was confirmed with blocking studies using different amounts of panitumumab (0.5 µg – 10 µg), demonstrating 70%, 85%, and 95% blocking at 0.5 µg, 1 µg, 5 µg and 10 µg, respectively (Figure 3.2. B). The immunoreactive fraction of ^{203}Pb-PSC-panitumumab was found to be ~30%, which is lower than the reported 68% for ^{89}Zr-labelled panitumumab measured in MDA-MB-468 cells (165) (Figure 3.2. C).

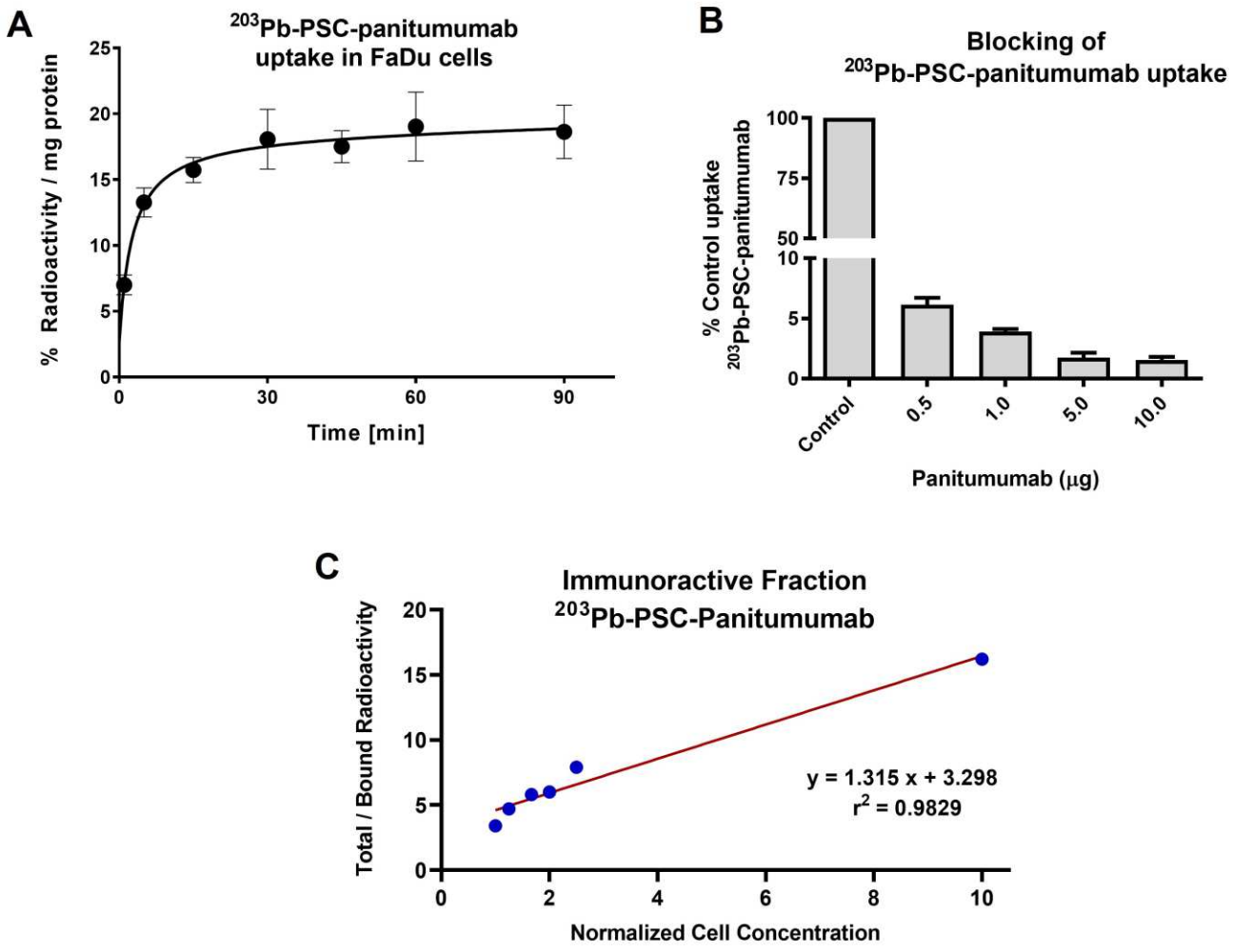

Figure 3.2. Cellular uptake of ^{203}Pb-PSC-panitumumab uptake in EGFR+ FaDu cells (A) and studies of ^{203}Pb-PSC-panitumumab binding competed with increasing amounts of panitumumab (B). Representative double inverse plot from Lindmo assay performed in FaDu cells with ^{203}Pb-PSC-panitumumab (C).

3.3.3. *In vivo* imaging (microSPECT/CT)

MicroSPECT/CT images were acquired to visualize the biodistribution of ^{203}Pb-PSC-panitumumab in NRG mice bearing subcutaneous EGFR+ HNSCC PDX tumors. EGFR specificity was tested with *in vivo* blocking studies by administering 1 mg of panitumumab before ^{203}Pb-PSC-

panitumumab injection to block EGFR (n=3). SPECT images were taken at two-time points of 48 and 120 hours p.i. of ^{203}Pb-PSC-panitumumab to monitor changes in tumor uptake and distribution of ^{203}Pb-PSC-panitumumab over time. The tumors were clearly visible in SPECT/CT images at both time points without noticeable radioactivity in other organs and tissues.

Under EGFR blocking conditions, SPECT/CT images after 48 h and 120 h indicated lower tumor uptake and somewhat increased radioactivity in the heart and blood pool. The remaining radioactivity observed in the tumor under blocking conditions at 48 and 120 h is presumably due to the EPR effect, as typically found in immunoPET and immune-SPECT experiments with solid tumors (166) (Figure 3.3).

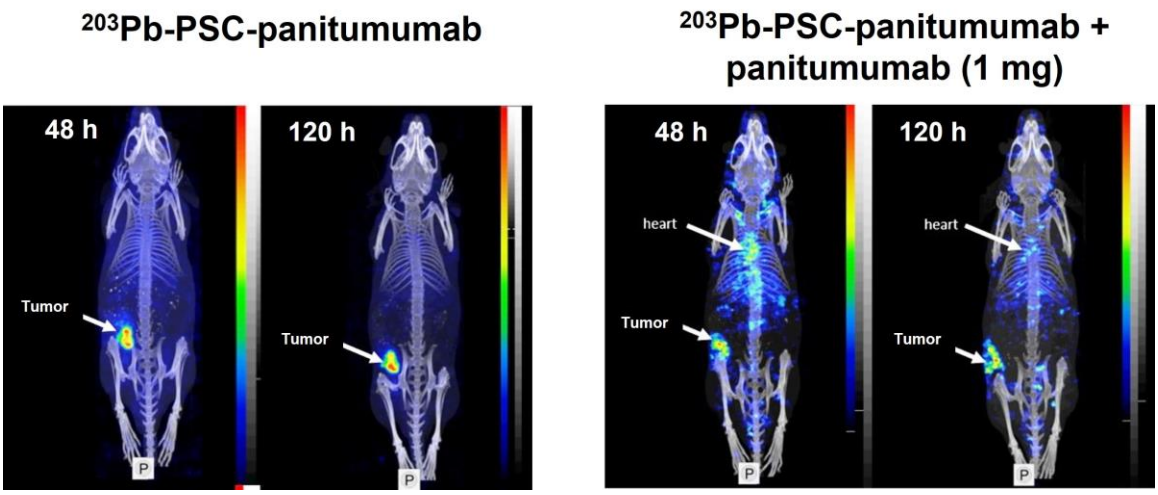

Figure 3.3. Representative SPECT/CT images of NRG mice engrafted with EGFR+ HNCC PDX at 48 and 120 h p.i. under control and blocking conditions. Tumors are highlighted with an arrow.

3.3.4. Biodistribution studies

NRG mice bearing EGFR+ PDX HNCC tumors were euthanized at 120 h p.i. either after ^{203}Pb-PSC-panitumumab (n=5) or 1 mg of panitumumab pre-injection with ^{203}Pb-PSC-panitumumab (n=5). The results (Table 3.1) indicated that baseline tumor uptake at 120 h p.i. was significantly higher (26±07 ID%/g) than in all other organs reaching tumor-to-blood (T/B) and tumor-to-muscle (T/M) radios of 4.2 and 37.3, respectively. Tumor uptake could be significantly reduced (6.2±1.0 ID%/g ($p<0.05$)) in mice pretreated with an excess panitumumab (1 mg) one hour before radiotracer administration.

In mice pretreated with panitumumab, tumor uptake was comparable to that of the blood at 120 min p.i. as represented by a T/B ratio of 0.94 at 120 h p.i. The remaining radioactivity in the tumor under EGFR-blocking conditions can be attributed to the EPR effect.

Table 3.1. Biodistribution of ^{203}Pb-PSC-panitumumab at 120 h p.i.

	PERCENT INJECTED DOSE PER GRAM (MEAN±SEM)	
Tissue	**^{203}Pb-PSC panitumumab (n=5)**	**^{203}Pb-PSC panitumumab + panitumumab (1 mg) (n=5)**
Blood	6.2±1.2	6.6±2.4
Heart	1.8±0.6	1.7±0.6
Lung	2.5±0.8	3.2±1.7
Liver	2.5±0.8	2.1±0.3
Kidney	1.8±0.4	2.1±0.7

Spleen	3.1±0.5	3.2±2.2
Pancreas	0.7±0.2	0.5±0.2
Stomach	0.7±0.2	0.6±0.3
Intestine	0.5±0.1	0.5±0.3
Muscle	0.7±0.3	0.7±0.3
Bone	1.1±0.3	0.9±0.4
Skin	1.3±0.5	1.4±0.4
Brain	0.1±0.0	0.2±0.1
Tumor	26.1±1.2	6.2±1.0
T/B ratio	4.2	0.94
T/M ratio	37.3	8.8

3.3.5. Polymer characterization

^{1}H NMR results confirmed that polymerization of BCL was successful for both reactions. However, some maleimide had fallen off the polymers during the reaction and it was revealed that ~70% of the maleimides remained on the synthesized mal-PEO- PBCL polymers. Also, the degree of polymerization of the BCL block for PEO-PBCL polymers and mal-PEO-PBCL were 29 and 24 respectively.

3.3.6. Characterization of panitumumab modified PEO-PBCL NPs

The size distribution results reported by DLS, for PEO-PBCL NPs showed one peak at 42.04 nm diameter with 100% intensity and PDI of 0.181 and for panitumumab modified NPs, one peak at 59.78 nm with 98.5% intensity and PDI of 0.335 was reported (Figure 3.4). Also, the count rates and antibody amount of collected fraction from the size exclusion chromatography column, indicated that 80% of the added panitumumab has been attached to NPs (Figure 3.5).

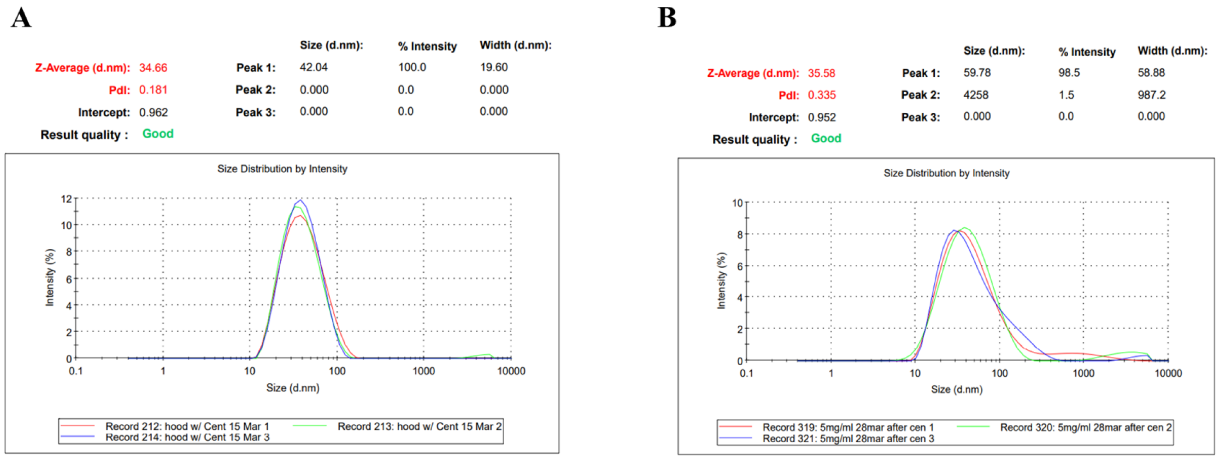

Figure 3.4. Size distribution measured by DLS for A) PEO-PBCL NPs and B) panitumumab modified NPs

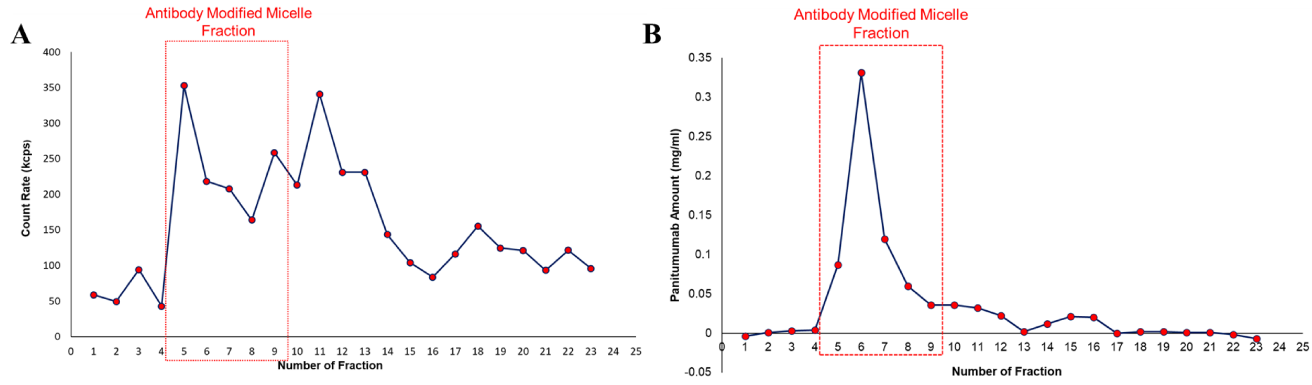

Figure 3.5. A) Count rate measured for each collected fraction from Sepharose® column by dynamic light scattering and B) Panitumumab concentration in each collected fraction from Sepharose® column by measuring their absorption at 280nm

3.3.7. ^{203}Pb labeling panitumumab modified PEO-PBCL NPs

The reverse-phase TLC results indicated that by attaching the ^{203}Pb-DOTA to panitumumab modified PEO-PBCL NPs, ~60% of the initially added ^{203}Pb will be attached to the panitumumab on the NPs surface. Also, after purification of the ^{203}Pb-DOTA-panitumumab-NPs by size exclusion chromatogaraphy column, ~27% of the initially added ^{203}Pb activity was retrieved as pure ^{203}Pb-DOTA-panitumumab-NPs.

3.3.8. *In vivo* imaging (microSPECT/CT) of ^{203}Pb-DOTA-panitumumab-NP

We used MicroSPECT/CT images to visualize the biodistribution of ^{203}Pb-DOTA-panitumumab-NP in NRG mice with EGFR+ HNSCC PDX tumors and have a mean of comparison with ^{203}Pb-PSC-panitumumab. To test EGFR specificity, *in vivo* blocking studies were performed. Prior to injection, a dose of 1 mg of panitumumab was given to block EGFR (n=3). The uptake and distribution of ^{203}Pb-PSC-panitumumab in tumors were monitored by taking SPECT images at two time points, 48 and 120 hours p.i. As shown in Figure 3.6 no radioactivity was observed at any of the time points within either of the study groups.

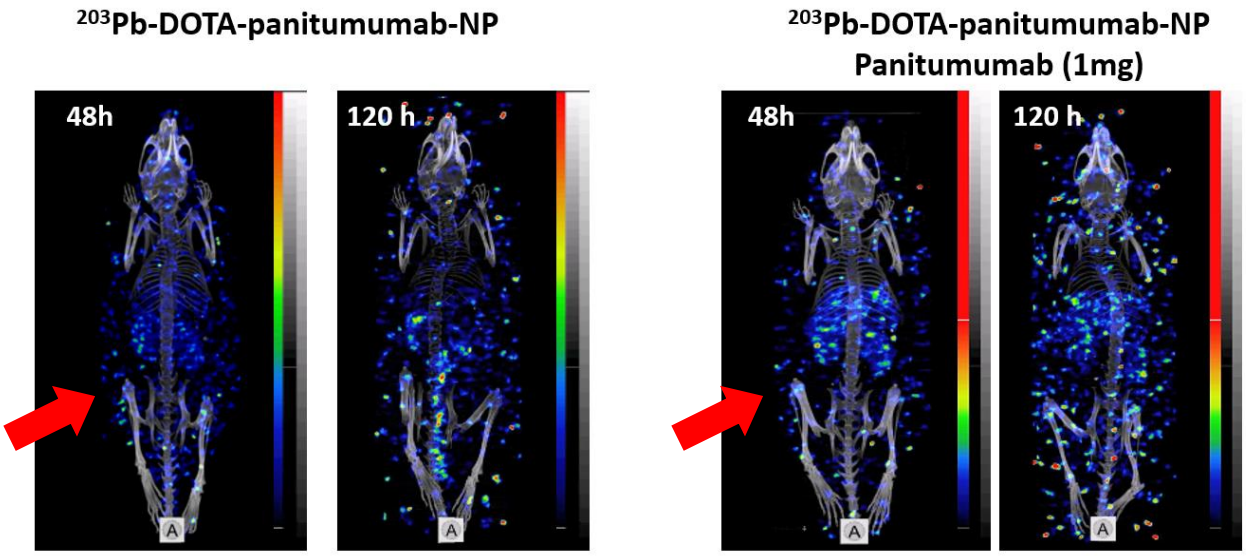

Figure 3.6. Representative SPECT/CT images of NRG mice engrafted with EGFR+ HNCC PDX at 48 and 120 h p.i. under control and blocking conditions. Tumors are highlighted with an arrow

3.4. Discussion

EGFR+ HNCC accounts for almost 90% of HNCC cases diagnosed in the clinic (167). This understanding offers EGFR as a suitable receptor to target head and neck cancer cells when developing radiotheranostics for HNCC. Creating a radiotheranostic pair using radionuclides of the same chemical element that targets EGFR provides a probe for imaging and treatment with similar pharmacokinetics, leading to similar biodistribution in EGFR+ tumors (147,168). As in the presented work, the uptake and biodistribution of ^{203}Pb-PSC-panitumumab was studied *in vitro* on EGFR+ HNCC FaDu cells as well as in mice bearing patient-derived xenografts which were taken from patients with EGFR+ HNCC.

Immuno-SPECT probe ^{203}Pb-PSC-panitumumab displayed EGFR-mediated uptake *in vitro* and *in vivo* with high tumor retention, enabling the detection of tumors at 48 h and 120 h p.i.. Previous reports in the literature for radiolabeling panitumumab with SPECT-detectable radioisotopes were labelling with ^{111}In (169) and ^{177}Lu(67); also, the Fab fragment of panitumumab was labelled with ^{177}Lu (170) and ^{99m}Tc (171); however, no previous studies describing labelling panitumumab with ^{203}Pb were reported. Antibody-based compounds such as trastuzumab (Herceptin) via DOTA (172), c8C3 via TCMC (149), and peptides such as α-melanocyte-stimulating hormone (173), and low molecular weight PSMA ligands (174) were labelled with ^{203}Pb using DOTA coordination chemistry. Also, the conditions required for labelling panitumumab with ^{111}In using diethylenetriamine-pentaacetic acid (DTPA) and/or ^{89}Zr using *p*-isothiocyanatobenzyl-desferrioxamine B included heating to 37 °C, and depending on the chelator administered, different reaction times of up to 4 h were required (175,176). Moreover, high temperatures (60-75°C) were reported for the radiolabeling of peptides with ^{203}Pb to achieve high incorporation efficiency with shorter incubation times (177,178). However, in the presented work, the PSC-NCS chelator labelling process did not require any elevated temperatures, and $^{203}Pb^{2+}$ incorporation proceeded with high efficiency (>99%) at short reaction times of 5-10 min at room temperature. The observed high labelling efficiency >99 aligns with previously reported data using PSC-NCS as a lead-specific bifunctional chelating agent for rapid coordination chemistry with $^{203}Pb^{2+}$ under mild conditions (164).

Figure 3.1. D indicates that both light and heavy chains of panitumumab are labelled with ^{203}Pb, confirming the bioconjugation of lysine residues through thiourea formation with the PSC-NCS chelator being present in both light and heavy chains of panitumumab (179). Modifying both heavy and light chains of panitumumab can also explain the only moderate immunoreactivity of ~30%

(Figure 3.2. C). However, ^{203}Pb-PSC-panitumumab still provided clear SPECT images for detecting EGFR+ HNSCC PDX tumors. The specific binding to EGFR was confirmed by blocking studies by pre-administering an excess of panitumumab. Also, ^{203}Pb-PSC-panitumumab provided several time points for SPECT/CT imaging by remaining in the tumor up to 120h post-injection in tumor-bearing mice. Our findings indicate that ^{203}Pb-PSC-panitumumab is a suitable SPECT probe with desirable biodistribution for EGFR+ HNCC.

^{203}Pb-PSC-panitumumab was taken up by FaDu cells, and the uptake could be reduced under blocking conditions in a concentration-dependent manner using panitumumab. SPECT/CT images acquired from tumor-bearing mice after the injection of ^{203}Pb-PSC-panitumumab allowed clear delineation of the tumor tissue, confirming high tumor uptake and retention of the radioligand in the EGFR+ HNSCC PDX model.

Our work aligns with reported PET and SPECT data in mice using ^{89}Zr-, ^{177}Lu- and ^{111}In-labelled panitumumab immunoconjugates (175–177), confirming that radioligand ^{203}Pb-PSC-panitumumab is a suitable immuno-SPECT probe for detecting EGFR+ tumors. The long physical half-life of ^{203}Pb ($t_{1/2}$ = 51.9 h) allows SPECT imaging protocols for several days at a high image quality.

The biodistribution data (%ID/g) in tissues and organs confirmed the SPECT/CT data in mice injected with ^{203}Pb-PSC-panitumumab. The highest radioactivity was measured in tumors (26.07±1.15) after 120 p.i. of ^{203}Pb-PSC-panitumumab, which is comparable to the radioactivity accumulation and retention in reported for LS-174T, SHAW and SKOV-3 xenografts using ^{111}In-CHX-A”-DTPA-panitumumab (175,180) and MDA-MB-468 xenografts using ^{89}Zr-labelled panitumumab (176). The observed biodistribution pattern was also similar to a study using ^{86}Y-

CHX-A"-DTPA-panitumumab in EGFR+ human colorectal, prostate, and epidermoid tumor xenografts (178). Radioactivity uptake in EGFR+ HNSCC PDX could be reduced by 75% by pre-dosing mice with panitumumab (1 mg), confirming EGFR-mediated uptake of radioligand ^{203}Pb-PSC-panitumumab. As panitumumab is a human antibody against human EGFR it does not bind to mouse EGFR; therefore, administering an excess of panitumumab before injecting ^{203}Pb-PSC-panitumumab will only block EGFR on the tumor. The remaining radioactivity amount (6.24±0.97 %ID/g) can be attributed to the EPR effect commonly observed during SPECT and PET imaging in solid tumors using radiolabeled immunoconjugates (181).

Our work with ^{203}Pb-PSC-panitumumab as a novel immuno-SPECT probe highlights the opportunity for developing $^{203/212}$Pb-PSC-panitumumab as ideal radiotheranostics for combined SPECT imaging and targeted alpha therapy of EGFR-expressing cancers. $^{203/212}$Pb radiotheranostics represent an attractive alternative to currently used ^{225}Ac-based radiotheranostics for targeted alpha therapy. The availability of ^{212}Pb through the emerging ^{224}Ra/^{212}Pb generator technology and the ideal radionuclide matching pair characteristics of radiometals ^{203}Pb and ^{212}Pb ensure identical coordination chemistry and identical biodistributions profiles of $^{203/212}$Pb radiotheranostics. This represents a significant advantage to currently used ^{225}Ac-based radiotheranostics for targeted alpha therapy relying on chemically different imaging surrogates, such as ^{133}La and ^{134}Ce (182).

However, the radiolabeled NPs did not remain in the mice body and could not detect the EGFR+ tumors in mice. This could be due to the fact that NPs were taken up by the reticuloendothelial systems (RES) (183) and washed away before the 48 hours SPECT/CT imaging time point.

Additionally, the chelator labeled with radioactivity could have been eliminated from the developed system and therefore removed by renal system of the animals. The chance of the radiolabeled panitumumab detaching from the NPs is low, as the results from the ^{203}Pb-PSC-panitumumab indicated accumulation and stay in the tumor for 120 hours.

As this method of labeling had shown successful detection of EGFR+ tumors *in vivo* by PEO-PBCL NPs modified with peptides against EGFR (146), we were not expecting for the ^{203}Pb-NOTA-panitumumab-NPs to be unstable *in vivo*.

3.5. Conclusion

In this study, panitumumab was successfully modified with PSC-NCS as a novel Pb-specific bifunctional chelating agent. PSC-decorated human antibody panitumumab was rapidly and reproducibly radiolabeled with $^{203}Pb(OAc)_2$ in good radiochemical yields under mild reaction conditions compatible with the structural and functional integrity of an antibody. Novel immunoSPECT probe ^{203}Pb-PSC-panitumumab showed EGFR-mediated uptake in FaDu cells and high uptake and retention in an EGFR+ HNSCC PDX model. EGFR-mediated uptake was confirmed by SPECT/CT and biodistribution studies using blocking experiments with panitumumab. Our work introduces ^{203}Pb-PSC-panitumumab as a novel immuno-SPECT probe for imaging EGFR+ tumors and an opportunity to develop $^{203/212}$Pb-PSC-panitumumab radiotheranostics for combined SPECT imaging and targeted alpha therapy of EGFR-expressing cancers. Panitumumab modified NPs did not show the expected biodistribution. Future studies should focus on modifying the chemical reactions and strategies used for the modification of NP surface with panitumumab.

Chapter 4

Glycan remodeling of panitumumab for developing radiolabeled targeted PEO-PBCL nanoparticles and its evaluation on metastatic non-small cell lung cancer

4.1. Introduction

Nanomedicines may offer improved solubility, stability, reduced side effects, as well as enhanced drug activity for the delivered medicine in cancer therapy (184). Nano-theranostics are nanotechnology-based systems that can not only provide the benefits of nanomedicine, but also act as imaging probes for diagnostic purposes. Nano-theranostics may be used to track the fate of nanomedicine in a living organism and identify cancerous lesions that can benefit from nanomedicine-based treatments. Nano-theranostics can also be used to optimize the timing and/or placement of anti-cancer treatment delivery based on the principles of precision medicine (185,186).

For decades, nanoparticles (NPs) were believed to achieve preferential accumulation in solid tumors by a mechanism known as the enhanced permeability and retention (EPR) effect (187). In recent years, active transport of NPs by tumor-associated endothelial cells which is mediated by the protein corona coating of NPs has been suggested as another major driver of NP tumor accumulation rather than passive EPR effect (187–189).

Cancer cell specific active targeting of NPs through their surface modification with ligands for receptors overexpressed by tumor cells or tumor vasculature has been reported extensively. Different ligands, including whole antibodies, antibodies fragments, peptides, aptamers, and carbohydrates have been used for this purpose (188). Among the available ligands, antibodies represent the highest specificity and binding affinity due to their two antigen-binding sites per molecule, making them a suitable candidate for NPs' surface modification (190). The challenge of using antibodies as ligands is their large size, extended half-life and control over their orientation

on the NP surface so that their interaction with the receptor of interest is not negatively affected following NP insertion (191).

A well-established method used to attach antibodies to NPs through covalent bonds, involves the thiolation of the lysine residue in the antibody's structure followed by the reaction of the thiolated antibody with maleimide poly (ethylene oxide) (PEO) modified NPs or NP components that are post inserted into NPs later. The main disadvantage of this approach is that it can lead to uncontrolled chemical modification of antibodies as the lysine residue can be in the variable and/or Fc region of the antibody. There are other methods for reaction of antibodies to NPs such as attachment through the amide bonds, adaptor molecules and physical adsorption (77).

If the antibodies are randomly orientated on the surface of the NPs, the antigen-binding site for the antibody may not be accessible for interaction with their receptor (192,193). Besides, the exposure of the Fc region to the biological milieu on the NP surface, may also mark the antibody-modified NPs for capture by the mononuclear phagocytic cells. To overcome this challenge, modifications such as adding a cysteine tail, to specific parts of antibodies away from their variable region responsible for receptor interaction, have been pursued in the literature (193). Addition of cysteine to the antibodies, can however, lead to the formation of disulphate bonds between the added cysteines and/or native cysteines on the antibody (192). Another option is the genetic modification of the antibody leading to the insertion of specific functional groups to the Fc region of the antibody. This approach, although effective, is very time consuming and would need sophisticated gene transfection technologies (192,194).

Alternatively, modification of the glycan groups represents another option that has been explored to introduce functionality to the Fc region of the antibodies for further chemical reactions (195).N-

glycans are located on asparagine-297 of the heavy chain (Fc) in immunoglobulin G (IgG) antibodies (196) which play a role in Fc-mediated functions such as cell-mediated cytotoxicity or complement-dependent cytotoxicity (197). These IgG antibodies have been reportedly modified by enzymes to develop antibody-drug conjugates (ADC) such as anti-CD 22 conjugated to doxorubicin (196), trastuzumab conjugated to SYNtansine (195) and trastuzumab conjugated to monomethyl auristatin E (198). During this synthesis approach, a portion of the glycan group is removed by an endoglycosidase enzyme. When using a glycosyltransferase enzyme, a functional group is added to the antibody which can further be involved in different chemical reactions (198,199).

Possible functional groups that can be added to antibodies through enzymatic modification, includes azides, alkynes, and ketones. Among these, azides are the most favorable ones as they are rarely available in biological settings and can be added to different substrates by various chemical reactions such as copper(I)-catalyzed/alkynecyclo addition “click chemistry” (196). The use of click chemistry is of particular interest in this case as this type of reaction does not require harsh chemical conditions and can take place with high yields in aqueous solutions. In addition, the reactant and product will not react with other functional biomolecules (87).

The cycloaddition of azides to alkynes is a well-known example of click chemistry (200). Initially, this reaction used Cu (I) as a catalyzer which, however, showed toxicity towards cells. Therefore, cyclooctenes replaced the alkynes in a copper-free reaction with azides (201). Not all cyclooctenes show similar conjugation efficiency with azides. Though bicyclononyne (BCN) resulted in a higher conjugation efficiency in comparison to dibenzoannulated cyclooctyne (202).

The long-term goal of the this research is to develop nano-theranostics useful for diagnostic localization and drug delivery in metastatic tumor lesions. In the present study, we have developed positron emission tomography (PET) traceable polymeric NPs through insertion of ^{64}Cu-NOTA-modified PEG-phospholipids into poly (ethylene oxide)-*b*-poly (a-benzyl carboxylate-e-caprolactone) (PEO-PBCL) NPs. These NPs were modified on their surface with an antibody for binding to epidermal growth factor receptors (EGFR) on EGFR expressing cancer cells. A control over the orientation of the anti-EGFR antibody on the NP surface was achieved via the glycan-remodeling of panitumumab, a clinically used humanized monoclonal anti EGFR antibody (203). The goal was to evaluate the potential of these novel nano-theranostics for PET imaging of a preclinical EGFR positive non-small cell lung cancer (NSCLC) model.

4.2. Materials and methods

4.2.1. Materials

Endo S (IgGZERO®) IdeS (FabRICATOR®) enzymes were obtained from Genovis Inc., USA. Beta-1,4-galactosyltransferase 1 enzyme, manganese (II) chloride ($MnCl_2$), methoxy-poly (ethylene oxide) (5KDa), and Sepharose® CL-6B were purchased from Millipore Sigma, USA. Panitumumab (Vectibix®) was a generous gift by Cross Cancer Institute pharmacy in Edmonton, Canada. UDP-N-azidoacetylgalactosamine was bought from Jena Biosciences, Germany. α-Benzyl carboxylate-ε-caprolactone (BCL) was prepared by Alberta Research Chemicals Inc., Canada based on previously published methods (144). Stannous octoate was purchased from MP Biomedicals Inc. Germany. DSPE-PEG-endo-BCN was obtained from Broad Pharm, USA. CF®488A-BCN dye was purchased from Biotium, USA, and Cyanine5 azide dye was obtained from Lumiprobe, USA. Chelex 100 Resin, Laemmili buffer, and SDS-PAGE Mini-PROTEAN TGX® Precast Protein Gels were purchased from Bio-Rad, USA. Aquastain protein staining reagent from Bulldog Bio, USA was used. NO2A-Azide was obtained from Macrocyclics, USA. Cell culture media DMEM, fetal bovine serum (FBS), and penicillin−streptomycin-L-glutamine were purchased from GIBCO, Life Technologies Inc. $^{64}CuCl_2$ was produced based on a previously reported method (148) at Medical Isotope and Cyclotron Facility (MICF) at the University of Alberta South Campus, Canada.

4.2.2. Cell lines and animals

H1299-luc+ cells were purchased from American Type Culture Collection (ATCC) (Manassas, VA, U.S.A.). H1299 cells were grown in a 5% CO_2 incubator at 37°C using DMEM/F12 media

containing 10% fetal bovine serum and 1% penicillin/streptomycin, with media changed 2-3 times weekly.

Female 6-10 weeks old NIH-III nude mice were obtained from Charles Rivers (Saint-Constant, QC, Canada). All animal experiments followed the Canadian Council on Animal Care (CCAC) guidelines and were approved by the Cross Cancer Institute local animal care committee (animal protocol AC 21256).

4.2.3. Glycan remodeling of panitumumab with azide

Figure 4.1 shows the scheme for different steps used to prepare azide modified antibody in addition to its insertion in the NPs. In the first step, to a 4 mg aliquot of panitumumab, 800U of Endo S enzyme was added. The reaction pH was set to 7.4 using Tris-buffered saline (TBS) and left on a thermoshaker for 30 minutes at 37°C at 700 rpm. The sample was purified using 100KDa centrifugal spin filters (Amicon®, Millipore Sigma, USA), and a sample was sent for matrix-assisted laser desorption/ionization (MALDI) to assess modifications on panitumumab. To understand which antibody segment had been modified, IdeS enzyme was added to panitumumab and modified panitumumab with the concentration of 1 U per 1 ug of protein, and the pH was set to 7.4. The samples were placed on a thermoshaker set to 30°C at 700 rpm for 30 min. After that, Laemmli buffer with a volume/volume ratio of 3:1 was added, and the reaction mixture was heated at 95°C for 10 min. From each sample, 25 µg of antibody was loaded into each pocket of the SDS-PAGE gel and ran at 110 V. Then, the gels were stained for further assessment.

The deglycosylated antibody mixture was then buffer exchanged to TBS supplemented with 150 nM $MnCl_2$ via Amicon® 100 KDa cutoff centrifugal spin filters. UDP-N-

azidoacetylgalactosamine with a mol/mol ratio of 40:1 to panitumumab and 5 U of Beta-1,4-galactosyltransferase 1 was added per one mg of panitumumab. The pH of the reaction was set to 7.4. The reaction mixture was placed again on a thermoshaker set to 25°C and 700 rpm overnight. After that, the antibody reaction mixture was washed with TBS using Amicon® 100 KDa cutoff centrifugal spin filters three times and set aside for use in the next steps.

4.2.4. Fluorescence labelling of azide-functionalized panitumumab

To attach CF®488A- BCN to azide-modified panitumumab (azide-panitumumab), a 5:1 mol/mol ratio of the dye to purified azide-panitumumab was added and left on a thermoshaker set to 25°C and 700 rpm overnight. The sample was purified via Amicon® 100KDa cutoff centrifugal spin filters. To assess the reaction's efficiency, an aliquot was submitted for MALDI. The degree of labeling (DOL) was also assessed using UV spectroscopy (UV2600i, Shimadzu, Japan). The following equations were used to calculate DOL. :

$$\text{DOL} = \frac{Absorbance\ at\ 495nm/\varepsilon\ of\ dye}{Absorbance\ at\ 280nm\ (CF * Absorbance\ at\ 495nm)/\varepsilon\ of\ IgG}$$

$$\text{Correction Factor (CF) for dye} = \frac{Absorbance\ of\ dye\ at\ 280nm}{absorbance\ of\ dye\ at\ 495nm}$$

$$\varepsilon\ of\ dye: 70{,}000\ \ and\ \varepsilon\ of\ IgG: 210{,}000$$

4.2.5. Preparation of PEO-PBCL NPs

Poly(ethylene oxide)-*block*-poly(α-benzyl carboxylate-ε-caprolactone) (PEO-PBCL) was prepared using the previously reported method (144). Briefly, mPEO and BCL were weighted in

an ampule with a mol/mol ratio of 1:30. Then, three drops of stannous octoate were added and while the ampule was connected to the vacuum line, the ampule was sealed using a flame. The sealed ampule was placed in an oven at 140°C and for 4 hours. The polymer was purified by dissolving the ampule contents in dichloromethane and adding it to hexane to precipitate the synthesized polymer. An aliquot of the synthesized polymer was dissolved in deuterated chloroform and analyzed with ^{1}H nuclear magnetic resonance (^{1}H NMR) for characterization using a 600-MHz Bruker spectrometer (Bruker Instruments, Inc., Billerica, MA, USA). On the ^{1}H NMR spectrum the peak intensity of PEO (-CH2CH2O-, δ 3.65 ppm) was compared to that of BCL (-OCH2-, δ 4.1 ppm) to assess the degree of polymerization of PBCL (144,204).

PEO-PBCL NPs were prepared by the co-solvent evaporation method as previously reported (144). Briefly, 10 mg of PEO-PBCL polymer was dissolved in 250 µL of acetone and added dropwise to 5 mL of double distilled water being stirred using a magnet bar. The sample was left overnight for acetone evaporation. The prepared NPs were characterized using dynamic light scattering (DLS) (Zetasizer Ultra, Malvern Panalytical, UK).

4.2.6. Modification of PEO-PBCL NPs with panitumumab

PEO-PBCL NPs were conjugated with panitumumab (pan modified PEO-PBCL NPs) via the post-insertion method as previously reported by Saqr et al. (97). Initially, a mol/mol ratio of 3:1 polymer to DSPE-PEG5000-BCN was weighted. The DSPE-PEG5000-BCN was dissolved in acetone in a 1 mg/mL concentration and added to TBS with a volume/volume ratio of 1:6 while being shaken. After acetone evaporation, azide functionalized panitumumab was added to DSPE-PEG5000-BCN in a mol/mol ratio of 1:3 and left on a thermoshaker for 4 hours at 700 rpm at room temperature.

Afterward, this solution was added to PEO-PBCL NPs and left overnight on a thermoshaker set to 500 rpm and room temperature. The sample was then purified using a Sepharose CL-6B® size-exclusion chromatography column by eluting the column with Phosphate-buffered saline (PBS) pH 7.4 and collecting 15 fractions of 2 mL. The fractions were characterized using DLS and BCA assay to determine NP size distribution and the number of panitumumab antibody units per NP, respectively.

4.2.7. Fluorescence labeling of plain and panitumumab-modified PEO-PBCL NPs with Cyanine 5 azide

The PEO-PBCL NPs were fluorescently labeled via the post-insertion method (97). Briefly, a 1:10 mol/mol ratio of DSPE-PEG5000-BCN to PEO-PBCL polymer was weighted and dissolved in acetone with 1 mg/mL concentration and added to TBS at a volume/volume ratio of 1:6 while being shaken. After acetone evaporation, the cyanine 5 azide with a 1:1 mol/mol ratio was added to DSPE-PEG5000-BCN and left on a thermoshaker set to 700 rpm at room temperature for 4 h. Then, PEO-PBCL NPs were added to this sample and left overnight on the thermoshaker shaker set to 500 rpm at room temperature. To purify the Cy5 labled PEO-PBCL NPs (Cy5-PEO-PBCL NPs), size exclusion chromatography column (PD midiTrap® G-25, GE healthcare) eluted with PBS (pH 7.4). From the column eluents, 15 fractions of 0.3 mL were collected and kept for further analysis.

To prepare fluorescence labeled panitumumab conjugated PEO-PBCL NP (pan modified cy5-PEO-PBCL NPs), initially panitumumab decorated PEO-PBCL NPs were prepared as detailed in *Modification of PEO-PBCL NPs with panitumumab* section and similar steps and concentrations

as described above for the labeling of PEO-PBCL NPs with cyanin 5 azide were used. The concentration (mol/L) of Cyanine 5 azide in each sample was determined by measuring the absorbance of each sample at 646 nm wavelength using a spectrophotometer (UV2600i, Shimadzu, Japan) and using the following formula the concentration (mol/L) of each sample was calculated.

$$A=\varepsilon Lc$$

A: absorbance ε: molar extinction coefficient (for Cyanine 5 azide is 250,000 $L^{-1}cm^{-1}mol$)

L: path length c: concentration (mol/L)

4.2.8. Radiolabeling of plain and panitumumab-conjugated PEO-PBCL NPs with ^{64}Cu

For ^{64}Cu radiolabeling of the plain PEO-PBCL NPs (^{64}Cu-PEO-PBCL NPs) or panitumumab-conjugated PEO-PBCL NPs (pan modified ^{64}Cu-PEO-PBCL NPs), similar steps were followed as described above under *Labeling PEO-PBCL polymeric nanoparticles with Cyanine 5 azide*. Briefly, to a mol/mol ratio of 1:10 DSPE-PEG5000-BCN to PEO-PBCL polymers was weighed and dissolved in acetone, then added to TBS. After acetone evaporation, NOTA-azide chelator was added with a 1:5 mol/mol ratio of chelator to DESPE-PEG5000-BCN. This solution was left for 4 h on a thermoshaker at 700 rpm and at room temperature. Then PEO-PBCL NPs were added to this solution and left overnight on the thermoshaker shaker set to 500 rpm at room temperature. The NPs were then purified from free chelators and concentrated to 50 mg/mL using 300 KDa cutoff centrifugal spin filters (Microcon®, Millipore Sigma, USA).

The Pan modified PEO-PBCL NPs, were prepared following the steps described under *Modification of PEO-PBCL NPs with panitumumab.* Following the same procedure as with PEO-

PBCL NPs, a 1:10 mol/mol ratio of DSPE-PEG5000-BCN to PEO-PBCL polymer was weighed and dissolved in acetone and added to TBS. Following acetone evaporation, the NOTA-azide chelator was mixed in at a 1:5 mol/mol ratio with DESPE-PEG5000-BCN. The solution sat on a thermoshaker at room temperature for 4 h at 700 rpm. The solution was then mixed with pan modified PEO-PBCL NPs and kept overnight on the thermoshaker shaker set at 500 rpm and room temperature. The pan modified PEO-PBCL NPs were purified from free chelators and concentrated to 50 mg/mL using centrifugal spin filters (Microcon®, Millipore Sigma, USA).

Table 4.1. Summarized description of the developed NPs

Polymeric NP [1]	**Composition (mol/mol)**
Pan modified PEO-PBCL NP	PEO-$PBCL_{22}$:Panitumumab-PEG-DSPS (30:1)
Cy5-PEO-PBCL NP	PEO-$PBCL_{22}$: Cy5-PEG-DSPE (10:1)
Pan modified Cy5-PEO-PBCL NP	PEO-$PBCL_{22}$:Panitumumab-PEG-DSPS: Cy5-PEG-DSPE (30:1:10)
^{64}Cu-PEO-PBCL NPs	PEO-$PBCL_{22}$: ^{64}Cu-PEG-DSPE (10:1)
Pan modified ^{64}Cu - PEO-PBCL NPs	PEO-$PBCL_{22}$:Panitumumab-PEG-DSPS: ^{64}Cu-PEG-DSPE (30:1:10)

1. The ^{64}Cu mentioned the table is the representative of the ^{64}Cu entrapped in NO2A chelator complex.

The pH of [^{64}Cu]$CuCl_2$ (0.5 mL in 0.1 N HCl) was adjusted to 5.5 using 15-20 µL of chelex-treated 2 M sodium acetate buffer (NaOAc) (pH 10). Then ~450 µL of ^{64}Cu was transferred to a 200 µL aliquot of 50 mg/mL NO2A-PEO-PBCL NPs (prepared as described above). The reaction mixture was then placed on a thermoshaker set at 700 rpm and 37°C for 1 h. The efficiency of ^{64}Cu incorporation was determined via radioactive thin-layer chromatography (radio-TLC) analysis. For assessing the chelation of ^{64}Cu into the chelators, to an 8 µL aliquot of the reaction mixture 2 µL of 10 mM EDTA was added and left for 5 min. Analysis was done with normal phase radio-TLC using citrate buffer as mobile phase.

To monitor the percentage of ^{64}Cu-NO2A not attached to NPs, reverse phase radio-TLC was used with MeOH / 1 M NH_4OAc with a 9:1volume/volume ratio as mobile phase.

^{64}Cu-PEO-PBCL NPs were finally purified by size exclusion chromatography (P25 column) eluting with PBS and collecting 300 µL fractions. The activity of each fraction was measured using an AtomlabTM 400 dose calibrator (Biodex Medical Systems, New York, NY, USA) followed by normal and reverse phase radio-TLC to determine the fractions' radio purity.

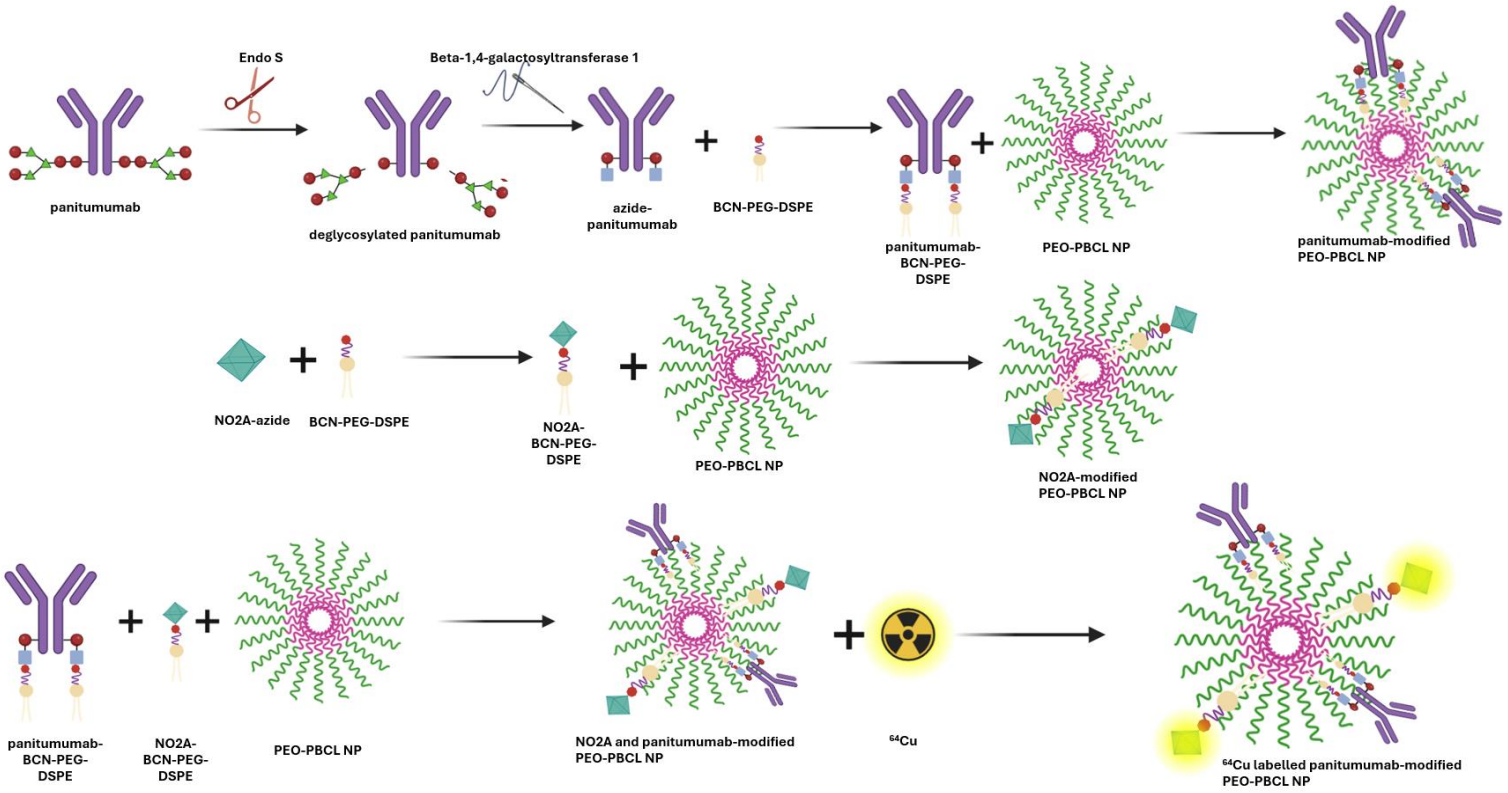

Figure 4.1. Overall view of the methods used for developing 64Cu labeled panitumumab modified PEO-PBCL NPs via glycan remodeling approach

4.2.9. cell uptake studies

In vitro cell uptake studies were performed using H1299 NSCLC cells (CRL-5803 from American Type Culture Collection (ATCC), Manassas, MD, U.S.A.). H1299 cells were initially seeded into each well of a 12-well plate and incubated overnight. The next day, the media with 10% FBS was replaced with an FBS-free media.

To measure the cell uptake of fluorescent labeled NPs, 0.2 ug/mL of Pan modified Cy5-PEO-PBCL NPs or Cy5-PEO-PBCL NPs were added to each well and the plate was kept in a 5% CO_2 incubator at 37 °C for 3 h. Cellular uptake was stopped with 0.5 mL of ice-cold PBS, and the cells were

washed twice with PBS and lysed in 0.4 mL radioimmunoprecipitation assay buffer (RIPA buffer). Fluorescence in 100 µL of cell lysates was determined using a Synergy H1 multimode microplate reader (BioTekInstruments Inc., Winooski, VT, U.S.A.) with 640 nm as excitation and 670 nm as emission wavelengths. Data were calculated as percent of measured fluorescence intensity of cells over the fluorescence intensity of each sample.

For blocking experiments, H1299 seeded plates were prepared as mentioned previously and cells were pre-treated with 250 µg of panitumumab per well for 2 h before adding fluorescence-labeled NPs. After that, 0.2 µg/mL of cyanin Pan modified Cy5-PEO-PBCL NPs was added to each well and the plate was kept in a 5% CO_2 incubator at 37 °C for 3 h. Cells were lysed and their fluorescence intensity was measured as described before.

To measure the cell uptake of ^{64}Cu labeled NPs, 0.2 MBq of Pan modified ^{64}Cu-PEO-PBCL NPs or ^{64}Cu-PEO-PBCL NPs were added to each well and the plate was kept in a 5% CO2 incubator at 37 °C for 3 h. After incubation, similar steps as measuring cell uptake for fluorescent labeled NPs were followed. Briefly, the cells were washed with ice cold PBS and RIPA buffer was added to lyse the cells and the radioactivity of each cell lysate was measured using a gamma counter.

The blocking studies was performed similar to fluorescent labeled NPs. In brief, cells were pretreated with 250 µg panitumumab 2 hours before addition of radiolabeled NPs followed by addition of 0.2MBq of Pan modified ^{64}Cu-PEO-PBCL NPs or ^{64}Cu-PEO-PBCL NPs and incubation for 3 hours. Cells were then washed with PBS, lysed with RIPA buffer and radioactivity measured using a gamma counter.

4.2.10. *In Vivo* experiments with radiolabeled NPs

The subcutaneous NSCLC xenograft mouse model was generated by injecting ~3×10^6 H1299-luc+ cells in 100 µL of 50% Matrigel / 50% PBS into the left shoulder of female NIH III nude mice. Tumors were used for PET experiments after about 3-4 weeks, when the tumor size reached approximately ≥ 5 x 5 mm.

4.2.11. PET imaging experiments

H1299 luc^+ tumor-bearing NIH III nude mice were anesthetized with isoflurane (100% O_2), and their body temperatures were kept constant at 37°C. Mice were injected intravenously with either 7-11 MBq Pan modified ^{64}Cu-PEO-PBCL NPs or ^{64}Cu-PEO-PBCL NPs in 100-150 µL PBS / saline through a tail vein catheter. Radioactivity present in the injection solution (0.5 mL syringe) was determined using a dose calibrator (Atomlab^{TM} 500; Biodex Medical Systems, New York, NY, USA). For blocking experiments, mice were injected intravenously with 1 mg panitumumab 24 h before injection of the Pan modified ^{64}Cu-PEO-PBCL NPs. Mice were positioned and immobilized in a prone position into the center of the field of view of an INVEON® PET/CT scanner (Siemens Preclinical Solutions, Knoxville, TN, USA). A transmission scan for attenuation correction was not acquired. Static PET scans were measured for 20 min at 24 h or 48 h post-injection. PET data were reconstructed using maximum a posteriori (MAP) reconstruction modes. No correction for partial volume effects was performed. Image files were further processed using Rover v.2.0.51 software e (ABX GmbH, Radeberg, Germany). Masks defining 3-dimensional regions of interest (ROI) were set and defined by 50% radioactivity thresholding. Mean standardized uptake values [SUV_{mean} = (activity/mL tissue) / (injected activity / body weight)] (mL/kg), were calculated for each ROI. Diagrams were generated using

GraphPad Prism 5.0 (GraphPad Software, San Diego, CA). All SUV PET data are presented as means ± SEM from n experiments. Statistical differences were tested by unpaired Student's t-test and considered significant for $p < 0.05$.

4.2.12. *Ex vivo* biodistribution experiments

For biodistribution experiments the same mice that have undergone PET live imaging were used. Directly after their PET scan, mice were euthanized by cervical dislocation after 24 or 48 h post-injection. Organs and tissue of interest including blood, lung, liver, spleen, muscle, and H1299 luc^+ tumors were collected and weighed. Radioactivity in all tissues was measured as Bq using a HIDEX automated gamma counter (Hidex Oy, Turku, Finland), and results were calculated as percentage of injected dose per gram of tissue (% ID/g). Experiments were performed from n=3-4 mice for each time point. Data are shown as mean ± standard error of measure (SEM).

4.2.13. Statistical analysis

The data from n experiments are expressed as means ± SD for all *in vitro*, *in vivo*, and *ex vivo* measurements. GraphPad Prism 8 software (GraphPad Software, San Diego, CA) was used to construct the graphs and statistically analyze the results. Statistical differences were assessed using an unpaired Student's t-test, one way ANOVA and were considered significant if $p < 0.05$ (*).

4.3. Results

4.3.1. Characterization of azide functionalized panitumumab

Figure 4.1 illustrated different steps involved in the preparation of azide functionalized panitumumab by glycan remodeling. Success of glycan group remodeling of panitumumab was analyzed using MALDI and SDS-PAGE electrophoreses. As shown in Figure 4.2. A, the value of mass-to-charge (m/z) was decreased by 2,376 when panitumumab was modified by Endo S. representing the removal of N-linked glycan from panitumumab(205), Moreover, the location of the modification on panitumumab was assessed via electrophoresis. The stained SDS-PAGE indicated a similar molecular weight for the $F(ab')_2$ segment of panitumumab and deglycosylated panitumumab. However, the Fc segment of deglycosylated panitumumab had a lower molecular weight in comparison to panitumumab (Figure 4.2. B) indicating that the Fc section of panitumumab has been modified and the $F(ab')_2$ has remained intact.

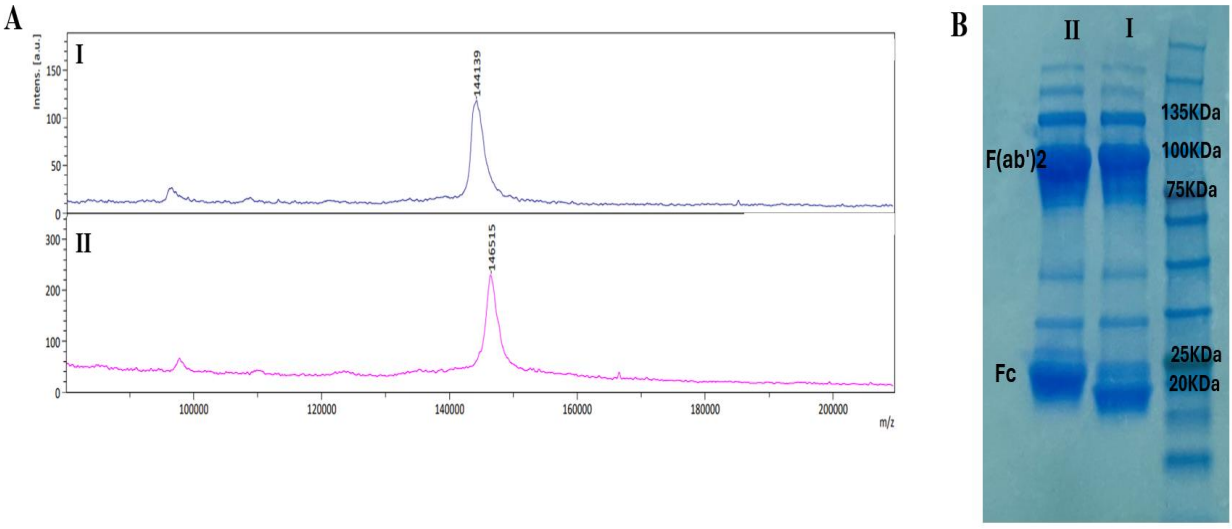

Figure 4.2. A) A representative low-resolution MALDI spectrum for deglycosylated panitumumab (I) and original panitumumab (II). B) stained SDS-PAGE representing F(ab′)2 and Fc segments for deglycosylated panitumumab (I) and original panitumumab (II).

After remodeling of the glycan group of panitumumab to azide, MALDI analysis and electrophoresis were done. As shown in Figure 4.3. A., the m/z ratio value decreased from 146,515 for panitumumab to 144,139 for the panitumumab without glycan group. For azide modified panitumumab, this value increased to 145,971. The stained SDS-PAGE showed a mass difference between panitumumab and the azide modified panitumumab for the Fc segment of the antibody. However, the molecular weight of Fab for all groups was similar (Figure 4.3. B).

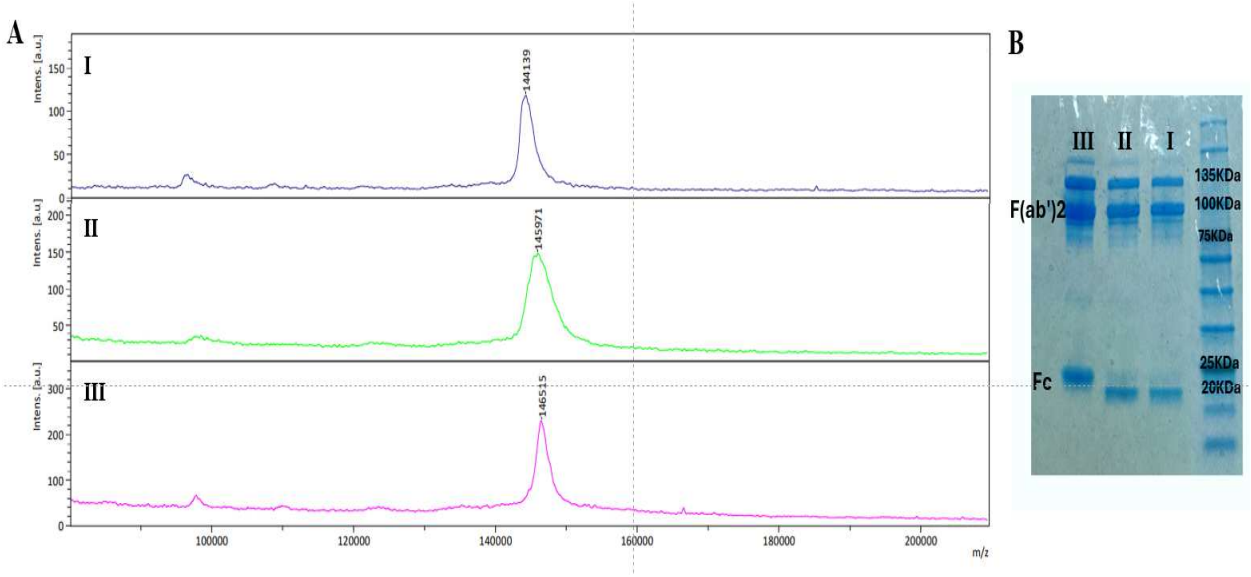

Figure 4.3. A) A representative low-resolution MALDI representative for deglycosylated (I), azide-modified (II), and original panitumumab (III) B) stained SDS-PAGE representing F(ab′)2 and Fc for deglycosylated (I), azide-modified (II), and original panitumumab (III).

4.3.2. Characterization of CF®488A labeled panitumumab

The efficiency of CF®488A-BCN attachment to azide-panitumumab was determined by MALDI and measurement of the absorbance of the sample at 280 and 495nm wavelengths. Using the DOL equation mentioned in *Fluorescence labeling of azide- functionalized panitumumab,* the efficiency of CF®488A-BCN attachment to azide-panitumumab was calculated 51.90±4.01%. Also, the MALDI result indicated an increase in m/z value from 144,948 to 145,979 for glycosyl-modified panitumumab and CF®488A labeled panitumumab, respectively (Figure 4.4).

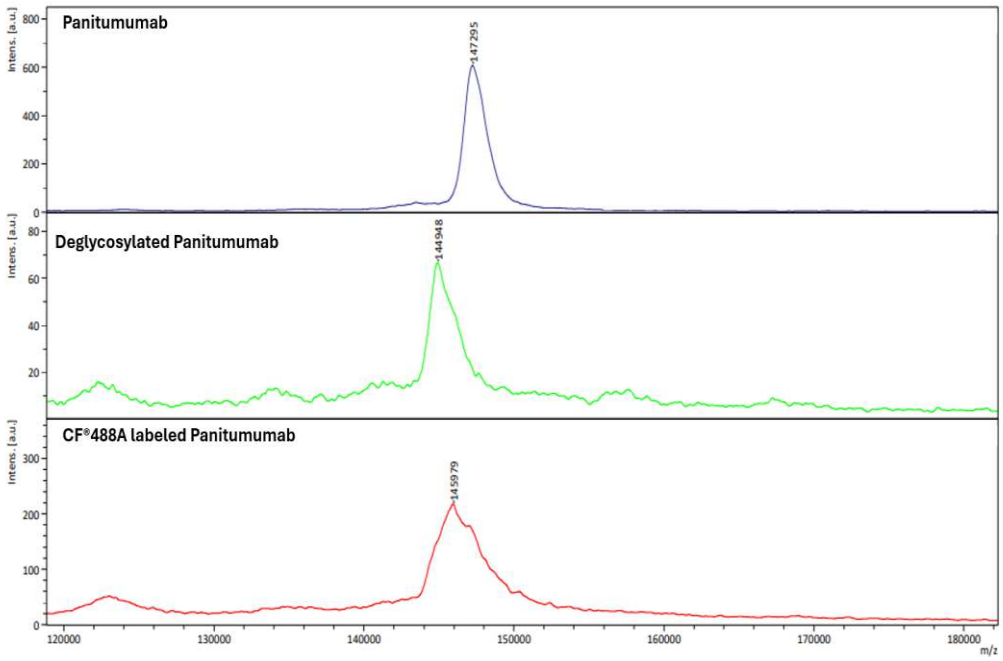

Figure 4.4. Low-resolution MALDI for panitumumab, deglycosylated panitumumab, and CF®488A labeled panitumumab.

4.3.3. Characterization of plain and panitumumab-conjugated PEO-PBCL NPs

The number average molecular weight (Mn) for the synthesized PEO-PBCL block copolymer and the degree of polymerization for the PBCL block were 11,700 g/mol and 22, respectively. The NPs were prepared using this polymer without or with insertion of the fluorescence tag, the radioisotope ^{64}Cu and/or panitumumab conjugated-PEG-DSPE as shown in Figure 4.1.

Upon antibody insertion, the NPs were purified using size-exclusion chromatography column to separate them from free antibodies. The characterization of the collected fractions (Figure 4.5) indicated that the PEO-PBCL NPs and the Pan modified PEO-PBCL NPs elute through the column as fractions 5-10 based on the count rate measured and the quality analysis given by DLS. For all

remaining fractions, other than the low count rate in comparison to fractions 5-10, the quality report indicated a high noise-to-signal ratio, weak scattering signal and a large population or number fluctuations.

The size (d.nm) and polydispersity index (PDI) for PEO-PBCL NPs and pan modified PEO-PBCL NPs are reported in Table 4.2. The modification of NPs with panitumumab led to slight increase in NPs size and PDI. The change in NPs size when panitumumab was added to PEO-PBCL NPs was not significant ($p>0.05$, t-test); however, the PDI value increased significantly ($p<0.05$, t-test). Also, the zeta potential of the prepared NPs remained near neutral with out significant changes ($p>0.05$, t-test).

Table 4.2. Characterization of nonradioactive labeled polymeric NPs

Polymeric NP[1]	**Size(d.nm)±SD**	**PDI±SD**	**Zeta potential±SD**
PEO-PBCL NP	49.28±2.03nm	0.14±0.00	-2.26+1.13
Pan modified NPs	52.5±2.75 nm	0.18±0.02	-3.48+1.94

1.The composition of the polymeric NPs is mentioned in Table 1.

As shown in Figure 4.5, an increase in count rates was seen from fraction 12-14 when the pan modified PEO-PBCL NPs were eluted through the size exclusion chromatography column which is contributed to free panitumumab being eluted from the column since this increase was not observed when eluting the PEO-PBCL NPs through the column. The BCA assay indicated an average mol/mol ratio of 1:136 of panitumumab to polymer present in the samples.

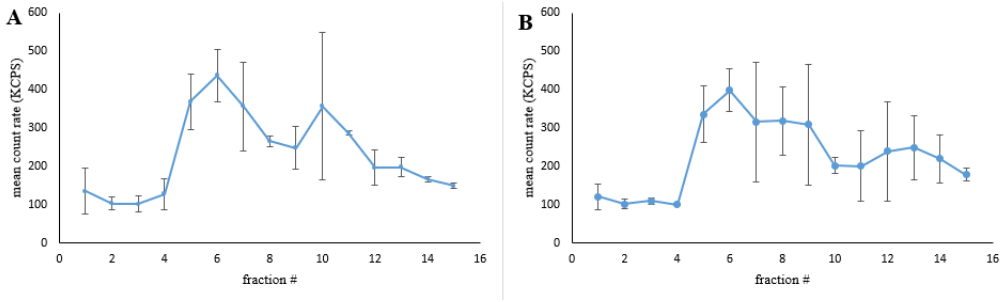

Figure 4.5. The count rate measured using DLS of eluted fraction from size-exclusion chromatography for A) PEO-PBCL NPs and B) panitumumab-modified PEO-PBCL NPs

4.3.4. Cyanine 5 labeling efficiency of plain and panitumumab-modified NPs

The fluorescence labeling efficiency of plain and pan modified PEO-PBCL NPs was measured using absorbance at 646 nm. For PEO-PBCL NPs, 29 +1% of the added Cyanine 5 was incorporated into NPs, similar to 29+1% incorporation into pan modified PEO-PBCL NPs.

4.3.5. ^{64}Cu labeling efficiency of plain and panitumumab modified NPs

The radiolabeling efficiency of PEO-PBCL NPs and pan modified PEO-PBCL NPs with ^{64}Cu was determined with normal and reverse phase radio-TLC. As shown in Figure 4.6, the amount of free ^{64}Cu in the radiolabeled samples was less than 20%. Also, the R_f value for the ^{64}Cu-NO2A complex in reverse phase ratio-TLC was 0.39. The reverse phase radio-TLC indicated that less than 35% of the radiolabeled sample was free ^{64}Cu-NO2A complex. Also, the normal and reverse phase radio-TLC showed that the size exclusion chromatography column purified the radiolabeled samples from free ^{64}Cu and ^{64}Cu-NO2A (Figure 4.6).

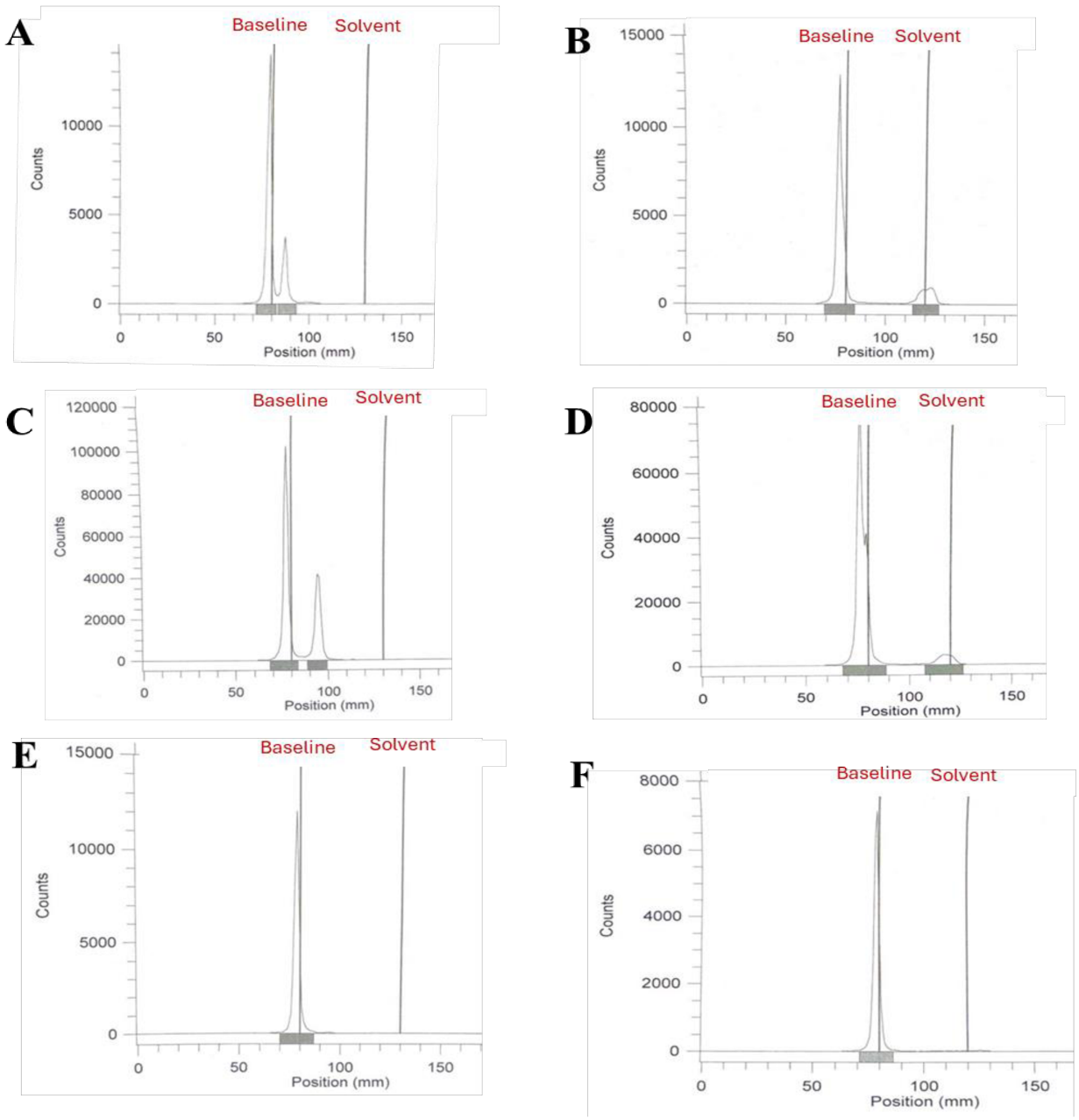

Figure 4.6. Representative radio-TLC scans of A) ^{64}Cu-PEO-PBCL NPs reverse phase TLC B) ^{64}Cu-PEO-PBCL NPs with normal phase TLC C) Pan modified ^{64}Cu-PEO-PBCL NPs with reverse phase TLC D) Pan modified ^{64}Cu-PEO-PBCL NPs with normal phase TLC E) Eluted fraction from size exclusion chromatography column with reverse phase TLC F) Eluted fraction from size exclusion chromatography column with normal phase TLC.

4.3.6. *In vitro* cell uptake

H1299 cells were incubated with Cy5-PEO-PBCL NPs for 3 hours and cell uptake was determined by measuring the amount of fluorescence in the cell lysates. The results indicated that pan modified Cy5-PEO-PBCL NPs have significantly higher uptake by H1299 cells compared to Cy5-PEO-PBCL NPs ($p<0.05$, One-way ANOVA) (Figure 4.7). Also, the cell uptake for the group of cells that received panitumumab in advance of treatment with Pan modified Cy5-PEO-PBCL NPs, was significantly lower in comparison to those that only received Pan modified Cy5-PEO-PBCL NPs ($p<0.05$, One way ANOVA) and comparable to that of Cy5-PEO-PBCL ($P>0.05$, One way ANOVA). The cell uptake results for NPs labeled with ^{64}Cu was in line with the Cy5 labeled NPs. As shown in Figure 4.7.B, the pan modified ^{64}Cu-PEO-PBCL NPs, were significantly up taken by H1299 cells in comparison to ^{64}Cu-PEO-PBCL NPs ($P<0.05$, One way ANOVA). Moreover, the NPs uptake of the cells which received panitumumab in advance of receiving Pan modified ^{64}Cu-PEO-PBCL NPs, was significantly lower than the cells which only received pan modified ^{64}Cu-PEO-PBCL NPs ($P<0.05$, One way ANOVA).

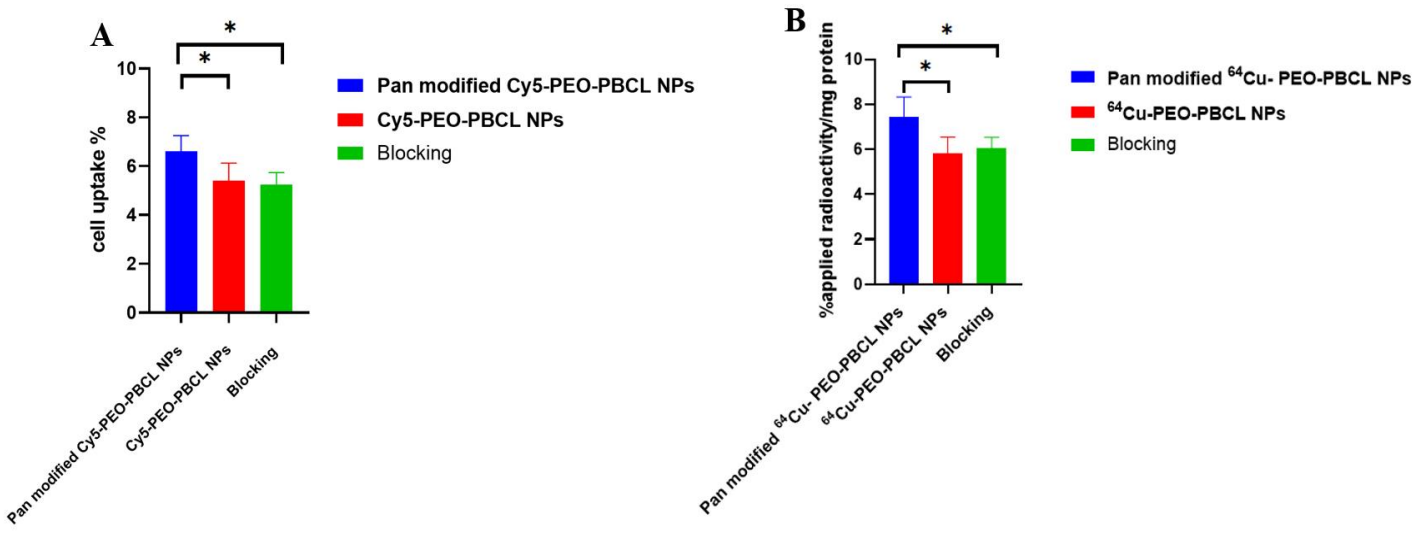

Figure 4.7. Uptake of plain and panitumumab- modified PEO-PBCL NPs by H1299 cells with or without panitumumab pretreatment for A) fluorescently labeled NPs and B) radioactively labeled NPs (* represents P<0.05, One way ANOVA n=3)

4.3.7. *In vivo* PET imaging

Representative images are shown after 24 and 48 h post-injection (p.i) of either ^{64}Cu-PEO-PBCL NPs or Pan modified ^{64}Cu-PEO-PBCL NPs (Figure 4.8). Radioactivity uptake into subcutaneous H1299 tumors is clearly visible. Below, the diagrams in Figure 4.8 summarize quantified mean standardized uptake values (SUV_{mean}) which were determined from regions of interest over the tumor area and over the contralateral muscle tissue. Radioactivity uptake into tumor tissue revealed SUVmean values of 0.87 ± 0.08 (n=3) after 24 h p.i. and 0.63 ± 0.01 (n=3) for 48 h p.i. indicating a slight washout. Corresponding muscle tissue uptake resulted in SUV_{mean} of 0.23 ± 0.01 after 24 h and 0.18 ± 0.03 after 48 h (both n=3), respectively. Panitumumab conjugation to the PEO-PBCL NPs did not change the tumor uptake after 24 h, however, after 48 h an increase of ~16% tumor uptake was detected: SUV_{mean} 0.73 ± 0.02 (n=3; $p < 0.05$).

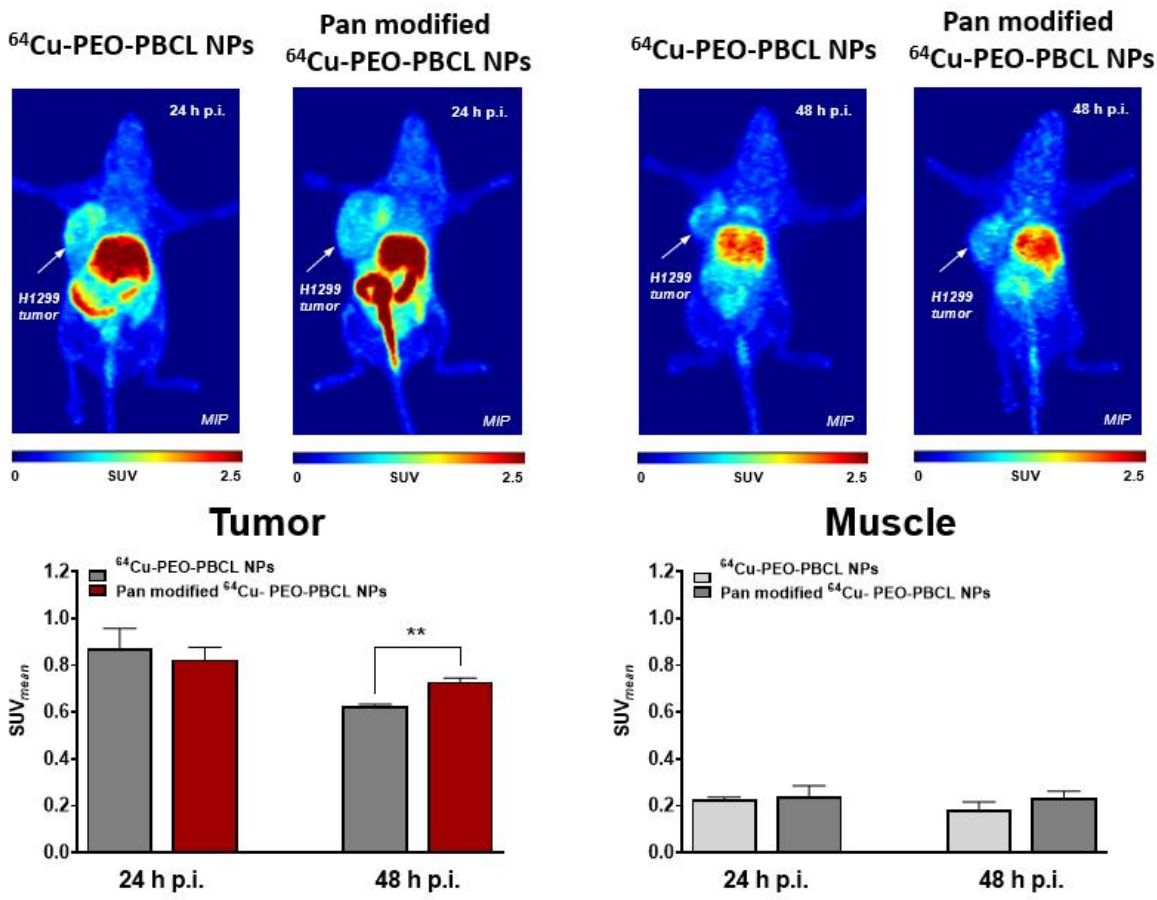

Figure 4.8. Top: Representative PET images as maximum intensity projections (MIP) of a H1299-luc tumor-bearing NIHIII mouse at 24 and 48 h after injection of 64Cu labeled PEO-PBCL NPs and 64Cu labeled panitumumab-modified PEO-PBCL NPs. Bottom: SUVmean values for radiotracer uptake into tumor (left) and muscle tissue (right).

Next, blocking experiments were performed to prove if a specific antibody-mediated tumor uptake was detectable. Figure 4.9 summarizes representative PET images of mice at 48 h p.i. Pan modified ^{64}Cu-PEO-PBCL NPs in the presence or absence of panitumumab (1 mg per mouse). The diagrams below present the SUV_{mean} values for these experiments: 0.72 ± 0.05 in the absence and 0.61 ± 0.09 in the presence of 1 mg panitumumab (both n=4) indicative of a 15% reduction, which was, however, not significant.

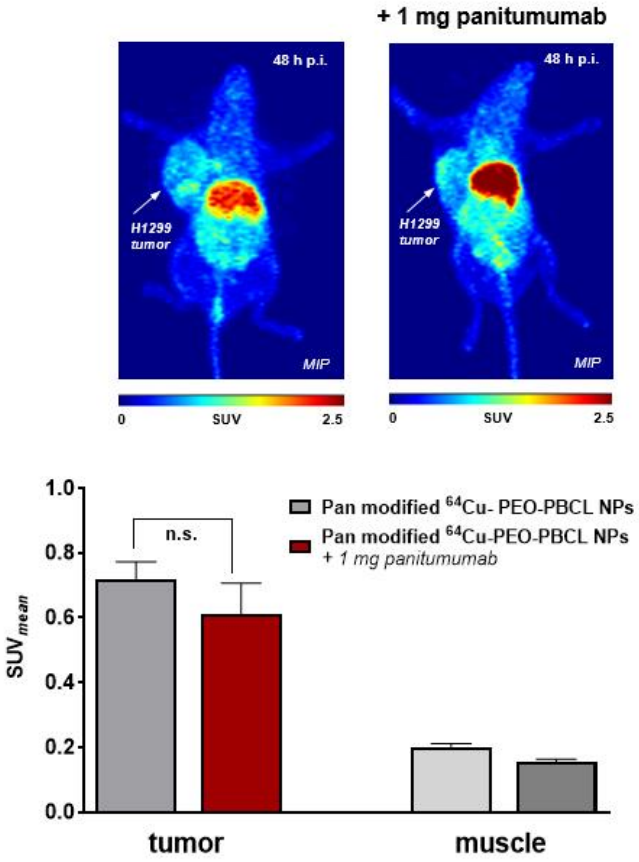

Figure 4.9. Top: Representative PET images as maximum intensity projections (MIP) of a H1299-luc tumor-bearing NIHIII mouse at 48 h after injection of 64Cu labeled panitumumab-modified PEO-PBCL NPs and its blocking group. Bottom: SUVmean values for radiotracer uptake into tumor (left) and muscle tissue (right).

4.3.8. *Ex vivo* biodistribution experiments

Biodistribution experiments using ^{64}Cu-PEO-PBCL NPs and Pan modified ^{64}Cu-PEO-PBCL NPs were carried out in the same mice as used for the PET imaging experiments. Figure 4.10 compares the biodistribution of ^{64}Cu-PEO-PBCL NPs with the one of Pan modified ^{64}Cu-PEO-PBCL NPs

in blood, lung, liver, spleen, muscle and H1299 tumor tissue at 24 and 48h p.i.. No significant differences were detected between ^{64}Cu-PEO-PBCL NPs and Pan modified ^{64}Cu-PEO-PBCL NPs at both time points.

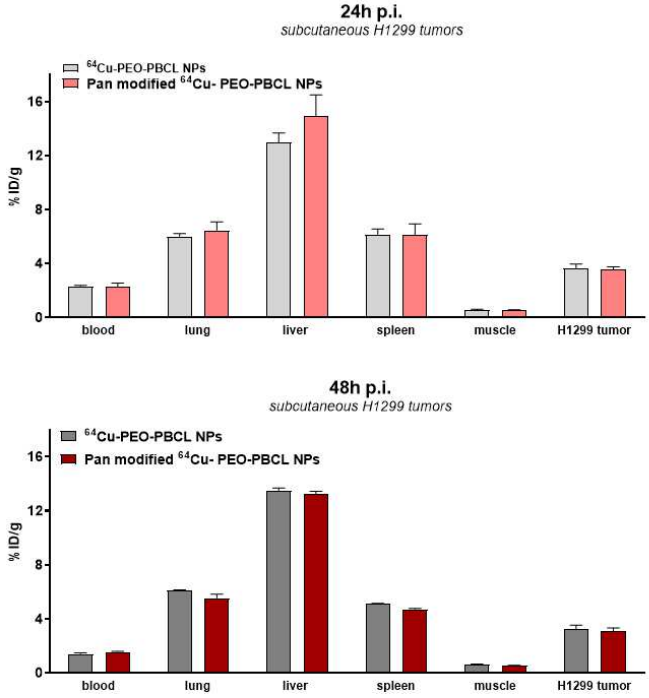

Figure 4.10. Biodistribution of ^{64}Cu-NOTA-PEO-PBCL NPs and ^{64}Cu-NOTA-panitumumab-PEO-PBCL NPs in subcutaneous H1299-luc+ tumor-bearing NIH-III mice at 24 h p.i (n=3) and 48 h p.i. (n=3).

However, when calculating the tumor-to-muscle (T/M) and tumor-to-blood ratios (T/B) a slight tendency of increased tumor uptake was determined but it was not significant (Figure 4.11) : + 9% for T/M and + 19% for T/B with Pan modified ^{64}Cu-PEO-PBCL NPs, respectively.

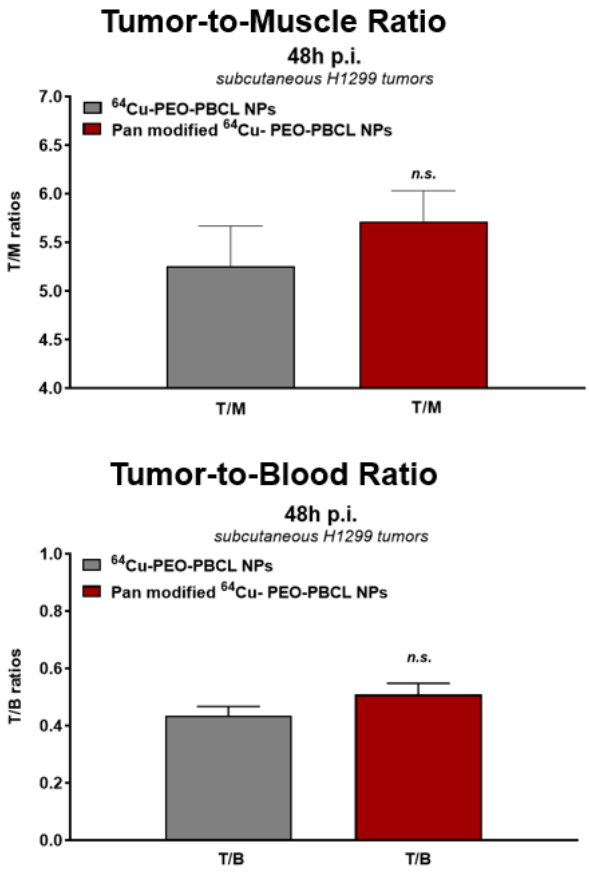

Figure 4.11. Tumor-to-muscle (T/M) and tumor-to-blood ratios (T/B) for 64Cu-NOTA-PEO-PBCL NPs and 64Cu-NOTA-panitumumab-PEO-PBCL NPs in subcutaneous H1299-luc+ tumor-bearing NIH-III mice at 48h p.i.

Next, *ex vivo* biodistribution was also analyzed under blocking conditions in the presence and absence of 1 mg panitumumab at 48h p.i.. (Figure 4.12). Again, no significant differences were detected in the selected organs.

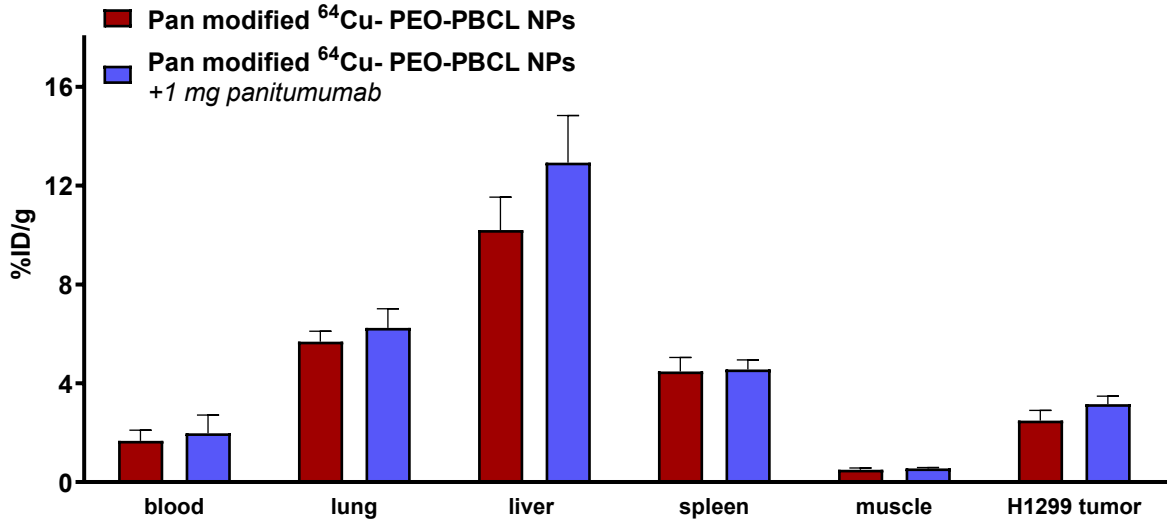

Figure 4.12. Biodistribution of ^{64}Cu-NOTA-panitumumab-PEO-PBCL NPs in the presence and absence of 1 mg panitumumab in subcutaneous H1299-luc^{+} tumor-bearing NIH-III mice (n=4).

In this case, the calculation of T/M and T/B did not result in any difference and therefore no blocking effect was detected (Figure 4.13).

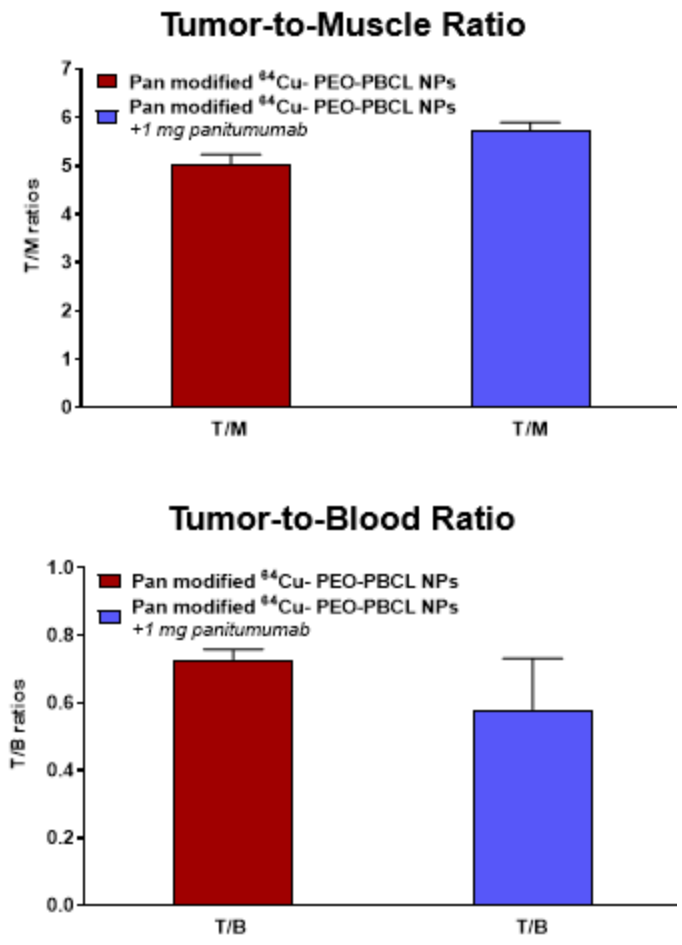

Figure 4.13. Tumor-to-muscle (T/M) and tumor-to-blood ratios (T/B) for ^{64}Cu-NOTA-panitumumab-PEO-PBCL and blocking group in subcutaneous H1299-luc+ tumor-bearing NIH-III mice at 48h p.i.

4.4. Discussion

Nano-theranostics systems, which combine diagnosis and therapy in a single nanocarrier, have gained attention for their precise detection and treatment capabilities (206). The developed nanotheranostic in this work was composed of the PEO-PBCL nanocarrier for improved drug delivery and ^{64}Cu radioisotope as the detecting probe. To improve the EGFR+ cancer cell targeting capability of the developed nanotherosntic, active targeting property was added to PEO-PBCL NPs. This feature was added to the nanotheronostic by introducing panitumumab with control over its orientation on the surface of PEO-PBCL NPs (Figure 4.1). The control over panitumumab's orientation on the NPs was obtained by modification of the glycan group presented on the Fc section of panitumumab. Initially, Endo S enzyme hydrolyzed the b-1,4 linkage between the first two N-acetyl glucosamine (205) resulting in a decrease in the molecular weight of panitumumab; moreover, since each heavy chain of Fc portion has a glycan group (207) therefore, the difference in molecular weight observed in MALDI was an even number (Figure 4.2). Also, the IdeS enzyme specifically cleaved panitumumab in its hinge region (208), leading to the two bands one for $F(ab')_2$ and one for Fc seen on SDS-PAGE, the molecular weight observed for $F(ab')_2$ was in line with the reported average molecular weight of 110KDa for IgG $F(ab')_2$ (209) (Figure 4.2). Since changes were only seen in the molecular weight of the Fc portion, it was confirmed that Endo S only modified the Fc portion of panitumumab. The transfer of N-azidoacetylgalactosamine to deglycosylated panitumumab was only observed using MALDI, as adding N-azidoacetylgalactosamine to both modified glycans of panitumumab would increase deglycosylated panitumumab's Mw maximum by 490 Da which could not be followed via SDS-PAGE. This was due to the small change in the molecular weight of the Fc and the presence of Fc

with different molecular weights within a small Mw range due to the enzymes' efficiency in producing the azide-panitumumab (Figure 4.3).

The attachment of CF®488A-BCN to azide-panitumumab happened through copper-free click chemistry (210) and confirmed that the azide-panitumumab is capable of reacting with the BCN functional group (Figure 4.4). These understandings and observations indicate that BCN-PEG-DSPE attaches to the Fc portion of azide-panitumumab and therefore during the post-insertion process to PEO-PBCL, panitumumab is not introduced in random orientation to the surface of NPs.

The hydrophobic nature of PEO-PBCL NPs allows the insertion of PEG-DSPE, enabling the phospholipid fragment to reach the core. Yet, the introduction of PEG-DSPE will not influence the thermodynamic stability of PEO-PBCL NPs (97) leading to the insertion of panitumumab and NO2A chelator to PEO-PBCL NPs (Figure 4.6). The introduction of panitumumab as the active targeting agent on the surface of PEO-PBCL NPs led to increased uptake of NP in comparison to PEO-PBCL NPs *in vitro* as a result of receptor-mediated endocytosis facilitating NPs uptake (190,211) (Figure 4.7). An increase in cell uptake were also reported when anti-EGFR antibodies were used to decorate other NPs delivery systems such as cetuximab decorated albumin NPs (212) targeting A549 lung cancer cell line, cetuximab modified hybrid lipid-polymer NPs targeting LoVo colorectal cancer cells (213) and panitumumab decorated polycaprolactone NPs targeting HCT116 colorectal cancer cells (214). Also, NPs modified with EGFR targeting peptides showed an increase in cell uptake by cancer cells over expressing EGFR such as the work done by Du et al. (215) and Pavia et al. (146) when for both studies GE11 peptide was used to decorate their NPs to

target U2OS and HCT 116 cancer cell lines respectively. However, the *ex vivo* biodistribution results did not show significant difference for tumor uptake between the injected groups.

The PET imaging in live animals showed a significant but small increase in tumor uptake between mice injected with ^{64}Cu-PEO-PBCL NPs and Pan modified ^{64}Cu-PEO-PBCL NPs at 48 h only (Figure 4.8); however, the biodistribution data is more accurate as it determines the absolute quantitative data for the radioactivity uptake into the tumors (216). PET data analysis can result in about 20% errors since its analysis is based on defining ROI by hand, thresholding of radioactivity uptake and partial volume effects (217).

The similar tumor distribution of ^{64}Cu-PEO-PBCL NPs and Pan modified ^{64}Cu-PEO-PBCL NPs seen in ex vivo biodistribution data of dissected organs (Figure 4.10) is perhaps a result of passive targeting. The surface modification of the NPs has no effect on passive targeting and tumor kinetics, but triggers internalization by EGFR expressing cells only after extravasation of the NPs into tumors. Therefore, although homing of panitumumab modified NPs in the subcutaneous tumor was not different from that of plain NPs, the effect of panitumumab may be observed in the therapeutic activity of the loaded drug as a result of better uptake of NPs by cancer cells overexpressing EGFR (218).

Furthermore, reports in literature indicated when complete monoclonal antibody structure is used as a targeting agent increased liver and spleen uptake is expected. This would lead to faster clearance of antibody modified NPs in comparison to non modified NPs. Rapid clearance of antibody modified NPs was attributed to the random orientation of the antibody on the surface of NPs, which triggered Fc-mediated uptake by the mononuclear phagocytic cells and accumulation of NPs in the liver and spleen (219,220). However, due to the control over the panitumumab

orientation on Pan modified ^{64}Cu-PEO-PBCL NPs higher liver and spleen uptake in comparison to ^{64}Cu-PEO-PBCL NPs was not seen in our biodistribution data.

In general, NPs are accumulated in organs with leaky endothelial wall such as liver, spleen, bone marrow and tumor (221) which was in line with the biodistribution seen in this study. However, in a similar work done by Paiva et al. (146), PEO-PBCL NPs were decorated with EGFR targeting peptide (GE11) and radiolabeled with ^{64}Cu, a higher %ID/g for spleen and blood and a lower %ID/g for liver was reported in comparison to our labeled NPs, which could be as a result of using peptide as targeting agent or attribution of radiolabeling method used in the present study. In the presented method the surface of NPs were modified with chelators and in Paiva et al. work the targeting agent was radiolabelled. Both studies used PEO-PBCL polymers with similar degree of polymerizations. Therefore, the observed differences are not attributed to PEO-PBCL NPs and may be an artifact of the presence of chelating agent on the surface of PEO-PBCL NPs triggering uptake by mononuclear phagocytic cells and liver/spleen distribution.

4.5. Conclusion

The presented work introduces a novel method for developing antibody modified NPs with control on the orientation of antibody on the surface of NPs, so that the Fc portion of the antibody is not exposed and/or antibody variable region is intact. The developed method discussed here for radiolabelling PEO-PBCL NPs, was capable of producing stable radiolabeled NPs in mice bearing NCSL tumors. Future studies should focus on the optimization of radiolabeled antibody modified NPs for enhanced *in vivo* performance and biodistribution.

Chapter 5

Development of methods for long-term storage of poly(ethylene glycol)-poly(α-benzyl carboxylate-ε-caprolactone) nanoparticles: the effect of cryoprotectant and storage conditions on nanoparticle aggregation

5.1. Introduction

Nanoparticles (NPs) are increasingly attracting attention for use as drug/gene delivery vectors in the pharmaceutical industry (222). This advancement is owed to the capacity of NPs as vehicles that can improve the bioavailability of hydrophobic compounds through their effective solubilization, control drug release kinetics and/or preferentially deliver drugs to their site of action in the biological system (223,224). These characteristics may eventually lead to a decrease in drugs' side effects and an increase in drugs' effectiveness (222).

For biological use, NPs are commonly prepared in aqueous media. Nanoparticles are thermodynamically unstable and prone to aggregate formation when stored for long periods (225). In the pharmaceutical industry, low-quality products are not acceptable and a factor determining the quality of the product is stability and reasonable shelf life at feasible storage conditions. Nanoparticles are required to retain their initial physicochemical properties and quality in terms of chemical structure integrity, average diameter, polydispersity, morphology and drug encapsulation as well as release properties throughout their shelf life (226). A rise in temperature, in a lot of instances, can jeopardize the stability of NPs with regards to one or a few of the above properties. For this reason, NP products are usually stored in cold temperatures or in a frozen state. This has been the case for COVID-19 mRNA vaccines that -80 storage were required (222). The requirement for such a storage condition imposes limitations in the distribution and storage of NPs in remote areas and locations that do not have access to devices with controlled freezing temperatures. An alternative solution is the removal of water from the prepared NPs and NP reconstitution at the time of use, which can not only facilitate the distribution and use of these products, but also extend the shelf life of the NP formulations.

In order to remove water from the formulations, freeze-drying also known as lyophilization is a popular method leading to an increase in the shelf life of nano formulations at room temperature (RT) (224,226). This method is comprised of three main steps, freezing, primary and secondary evaporation (227). Briefly, after the sample is frozen, sublimation of frozen water accrues during the primary evaporation followed by desorption of the remaining water during the secondary evaporation (224,226–228). All three freeze-drying steps cause stress on NP formulations (228). Among these steps, the freezing step causes the most stress and can lead to challenges such as aggregation of particles and growth in NP size (229,230). Freeze-drying of NPs is considered successful when the physicochemical properties of the NP, such as particle size, polydispersity and drug encapsulation, are preserved following reconstitution, and the dried product shows rapid reconstitution (231,232).

To overcome the stresses caused by freezing and/or freeze-drying, cryoprotectants are required (231). Different compounds such as sugars, e.g., sucrose, mannose, trehalose, (233), poly(ethylene glycol) (PEG) (225), and polyvinylpyrrolidone (234) have been reported to function as cryoprotectants. In general, the higher the concentration of cryoprotectant, and the faster the freezing rate, a better NP re-dispersion is obtained (228).

Each NP formulation requires its unique conditions for lyophilization since this process is dependent on the nature of the particles and their chemical structure (225). Most reports in the literature have focused on the lyophilization of liposomes and solid lipid NPs. Reports on freeze-drying of polymeric NPs are limited (229).

The focus of the present study was to investigate proper conditions for long term storage of poly (ethylene oxide)-*block*-poly (α-benzyl carboxylate-ε-caprolactone) (PEO-PBCL) NPs through

lyophilization or freeze-thaw methods. In this context, the effect of different cryoprotectants, their concentration, freezing and storage conditions on the physicochemical properties of reconstituted or thawed PEO-PBCL NPs was assessed to determine the most optimum storage conditions for these formulations.

PEO-PBCL is a biocompatible and biodegradable block copolymer that has been used to improve the water solubility of poorly soluble drugs as well as preferential delivery of anticancer agents to solid tumors (145,235,236). Accordingly, the effect of storage conditions on the physicochemical properties of drug loaded PEO-PBCL NPs is of interest. We investigated the effect of storage conditions on the properties of PEO-PBCL NP formulation of two model investigational drugs namely A83B4C63 and A4, which can potentially be used as chemo and radio-sensitizers in cancer therapy. A83B4C63 is a novel poorly water-soluble compound that inhibits a DNA repair enzyme known as polynucleotide kinase-phosphatase (PNKP). A4 is a novel inhibitor of another DNA repair enzyme known as ERCC1-XPF heterodimer. Development of PEO-PBCL formulations of A83B4C63 and A4 have been reported by our team previously (145,237)

5.2. Materials and Methods

5.2.1. Materials

Poly (ethylene glycol) (PEG) average molecular weight of 1450, 3350, and 8000 g/mol (CAS No.:25322-68-3), methoxy PEG with average molecular weight of 2000 and 5000 g/mol (CAS Number:9004-74-4) sucrose, and all solvents were purchased from Sigma (St. Louis, USA.). ε-Caprolactone was obtained from Lancaster Synthesis (Lancashire, England). α-Benzyl carboxylate-ε-caprolactone (BCL) monomer was prepared by Alberta Research Chemicals Inc. (Edmonton, Canada) based on previously reported methods (144). Stannous octoate was purchased from MPBiomedicals Inc. (Tuttlingen, Germany). A83B4C63 and A4 were synthesized by the laboratory of Dr F. West based on protocols reported in previous publications (237,238) . Sucrose, sorbitol, lactose, and mannitol were purchased from Merck, Germany.

5.2.2. Polymer synthesis

Block copolymers were synthesized based on previously reported studies through ring opening polymerization (144,237,239). Briefly, depending on the desired degree of polymerization (DP) for the PBCL block, methoxy PEG (5000 g/mol) and BCL were weighed and transferred to an ampule. This was followed by the addition of stannous octoate as catalyst. Afterward, the ampule was connected to a vacuum line and sealed. The ampule was placed in a 140°C oven for 4 hours. BCL to PEO molar ratios of 10, 15, and 30 were used. To purify the synthesized polymer from unreacted starting materials and catalyzer, the ampule contents were dissolved in dichloromethane and added to hexane to precipitate the synthesized polymer. The polymer was left under vacuum for hexane to evaporate. The synthesized polymers were characterized for the DP of PBCL using

a 600-MHz Bruker NMR spectrometer (Bruker Instruments, Inc., Billerica, MA, USA). Polymers were dissolved in deuterated chloroform for ^{1}H NMR analysis. The peak intensity of PEO (-CH2CH2O-, δ 3.65 ppm) to that of PBCL (-OCH2-, δ 4.1 ppm) in the 1H NMR spectra, were compared to calculate the average molecular weight of PBCL block assuming a 5000 Da molecular weight for the PEO block (144,204).

5.2.3. Nanoparticle preparation

PEO-PBCL NPs were prepared based on previous works (143,144). In brief, 10 mg of the polymer was weighed and dissolved in 0.25 mL acetone and added dropwise to 5 mL double distilled water (DDH_2O) while stirring with a magnet bar on a stirrer leaving the sample overnight for the acetone to evaporate. After acetone evaporation, the NP size and polydispersity were measured using dynamic light scattering (DLS) (either MALVERN Nano-ZS90 ZETA-SIZER, Malvern Instruments Ltd, Malvern, UK or Zetasizer Ultra, Malvern Instruments Ltd, Malvern, UK were used). All samples were measured at 2 mg/mL polymer concentration at 25°C with a 173° angle scattering unless mentioned otherwise.

For developing A83B4C63 loaded PEO-PBCL NPs a previously developed method was used (145,237). Briefly, 1 mg of A83B4C63 and 10 mg of PEO-PBCL polymer were weighed and dissolved in 0.25 mL acetone and added dropwise to 5 mL of DDH_2O under stirring. Then the sample was left overnight for the acetone to evaporate. After acetone evaporation, the sample was centrifuged at 10,000 x g for 10 minutes to spin down the un-encapsulated A83B4C63. To determine encapsulation efficiency, a 20 µL sample of the purified A83B4C63 loaded NPs was taken and 80 µL dimethyl sulfoxide (DMSO) was added, followed by the UV absorbance measured at 400 nm wavelength using a plate reader (BioTekInstruments Inc.).

PEO-PBCL NPs encapsulating A4 were developed based on previous work (240). In general, 0.5 mg of A4 and 10 mg of PEO-PBCL were weighed and dissolved in 0.25 mL acetone followed by dropwise addition to 5 mL DDH_2O under stirring and leaving the sample overnight for acetone to evaporate. To purify the sample from un-encapsulated A4, the prepared sample was centrifuged at 10,000 x g for 10 minutes. To calculate the encapsulation efficiency, to a 20 µL sample from the purified sample 80 µL DMSO was added, and UV absorption was measured via a plate reader set to 470 nm wavelength.

The encapsulation efficiency was calculated using the following equation:

$$EE\ \%= \frac{the\ amount\ of\ encapsulated\ drug}{the\ total\ amount\ of\ drug} X100$$

5.2.4. Freeze-drying method

5.2.4.1. Selection of the best sugar as cytoprotectant

NP solutions were placed in Eppendorf tubes (Eppendorf, USA) and rapidly frozen in a mixture of dried ice and acetone. The freeze-drying process was carried out by VirTis Lyo-Centre lyophilizer, USA. The freeze-dried sample was reconstituted with 1 mL of double distilled water with manual shaking. The resulting colloidal dispersion were then used for particle size analysis by DLS (MALVERN Nano-ZS90 ZETA-SIZER (Malvern Instruments Ltd, Malvern, UK).

Different sugars (sucrose, mannitol, trehalose, lactose, and sorbitol) were first evaluated to find the appropriate cytoprotectant for the storage of PEO-PBCL NPs dried using freeze-drying method. The concentration of sugars was 5mg/mL and it was added to PEO-PBCL NPs in a 1:10 w/w ratio respectively.

5.2.4.2. Assessing the effect of PEG as cytoprotectant

PEO-PBCL NPs (2 mg) were divided into 1 mL aliquots and transferred to 2 mL Eppendorf tubes (Eppendorf, USA). Appropriate volumes of PEG or methoxy PEG from stock solution were added to each aliquot. The samples with or without cryoprotectants were completely frozen at -80 freezer. Frozen samples were transferred to the freeze-dryer chamber (Labconco, USA) with the collector set to -85°C and vacuum set to 0 mbar for 48 hours. Freeze-dried samples were reconstituted in 1 mL of DDH_2O with moderate shaking. No sonication was used to reconstitute the samples. Nanoparticle average diameter and PDI were measured via DLS (either MALVERN Nano-ZS90 ZETA-SIZER, or Zetasizer Ultra, Malvern Instruments Ltd, Malvern, UK were used as indicated under each experimental condition).

5.2.5. Freeze-Thaw method

The PEO-$PBCL_9$ NPs (2 mg/mL) were divided into 1 mL samples and frozen by either snap-freezing via liquid nitrogen or placed in a -20 or -80 °C freezer. After samples were completely frozen for 4-5 hours, they were transferred to a heat block (VWR digital heat block, VWR, USA) set to 25 °C until thawed. Nanoparticles' size and PDI were measured by DLS (Zetasizer Ultra, Malvern Instruments Ltd, Malvern, UK).

To assess the role of cryoprotectants, 1 mL of PEO-PBCL NPs (2mg/mL) with or without cryoprotectants were subjected to freezing at -80 °C freezer and thawed on a heat block (VWR digital heat block, VWR, USA) set to 25 °C. Nanoparticles' size and PDI were measured using DLS (either MALVERN Nano-ZS90 ZETA-SIZER, or Zetasizer Ultra ,Malvern Instruments Ltd, Malvern, UK were used). Cryprotectants tried included PEGs with molecular weights of 1450,

3350, and 8000 g/mol and methoxy PEG with molecular weights of 2000 and 5000 g/mol, prepared as a stock solution of 20 mg/mL. The w/w ratio of PEG to the PEO-PBCL polymer of 0.25:1, 0.5:1, 1:1, 2:1 and 4:1 were used. The w/w ratio of sucrose to the PEO-PBCL polymer was 13.25:1.

Response measurement

The Z average diameters before and after the freeze-thawing and freeze-drying processes of samples without or with different concentrations of the cryoprotectant were measured by DLS (either MALVERN Nano-ZS90 ZETA-SIZER, or Zetasizer Ultra, Malvern Instruments Ltd, Malvern, UK). The response for each sample was calculated as follows:

$$Response = Sf/Si$$

Si and Sf are the sizes immediately after the addition of the cryoprotectant (before the freeze-thawing or freeze-drying process) and the size after the freeze-thawing or freeze-drying treatment, respectively. The size ratio was used as a response (dependent variable) for the optimization study

5.2.6. Transmission electron microscopy (TEM)

The morphology of PEO-PBCL$_9$ and PEO-PBCL$_{22}$ NPs with or without methoxy-PEG5000 before and after freeze-drying was determined by TEM, Morgagni TEM (Field Emission Inc., USA). In brief, a drop of NP solution with a polymer concentration of 2 mg/mL was spotted on a copper-coated grid. The grid was kept horizontal for 1 min. allowing the particles to settle. Afterward, the excess sample was removed from the grid. The grid was negatively stained with 2%

phosphotungstic acid and the excess was removed after 2 minutes. Then the grid was placed into the TEM for visualization.

5.2.7. Differential Scanning Calorimetry (DSC)

The melting temperatures for PEO-PBCL block copolymers and PEO-PBCL$_{22}$ NPs after freeze-drying with and without PEG were assessed by DSC, (-1576 TA instrument, USA). The samples were weighed (1–5 mg) and sealed in Tzero aluminum pans. The heating rate was 10 °C/min starting from 25 to 120 °C under a nitrogen atmosphere. An empty Tzero pan was set as the reference.

5.2.8. Statistical analysis

The experimental design and regression analysis were carried out by either SPSS 22 or Prism 8.0 as mentioned in each case in the text. The significance of independent variables and their interactions were tested by t test, one-way and two-way analysis of variance (ANOVA). P value of 0.05 was used to determine the statistical significance. Various statistical indices such as t value, p value, F value, correlation coefficient (R), determination coefficient (R^2), and adjusted determination coefficient (adj R^2), were used to assess the statistical significance of the quadratic models. Composite desirability values were used for comparison of different fabrication conditions.

5.3. Results

5.3.1. Characterization of synthesized polymers

Comparison of the peak intensity of PEO (-CH_2CH_2O-, δ 3.65 ppm) to that of PBCL (-OCH_2-, δ 4.1 ppm) showed the preparation of PEO-PBCL polymers with a DP of 9, 14 or 22 for the PBCL block from the polymerization procedures where PEO: PBCL molar ratios of 1:10 to 1:30 were applied. The DP of polymers is shown as a subscript for polymers under study from here on in the paper.

5.3.2. Selection of the best sugar as cryoprotectant for the freeze-drying of PEO-$PBCL_{14}$ NPs

In a preliminary study, different sugars were tested to find the appropriate cryoprotectant for the storage of PEO-PBCL NPs. Table 5.1 shows the results for 6 different sugars under study. The concentration of NPs and sugars was chosen according to previous literature and pilot studies (229,241). Table 5.2 shows the results of different sugars on the size of NPs before and after freeze-drying and reconstitution. As evident from the ratio of average diameter of NPs after to before freeze-drying and reconstitution, addition of sucrose as cryoprotectant lead to the least increase in size or minimum NP aggregation. Therefore, sucrose was chosen as the sugar cryoprotectant for studies in the next steps.

In the next step, the effect of sucrose concentration on the average diameter of NPs before and after Freeze-drying and reconstitution was assessed. Three different concentrations of PEO-PBCL and sucrose were studied to monitor the effect of polymer and sucrose concentration on NPs size

after freeze-drying (Table 5.2). Table 5.3 summarizes the results of this study which was performed using a central composite design. In general, the data showed that a sucrose concentration of ≥ 26.5 mg/mL was needed for PEO-PBCL NPs at 2-3 mg/mL to show ~ 2-fold aggregation upon freeze drying and reconstitution. A concentration of 3 mg/mL of sucrose was not adequate to prevent the aggregation of PEO-PBCL NPs upon freeze-drying and reconstitution.

Table 5.1. Z average diameter of NPs before (Si) and after the freeze-drying process and the ratio of Sf/Si of different sugar as lyoprotectant for PEO-PBCL$_{14}$.

Name of sugar	Si (nm) N=2	Sf (nm) N=2	Ratio Sf/Si
Sucrose	46.3±1.8	81.36±2.1	1.8
Mannitol	47.3±2.2	92.24±3.4	2
Trehalose	48.5±2.3	654.5±5.4	13.5
Lactose	46.7±1.9	117.2±6.3	2.5
sorbitol	46.1±1.9	178.8±7.1	3.9

Table 5.2. The two factors and the corresponding three-level settings for lyophilization of diblock copolymer NPs: X1(sucrose concentration); X2 (copolymer concentration).

Level	X1 (mg/mL)	X2 (mg/mL)
-1	3	1
0	26.5	2
+1	50	3

Table 5.3. Experimental conditions for central composite design and Z average diameter of micelles before (Si) and after freeze-drying process and the ratio of Sf/Si (as a response) of different concentration of sucrose for PEO-PBCL$_{14}$.

Trial	X1	X2	Si (nm) N=3	Sf (nm) N=3	Response (Sf/Si)
1	+	+	23.57±1.3	86.03±1.9	3.62
2	+	-	23.08±1.1	49.51±1.7	2.15
3	-	+	20.13±1.4	9005±5.2	447.34
4	-	-	19.85±1.2	1585±4.4	49.95
5	+	0	22.68±1.3	44.74±1.5	1.97
6	-	0	18.49±1.1	3511±4.5	189.89
7	0	+	20.22±1.2	42.07±1.2	2.08
8	0	-	20.72±1.2	44.77±1.1	2.16
9	0	0	19.86±1.3	57.39±1.6	2.86
10	0	0	20.32±1.2	50.50±1.4	2.49
11	0	0	20.24±1.3	55.86±1.4	2.76

5.3.3. Freeze-drying of PEO-PBCL$_9$ NPs using PEG as cryoprotectant

Free PEG was used as the cryoprotectant after PEO-PBCL$_9$ NP preparation. The effect of the molecular weight of PEG and its ratio (w/w) to that of PEO-PBCL on the average diameter and polydispersity index of freeze-dried and reconstituted NPs was compared to NPs with the addition of PEG before freeze drying. As shown in Figure 5.1. A, after the addition of PEG to the PEO-

PBCL$_9$ NPs before freeze-drying, the size of the NPs increased from 36.93±0.14 nm to ~40nm ($p<0.05$, Two-way ANOVA). However, the PDI did not significantly change with different ratios of PEG ($p>0.05$, Two-way ANOVA) other than the 4:1 w/w ratio of PEG to polymer ($p<0.05$, Two-way ANOVA) (Figure 5.1. B) (Figure S2.)

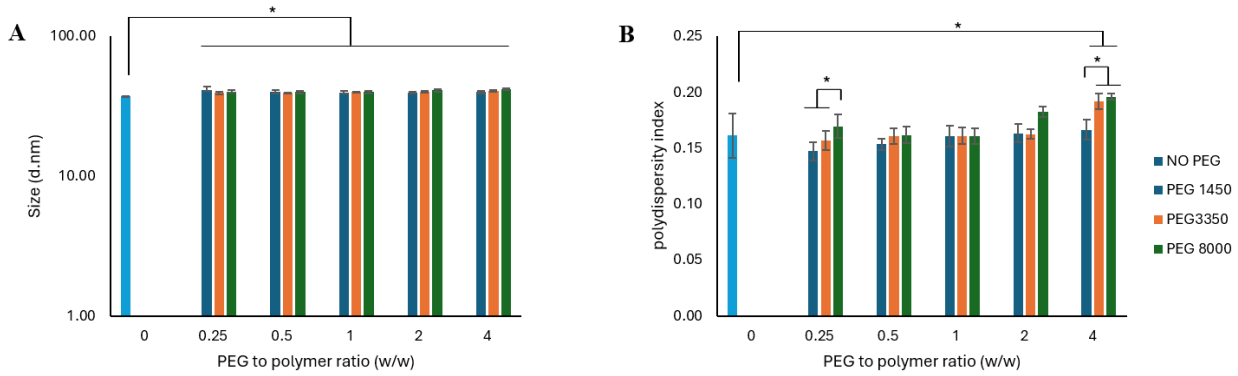

Figure 5.1. A) PEO-PBCL$_9$ NPs' size and B) PDI after the addition of different molecular weight PEGs at different concentrations before freeze-drying. All samples were measured at RT. (* represents $p<0.05$, Two-way ANOVA, n=3)

Nanoparticles' average diameter and PDI increased after freeze-drying for all samples including those that contained PEGs of different MWts at various ratios (Figure 5.2). Among different PEG MWts, PEG 3350 and 8000 g/mol seemed to be more efficient cryoprotectants compared to PEG 1450 g/mole. A similar trend was observed for the PDI of the PEO-PBCL$_9$ NPs. Original DLS size populations are shown in Figure S3. The least degree of increase in the average diameter of reconstituted NPs was observed when PEG 3350 and 8000 g/mol, particularly at w/w ratios of 2 and 4 were added to PEO-PBCL$_9$ (Figure 5.2. A). The comparison of the average diameter of NPs between these two groups was not significant ($p>0.05$, Two-way ANOVA). Similar to the average diameter, the PDI of NPs was the lowest for PEG 3350 and 8000 g/mol as cryoprotectant at a w/w

ratio of 4. The PDI of PEO-PBCL$_9$ NPs showed a decreasing trend as the weight ratio of PEG as cryoprotectant was increased. This PEG: PEO-PBCL weight ratio-dependent decreasing trend in PDI was observed for all PEGs under study (Figure 5.2. B) (Figure S3).

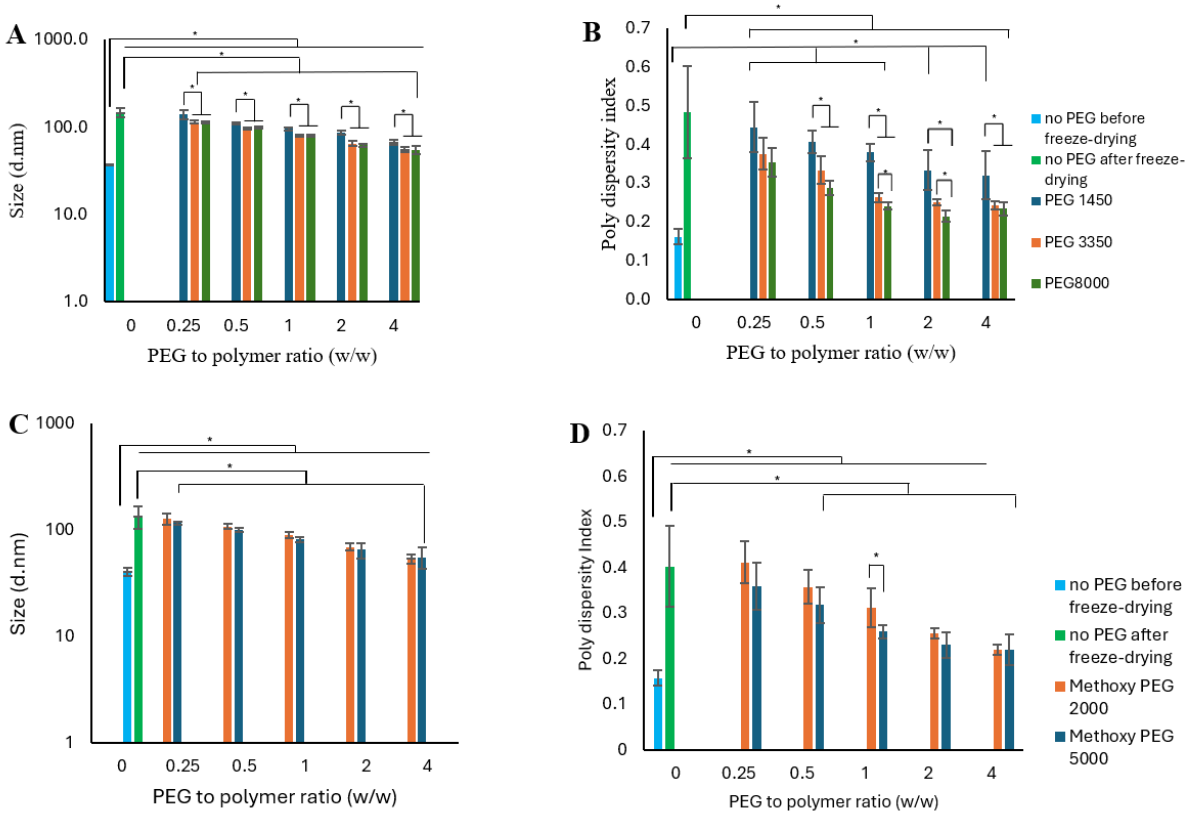

Figure 5.2. A) PEO-PBCL$_9$ NPs' average diameter and B) PDI after freeze-drying and reconstitution in DDH$_2$O using different molecular weight PEGs at different concentrations as cryoprotectant; C)) PEO-PBCL$_9$ NPs' average diameter and D) PDI after freeze-drying and reconstitution in DDH$_2$O using different molecular weight mPEG at different concentrations as cryoprotectantt (* represents p<0.05, Two-way ANOVA, n=3)

Table 5.4. The effect of freeze drying and cryoprotectant on the average diameter of PEO-PBCL$_9$ NPs. The initial size of NPs before freeze drying in the absence of cryoprotectant (Si) was 36.93+0.14 and 40.85± 3.64 nm for the NPs that were

freeze-dried with PEG and methoxy PEG respectively. The average diameter without cryoprotectant ranged between 135-146 nm.

PEO-PBCL sample additive	w/w ratio	Nanoparticle size(Sf)(d.nm)+SD (n=3)	Response (Sf/Si)
PEG 1450	0.25:1	139.7+16.52	3.78
PEG 3350		114.3+4.99	3.10
PEG 8000		113.8+3.30	3.08
Methoxy PEG 2000		127.5+15	3.12
Methoxy PEG 5000		116+4.66	2.85
PEG 1450	0.5:1	111.6+3.19	3.02
PEG 3350		96.8+2.86	2.62
PEG 8000		100.1+2.83	2.71
Methoxy PEG 2000		108.5+6.27	2.66
Methoxy PEG 5000		100.6+4.75	2.46
PEG 1450	1:1	95.7+4.42	2.59
PEG 3350		79.5+2.02	2.15
PEG 8000		80.4+2.38	2.18
Methoxy PEG 2000		90.04+6.23	2.20
Methoxy PEG 5000		81.68+4.68	2.00
PEG 1450	2:1	86.4+4.54	2.34
PEG 3350		64.7+4.48	1.75
PEG 8000		62.0+2.07	1.68
Methoxy PEG 2000		69.72+4.85	1.71
Methoxy PEG 5000		65.29+10.76	1.60
PEG 1450	4:1	66.7+4.58	1.81
PEG 3350		55.3+3.35	1.50
PEG 8000		55.1+6.44	1.49
Methoxy PEG 2000		53.91+5.37	1.32
Methoxy PEG 5000		55.73+12.58	1.36

To study the effect of the end group of PEG on its cryoprotectant properties, methoxy PEG with 2 molecular weights of 2000 and 5000 g/mol was used as a cryoprotectant during freeze-drying PEO-$PBCL_9$ NPs. Similar to what has been observed for the OH-terminated PEGs, the addition of methoxy-terminated PEGs was not able to make the average diameter and PDI of reconstituted PEO-PBCL NPs similar to that before freeze drying (Figure 5.2. C and D). In other words, irrespective of the MWt and ratio of methoxy PEG added as a cryoprotectant, PEO-$PBCL_9$ NPs showed an increase in average diameter and PDI following freeze-drying and reconstitution. However, the degree of this increase was less compared to the PEO-$PBCL_9$ NPs for which no cryoprotectant was used. Among different ratios, the NPs' size was the lowest for PEG: PEO-$PBCL_9$ w/w ratio of ≥ 2, irrespective of the MWt of PEG. The PDI of NPs seems to decrease significantly as the w/w ratio of PEG to PBCL is increased ≥ 0.25 irrespective of PEG MWt although the dose-dependent decrease in PDI seemed steeper for PEG 5000 compared to 2000 g/mol (Figure S4.) Overall, the best results in terms of inhibition of NP aggregation appeared to be achieved by PEG 3350 and methoxy PEG 5000 at 4:1 w/w ratio (Figure S3 and S4).

5.3.4. Freeze-drying of PEO-$PBCL_{22}$ NPs using PEG or sucrose as cryo protectant

Based on the data obtained on PEO-$PBCL_9$ NPs, we have selected methoxy PEG 2000, methoxy PEG 5000 and PEG 3350 at w/w ratios of 1:2 and 1:4 to PEO-PBCL; also, based on Table 5.3. sucrose with the w/w ratio of 13.25:1 to PEO-PBCL polymer as cryoprotectants for PEO-$PBCL_{22}$ NPs. As shown in Figure 5.3, adding sucrose led to a 4 to 5- fold increase in the average PEO-$PBCL_{22}$ NP diameter. The fold increase in size when PEGs were used as cryoprotectants was 2 to 3-fold on average (Table 5.5) Also, the visual observation of the samples were in line with the

results reported by DLS. The samples without cryoprotectant sedimented after being left intact after 2-3 minutes (Figure 5.3 B and D).

In general, the increase in NPs' size after freeze-drying compared to before freeze-drying was lower when a PEG: PEO-PBCL ratio of 4:1 was used and also when the MWt of PEG was raised. For comparison, the increase in NPs' size after freeze-drying compared to before freeze-drying without any cryoprotectant was 23.09. At the 4:1 ratio of PEG 3350 g/mol and methoxy PEG 5000 g/mol to PEO-PBCL, there was no significant difference in the measured PDI value for NPs before and after freeze-drying, pointing to the success of these two materials as cryoprotectants compared to other cryoprotectants under study in the freeze-drying process ($p>0.05$, One-way ANOVA) (Figure S5 and S6).

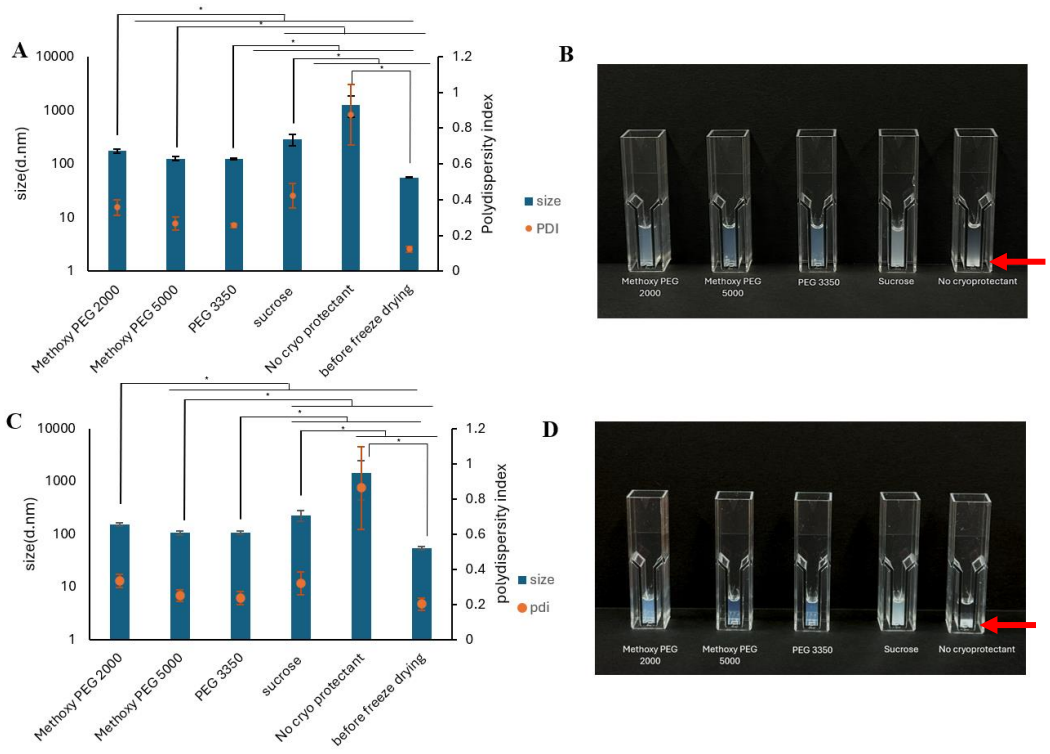

Figure 5.3. A & C) Nanoparticles' size and PDI after reconstitution of freeze dried NPs using different cryoprotectants in 1 mL of DDH_2O compared to NP size and PDI before freeze drying. B & D) visual appearance of reconstituted PEO-PBCL NPs with different cryoprotectants. The w/w ratio of PEG: and sucrose to PEO-$PBCL_{22}$ was 2:1 and 13.25:1, respectively in Figures A and B (* represent $p<0.05$, One-way ANOVA, n=3). The w/w ratio of PEG: and sucrose to PEO-PBCL 22 was 4:1 and 13.25:1, respectively, in Figures C and D. (* represent $p<0.05$, One-way ANOVA, n=3). Red arrow indicates the precipitation of PEO-PBCL NPs.

Table 5.5. The effect of freeze-drying and cryoprotectant on the average diameter of PEO-$PBCL_{22}$ NPs. The initial size of NPs before freeze drying in the absence of cryoprotectant (Si) was 54.5± 3.67 nm.

PEO-PBCL sample additive	w/w ratio	Nanoparticle size (Sf) (d.nm)+SD (n=3)	Response (Sf/Si)
Methoxy PEG 2000		173.8±12.72	3.14
Methoxy PEG 5000	2:1	126±9.683	2.27

PEG 3350		124.5±4.933	2.25
sucrose	13.25: 1	287.9±68.66	5.19
no cryoprotectant	NA	1280±549.5	23.09
Methoxy PEG 2000	4:1	155.3±10.93	2.85
Methoxy PEG 5000		105.3±11.05	1.93
PEG 3350		105.8±8.05	1.94
sucrose	13.25: 1	229.9±51.13	4.22
no cryoprotectant	NA	1455±1016	26.70

5.3.5. The effect of freeze-thaw method on the size and polydispersity of PEO-PBCL NPs without cryoprotectant

The effect of freezing conditions on the size of PEO-PBCL$_9$ NPs thawed to RT without any cryoprotectant is shown in Figure 5.4. The NP average diameter at RT was 37.3$\pm$0.46 nm and the NP population PDI was 0.16$\pm$0.01. After freeze-thaw the NPs' size significantly increased to 57.1$\pm$3.88 nm, 60.2$\pm$1.14 nm, and 68.6$\pm$5.65 nm for NPs that were frozen using liquid nitrogen, -80, and -20 freezer, respectively ($p<0.05$, One-way ANOVA, compared to NP size before freeze-thaw). Accordingly, the PDI of NPs significantly increased from 0.16$\pm$0.01 at RT to 0.20$\pm$0.01, 0.19$\pm$0.01, and 0.28$\pm$0.02 for NPs that were frozen using liquid nitrogen, -80 °C, and -20 °C freezer, respectively ($p<0.05$, One-way ANOVA, compared to PDI of NPs before freeze-thaw). Moreover, the NPs' average diameter and PDI was significantly higher for NPs that were frozen at -20 °C compared to the ones frozen either in liquid nitrogen or the -80 °C freezer ($p<0.05$, One-way ANOVA). However, these values did not significantly change between NPs that were frozen in liquid nitrogen and the -80 °C freezer ($p>0.05$, One-way ANOVA) (Figure S7.)

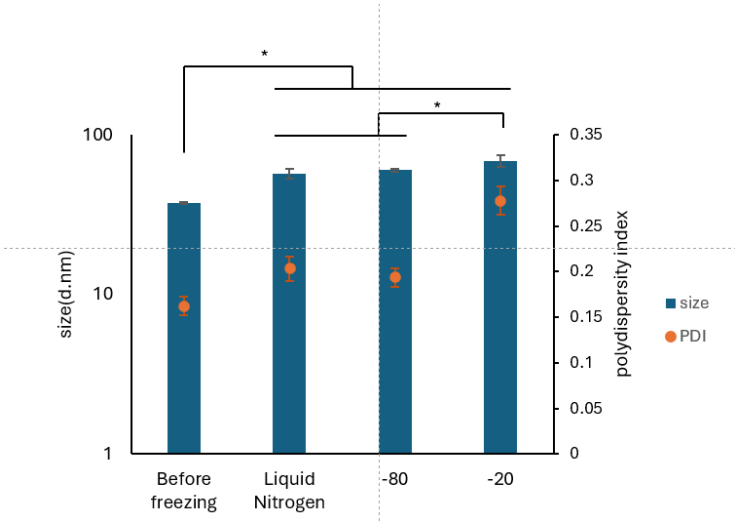

Figure 5.4. PEO-PBCL9 NPs' size and PDI after freeze-thaw at different freezing conditions (* represents $p<0.05$, One-way ANOVA, n=3)

5.3.6. Freeze-thawing of PEO-PBCL NPs using PEG or sucrose as cryoprotectant

In this experiment, PEGs of different MWt and end groups as well as sucrose were used as cryoprotectant. The w/w ratio of PEG was 2:1 to PEO-PBCL while sucrose concentration was 13.25:1 to PEO-PBCL. The NPs were then frozen at -80 °C and thawed at RT to evaluate the effect of PEG on NP average diameter and PDI by freeze and thaw procedure. As illustrated in Figure 5.5, for PEO-PBCL$_9$, the NPs' average diameter significantly increased when no cryoprotectant was added ($p<0.05$, One-way ANOVA). The NPs' average size difference was not significant between the NPs that had PEG as cryoprotectant and NPs before freezing ($p>0.05$, One-way ANOVA). Nanoparticles' average diameter when sucrose was used as a cryoprotectant was significantly higher than those before freeze-thawing but lower than the NPs without any cryoprotectant ($p<0.05$, One-way ANOVA). The PDI values for NPs that were not freeze-thawed and the NPs that were frozen with either sucrose or methoxy PEG 2000 g/mol were significantly

different ($p<0.05$, One-way ANOVA). However, the difference among PDI values for other groups was not significant ($p>0.05$, One-way ANOVA) (Figure S9.)

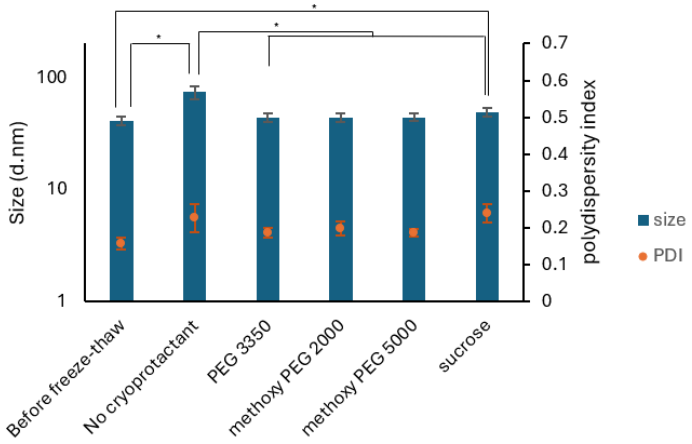

Figure 5.5. PEO-PBCL$_9$ NPs' average diameter and PDI before and after freeze-thawing without or with using different PEGs or sucrose as cryoprotectant. The (w/w) ratio of PEGs and sucrose to PEO-PBCL9 were 2:1 and 13.25:1, respectively. (* represent $p<0.05$, One-way ANOVA, n=3)

Table 5.6. The effect of freeze-thaw and cryoprotectant on the average diameter of PEO-PBCL$_9$ NPs. The initial size of NPs before freeze drying in the absence of cryoprotectant (Si) was 40.85± 3.64 nm.

PEO-PBCL$_9$ sample additive	Nanoparticle size (Sf) (d.nm)+SD (n=3)	Response (Sf/Si)
Methoxy PEG 2000	43.61±3.6	1.07
Methoxy PEG 5000	43.91±3.44	1.07
PEG 3350	43.58±3.71	1.06
sucrose	48.91±4.54	1.20
no cryoprotectant	73.72±9.89	1.80

When PEO-PBCL$_{22}$ NPs were subjected to the freeze-thaw procedure, the average size and polydispersity of NPs significantly enhanced when no cryoprotectant was used. In contrast, the NP size and PDI remained the same before and after freeze-thaw when a cryoprotectant was used ($p > 0.05$, One-way ANOVA). This effect was independent of the type and concentration of cryoprotectants under study (Figure 5.6) (Figure S10).

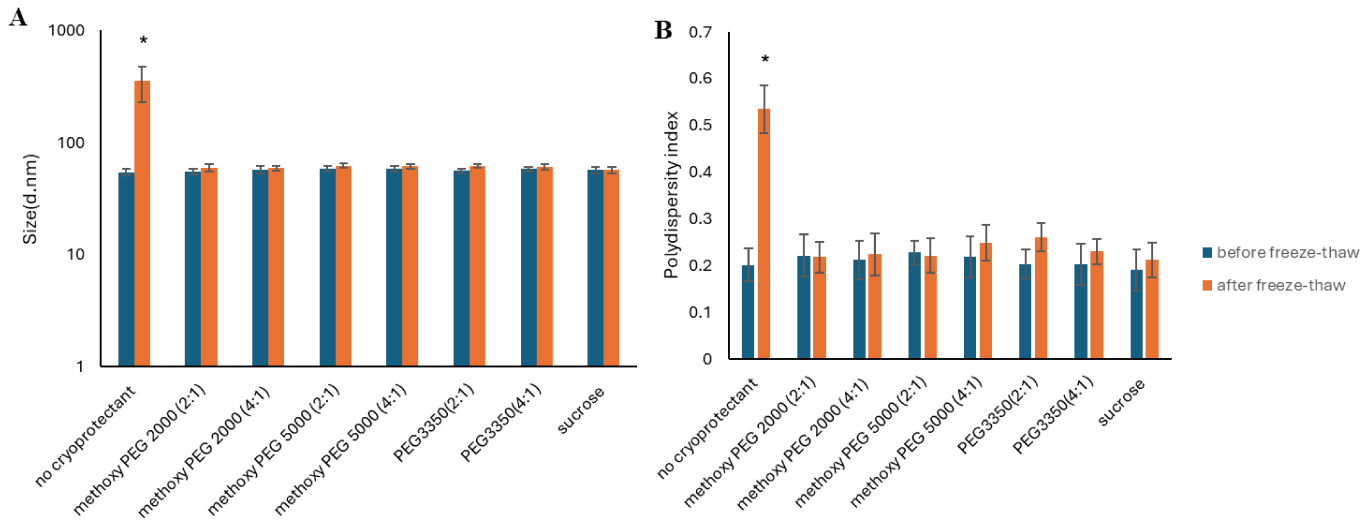

Figure 5.6. PEO-PBCL$_{22}$ NPs' A) average diameter and B) PDI before and after freeze-thawing without or with using cryoprotectant. The (w/w) ratio of PEGs and sucrose to PEO-PBCl22 were 2:1,4:1 and 13.25:1, respectively. (* represent $p<0.05$, One-way ANOVA)

Table 5.7. The effect of freeze thawing and cryoprotectant on the average diameter of PEO-PBCL$_{22}$ NPs. The initial size of NPs before freeze drying in the absence of cryoprotectant (Si) was 54.5± 3.67 nm.

PEO-PBCL sample additive	w/w ratio	Nanoparticle size (Sf) (d.nm)+SD (n=3)	Response (Sf/Si)

Methoxy PEG 2000 before freeze-thaw	2:1	55.68±3.14	1.02
Methoxy PEG 2000 after freeze-thaw		59.58±4.74	1.09
Methoxy PEG 5000 before freeze-thaw		58.05±3.34	1.07
Methoxy PEG 5000 after freeze-thaw		62.09±2.97	1.14
PEG 3350 before freeze-thaw		55.87±2.54	1.03
PEG 3350 after freeze-thaw		62.17±2.65	1.14
Methoxy PEG 2000 before freeze-thaw	4:1	57.66±4.58	1.06
Methoxy PEG 2000 after freeze-thaw		59.26±2.72	1.09
Methoxy PEG 5000 before freeze-thaw		58.59±3.92	1.08
Methoxy PEG 5000 after freeze-thaw		61.44±2.74	1.13
PEG 3350 before freeze-thaw		58.23±2.96	1.07
PEG 3350 after freeze-thaw		60.39±3.58	1.11
sucrose before freeze-thaw	13.25: 1	57.01±3.59	1.05
sucrose after freeze-thaw		57.24±3.96	1.05
no cryoprotectant	NA	353.7±126.1	6.49

5.3.7. TEM

Figure 5.7 shows the TEM images of PEO-PBCL NPs of two different PBCL MWts before and after freeze-drying, with and without PEG. The NP sizes from TEM images seem to be in line with what was measured previously with DLS. Also, when PEO-PBCL NPs were freeze-dried without PEG, aggregation of PEO-PBCL NPs was seen. However, these aggregations were not seen when PEG was added as a cryoprotectant.

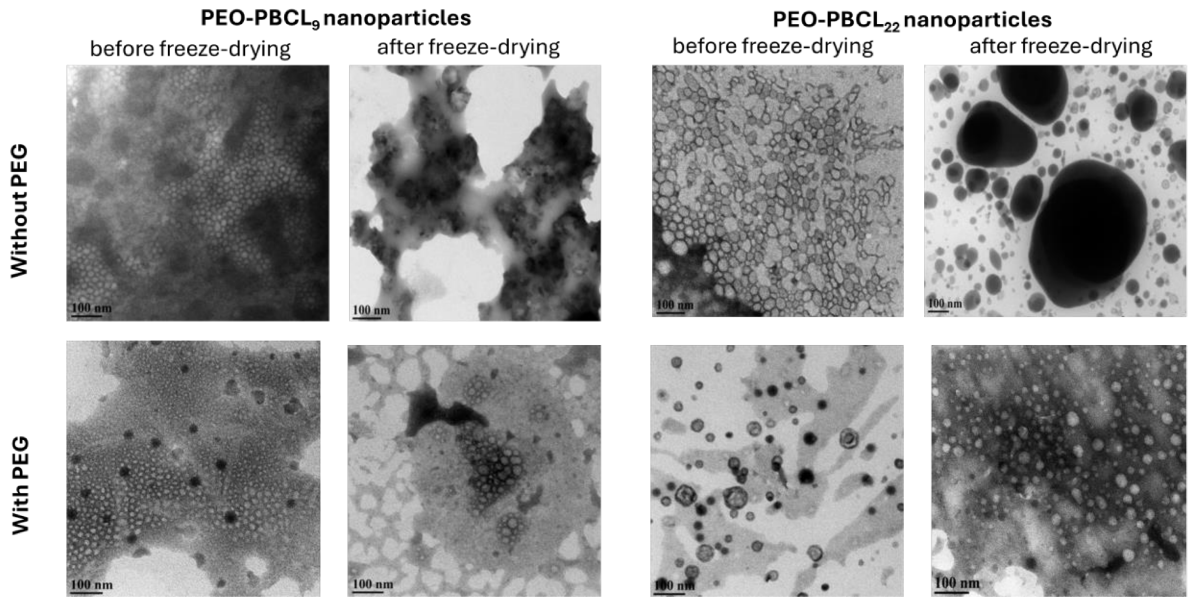

Figure 5.7. TEM images of PEO-PBCL NPs before and after freeze-drying that were reconstituted samples in 1mL of double distilled water.

5.3.8. Freeze-drying A83B4C63-loaded PEO-PBCL$_{22}$ NPs

PEO-PBCL NPs are suitable candidates for delivering hydrophobic compounds due to their hydrophobic core. We studied, the impact of freeze-drying on the drug-loaded PEO-PBCL NPs while the cryoprotectant methoxy PEG (MW=5000 g/mol) with the w/w ratio of 4:1 of PEG: PEO-PBCL$_{22}$ was used. Initially, the encapsulation efficiency of A83B4C63 into the PEO-PBCL NPs was 88.2±1.4%, and the NPs' size and PDI were 51.87$\pm$87 nm and 0.09$\pm$0.01, respectively (Figure 5.8).

After freeze-drying and reconstitution in 1 mL DDH$_2$O, the NPs' size and PDI for the group with methoxy PEG as cryoprotectant were 95.09$\pm$14.55 nm and 0.24$\pm$0.02, respectively. The encapsulation efficiency % after freeze-drying was 78.3±7.0%. The NPs' size and PDI following

centrifugation were 78.4±6.45 nm and 0.15±0.01 respectively, significantly lower than the values measured before centrifugation ($p<0.05$, One-way ANOVA) (Figure 5.8. A) (Figure S11.).

The visual examination of the samples matched the findings from DLS. The cryoprotectant-free samples sedimented after 2-3 minutes (figure 5.8. B).

5.3.9. Freeze-drying of A4-loaded PEO-PBCL$_{22}$ NPs

Another hydrophobic compound (A4) was encapsulated in PEO-PBCL$_{22}$ NPs. The A4 encapsulation efficiency % into PEO-PBCL NPs before freeze-drying was 79.02±14.77%. The NPs' size and PDI were 44.47±0.61 nm and 0.17±0.01, respectively. As shown in Figure 5.8. C, the NPs' size and PDI significantly increased in the group of NPs that had methoxy PEG (MW=5000 g/mol) as cryoprotectant to 102.90±12.16 nm and 0.31±0.04, respectively ($p<0.05$, One-way ANOVA).

After centrifugation of the reconstituted NPs, the encapsulation efficiency of A4 after freeze-drying was 77.91±12.43%. The encapsulation efficiency did not change significantly ($p>0.05$, One-way ANOVA). However, the NPs' size and PDI significantly decreased after centrifugation to 76.11±4.18 nm and 0.21±0.01 compared to 102.90±12.16 nm and 0.31±0.04 respectively (Figure S12.).

The results from DLS were consistent with the visual examination of the samples. The cryoprotectant-free samples sedimented after 2-3 minutes (Figure 5.8. D).

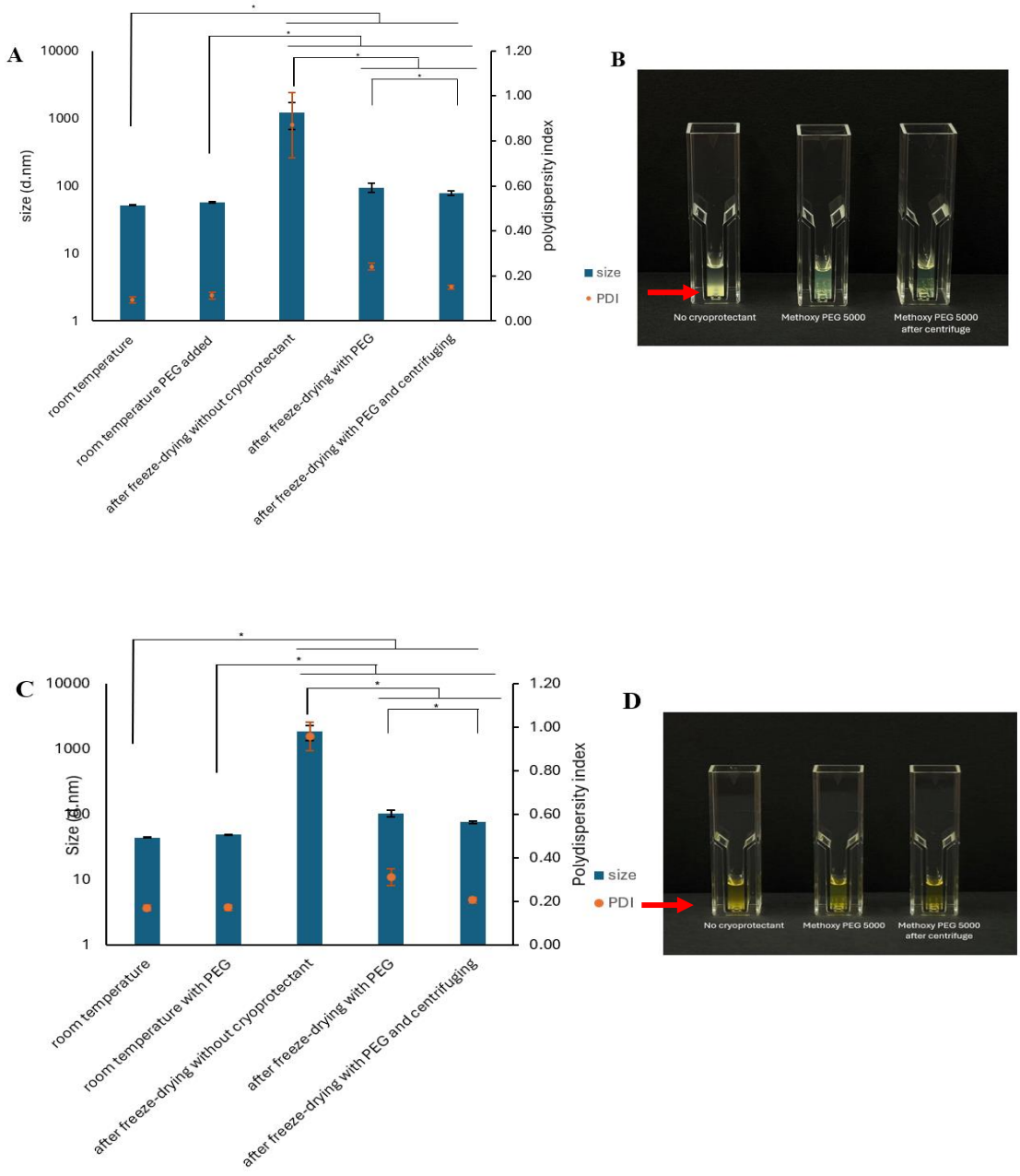

Figure 5.8. Nanoparticles' size and PDI after freeze-drying and redispersing PEO-PBCL$_{22}$ NPs loaded with A83B4C63 in 1 mL of DDH$_2$O. The w/w ratio of methoxy PEG (5000 MWt): PEO-PBCL$_{22}$ was 4:1 (*=p<0.05, One-way ANOVA, n=3). B) Visual appearance of reconstituted PEG-PBCL nanoparticles with and without cryoprotectant. C) Nanoparticles' size and PDI after freeze-drying and redispersing PEO-PBCL$_{22}$ NPs loaded with A4 in 1 mL of DDH$_2$O. The w/w ratio of methoxy PEG (5000 MWt): PEO-PBCL$_{22}$ was 4:1 (*=p<0.05, One-way ANOVA, n=3). D) Visual appearance of

reconstituted PEG-PBCL nanoparticles with and without cryoprotectant. Red arrow indicates the precipitation of PEO-PBCL NPs.

Table 5.8. The effect of freeze-drying on the average diameter of PEO-PBCL$_{22}$ NPs loaded with A83B4C63 and A4. The initial size of NPs before freeze drying in the absence of cryoprotectant (Si) was 54.5± 3.67 nm, 51.87±0.87nm and 44.47±0.61nm for empty, A83B4C63 and A4 loaded NPs respectively.

PEO-PBCL sample	Drug content	NP size (Sf) (d.nm)+SD (n=3)	Response (Sf/Si)
Methoxy PEG 5000 (after centrifuge)	A83B4C63	78.41±6.45	1.51
Methoxy PEG 5000 (before centrifuge)		95.09±14.55	1.83
no cryoprotectant		1212±526.3	23.37
Methoxy PEG 5000 (after centrifuge)	A4	76.11±4.18	1.71
Methoxy PEG 5000 (before centrifuge)		102.9±12.16	2.31
no cryoprotectant		1851±487	41.62
Methoxy PEG 5000	NA	105.3±11.05	1.93
no cryoprotectant		1455±1016	26.70

5.3.10. DSC

To assess the effect of freeze-drying and PEG addition as cryoprotectant on the thermal behavior of PEO-PBCL, DSC was performed. The DSC results as shown in Figure 12. indicated only one peak around 50°C for PEO-PBCL polymer and PEO-PBCL NPs without PEG. This peak is perhaps related to the melting point of PEO. PBCL did not show a separate peak, but its presence in the block copolymer structure seems to have affect the melting temperature of PEO.

Methoxy PEG 5000 Da has shown a crystallization (~41 °C) and a melting peak (~ 62.98 °C). In PEO-PBCL plus PEG 5000 Da as cryoprotectant these two peaks were also observed, but the melting peak of PEO from PEO-PBCL NPs was not seen. (Figure 5.9).

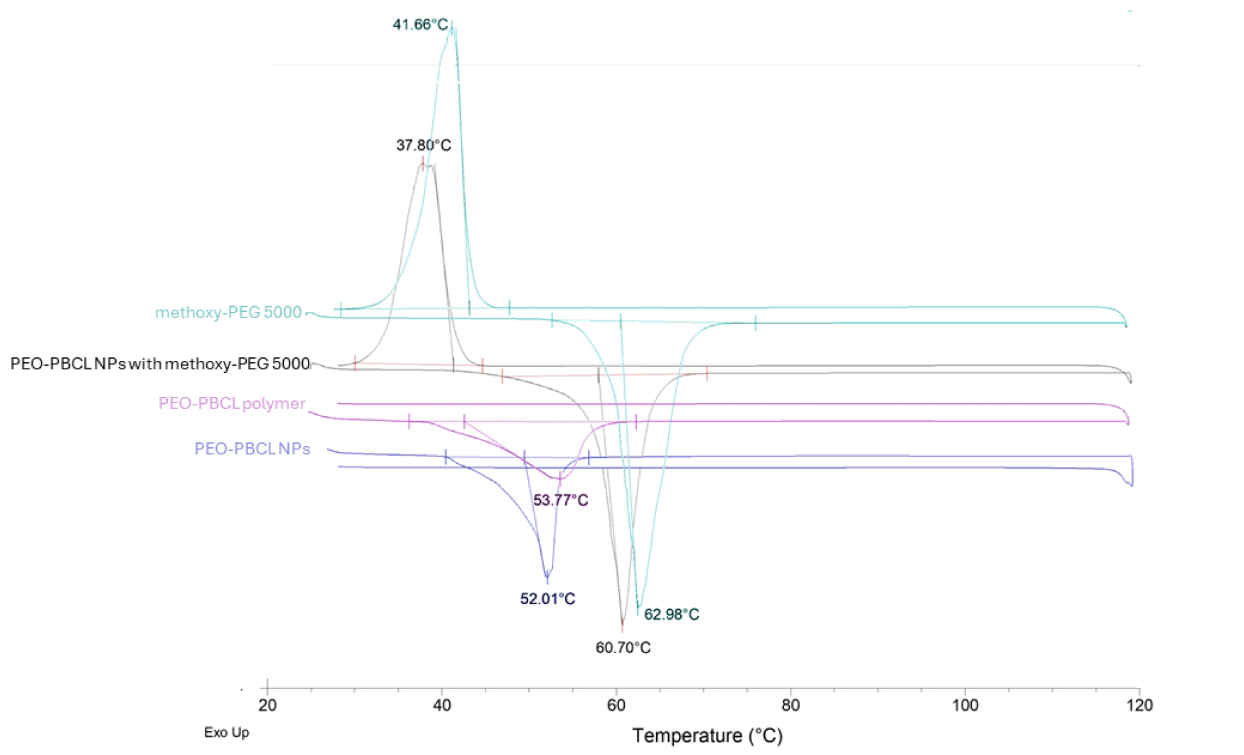

Figure 5.9. DSC thermograms for methoxy-PEG 5000, freeze-dried PEO-PBCL$_{22}$ NPs with or without PEG with the ratio of 4:1 and PEO-PBCL$_{22}$ polymers.

5.4. Discussion

Freeze-drying is a desired method to improve the shelf life of pharmaceutical products including NPs. Usually cryo- or lyoprotectants need to be used before NP freeze-drying to prevent NP aggregation during the process. The optimum type and concentration of cryo- or lyoprotectants should be identified for each NP structure (242,243). Here, we investigated the impact of different cryo/lyo protectants on PEO-PBCL NPs stored using freeze-drying or freeze-thaw method in order to identify the best storage condition for these NPs. The initial evaluation focused on the impact of freezing conditions on the NPs , which imposes the most stress on the NPs (229,230). The size and PDI of PEO-PBCL NPs showed an increase during freeze-thaw, irrespective of the freezing method, due to an increase in NPs' concentration in parts of the sample that are still in liquid state as the water media starts to form ice during freezing (231,244). However, the ratio of size increase was not similar in all employed freezing conditions. As a lower freezing temperature was used (i.e. freezing using liquid nitrogen or -80°C freezer), the increase in size (or aggregation of NPs) was less in comparison to freezing at -20°C freezer. This observation could be a result of forming a higher quantity and finer ice crystals at -80 °C compared to -20 °C (245). Snap freeing using liquid nitrogen can also assist in this process, although we did not see any difference between the use of liquid nitrogen or storage at -80 °C freezer in the current study. Therefore, freezing NPs using the -80 °C freezer was considered the best approach, as it is more accessible than liquid nitrogen.

The PEO-PBCL NPs were protected from freeze-drying stress using either saccharide or polymers. The NPs' size growth was inhibited by incorporating cryoprotectants perhaps through formation of spatial obstacles that prevent NP aggregation (229).

After freeze-drying the PEO-PBCL NPs, the reconstitution of the particles without lyoprotectants led to the formation of suspensions showing precipitation. This was not the case for any of the samples that had lyoprotectants, irrespective of the type and concentration. This observation was in line with other reported NPs when freeze-dried without cryoprotectants (246,247). This observation highlights the impact of lyoprotectants in freeze-drying PEO-PBCL NPs.

As previously reported, sucrose protects the NPs by replacing the water molecules between the building blocks of the particles and forming hydrogen bonds with the PEG blocks which keep them stable during the drying process (224). However, PEG polymer showed better protection than sucrose for PEO-PBCL NPs against the freeze-drying stresses. As described in the literature, the polymeric NPs' hydrophobic cores tend toward each other, and when a core is exposed, NPs aggregate. However, adding PEG to the samples not only creates steric hindrances but also coats the NPs and prevents the cores from exposure (248,249). On the other hand, it has been reported that the addition of polymers such as poly vinyl alcohol (PVA) can stabilize and keep the NPs distant while going through the drying step of freeze-drying either by forming a matrix or coating the surface of the NPs (224,250).

TEM images also showed that the NPs' integrity was preserved when freeze-dried using PEG.

Methoxy-PEG 5000 showed a crystallization and a melting peak (Table S12). This was d in line with previous reports (251,252). PEO-PBCL NPs and PEO-PBCL polymer that were prepared using ROP of PBCL on methoxy PEO 5000 Da, showed only one melting peak at around 52-53 °C indicating the interference of PBCL with the crystallization of PEO. PBCL is an amorphous polymer (due to atactic structure of PBCL) that is not expected to show crystallization and melting.

Addition of PEG 5000 Da as cryo-protectant, however led to the disappearance of PEO-PBCL melting peak pointing to the possible interference of PEG 5000Da in the interaction of PEO from different NPs keeping the PEO-PBCLs NPs distant from each other in the solid state. We found that the stability of drug encapsulated PEO-PBCL NPs during freeze-drying process, depends on the encapsulated drug. Reconstitution of freeze-dried A83B4C63 loaded PEO-PBCL NPs led to a decrease in drug loading in NPs, but this did not occur for A4 loaded NPs. This could be due to the leakage of A83B4C63 and/or precipitation of A83B4C63 NPs. In terms of NP size, after reconstitution of freeze-dried A83B4C63 NPs using methoxy PEG 5000 g/mol as cryoprotectant 1.83-fold increase in NP size was observed. This increase for A4 loaded NPs was 2.31-fold. The fold increase in NP size was 0.95 and 1.20 for A83B4C63 and A4 loaded NPs compared to unloaded NPs using the same freeze-drying condition and cryoprotectant, respectively.

Overall, taking all data together, the best storage condition and cryoprotectant was found to be Freezing at -80 C and thawing the NPs using PEG 3350 Da, methoxy PEG 2000, 5000 Da or sucrose as cryoprotectant.

5.5. Conclusion

The freeze-drying process of PEO-PBCL NPs necessitates a cryo/lyoprotectant, regardless of the polymerization degree. The freeze-drying results of PEO-PBCL NP exhibited an increase in both the size and PDI of PEO-PBCL NPs. However, the use of cryo/lyoprotectants reduced the NPs aggregation. Among tested cry/lyoprotectants, sucrose, PEG of 3350 and methoxy-PEG 5000 g/mol exhibited superior control over NP size growth. Our studies suggest that the use of freeze-

thaw method using sucrose, PEG of 3350 and methoxy-PEG 2000 or 5000 g/mol can preserve the original particle size and size distribution of NPs to better extent compared to freeze-drying method.

5.6. Supplementary Data

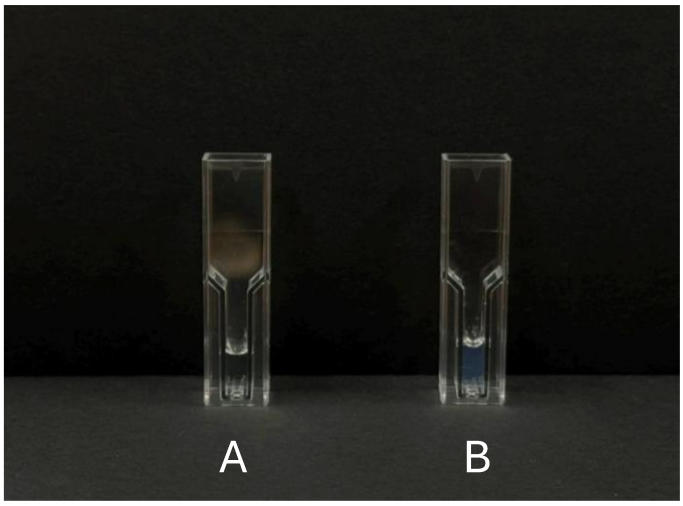

Figure S1. The visual appearance of PEO-PBCL micelles A) micelles made with PEO-PBCL$_9$ and B) PEO-PBCL$_{22}$

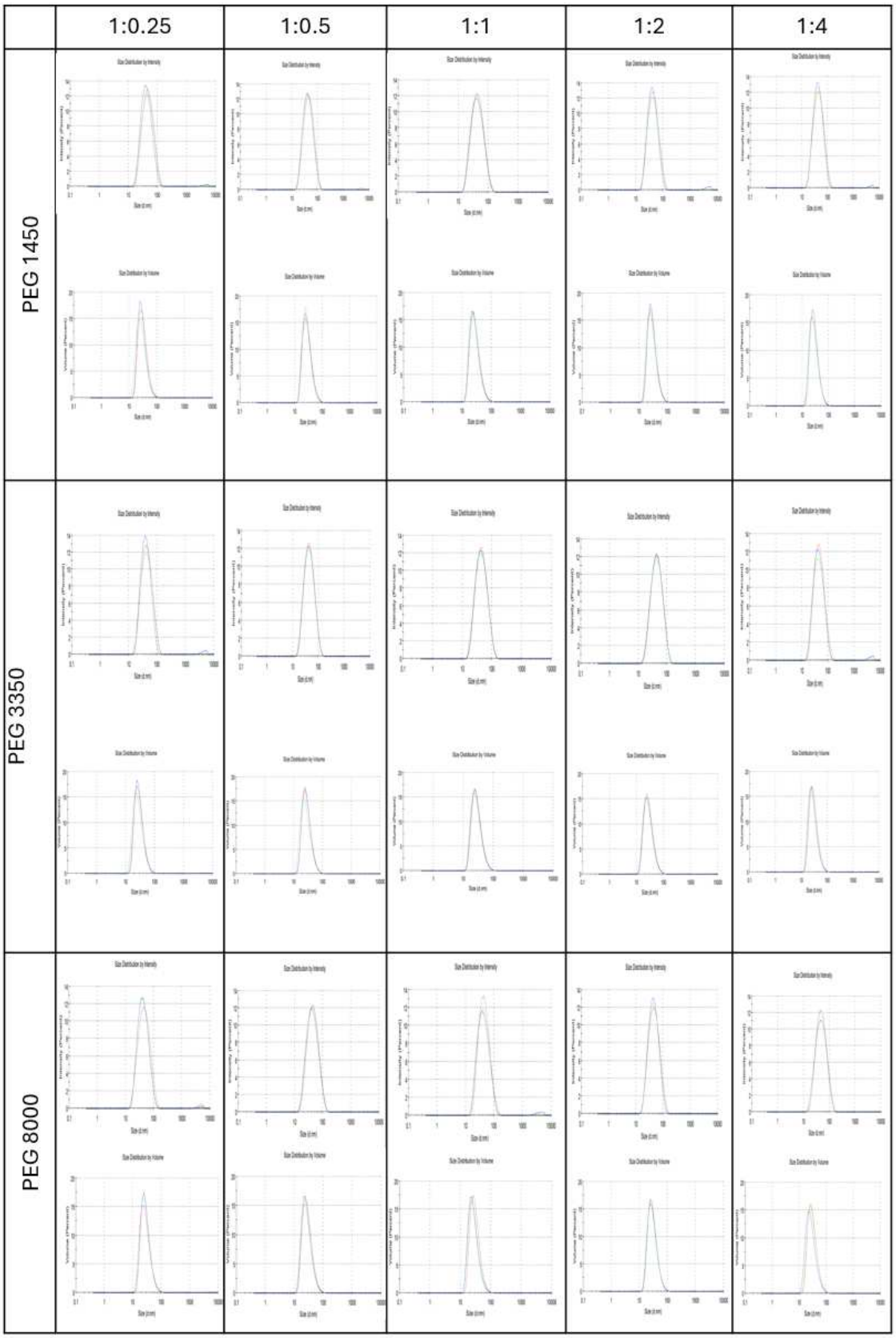

Figure S2. Size distribution of PEO-PBCL$_9$ micelles after addition of different Mw of PEG at room temperature

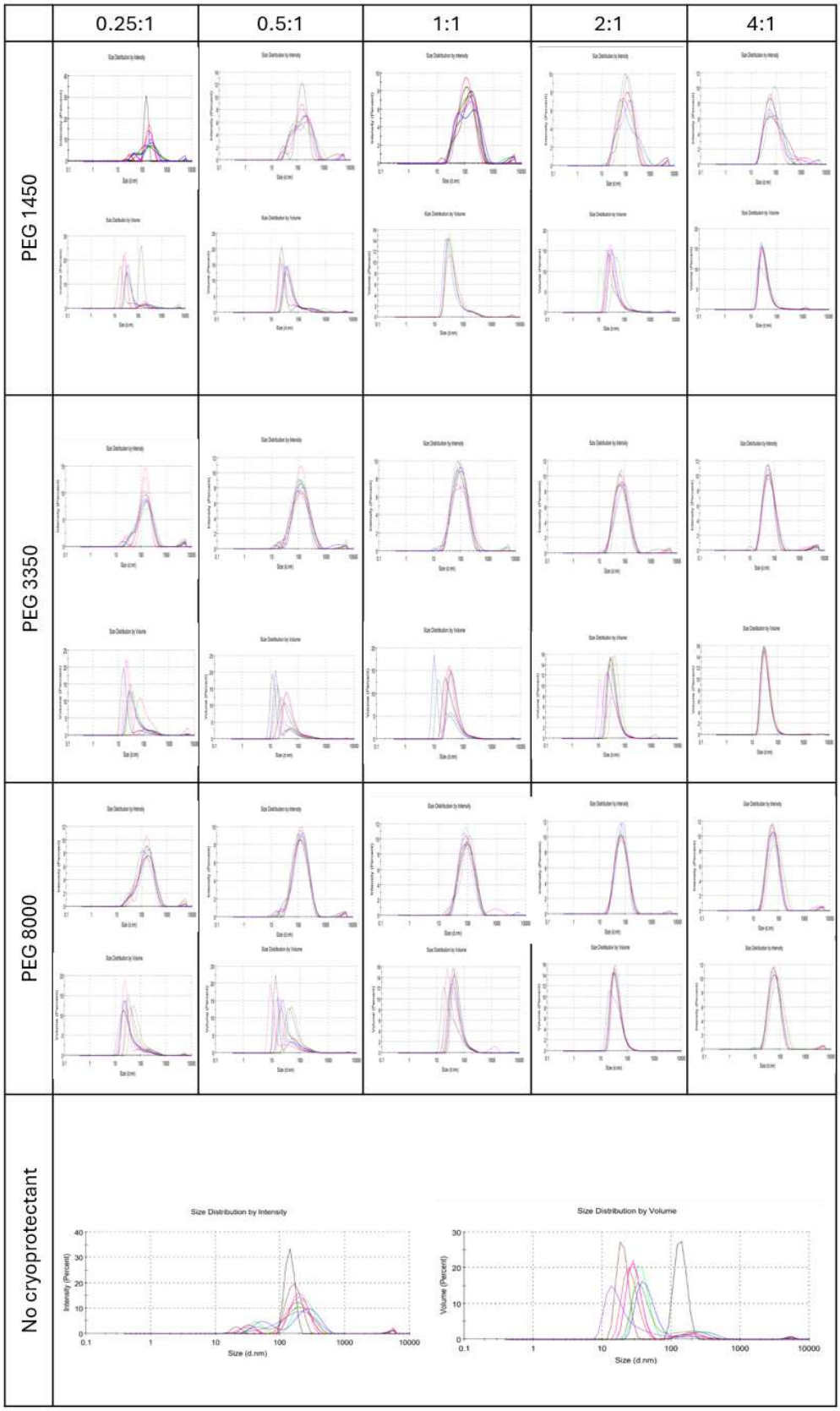

Figure S3. Size distribution of PEO-PBCL$_9$ micelles after freeze-drying with different ratios and Mw of PEG

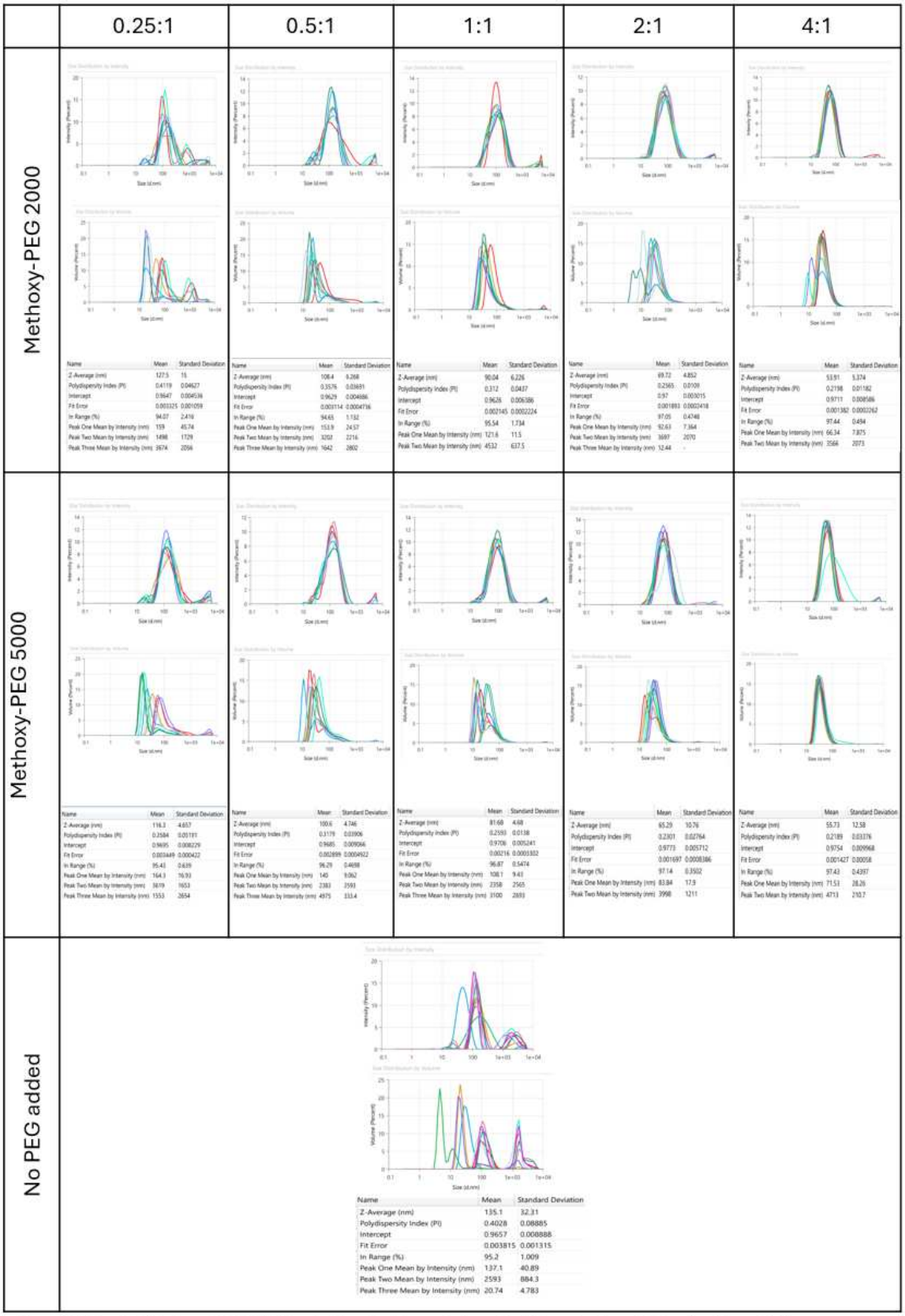

Figure S4. Size distribution of PEO-PBCL$_9$ micelles after freeze-drying with different ratios and Mw of methoxy-PEG

Cryoprotectant	Size distribution
No cryoprotectant before freeze-drying	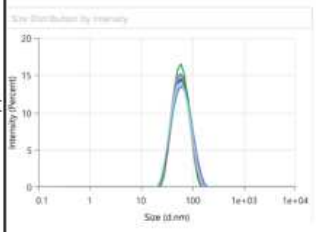 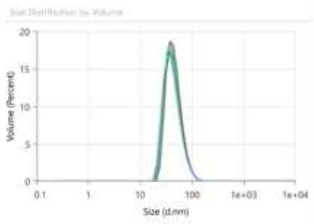

Name	Mean	Standard Deviation
Z-Average (nm)	55.43	0.9756
Polydispersity Index (PI)	0.1223	0.01652
Intercept	0.9606	0.01376
Fit Error	0.0005088	0.0001278
In Range (%)	97.57	0.2746
Peak One Mean by Intensity (nm)	63.65	1.534

No cryoprotectant After freeze - drying	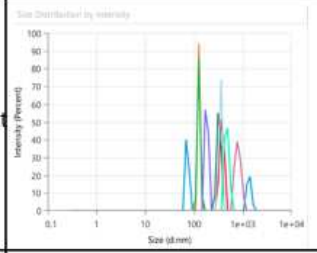 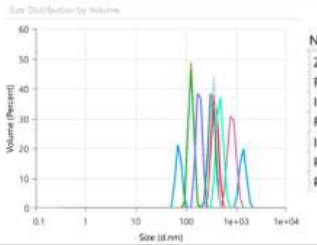

Name	Mean	Standard Deviation
Z-Average (nm)	1280	549.5
Polydispersity Index (PI)	0.8748	0.1696
Intercept	0.9092	0.02302
Fit Error	0.01892	0.01416
In Range (%)	87.45	4.524
Peak One Mean by Intensity (nm)	313.8	226.8
Peak Two Mean by Intensity (nm)	1348	-

PEG 3350	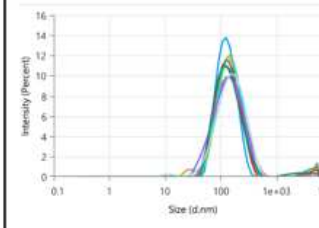 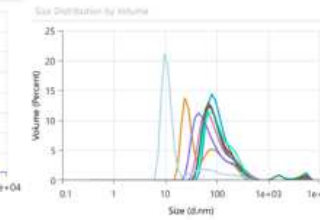

Name	Mean	Standard Deviation
Z-Average (nm)	124.5	4.933
Polydispersity Index (PI)	0.2554	0.01179
Intercept	0.9659	0.00815
Fit Error	0.001996	0.0004257
In Range (%)	95.08	1.038
Peak One Mean by Intensity (nm)	155.5	10.88
Peak Two Mean by Intensity (nm)	3032	2154
Peak Three Mean by Intensity (nm)	5079	-

Methoxy-PEG 2000	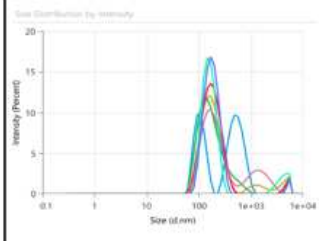 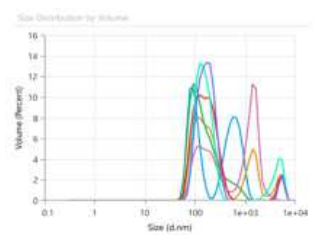

Name	Mean	Standard Deviation
Z-Average (nm)	173.8	12.72
Polydispersity Index (PI)	0.3557	0.04551
Intercept	0.9604	0.01106
Fit Error	0.002813	0.0005993
In Range (%)	94.13	1.144
Peak One Mean by Intensity (nm)	236.1	136.6
Peak Two Mean by Intensity (nm)	3636	2011
Peak Three Mean by Intensity (nm)	1421	-

Methoxy-PEG 5000	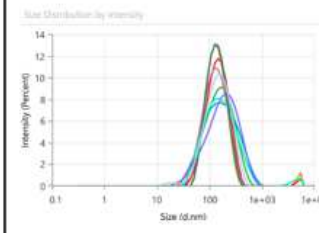 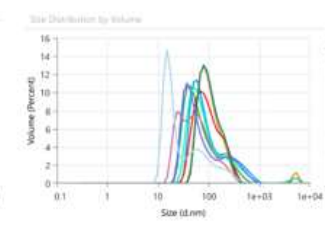

Name	Mean	Standard Deviation
Z-Average (nm)	126	9.683
Polydispersity Index (PI)	0.2657	0.03666
Intercept	0.9694	0.005502
Fit Error	0.002327	0.0006552
In Range (%)	96	0.7891
Peak One Mean by Intensity (nm)	171.3	27.89
Peak Two Mean by Intensity (nm)	3629	2423

Sucrose	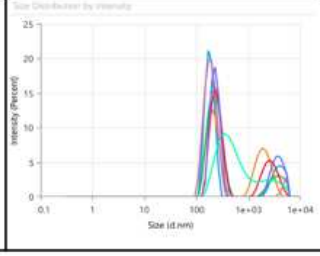 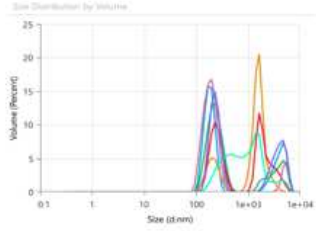

Name	Mean	Standard Deviation
Z-Average (nm)	287.9	68.66
Polydispersity Index (PI)	0.4229	0.06861
Intercept	0.9513	0.0103
Fit Error	0.002632	0.0008875
In Range (%)	94.67	0.6204
Peak One Mean by Intensity (nm)	254.7	107.4
Peak Two Mean by Intensity (nm)	3415	976.1

Figure S5. Size distribution of PEO-PBCL$_{22}$ micelles after freeze-drying with and with w/w 2:1 of PEG: polymer and 13.25:1 of sucrose to polymer Mw of PEG

Cryoprotectant	Size distribution
No cryoprotectant before freeze-drying	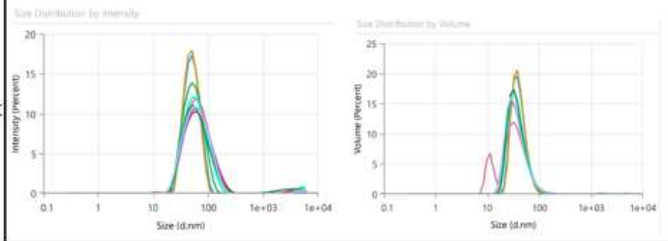
No cryoprotectant After freeze - drying	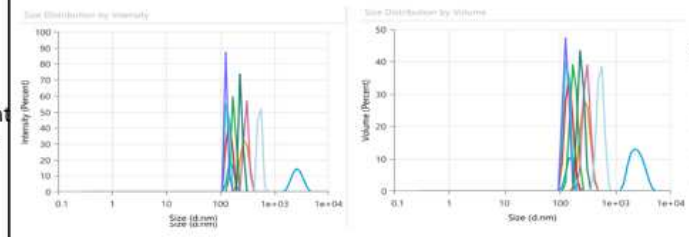
PEG 3350	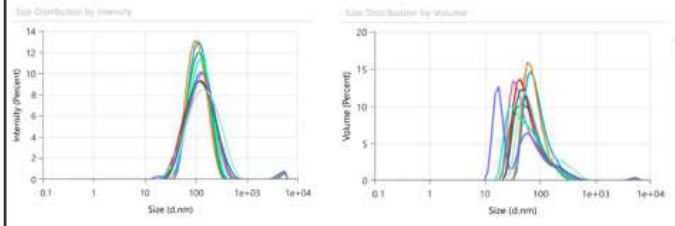
Methoxy-PEG 2000	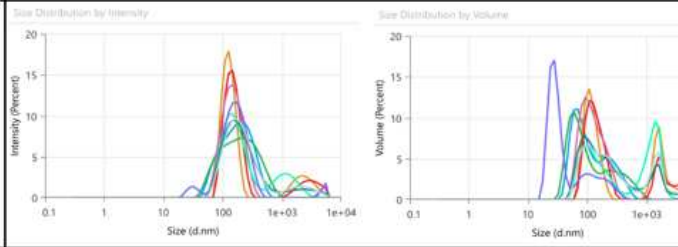
Methoxy-PEG 5000	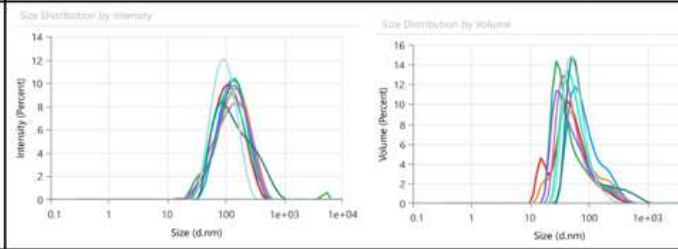
Sucrose	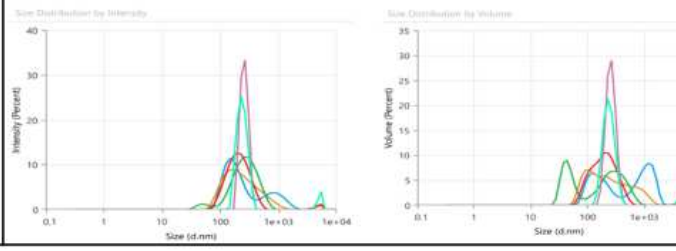

Name	Mean	Standard Deviation
Z-Average (nm)	54.5	3.67
Polydispersity Index (PI)	0.2013	0.03523
Intercept	0.9655	0.01058
Fit Error	0.0007165	0.0001743
In Range (%)	94.75	1.434
Peak One Mean by Intensity (nm)	63.83	7.984
Peak Two Mean by Intensity (nm)	4409	661.7
Peak Three Mean by Intensity (nm)	11.82	-

Name	Mean	Standard Deviation
Z-Average (nm)	1455	1016
Polydispersity Index (PI)	0.8627	0.2339
Intercept	0.9213	0.02003
Fit Error	0.01451	0.007413
In Range (%)	87.59	3.034
Peak One Mean by Intensity (nm)	514.7	824.1
Peak Two Mean by Intensity (nm)	157.6	-

Name	Mean	Standard Deviation
Z-Average (nm)	105.8	8.054
Polydispersity Index (PI)	0.2359	0.03758
Intercept	0.9692	0.003214
Fit Error	0.001574	0.0006149
In Range (%)	96.45	0.5029
Peak One Mean by Intensity (nm)	136.3	19.19
Peak Two Mean by Intensity (nm)	4825	244.7
Peak Three Mean by Intensity (nm)	19.39	-

Name	Mean	Standard Deviation
Z-Average (nm)	155.3	10.93
Polydispersity Index (PI)	0.3338	0.03878
Intercept	0.9623	0.004808
Fit Error	0.002045	0.0005968
In Range (%)	95.41	1.595
Peak One Mean by Intensity (nm)	182.9	35.81
Peak Two Mean by Intensity (nm)	2412	1567
Peak Three Mean by Intensity (nm)	4946	-

Name	Mean	Standard Deviation
Z-Average (nm)	105.3	11.05
Polydispersity Index (PI)	0.2503	0.03259
Intercept	0.9655	0.004272
Fit Error	0.001942	0.0006092
In Range (%)	96.28	0.7596
Peak One Mean by Intensity (nm)	144.4	21.97
Peak Two Mean by Intensity (nm)	2489	3496

Name	Mean	Standard Deviation
Z-Average (nm)	229.9	51.13
Polydispersity Index (PI)	0.319	0.06412
Intercept	0.9578	0.005978
Fit Error	0.003677	0.001921
In Range (%)	95.49	0.3308
Peak One Mean by Intensity (nm)	247.6	41.81
Peak Two Mean by Intensity (nm)	3147	2465

Figure S6. Size distribution of PEO-PBCL$_{22}$ micelles after freeze-drying with and with w/w 4:1 of PEG: polymer and 13.25:1 of sucrose to polymer Mw of PEG

Freezing condition	Size distribution measured by DLS
Room-temperature	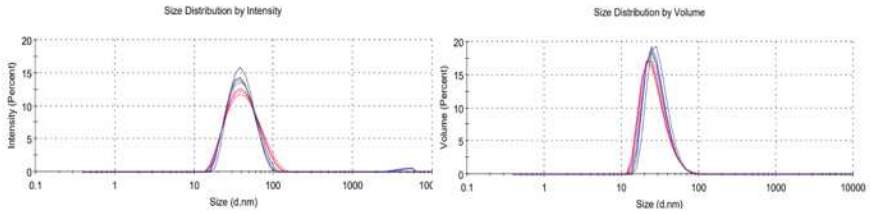
Liquid nitrogen	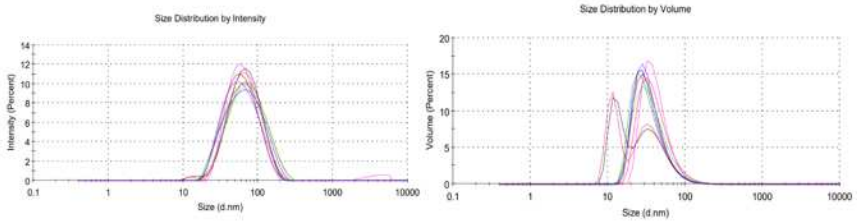
-80°C freezer	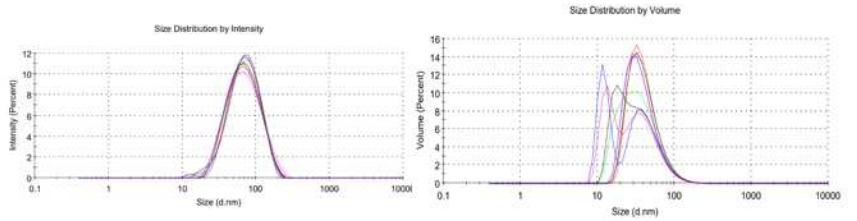
-20°C freezer	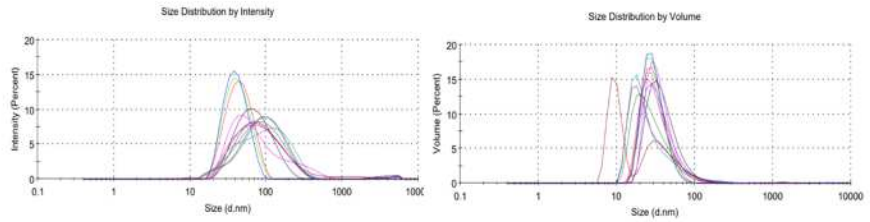

FigureS7. Size distribution of PEO-PBCL$_9$ micelles after freeze-thawing at different freezing conditions.

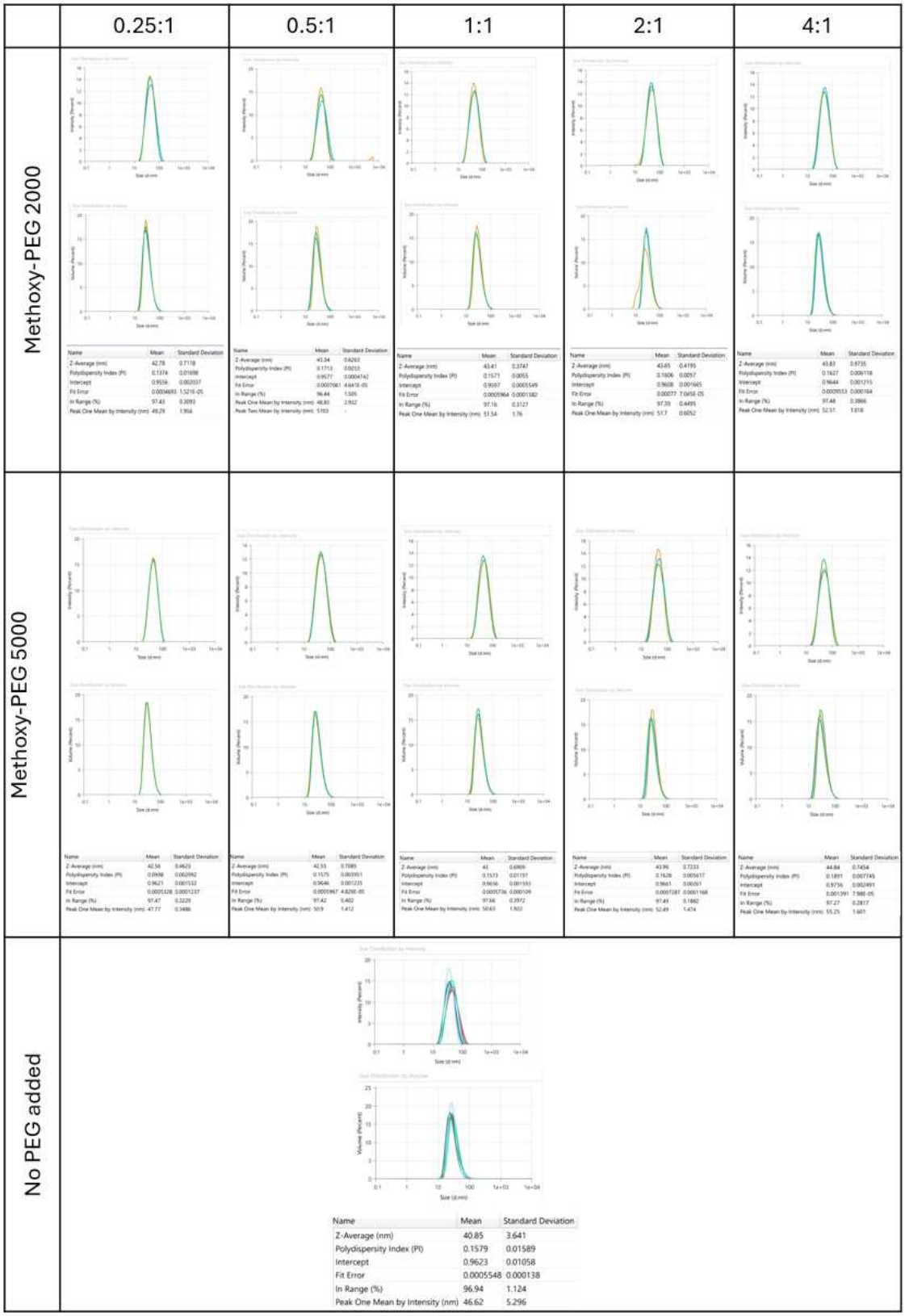

Figure S8. Size distribution of PEO-PBCL$_9$ micelles after adding different w/w ratios and Mw of methoxy PEG

Cryoprotectant	Size distribution
No cryoprotectant before freeze-thawing	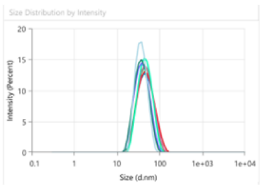 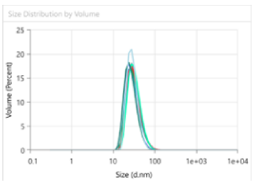

Name	Mean	Standard Deviation
Z-Average (nm)	40.85	3.641
Polydispersity Index (PI)	0.1579	0.01589
Intercept	0.9623	0.01058
Fit Error	0.0005548	0.000138
In Range (%)	96.94	1.124
Peak One Mean by Intensity (nm)	46.62	5.296

No cryoprotectant After freeze-thawing	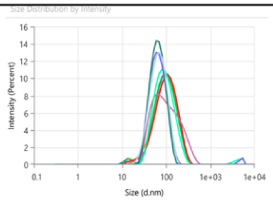 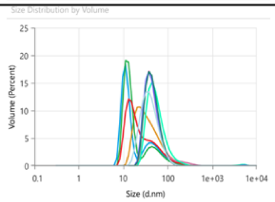

Name	Mean	Standard Deviation
Z-Average (nm)	73.72	9.889
Polydispersity Index (PI)	0.2267	0.03818
Intercept	0.9654	0.004857
Fit Error	0.001618	0.0005823
In Range (%)	96.43	1.388
Peak One Mean by Intensity (nm)	96.02	20.61
Peak Two Mean by Intensity (nm)	2311	2662

PEG 3350	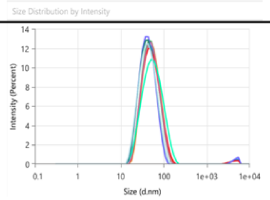 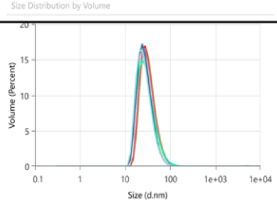

Name	Mean	Standard Deviation
Z-Average (nm)	43.58	3.709
Polydispersity Index (PI)	0.1869	0.01319
Intercept	0.9627	0.004007
Fit Error	0.000706	0.0001085
In Range (%)	97.18	0.3943
Peak One Mean by Intensity (nm)	52.05	5.453
Peak Two Mean by Intensity (nm)	4470	230.2

Methoxy-PEG 2000	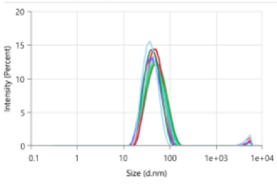 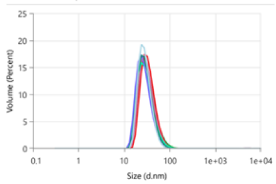

Name	Mean	Standard Deviation
Z-Average (nm)	43.61	3.6
Polydispersity Index (PI)	0.1978	0.01952
Intercept	0.9614	0.007686
Fit Error	0.0007565	0.0001466
In Range (%)	97.17	0.7786
Peak One Mean by Intensity (nm)	49.93	5.881
Peak Two Mean by Intensity (nm)	4852	205.8

Methoxy-PEG 5000	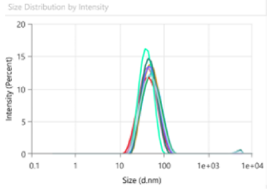 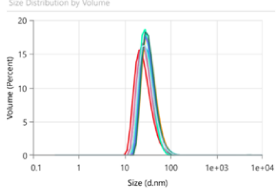

Name	Mean	Standard Deviation
Z-Average (nm)	43.91	3.435
Polydispersity Index (PI)	0.1868	0.01115
Intercept	0.9665	0.002933
Fit Error	0.0008356	0.0001291
In Range (%)	97.43	0.4506
Peak One Mean by Intensity (nm)	51.38	5.346
Peak Two Mean by Intensity (nm)	4832	61

Sucrose	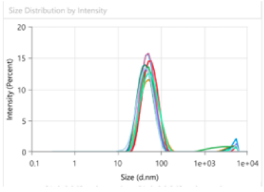 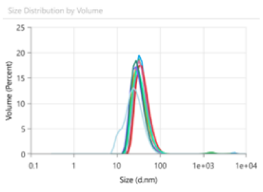

Name	Mean	Standard Deviation
Z-Average (nm)	48.91	4.542
Polydispersity Index (PI)	0.2397	0.02554
Intercept	0.9723	0.003317
Fit Error	0.000999	0.0003401
In Range (%)	95.76	0.9605
Peak One Mean by Intensity (nm)	52.88	5.246
Peak Two Mean by Intensity (nm)	4498	800.9

Figure S9. Size distribution of PEO-PBCL$_9$ micelles after freeze-thawing with different 2:1 w/w of PEG to polymer and 13.25:1 of sucrose to polymer

Cryoprotectant	Size distribution
No cryoprotectant before freeze-thawing	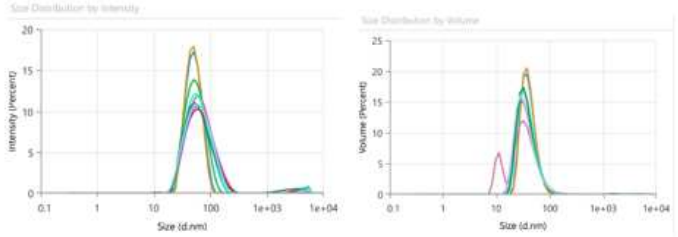
No cryoprotectant After freeze - thawing	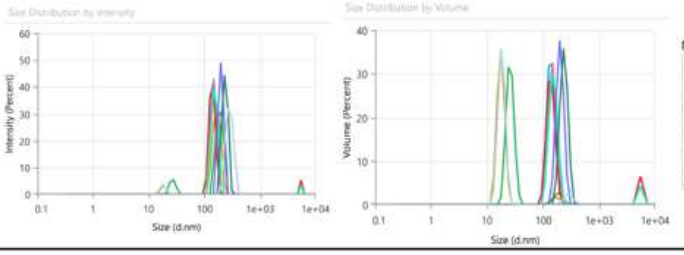
PEG 3350 (w/w 2:1)	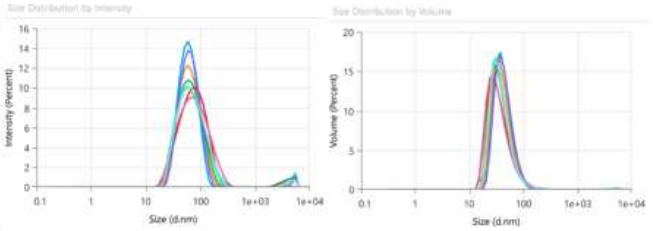
Methoxy-PEG 2000 (w/w 2:1)	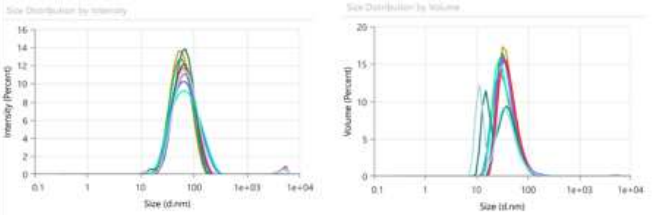
Methoxy-PEG 5000 (w/w 2:1)	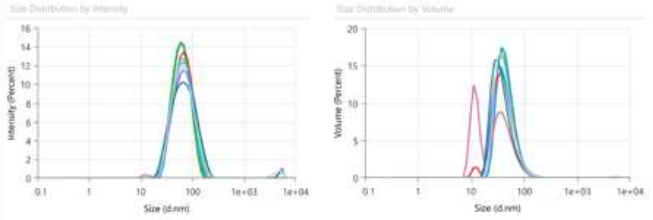
Sucrose	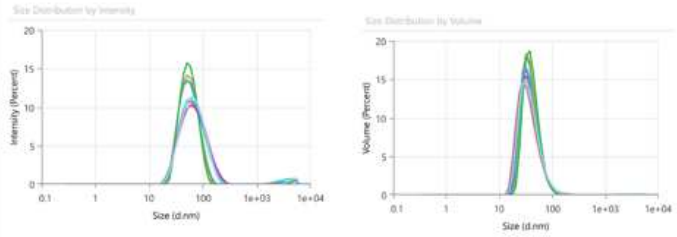

Name	Mean	Standard Deviation
Z-Average (nm)	54.5	3.67
Polydispersity Index (PI)	0.2013	0.03523
Intercept	0.9655	0.01058
Fit Error	0.0007165	0.0001743
In Range (%)	94.75	1.434
Peak One Mean by Intensity (nm)	63.83	7.984
Peak Two Mean by Intensity (nm)	4409	661.7
Peak Three Mean by Intensity (nm)	11.82	-

Name	Mean	Standard Deviation
Z-Average (nm)	353.7	126.1
Polydispersity Index (PI)	0.5349	0.05062
Intercept	0.9301	0.01631
Fit Error	0.0105	0.005817
In Range (%)	92.62	1.562
Peak One Mean by Intensity (nm)	183.7	48.69
Peak Two Mean by Intensity (nm)	2744	2983

Name	Mean	Standard Deviation
Z-Average (nm)	62.17	2.652
Polydispersity Index (PI)	0.2612	0.0301
Intercept	0.9664	0.00416
Fit Error	0.001066	0.0005094
In Range (%)	94.15	2.319
Peak One Mean by Intensity (nm)	73.97	7.694
Peak Two Mean by Intensity (nm)	4672	465.1

Name	Mean	Standard Deviation
Z-Average (nm)	59.58	4.474
Polydispersity Index (PI)	0.2182	0.03334
Intercept	0.9702	0.002501
Fit Error	0.0009855	0.0003884
In Range (%)	96.3	1.274
Peak One Mean by Intensity (nm)	71.56	6.912
Peak Two Mean by Intensity (nm)	3864	2153
Peak Three Mean by Intensity (nm)	12.61	-

Name	Mean	Standard Deviation
Z-Average (nm)	62.09	2.968
Polydispersity Index (PI)	0.2215	0.03647
Intercept	0.968	0.005171
Fit Error	0.0009806	0.0003531
In Range (%)	95.13	0.7839
Peak One Mean by Intensity (nm)	70.49	4.303
Peak Two Mean by Intensity (nm)	4194	2065
Peak Three Mean by Intensity (nm)	13.01	-

Name	Mean	Standard Deviation
Z-Average (nm)	57.24	3.963
Polydispersity Index (PI)	0.2119	0.03699
Intercept	0.9695	0.003182
Fit Error	0.0008351	0.0003127
In Range (%)	97.33	0.6495
Peak One Mean by Intensity (nm)	67.65	7.246
Peak Two Mean by Intensity (nm)	4396	500

Figure S10. Size distribution of PEO-PBCL$_{22}$ micelles after freeze-thawing with different w/w of PEG to polymer and 13.25:1 of sucrose to polymer

Cryoprotectant	Size distribution
PEG 3350 (w/w 4:1)	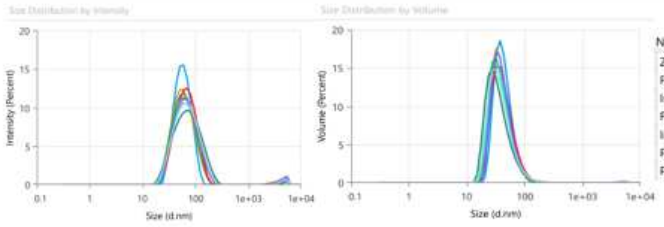
Methoxy-PEG 2000 (w/w 4:1)	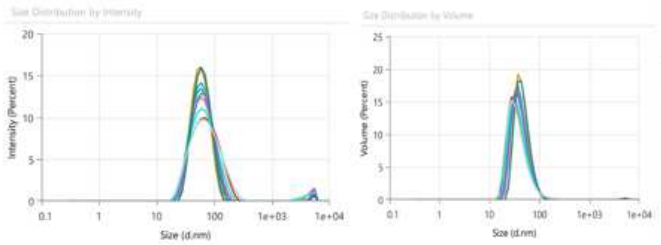
Methoxy-PEG 5000 (w/w 4:1)	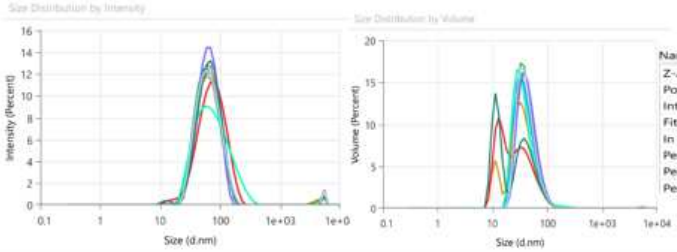

Name	Mean	Standard Deviation
Z-Average (nm)	60.39	3.58
Polydispersity Index (PI)	0.2299	0.02676
Intercept	0.9748	0.00392
Fit Error	0.001059	0.0003766
In Range (%)	95.93	0.7987
Peak One Mean by Intensity (nm)	70.99	6.348
Peak Two Mean by Intensity (nm)	4635	374.4

Name	Mean	Standard Deviation
Z-Average (nm)	59.26	2.719
Polydispersity Index (PI)	0.224	0.04552
Intercept	0.9735	0.003801
Fit Error	0.0009645	0.0002316
In Range (%)	95.52	1.6
Peak One Mean by Intensity (nm)	68.6	6.867
Peak Two Mean by Intensity (nm)	4921	423.3

Name	Mean	Standard Deviation
Z-Average (nm)	61.44	2.741
Polydispersity Index (PI)	0.2485	0.03871
Intercept	0.972	0.005675
Fit Error	0.001053	0.0002633
In Range (%)	94.63	2.464
Peak One Mean by Intensity (nm)	71.58	6.965
Peak Two Mean by Intensity (nm)	3979	2240
Peak Three Mean by Intensity (nm)	2653	3735

Figure S10. Continues.

Cryoprotectant	Size distribution
No cryoprotectant before freeze-drying	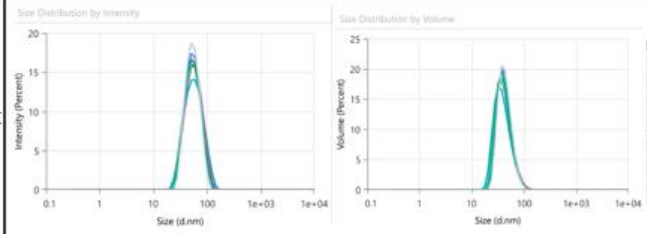
No cryoprotectant After freeze - drying	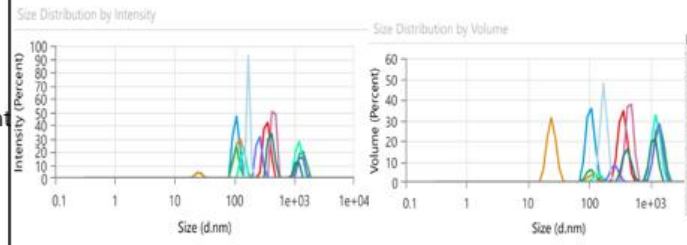
Methoxy-PEG 5000 (1:4 polymer to PEG ratio) Before centrifugation	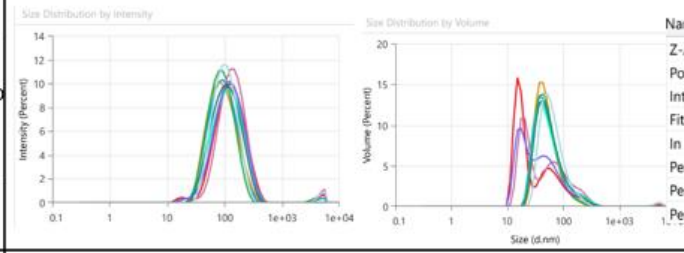
Methoxy-PEG 5000 (1:4 polymer to PEG ratio) After centrifugation	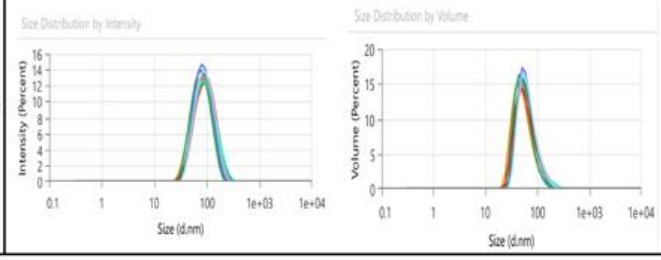

Name	Mean	Standard Deviation
Z-Average (nm)	51.87	0.8711
Polydispersity Index (PI)	0.09432	0.01254
Intercept	0.9659	0.003732
Fit Error	0.0008437	0.0001947
In Range (%)	97.3	0.2482
Peak One Mean by Intensity (nm)	57.85	1.507

Name	Mean	Standard Deviation
Z-Average (nm)	1212	526.3
Polydispersity Index (PI)	0.8705	0.1454
Intercept	0.8623	0.03104
Fit Error	0.01936	0.009538
In Range (%)	86.72	3.672
Peak One Mean by Intensity (nm)	490.2	459.7
Peak Two Mean by Intensity (nm)	539.2	619.9

Name	Mean	Standard Deviation
Z-Average (nm)	95.09	14.55
Polydispersity Index (PI)	0.2418	0.01559
Intercept	0.9611	0.01124
Fit Error	0.001617	0.000408
In Range (%)	96.59	0.5794
Peak One Mean by Intensity (nm)	121.9	18.27
Peak Two Mean by Intensity (nm)	3744	2090
Peak Three Mean by Intensity (nm)	2387	3341

Name	Mean	Standard Deviation
Z-Average (nm)	78.41	6.454
Polydispersity Index (PI)	0.1502	0.009382
Intercept	0.9667	0.004977
Fit Error	0.0007299	8.159E-05
In Range (%)	97.04	0.2073
Peak One Mean by Intensity (nm)	92.43	8.023

Figure S11. Size distribution of PEO-PBCL$_{22}$ micelles loaded with A83B4C63 after freeze-drying with 4:1 ratio of methoxy-PEG 5000 to polymer

Cryoprotectant	Size distribution
No cryoprotectant before freeze-drying	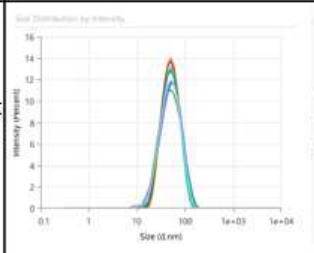
No cryoprotectant After freeze - drying	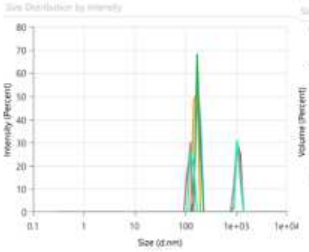
Methoxy-PEG 5000 (1:4 polymer to PEG ratio) Before centrifugation	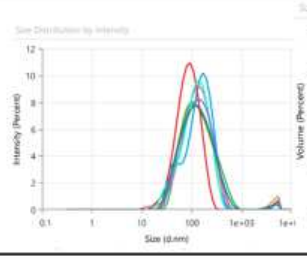
Methoxy-PEG 5000 (1:4 polymer to PEG ratio) After centrifugation	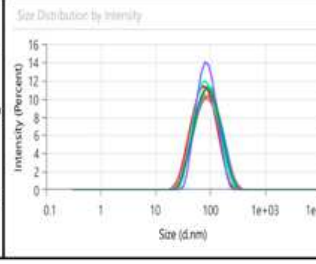

Name	Mean	Standard Deviation
Z-Average (nm)	44.47	0.6119
Polydispersity Index (PI)	0.1707	0.01369
Intercept	0.9668	0.01218
Fit Error	0.001137	0.0001183
In Range (%)	97.64	0.3382
Peak One Mean by Intensity (nm)	54.39	1.378
Peak Two Mean by Intensity (nm)	9.892	-

Name	Mean	Standard Deviation
Z-Average (nm)	1851	487
Polydispersity Index (PI)	0.9585	0.06428
Intercept	0.8614	0.02096
Fit Error	0.01819	0.004952
In Range (%)	86.55	1.906
Peak One Mean by Intensity (nm)	628.1	500.7
Peak Two Mean by Intensity (nm)	124.5	8.793

Name	Mean	Standard Deviation
Z-Average (nm)	102.9	12.16
Polydispersity Index (PI)	0.3105	0.03877
Intercept	0.9648	0.003537
Fit Error	0.002533	0.0008242
In Range (%)	96.76	0.4968
Peak One Mean by Intensity (nm)	148.5	24.44
Peak Two Mean by Intensity (nm)	4092	1804

Name	Mean	Standard Deviation
Z-Average (nm)	76.11	4.176
Polydispersity Index (PI)	0.2062	0.01271
Intercept	0.9712	0.002015
Fit Error	0.001254	8.129E-05
In Range (%)	97.11	0.4563
Peak One Mean by Intensity (nm)	96.28	6.188

Figure S12. Size distribution of PEO-PBCL$_{22}$ micelles loaded with A4 after freeze-drying with 4:1 ratio of methoxy-PEG 5000 to polymer

Chapter 6

General discussion and conclusions

6.1. General Discussion and conclusions

Cancer is of the leading causes of diseases related deaths for many years. Although there has been many efforts to manage and treat cancer cases, mortality rates still remain high (138,139).

The importance of early diagnosis of cancer cannot be overstated in cancer management as starting treatment immediately can significantly improve survival rates in cancer patients (253,254). A way to shorten the time between cancer diagnosis and treatment is to integrate both steps into a single process by developing theranostics. Combining the latest developments in areas of cancer detection and therapy can provide a powerful tool to manage cancer and lead to treatment optimization for individual patients (255). The long-term objective of this research is to develop a cancer theranostic that can detect and home on EGFR+ tumors and deliver radio of chemotherapeutics on these target cells efficiently. In this thesis, we assessed the activity of an anti-EGFR antibody modified with two different radionuclide as PET and SPECT imaging probes for the detection of two different EGFR positive tumors (Chapters 2-3). We also developed traceable nano-particle for future development to nano-theranostics in cancer (Chapter 4). Finally different methods and additives for long term storage of polymeric NPs under study was evaluated (Chapter 5).

Due to the discrepancies observed between subcutaneous tumor models and clinical outcomes, it is crucial to establish an animal model that mimics cancer progression in patients specially an animals model that represents the metastasis stage of the cancers (256,257). Therefore, in chapter 2 of this thesis, we investigated the development of an EGFR+ metastatic non-small cell lung cancer model using the minimum techniques required. The results indicated detectable tumor metastasis on the liver and lungs which in lung cancer patients, liver is also an organ with high

metastasis rate (258). Moreover, it was shown that ^{64}Cu labeled panitumumab could be up taken and retained on EGFR+ H1299 cells in vitro and in mice bearing subcutaneous H1299 tumors. Also, ^{64}Cu labeled panitumumab could not only detect metastatic tumors but also had a higher tumor biodistribution in comparison to the subcutaneous mice model which could be a result of high blood supply to the liver. Moreover, our results indicated that ^{64}Cu labeled panitumumab enhanced the detection of the tumors via PET images in comparison to ^{18}F[FLT](259). The difference observed is due the fact that detection of cancer via ^{18}F[FLT] is dependent to cell proliferation. This understanding highlighted the importance of active targeting.

In addition, it's important to mention that ^{64}Cu has a paired radioisotope which is ^{67}Cu an β-emitter with therapeutical values (260). It has been shown that these paired radioisotopes have similar biodistribution *in vivo* (261). Therefore, a theranostic with the base of panitumumab for EGFR+ non-small cell lung cancer that has the capability of detecting metastasis can be develop by a simple substitution of ^{64}Cu, with ^{67}Cu.

In chapter 3, the potential of ^{203}Pb labeled panitumumab for detecting EGFR+ head and neck cancer *in vitro* and in mice bearing patient derived xenografts tumors was investigated. The EGFR+ head and neck cell line showed the uptake of ^{203}Pb labeled panitumumab. In addition, due to the longer half-life of lead, the opportunity to scan the animals at longer time points was provided. Moreover, understandings from this study and the previous chapter indicated that radiolabeled panitumumab can detect EGFR regardless of the cancer origin. Also, the ^{203}Pb labeled panitumumab, which was not reported in the literature before, indicated its potential to not only detect but also remain in the tumor even after 120 hours post injection of radiolabeled sample through acquired SPECT images and biodistribution studies.

Moreover, similar to ^{64}Cu, ^{203}Pb has a pair radioisotope, ^{212}Pb an α-emitter with anticancer effects (262). Therefore, a theranostic against $EGFR^{+}$ head and neck cancer can be developed by using $^{203}Pb/^{212}Pb$ radioisotopes.

We have also developed PEO-PBCL NPs modified on their surface with ^{203}Pb-modified panitumumab. Despite homing of these NPs on EGFR positive cell lines in vitro, the NPs did not shown tumor homing and distribution in the PDX model of head and neck cancer. No effect for the competition assay with cold panitumumab pretreatment on the biodistribution of NPs was detected. This observation can be attributed to the instability of radiolabeling in the structure in vivo or rapid clearance of NPs by mononuclear phagocytic cells.

In chapter 4, we assessed the possibility of developing a nanotheranostic, using the actively targeted PEO-PBCL NPs. As the targeting potential of panitumumab was previously shown in chapter 2, it was the agent of choice. The modification of the NPs was done with a control over the orientation of panitumumab on the surface since the random orientation of the panitumumab on NPs could increase the chance of being up taken by the immune cells. These NPs were then labeled with ^{64}Cu, to elevate them into the nanotheranostic and be detectable with PET. The acquired PET images and biodistribution studies indicated the radiolabeled NPs were detectable even after 48 hours post-injection. However, other than the tumor, uptakes in liver, spleen and lungs were seen when mice were injected with either radiolabeled PEO-PBCL NP or radiolabeled panitumumab modified PEO-PBCL NP which means the NPs were up taken by the immune cells present in the mice body.

Also, no significant differences in the biodistribution of radiolabeled PEO-PBCL NP or radiolabeled panitumumab modified PEO-PBCL NP in mice was seen. This could be as a result of

EPR effect happening in the tumor of the mice overshadowing the effect of antibody although the possibility for the cleavage of antibody conjugated-PEG-DSPE from the NP structures in vivo cannot be ruled out. Rapid clearance of NPs or inadequate number of mAbs on the NPs for significant interaction with target cells are other potential reasons for this observation

It is possible, both types of NPs were penetrated into the tumor because of the passive targeting but the radiolabeled panitumumab modified PEO-PBCL NP was internalized more than the radiolabeled PEO-PBCL NP such as the results seen for the *in vitro* cell uptake and since biodistribution and PET imaging cannot distinguish between the internalized and non internalized NP that's why no difference was reported. Other possible scenarios are either since we have the right orientation of the panitumumab on the NPs no additional uptake was seen or that the panitumumab fell off the developed NP therefore, no difference was reported.

Since most studies focus on freshly prepared PEO-PBCL NPs, it is crucial to investigate their long-term storage as this will not be a possible to prepare NPs fresh in future preclinical and clinical studies. In chapter 5, freeze-drying and frozen storage conditions with use of different cryoprotectants were studied. Initially, it was understood that freezing and freeze-drying PEO-PBCL NPs requires the addition of cryoprotectants as these storing processes will affect the quality and size of the NPs. Then, when comparing PEG and sucrose as cryoprotectants for freeze-drying, PEG showed better NP protection properties in comparison to sucrose which could be due the difference in the mechanism of protection of each cryoprotectant. However, growth in the NPs sizes was unavoidable by freeze-drying. The NPs size growth during the freeze-thaw (via freezing at -80°C and thawing at 25 °C in presence of either PEG or sucrose) was smaller than freeze-drying

method, indicating that storing PEO-PBCL NPs using cytoprotectants in at -80°C is the better option.

6.2. Limitations

Our developed non-small cell lung cancer metastasis model did not show brain metastasis, which has been reported in 25-40% of cases diagnosed with non-small cell lung cancer metastasis (263). This could be an artifact of study conditions such as duration of study not being enough for lesions to develop in the brain, or the use of immunodeficient mice. Therefore, it stays unclear if the ^{64}Cu labeled panitumumab could detect the tumors in the brain

One limitation when using human anti- EGFR agent in mice bearing human tumors is that the human anti-EGFR cannot react with mouse EGFR therefore the biodistribution profile could alter when the anti-EGFR is used in human (264). Moreover, during the *in vivo* studies of the developed PEO-PBCL nanothranostics, the attachment of the panitumumab on the NPs cannot be monitored. Moreover, through PET and biodistribution studies we cannot detect the NPs internalization and differential homing of cancer versus noncancerus cells in the tumor microenvironemnt.

6.3. Future directions

Future studies can focus on the development of ^{67}Cu labeled panitumumab and assessment of its therapeutic activity in mice bearing metastatic non-small cell lung cancer. ^{64}Cu/^{67}Cu labeled panitumumab can also be developed as EGFR targeted theranostic for detection and treatment of non-small cell lung cancer, head and neck cancer or other EGFR positive solid tumors.. Also, the

therapeutical effects of ^{212}Pb labeled panitumumab on mice bearing head and neck cancer needs to be studied for better understating of the ^{203}Pb/^{212}Pb potential as theranostics. .

More in-depth studies are required to understand the stability of the panitumumabs on NPs when they are injected to animals. Studies such as increasing the time of scanning by using longer lived radioisotopes could provide a better vision on the distribution of the active targeted and radiolabeled PEO-PBCL NPs. Additionally, a higher concentration of panitumumab per NPs could lead to an increase in active targeting, resulting in detectable higher tumor uptake of ^{64}Cu labeled panitumumab modified PEO-PBCL NPs at earlier time points than 24 hours.

On the other hand, for storage of PEO-PBCL NPs through freeze-drying and freezing at -80°C, monitoring the effect of combination of PEG and sucrose as cryoprotectants with different ratios could be considered. Future studies should determine the long-term stability and shelf life of NPs under the identified optimum storage conditions.

6.4. Conclusion

The results of this research led to the preparation of panitumumab as immune- PET or SPECT probes for detection of EGFR targeted lesions in NSCLC and Head and Neck cancer. These developed immune probes showed the potential to be produced reproducibly and accumulate in the EGFR+ tumors. As the utilized radionuclides for developing the imaging probes have same element pair radioisotopes; therefore, the developed immunoprobes can be further developed to EGFR targeted theranostics without the need to study biodistribution of the therapeutical pairs as they will be similar to the developed imaging probes in this thesis. The results also led to the development of PET traceable NPs for further development to nanotheranostics which indicated

that they are accumulated in the tumors; however, the addition of chelator on the surface of the NPs affected the uptake of NPs by the immune system. The results also identified freezing of PEO-PBCL NPs in the presence of PEG 3350 or 5000 Da or sucrose at -80 C as a suitable method for the storage of PEO-PBCL NPs leading to the least increase in size and aggregation of NPs.

Acknowledgments

We would like to thank Dr. John Wilson, David Clendening, Blake Lazurko, Lloyd Barker and Endrit Pllana from the Edmonton Radiopharmaceutical Center (ERC) for ^{18}F production at the cyclotron facility of the Cross Cancer Institute (CCI, Edmonton, AB, Canada) and the ^{64}Cu production at the Medical Isotope and Cyclotron Facility (MICF, Edmonton, AB, Canada). The authors are also grateful to Cody Bergman (Dept. of Oncology, University of Alberta) for the synthesis of [^{18}F]FLT, Dan McGinn (Vivarium of the Cross Cancer Institute, Edmonton, AB, Canada) for supporting the animal work and Dr. Hans-Soenke Jans (Dept. of Oncology, University of Alberta) for technical help and support of the PET imaging experiments. We also thank Jennifer Dufour for her help with the cell culture work. Moreover, Mr. Vishwanatha Somayaji's contribution with ^{1}H NMR experiments from FoPPS/UofA is greatly appreciated.

References

1. Calabria F, Leporace M, Tavolaro R, Bagnato A. Radiopharmaceuticals. In: Gholamrezanezhad A, Assadi M, Jadvar H, editors. Radiology-Nuclear Medicine Diagnostic Imaging [Internet]. 1st ed. Wiley; 2023 [cited 2024 Aug 5]. p. 133–62. Available from: https://onlinelibrary.wiley.com/doi/10.1002/9781119603627.ch4

2. Knapp FF, Dash A. Introduction: Radiopharmaceuticals Play an Important Role in Both Diagnostic and Therapeutic Nuclear Medicine. In: Radiopharmaceuticals for Therapy [Internet]. New Delhi: Springer India; 2016 [cited 2024 Aug 5]. p. 3–4. Available from: http://link.springer.com/10.1007/978-81-322-2607-9_1

3. Pimlott SL, Sutherland A. Molecular tracers for the PET and SPECT imaging of disease. Chem Soc Rev. 2011;40(1):149–62.

4. Anderson CJ, Ferdani R. Copper-64 radiopharmaceuticals for PET imaging of cancer: advances in preclinical and clinical research. Cancer Biother Radiopharm. 2009 Aug;24(4):379–93.

5. Ermert J, Neumaier B. The Radiopharmaceutical Chemistry of Fluorine-18: Nucleophilic Fluorinations. In: Lewis JS, Windhorst AD, Zeglis BM, editors. Radiopharmaceutical Chemistry [Internet]. Cham: Springer International Publishing; 2019 [cited 2024 Sep 13]. p. 273–83. Available from: http://link.springer.com/10.1007/978-3-319-98947-1_15

6. Wong C. Beta Decay of \mathrmF^17 and \mathrmC^11. Phys Rev. 1954 Aug;95(3):765–6.

7. Gnanasegaran G, Ballinger JR. Molecular imaging agents for SPECT (and SPECT/CT). Eur J Nucl Med Mol Imaging. 2014 May;41(S1):26–35.

8. Crișan G, Moldovean-Cioroianu NS, Timaru DG, Andrieș G, Căinap C, Chiș V. Radiopharmaceuticals for PET and SPECT Imaging: A Literature Review over the Last Decade. IJMS. 2022 Apr 30;23(9):5023.

9. Müller C, Fischer E, Behe M, Köster U, Dorrer H, Reber J, et al. Future prospects for SPECT imaging using the radiolanthanide terbium-155 — production and preclinical evaluation in tumor-bearing mice. Nuclear Medicine and Biology. 2014 May;41:e58–65.

10. Kelutur FJ, Abdul Holik H. Use of 99m Tc in The Field of Radiofarmation: A Review. BJI. 2021 Jan 29;7(1):1–10.

11. Ziessman HA, O'Malley JP, Thrall JH, editors. Chapter 14 - Infection and Inflammation. In: Nuclear Medicine (Fourth Edition) [Internet]. Philadelphia: W.B. Saunders; 2014. p. 322–49. Available from: https://www.sciencedirect.com/science/article/pii/B9780323082990000146

12. McNeil BL, Robertson AKH, Fu W, Yang H, Hoehr C, Ramogida CF, et al. Production, purification, and radiolabeling of the 203Pb/212Pb theranostic pair. EJNMMI radiopharm chem. 2021 Dec;6(1):6.

13. Nitipir C, Niculae D, Orlov C, Barbu M, Popescu B, Popa A, et al. Update on radionuclide therapy in oncology (Review). Oncol Lett [Internet]. 2017 Oct 5 [cited 2024 Aug 14]; Available from: http://www.spandidos-publications.com/10.3892/ol.2017.7141

14. Goldsmith SJ. Targeted Radionuclide Therapy: A Historical and Personal Review. Seminars in Nuclear Medicine. 2020 Jan;50(1):87–97.

15. Coursey BM, Nath R. Radionuclide Therapy. Physics Today. 2000 Apr 1;53(4):25–30.

16. Hanaoka H, Hashimoto K, Watanabe S, Matsumoto S, Sakashita T, Watanabe S, et al. Comparative evaluation of radionuclide therapy using 90Y and 177Lu. Ann Nucl Med. 2023 Jan;37(1):52–9.

17. Dash A, Pillai MRA, Knapp FF. Production of (177)Lu for Targeted Radionuclide Therapy: Available Options. Nucl Med Mol Imaging. 2015 Jun;49(2):85–107.

18. Deshmukh R, Singh AN, Martinez M, Gandhi N, Cotta KI, Parihar H, et al. Thyroid hormones, Iodine and Iodides, and Antithyroid Drugs. In: Side Effects of Drugs Annual [Internet]. Elsevier; 2016 [cited 2024 Sep 13]. p. 443–52. Available from: https://linkinghub.elsevier.com/retrieve/pii/S0378608016300411

19. Aljubeh wal'a, Shaheen A, Zalloum O. Radioiodine I-131 for Diagnosing and Treatment of Thyroid Diseases. 2012.

20. Lever SZ, Lydon JD, Cutler CS, Jurisson SS. Radioactive Metals in Imaging and Therapy. In: Comprehensive Coordination Chemistry II [Internet]. Elsevier; 2003 [cited 2024 Sep 13]. p. 883–911. Available from: https://linkinghub.elsevier.com/retrieve/pii/B0080437486090174

21. Orcutt KD, Henry KE, Habjan C, Palmer K, Heimann J, Cupido JM, et al. Dosimetry of [212Pb]VMT01, a MC1R-Targeted Alpha Therapeutic Compound, and Effect of Free 208Tl on Tissue Absorbed Doses. Molecules. 2022 Sep 8;27(18):5831.

22. Mou L, Martini P, Pupillo G, Cieszykowska I, Cutler CS, Mikołajczak R. 67Cu Production Capabilities: A Mini Review. Molecules. 2022 Feb 23;27(5):1501.

23. Sarkar P, Khatana S, Mukherjee B, Shukla J, Das B, Dutta G. Application of Radiopharmaceuticals in Diagnostics and Therapy. In: Dutta G, editor. Next-Generation Nanobiosensor Devices for Point-Of-Care Diagnostics [Internet]. Singapore: Springer Nature Singapore; 2023 [cited 2023 Jan 1]. p. 227–49. Available from: https://link.springer.com/10.1007/978-981-19-7130-3_10

24. Vermeulen K, Vandamme M, Bormans G, Cleeren F. Design and Challenges of Radiopharmaceuticals. Seminars in Nuclear Medicine. 2019 Sep;49(5):339–56.

25. Namavari M, Cheng Z, Zhang R, De A, Levi J, Hoerner JK, et al. A novel method for direct site-specific radiolabeling of peptides using [18F]FDG. Bioconjug Chem. 2009 Mar 18;20(3):432–6.

26. Bhise A, Park H, Rajkumar S, Lee K, Cho SH, Lim JE, et al. Optimizing and determining the click chemistry mediated Cu-64 radiolabeling and physiochemical characteristics of trastuzumab conjugates. Biochemical and Biophysical Research Communications. 2023 Jan;638:28–35.

27. Kelkar SS, Reineke TM. Theranostics: Combining Imaging and Therapy. Bioconjugate Chem. 2011 Oct 19;22(10):1879–903.

28. Yordanova A, Eppard E, Kürpig S, Bundschuh RA, Schönberger S, Gonzalez-Carmona M, et al. Theranostics in nuclear medicine practice. OncoTargets and Therapy. 2017 Oct 3;10(null):4821–8.

29. Avram AM. Radioiodine Theranostics of Differentiated Thyroid Carcinoma. In: Giovanella L, editor. Integrated Diagnostics and Theranostics of Thyroid Diseases [Internet]. Cham: Springer International Publishing; 2023. p. 111–27. Available from: https://doi.org/10.1007/978-3-031-35213-3_7

30. Yavuz S, Puckett Y. Iodine-131 Uptake Study. In: StatPearls [Internet]. Treasure Island (FL): StatPearls Publishing; 2024 [cited 2024 Aug 15]. Available from: http://www.ncbi.nlm.nih.gov/books/NBK559283/

31. Jeyamogan S, Khan NA, Siddiqui R. Application and Importance of Theranostics in the Diagnosis and Treatment of Cancer. Archives of Medical Research. 2021 Feb;52(2):131–42.

32. Chen X, Wong STC. Chapter 1 - Cancer Theranostics: An Introduction. In: Chen X, Wong S, editors. Cancer Theranostics [Internet]. Oxford: Academic Press; 2014. p. 3–8. Available from: https://www.sciencedirect.com/science/article/pii/B9780124077225000013

33. Coura-Filho GB, Torres Silva De Oliveira M, Morais De Campos AL. Principles of Radionuclide Treatments. In: Nuclear Medicine in Endocrine Disorders [Internet]. Cham:

Springer International Publishing; 2022 [cited 2024 Aug 5]. p. 21–31. Available from: https://link.springer.com/10.1007/978-3-031-13224-7_4

34. Muthu MS, Leong DT, Mei L, Feng SS. Nanotheranostics - application and further development of nanomedicine strategies for advanced theranostics. Theranostics. 2014;4(6):660–77.

35. Wang LS, Chuang MC, Ho J an A. Nanotheranostics – a review of recent publications. International Journal of Nanomedicine. 2012 Aug 23;7(null):4679–95.

36. Roy I, Krishnan S, Kabashin AV, Zavestovskaya IN, Prasad PN. Transforming Nuclear Medicine with Nanoradiopharmaceuticals. ACS Nano. 2022 Apr 26;16(4):5036–61.

37. Dennahy IS, Han Z, MacCuaig WM, Chalfant HM, Condacse A, Hagood JM, et al. Nanotheranostics for Image-Guided Cancer Treatment. Pharmaceutics. 2022 Apr 22;14(5):917.

38. Zahavi D, Weiner L. Monoclonal Antibodies in Cancer Therapy. Antibodies. 2020 Jul 20;9(3):34.

39. Justiz Vaillant A, Jamal Z, Patel P. Immunoglobulin.[Updated 2023 Aug 28]. StatPearls [Internet] Treasure Island (FL): StatPearls Publishing. 2024;

40. Carter PJ, Rajpal A. Designing antibodies as therapeutics. Cell. 2022 Jul;185(15):2789–805.

41. Tsao LC, Force J, Hartman ZC. Mechanisms of Therapeutic Antitumor Monoclonal Antibodies. Cancer Research. 2021 Sep 15;81(18):4641–51.

42. Luo R, Liu H, Cheng Z. Protein scaffolds: antibody alternatives for cancer diagnosis and therapy. RSC Chem Biol. 2022;3(7):830–47.

43. Malik B, Ghatol A. Understanding how monoclonal antibodies work. 2021;

44. Martinelli E, De Palma R, Orditura M, De Vita F, Ciardiello F. Anti-epidermal growth factor receptor monoclonal antibodies in cancer therapy. Clin Exp Immunol. 2009 Oct;158(1):1–9.

45. Crescioli S, Correa I, Karagiannis P, Davies AM, Sutton BJ, Nestle FO, et al. IgG4 Characteristics and Functions in Cancer Immunity. Curr Allergy Asthma Rep. 2016 Jan;16(1):7.

46. Yu J, Song Y, Tian W. How to select IgG subclasses in developing anti-tumor therapeutic antibodies. J Hematol Oncol. 2020 Dec;13(1):45.

47. Vidarsson G, Dekkers G, Rispens T. IgG Subclasses and Allotypes: From Structure to Effector Functions. Front Immunol [Internet]. 2014 Oct 20 [cited 2024 Aug 15];5. Available from: http://www.frontiersin.org/Immunotherapies_and_Vaccines/10.3389/fimmu.2014.00520/abstract

48. Napodano C, Marino M, Stefanile A, Pocino K, Scatena R, Gulli F, et al. Immunological Role of IgG Subclasses. Immunological Investigations. 2021 May 19;50(4):427–44.

49. Beck A, Goetsch L, Dumontet C, Corvaïa N. Strategies and challenges for the next generation of antibody–drug conjugates. Nat Rev Drug Discov. 2017 May;16(5):315–37.

50. Parakh S, Lee ST, Gan HK, Scott AM. Radiolabeled Antibodies for Cancer Imaging and Therapy. Cancers. 2022 Mar 11;14(6):1454.

51. Normanno N, De Luca A, Bianco C, Strizzi L, Mancino M, Maiello MR, et al. Epidermal growth factor receptor (EGFR) signaling in cancer. Gene. 2006 Jan;366(1):2–16.

52. Thomas R, Weihua Z. Rethink of EGFR in Cancer With Its Kinase Independent Function on Board. Front Oncol. 2019 Aug 23;9:800.

53. Rogers SJ, Harrington KJ, Rhys-Evans P, O-Charoenrat P, Eccles SA. Biological significance of c-erbB family oncogenes in head and neck cancer. Cancer Metastasis Rev. 2005 Jan;24(1):47–69.

54. Braun AC, de Mello CAL, Corassa M, Abdallah EA, Urvanegia AC, Alves VS, et al. EGFR expression in circulating tumor cells from high-grade metastatic soft tissue sarcomas. Cancer Biology & Therapy. 2018 Jun 3;19(6):454–60.

55. Brenner DR, Gillis J, Demers AA, Ellison LF, Billette JM, Zhang SX, et al. Projected estimates of cancer in Canada in 2024. CMAJ. 2024 May 13;196(18):E615–23.

56. Brenner DR, Poirier A, Woods RR, Ellison LF, Billette JM, Demers AA, et al. Projected estimates of cancer in Canada in 2022. CMAJ. 2022 May 2;194(17):E601–7.

57. Butcher L. Solid tumors: prevalence, economics, and implications for payers and purchasers. Biotechnol Healthc. 2008 May;5(1):20–1.

58. Bertotti A, Sassi F. Molecular Pathways: Sensitivity and Resistance to Anti-EGFR Antibodies. Clinical Cancer Research. 2015 Aug 1;21(15):3377–83.

59. Boross P, Lohse S, Nederend M, Jansen JHM, Van Tetering G, Dechant M, et al. Ig A EGFR antibodies mediate tumour killing *in vivo*. EMBO Mol Med. 2013 Aug;5(8):1213–26.

60. Rocha-Lima CM, Soares HP, Raez LE, Singal R. EGFR Targeting of Solid Tumors. Cancer Control. 2007 Jul;14(3):295–304.

61. Nguyen PV, Hervé-Aubert K, Chourpa I, Allard-Vannier E. Active targeting strategy in nanomedicines using anti-EGFR ligands – A promising approach for cancer therapy and diagnosis. International Journal of Pharmaceutics. 2021 Nov;609:121134.

62. Cohenuram M, Saif MW. Panitumumab the first fully human monoclonal antibody: from the bench to the clinic. Anti-Cancer Drugs. 2007 Jan;18(1):7–15.

63. Addeo R, Caraglia M, Cerbone D, Frega N, Cimmino G, Abbruzzese A, et al. Panitumumab: a new frontier of target therapy for the treatment of metastatic colorectal cancer. Expert Review of Anticancer Therapy. 2010 Apr;10(4):499–505.

64. Wei L, Shi J, Afari G, Bhattacharyya S. Preparation of clinical-grade ^{89} Zr-panitumumab as a positron emission tomography biomarker for evaluating epidermal growth factor receptor-targeted therapy: ^{89} Zr-panitumumab for medical use. J Label Compd Radiopharm. 2014 Jan;57(1):25–35.

65. Facca VJ, Cai Z, Gopal NEK, Reilly RM. Panitumumab-DOTA- ^{111} In: An Epidermal Growth Factor Receptor Targeted Theranostic for SPECT/CT Imaging and Meitner–Auger

Electron Radioimmunotherapy of Triple-Negative Breast Cancer. Mol Pharmaceutics. 2022 Oct 3;19(10):3652–63.

66. Milenic DE, Baidoo KE, Kim YS, Barkley R, Brechbiel MW. Targeted α-Particle Radiation Therapy of HER1-Positive Disseminated Intraperitoneal Disease: An Investigation of the Human Anti-EGFR Monoclonal Antibody, Panitumumab. Translational Oncology. 2017 Aug;10(4):535–45.

67. Aghevlian S, Lu Y, Winnik MA, Hedley DW, Reilly RM. Panitumumab Modified with Metal-Chelating Polymers (MCP) Complexed to ^{111} In and ^{177} Lu—An EGFR-Targeted Theranostic for Pancreatic Cancer. Mol Pharmaceutics. 2018 Mar 5;15(3):1150–9.

68. Mohanraj VJ, Chen Y. Nanoparticles - A review. Trop J Pharm Res. 2007 Jul 31;5(1):561–73.

69. Gavas S, Quazi S, Karpiński TM. Nanoparticles for Cancer Therapy: Current Progress and Challenges. Nanoscale Res Lett. 2021 Dec;16(1):173.

70. Ngoune R, Peters A, Von Elverfeldt D, Winkler K, Pütz G. Accumulating nanoparticles by EPR: A route of no return. Journal of Controlled Release. 2016 Sep;238:58–70.

71. Bazak R, Houri M, El Achy S, Kamel S, Refaat T. Cancer active targeting by nanoparticles: a comprehensive review of literature. J Cancer Res Clin Oncol. 2015 May;141(5):769–84.

72. Byrne JD, Betancourt T, Brannon-Peppas L. Active targeting schemes for nanoparticle systems in cancer therapeutics. Advanced Drug Delivery Reviews. 2008 Dec;60(15):1615–26.

73. Marques AC, Costa PC, Velho S, Amaral MH. Lipid Nanoparticles Functionalized with Antibodies for Anticancer Drug Therapy. Pharmaceutics. 2023 Jan 8;15(1):216.

74. Tewabe A, Abate A, Tamrie M, Seyfu A, Abdela Siraj E. Targeted Drug Delivery - From Magic Bullet to Nanomedicine: Principles, Challenges, and Future Perspectives. J Multidiscip Healthc. 2021;14:1711–24.

75. Attia MF, Anton N, Wallyn J, Omran Z, Vandamme TF. An overview of active and passive targeting strategies to improve the nanocarriers efficiency to tumour sites. Journal of Pharmacy and Pharmacology. 2019 Jul 3;71(8):1185–98.

76. Marques A, Costa P, Velho S, Amaral M. Analytical Techniques for Characterizing Tumor-Targeted Antibody-Functionalized Nanoparticles. Life. 2024 Apr 10;14(4):489.

77. Sivaram AJ, Wardiana A, Howard CB, Mahler SM, Thurecht KJ. Recent Advances in the Generation of Antibody-Nanomaterial Conjugates. Adv Healthcare Mater. 2018 Jan;7(1):1700607.

78. Juan A, Cimas FJ, Bravo I, Pandiella A, Ocaña A, Alonso-Moreno C. An Overview of Antibody Conjugated Polymeric Nanoparticles for Breast Cancer Therapy. Pharmaceutics. 2020 Aug 25;12(9):802.

79. Montenegro JM, Grazu V, Sukhanova A, Agarwal S, De La Fuente JM, Nabiev I, et al. Controlled antibody/(bio-) conjugation of inorganic nanoparticles for targeted delivery. Advanced Drug Delivery Reviews. 2013 May;65(5):677–88.

80. Marques AC, Costa PJ, Velho S, Amaral MH. Functionalizing nanoparticles with cancer-targeting antibodies: A comparison of strategies. Journal of Controlled Release. 2020 Apr;320:180–200.

81. Pei Z, Anderson H, Myrskog A, Dunér G, Ingemarsson B, Aastrup T. Optimizing immobilization on two-dimensional carboxyl surface: pH dependence of antibody orientation and antigen binding capacity. Analytical Biochemistry. 2010 Mar;398(2):161–8.

82. Juan A, Cimas FJ, Bravo I, Pandiella A, Ocaña A, Alonso-Moreno C. Antibody Conjugation of Nanoparticles as Therapeutics for Breast Cancer Treatment. IJMS. 2020 Aug 21;21(17):6018.

83. Wu S, Wu F, Chen X. Antibody-Incorporated Nanomedicines for Cancer Therapy. Advanced Materials. 2022 Jun;34(24):2109210.

84. Weber C, Reiss S, Langer K. Preparation of surface modified protein nanoparticles by introduction of sulfhydryl groups. International Journal of Pharmaceutics. 2000 Dec;211(1–2):67–78.

85. Henkel M, Röckendorf N, Frey A. Selective and Efficient Cysteine Conjugation by Maleimides in the Presence of Phosphine Reductants. Bioconjugate Chem. 2016 Oct 19;27(10):2260–5.

86. Devaraj NK, Finn MG. Introduction: Click Chemistry. Chem Rev. 2021 Jun 23;121(12):6697–8.

87. Taiariol L, Chaix C, Farre C, Moreau E. Click and Bioorthogonal Chemistry: The Future of Active Targeting of Nanoparticles for Nanomedicines? Chem Rev. 2022 Jan 12;122(1):340–84.

88. Kumari M, Acharya A, Krishnamurthy PT. Antibody-conjugated nanoparticles for target-specific drug delivery of chemotherapeutics. Beilstein J Nanotechnol. 2023 Sep 4;14:912–26.

89. Kadkhoda J, Akrami-Hasan-Kohal M, Tohidkia MR, Khaledi S, Davaran S, Aghanejad A. Advances in antibody nanoconjugates for diagnosis and therapy: A review of recent studies and trends. International Journal of Biological Macromolecules. 2021 Aug;185:664–78.

90. Jain A, Barve A, Zhao Z, Jin W, Cheng K. Comparison of Avidin, Neutravidin, and Streptavidin as Nanocarriers for Efficient siRNA Delivery. Mol Pharm. 2017 May 1;14(5):1517–27.

91. Zhang K, Hao L, Hurst SJ, Mirkin CA. Antibody-Linked Spherical Nucleic Acids for Cellular Targeting. J Am Chem Soc. 2012;4.

92. Geng SB, Wu J, Alam ME, Schultz JS, Dickinson CD, Seminer CR, et al. Facile Preparation of Stable Antibody–Gold Conjugates and Application to Affinity-Capture Self-Interaction Nanoparticle Spectroscopy. Bioconjugate Chem. 2016 Oct 19;27(10):2287–300.

93. Zhuang J, Zhou L, Tang W, Ma T, Li H, Wang X, et al. Tumor targeting antibody-conjugated nanocarrier with pH/thermo dual-responsive macromolecular film layer for

enhanced cancer chemotherapy. Materials Science and Engineering: C. 2021 Jan;118:111361.

94. Zhou Y, Que KT, Tang HM, Zhang P, Fu QM, Liu ZJ. Anti-CD206 antibody-conjugated Fe3O4-based PLGA nanoparticles selectively promote tumor-associated macrophages to polarize to the pro-inflammatory subtype. Oncol Lett. 2020 Sep 28;20(6):1–1.

95. Taheri H, Amini B, Kamali M, Asadi M, Naderlou E. Functionalization of anti-Brucella antibody based on SNP and MNP nanoparticles for visual and spectrophotometric detection of Brucella. Spectrochimica Acta Part A: Molecular and Biomolecular Spectroscopy. 2020 Mar;229:117891.

96. Ivanova AV, Nikitin AA, Gabashvily AN, Vishnevskiy DA, Abakumov MA. Synthesis and intensive analysis of antibody labeled single core magnetic nanoparticles for targeted delivery to the cell membrane. Journal of Magnetism and Magnetic Materials. 2021 Mar;521:167487.

97. Saqr A, Vakili MR, Huang YH, Lai R, Lavasanifar A. Development of Traceable Rituximab-Modified PEO-Polyester Micelles by Postinsertion of PEG-phospholipids for Targeting of B-cell Lymphoma. ACS Omega. 2019 Nov 1;4(20):18867–79.

98. Emami F, Banstola A, Vatanara A, Lee S, Kim JO, Jeong JH, et al. Doxorubicin and Anti-PD-L1 Antibody Conjugated Gold Nanoparticles for Colorectal Cancer Photochemotherapy. Mol Pharmaceutics. 2019 Mar 4;16(3):1184–99.

99. Kunc F, Moore CJ, Sully RE, Hall AJ, Gubala V. Polycarboxylated Dextran as a Multivalent Linker: Synthesis and Target Recognition of the Antibody–Nanoparticle Bioconjugates in PBS and Serum. Langmuir. 2019 Apr 9;35(14):4909–17.

100. Reda M, Ngamcherdtrakul W, Gu S, Bejan DS, Siriwon N, Gray JW, et al. PLK1 and EGFR targeted nanoparticle as a radiation sensitizer for non-small cell lung cancer. Cancer Letters. 2019 Dec 28;467:9–18.

101. Hassanzadeganroudsari M, Soltani M, Heydarinasab A, Apostolopoulos V, Akbarzadehkhiyavi A, Nurgali K. Targeted nano-drug delivery system for glioblastoma therapy: In vitro and in vivo study. Journal of Drug Delivery Science and Technology. 2020 Dec;60:102039.

102. Johnsen KB, Bak M, Melander F, Thomsen MS, Burkhart A, Kempen PJ, et al. Modulating the antibody density changes the uptake and transport at the blood-brain barrier of both transferrin receptor-targeted gold nanoparticles and liposomal cargo. Journal of Controlled Release. 2019 Feb;295:237–49.

103. Lin PC, Chen SH, Wang KY, Chen ML, Adak AK, Hwu JRR, et al. Fabrication of Oriented Antibody-Conjugated Magnetic Nanoprobes and Their Immunoaffinity Application. Anal Chem. 2009 Nov;81(21):8774–82.

104. Pollok NE, Rabin C, Smith L, Crooks RM. Orientation-Controlled Bioconjugation of Antibodies to Silver Nanoparticles. Bioconjugate Chem. 2019 Dec 18;30(12):3078–86.

105. Kotagiri N, Li Z, Xu X, Mondal S, Nehorai A, Achilefu S. Antibody Quantum Dot Conjugates Developed via Copper-Free Click Chemistry for Rapid Analysis of Biological Samples Using a Microfluidic Microsphere Array System. Bioconjugate Chem. 2014 Jul 16;25(7):1272–81.

106. Thorek DLJ, Elias ew R, Tsourkas A. Comparative Analysis of Nanoparticle-Antibody Conjugations: Carbodiimide Versus Click Chemistry. Mol Imaging. 2009 Jul 1;8(4):7290.2009.00021.

107. Dinauer N, Balthasar S, Weber C, Kreuter J, Langer K, von Briesen H. Selective targeting of antibody-conjugated nanoparticles to leukemic cells and primary T-lymphocytes. Biomaterials. 2005 Oct;26(29):5898–906.

108. Lim SI, Lukianov CI, Champion JA. Self-assembled protein nanocarrier for intracellular delivery of antibody. Journal of Controlled Release. 2017 Mar;249:1–10.

109. Jin T, Tiwari DK, Tanaka S ichi, Inouye Y, Yoshizawa K, Watanabe TM. Antibody–ProteinA conjugated quantum dots for multiplexed imaging of surface receptors in living cells. Mol BioSyst. 2010;6(11):2325.

110. Kim C, Galloway JF, Lee KH, Searson PC. Universal Antibody Conjugation to Nanoparticles Using the Fcγ Receptor I (FcγRI): Quantitative Profiling Of Membrane Biomarkers. Bioconjugate Chem. 2014 Oct 15;25(10):1893–901.

111. Srivastava S, Dadachova E. Recent advances in radionuclide therapy. Seminars in Nuclear Medicine. 2001 Oct;31(4):330–41.

112. Aghevlian S, Boyle AJ, Reilly RM. Radioimmunotherapy of cancer with high linear energy transfer (LET) radiation delivered by radionuclides emitting α-particles or Auger electrons. Advanced Drug Delivery Reviews. 2017 Jan;109:102–18.

113. Alotiby M, Greguric I, Kibédi T, Lee BQ, Roberts M, Stuchbery AE, et al. Measurement of the intensity ratio of Auger and conversion electrons for the electron capture decay of ^{125}I. Phys Med Biol. 2018 Mar 21;63(6):06NT04.

114. Ku A, Facca VJ, Cai Z, Reilly RM. Auger electrons for cancer therapy – a review. EJNMMI radiopharm chem. 2019 Dec;4(1):27.

115. Gill MR, Falzone N, Du Y, Vallis KA. Targeted radionuclide therapy in combined-modality regimens. The Lancet Oncology. 2017 Jul;18(7):e414–23.

116. Yamamoto Y, Nishiyama Y, Monden T, Matsumura Y, Satoh K, Ohkawa M. Clinical usefulness of fusion of 131I SPECT and CT images in patients with differentiated thyroid carcinoma. J Nucl Med. 2003 Dec;44(12):1905–10.

117. Psimadas D, Oliveira H, Thevenot J, Lecommandoux S, Bouziotis P, Varvarigou AD, et al. Polymeric micelles and vesicles: biological behavior evaluation using radiolabeling techniques. Pharmaceutical Development and Technology. 2014 Mar;19(2):189–93.

118. Boerman OC, Laverman P, Oyen WJG, Corstens FHM, Storm G. Radiolabeled liposomes for scintigraphic imaging. Progress in Lipid Research. 2000 Sep;39(5):461–75.

119. Marik J, Tartis MS, Zhang H, Fung JY, Kheirolomoom A, Sutcliffe JL, et al. Long-circulating liposomes radiolabeled with [18F]fluorodipalmitin ([18F]FDP). Nuclear Medicine and Biology. 2007 Feb;34(2):165–71.

120. Yang L, Zhang C, Liu J, Huang F, Zhang Y, Liang X, et al. ICG-Conjugated and ^{125} I-Labeled Polymeric Micelles with High Biosafety for Multimodality Imaging-Guided Photothermal Therapy of Tumors. Adv Healthcare Mater. 2020 Mar;9(5):1901616.

121. Pellico J, Gawne PJ, T. M. De Rosales R. Radiolabelling of nanomaterials for medical imaging and therapy. Chem Soc Rev. 2021;50(5):3355–423.

122. Lamichhane N, Dewkar G, Sundaresan G, Mahon R, Zweit J. [18F]-Fluorinated Carboplatin and [111In]-Liposome for Image-Guided Drug Delivery. IJMS. 2017 May 18;18(5):1079.

123. Cardinale J, Giammei C, Jouini N, Mindt TL. Bioconjugation Methods for Radiopharmaceutical Chemistry. In: Lewis JS, Windhorst AD, Zeglis BM, editors. Radiopharmaceutical Chemistry [Internet]. Cham: Springer International Publishing; 2019 [cited 2021 Sep 24]. p. 449–66. Available from: http://link.springer.com/10.1007/978-3-319-98947-1_25

124. Glaus C, Rossin R, Welch MJ, Bao G. In Vivo Evaluation of 64Cu-Labeled Magnetic Nanoparticles as a Dual-Modality PET/MR Imaging Agent. Bioconjugate Chem. 2010 Apr 21;21(4):715–22.

125. Cao Y, Suresh M. A simple and efficient method for radiolabeling of preformed liposomes. Journal of Pharmacy and Pharmaceutical Sciences. 1998;1(1):31–7.

126. Sobol NB, Korsen JA, Younes A, Edwards KJ, Lewis JS. ImmunoPET Imaging of Pancreatic Tumors with 89Zr-Labeled Gold Nanoparticle–Antibody Conjugates. Mol Imaging Biol. 2021 Feb;23(1):84–94.

127. Sousa F, Castro P, Fonte P, Kennedy PJ, Neves-Petersen MT, Sarmento B. Nanoparticles for the delivery of therapeutic antibodies: Dogma or promising strategy? Expert Opinion on Drug Delivery. 2017 Oct 3;14(10):1163–76.

128. Karmani L, Labar D, Valembois V, Bouchat V, Nagaswaran PG, Bol A, et al. Antibody-functionalized nanoparticles for imaging cancer: influence of conjugation to gold nanoparticles on the biodistribution of ^{89} Zr-labeled cetuximab in mice. Contrast Media & Molecular. 2013 Sep;8(5):402–8.

129. El-Shershaby HM, Farrag NS, Ebeid NH, Moustafa KA. Radiolabeling and cytotoxicity of monoclonal antibody Isatuximab functionalized silver nanoparticles on the growth of multiple myeloma. International Journal of Pharmaceutics. 2022 Aug;624:122019.

130. Cheng CC, Chang, Ho, Peng, Chang, Mai, et al. Novel targeted nuclear imaging agent for gastric cancer diagnosis: glucose-regulated protein 78 binding peptide-guided 111In-labeled polymeric micelles. IJN. 2013 Apr;1385.

131. Makhlouf A, Hajdu I, Hartimath SV, Alizadeh E, Wharton K, Wasan KM, et al. ^{111} In-Labeled Glycoprotein Nonmetastatic b (GPNMB) Targeted Gemini Surfactant-Based

Nanoparticles against Melanoma: In Vitro Characterization and in Vivo Evaluation in Melanoma Mouse Xenograft Model. Mol Pharmaceutics. 2019 Feb 4;16(2):542–51.

132. Werner ME, Karve S, Sukumar R, Cummings ND, Copp JA, Chen RC, et al. Folate-targeted nanoparticle delivery of chemo- and radiotherapeutics for the treatment of ovarian cancer peritoneal metastasis. Biomaterials. 2011 Nov;32(33):8548–54.

133. Zhou M, Chen Y, Adachi M, Wen X, Erwin B, Mawlawi O, et al. Single agent nanoparticle for radiotherapy and radio-photothermal therapy in anaplastic thyroid cancer. Biomaterials. 2015 Jul;57:41–9.

134. Chen L, Zhong X, Yi X, Huang M, Ning P, Liu T, et al. Radionuclide 131I labeled reduced graphene oxide for nuclear imaging guided combined radio- and photothermal therapy of cancer. Biomaterials. 2015 Oct;66:21–8.

135. Song X, Liang C, Feng L, Yang K, Liu Z. Iodine-131-labeled, transferrin-capped polypyrrole nanoparticles for tumor-targeted synergistic photothermal-radioisotope therapy. Biomater Sci. 2017;5(9):1828–35.

136. Song L, Falzone N, Vallis KA. EGF-coated gold nanoparticles provide an efficient nano-scale delivery system for the molecular radiotherapy of EGFR-positive cancer. International Journal of Radiation Biology. 2016 Nov 1;92(11):716–23.

137. Huang S, Zhang L, Xu M, Li C, Fu H, Huang J, et al. Co-Delivery of ^{131} I and Prima-1 by Self-Assembled CD44-Targeted Nanoparticles for Anaplastic Thyroid Carcinoma Theranostics. Adv Healthcare Mater. 2021 Feb;10(3):2001029.

138. Siegel RL, Miller KD, Wagle NS, Jemal A. Cancer statistics, 2023. CA A Cancer J Clinicians. 2023 Jan;73(1):17–48.

139. Bray F, Laversanne M, Sung H, Ferlay J, Siegel RL, Soerjomataram I, et al. Global cancer statistics 2022: GLOBOCAN estimates of incidence and mortality worldwide for 36 cancers in 185 countries. CA A Cancer J Clinicians. 2024 May;74(3):229–63.

140. Jassim A, Rahrmann EP, Simons BD, Gilbertson RJ. Cancers make their own luck: theories of cancer origins. Nat Rev Cancer. 2023 Oct;23(10):710–24.

141. Banik BL, Fattahi P, Brown JL. Polymeric nanoparticles: the future of nanomedicine. WIREs Nanomed Nanobiotechnol. 2016 Mar;8(2):271–99.

142. El-Say KM, El-Sawy HS. Polymeric nanoparticles: Promising platform for drug delivery. International Journal of Pharmaceutics. 2017 Aug;528(1–2):675–91.

143. Sadat SMA, Wuest M, Paiva IM, Munira S, Sarrami N, Sanaee F, et al. Nano-Delivery of a Novel Inhibitor of Polynucleotide Kinase/Phosphatase (PNKP) for Targeted Sensitization of Colorectal Cancer to Radiation-Induced DNA Damage. Front Oncol. 2021 Dec 23;11:772920.

144. Mahmud A, Xiong XB, Lavasanifar A. Novel Self-Associating Poly(ethylene oxide)- *b lock* -poly(ε-caprolactone) Block Copolymers with Functional Side Groups on the Polyester Block for Drug Delivery. Macromolecules. 2006 Dec 1;39(26):9419–28.

145. Sadat SMA, Paiva IM, Shire Z, Sanaee F, Morgan TDR, Paladino M, et al. A synthetically lethal nanomedicine delivering novel inhibitors of polynucleotide kinase 3′-

phosphatase (PNKP) for targeted therapy of PTEN-deficient colorectal cancer. Journal of Controlled Release. 2021 Jun;334:335–52.

146. Paiva I, Mattingly S, Wuest M, Leier S, Vakili MR, Weinfeld M, et al. Synthesis and Analysis of ^{64} Cu-Labeled GE11-Modified Polymeric Micellar Nanoparticles for EGFR-Targeted Molecular Imaging in a Colorectal Cancer Model. Mol Pharmaceutics. 2020 May 4;17(5):1470–81.

147. Li M, Sagastume EA, Lee D, McAlister D, DeGraffenreid AJ, Olewine KR, et al. 203/212Pb Theranostic Radiopharmaceuticals for Image-guided Radionuclide Therapy for Cancer. CMC. 2020 Dec 8;27(41):7003–31.

148. Nelson BJB, Leier S, Wilson J, Wuest M, Doupe J, Andersson JD, et al. 64Cu production via the 68Zn(p,nα)64Cu nuclear reaction: An untapped, cost-effective and high energy production route. Nuclear Medicine and Biology. 2024 Jan;128–129:108875.

149. Jiao R, Allen KJH, Malo ME, Yilmaz O, Wilson J, Nelson BJB, et al. A Theranostic Approach to Imaging and Treating Melanoma with 203Pb/212Pb-Labeled Antibody Targeting Melanin. Cancers. 2023 Jul 29;15(15):3856.

150. Mathieu A, Remmelink M, D'Haene N, Penant S, Gaussin J, Van Ginckel R, et al. Development of a chemoresistant orthotopic human nonsmall cell lung carcinoma model in nude mice: Analyses of tumor heterogeneity in relation to the immunohistochemical levels of expression of cyclooxygenase-2, ornithine decarboxylase, lung-related resistance protein, prostaglandin E synthetase, and glutathione-S-transferase (GST)-α, GST-μ, and GST-π. Cancer. 2004 Oct 15;101(8):1908–18.

151. Cui ZY, Ahn JS, Lee JY, Kim WS, Lim HY, Jeon HJ, et al. Mouse orthotopic lung cancer model induced by PC14PE6. Cancer Res Treat. 2006 Dec;38(4):234–9.

152. Johnston MR, Mullen JBM, Pagura ME, Howard RB. Validation of an orthotopic model of human lung cancer with regional and systemic metastases. The Annals of Thoracic Surgery. 2001 Apr;71(4):1120–5.

153. Sun Y, Yang J, Li Y, Luo J, Sun J, Li D, et al. Single low-dose INC280-loaded theranostic nanoparticles achieve multirooted delivery for MET-targeted primary and liver metastatic NSCLC. Mol Cancer. 2022 Dec 1;21(1):212.

154. Lou R, Cao H, Dong S, Shi C, Xu X, Ma R, et al. Liver X receptor agonist T0901317 inhibits the migration and invasion of non-small-cell lung cancer cells in vivo and in vitro. Anti-Cancer Drugs. 2019 Jun;30(5):495–500.

155. Weiss ID, Ella E, Dominsky O, Smith Y, Abraham M, Wald H, et al. In the Hunt for Therapeutic Targets: Mimicking the Growth, Metastasis, and Stromal Associations of Early-Stage Lung Cancer Using a Novel Orthotopic Animal Model. Journal of Thoracic Oncology. 2015 Jan;10(1):46–58.

156. Jarry U, Bostoën M, Pineau R, Chaillot L, Mennessier V, Montagne P, et al. Orthotopic model of lung cancer: isolation of bone micro-metastases after tumor escape from Osimertinib treatment. BMC Cancer. 2021 Dec;21(1):530.

157. Slebe M, Pouw JEE, Hashemi SMS, Menke-van Der Houven Van Oordt CW, Yaqub MM, Bahce I. Current state and upcoming opportunities for immunoPET biomarkers in lung cancer. Lung Cancer. 2022 Jul;169:84–93.

158. Pereira PMR, Norfleet J, Lewis JS, Escorcia FE. Immuno-PET Detects Changes in Multi-RTK Tumor Cell Expression Levels in Response to Targeted Kinase Inhibition. J Nucl Med. 2021 Mar;62(3):366–71.

159. Lindenberg L, Adler S, Turkbey IB, Mertan F, Ton A, Do K, et al. Dosimetry and first human experience with 89Zr-panitumumab. Am J Nucl Med Mol Imaging. 2017;7(4):195–203.

160. Niu G, Li Z, Xie J, Le QT, Chen X. PET of EGFR antibody distribution in head and neck squamous cell carcinoma models. J Nucl Med. 2009 Jul;50(7):1116–23.

161. Boyle AJ, Cao PJ, Hedley DW, Sidhu SS, Winnik MA, Reilly RM. MicroPET/CT imaging of patient-derived pancreatic cancer xenografts implanted subcutaneously or orthotopically in NOD-scid mice using (64)Cu-NOTA-panitumumab F(ab')2 fragments. Nucl Med Biol. 2015 Feb;42(2):71–7.

162. Boyle AJ, Cai Z, O'Brien S, Crick J, Angers S, Reilly RM. Relative Biological Effectiveness (RBE) of [64Cu]Cu and [177Lu]Lu-NOTA-panitumumab F (ab')2 radioimmunotherapeutic agents vs. γ-radiation for decreasing the clonogenic survival in vitro of human pancreatic ductal adenocarcinoma (PDAC) cells. Nucl Med Biol. 2023;122–123:108367.

163. Heneweer C, Holland JP, Divilov V, Carlin S, Lewis JS. Magnitude of enhanced permeability and retention effect in tumors with different phenotypes: 89Zr-albumin as a model system. J Nucl Med. 2011 Apr;52(4):625–33.

164. Nelson BJB, Wilson J, Schultz MK, Andersson JD, Wuest F. High-yield cyclotron production of 203Pb using a sealed 205Tl solid target. Nuclear Medicine and Biology. 2023 Jan;116–117:108314.

165. Bhattacharyya S, Kurdziel K, Wei L, Riffle L, Kaur G, Hill GC, et al. Zirconium-89 labeled panitumumab: a potential immuno-PET probe for HER1-expressing carcinomas. Nuclear Medicine and Biology. 2013 May;40(4):451–7.

166. Dewulf J, Adhikari K, Vangestel C, Wyngaert TVD, Elvas F. Development of Antibody Immuno-PET/SPECT Radiopharmaceuticals for Imaging of Oncological Disorders—An Update. Cancers. 2020 Jul 11;12(7):1868.

167. Fasano M, Della Corte CM, Viscardi G, Di Liello R, Paragliola F, Sparano F, et al. Head and neck cancer: the role of anti-EGFR agents in the era of immunotherapy. Ther Adv Med Oncol. 2021 Jan;13:175883592094941.

168. Srivastava SC. Paving the Way to Personalized Medicine: Production of Some Promising Theragnostic Radionuclides at Brookhaven National Laboratory. Seminars in Nuclear Medicine. 2012 May;42(3):151–63.

169. Facca VJ, Cai Z, Ku A, Georgiou CJ, Reilly RM. Adjuvant Auger Electron-Emitting Radioimmunotherapy with [^{111} In]In-DOTA-Panitumumab in a Mouse Model of Local

Recurrence and Metastatic Progression of Human Triple-Negative Breast Cancer. Mol Pharmaceutics. 2023 Dec 4;20(12):6407–19.

170. Ku A, Kondo M, Cai Z, Meens J, Li MR, Ailles L, et al. Dose predictions for [177Lu]Lu-DOTA-panitumumab F(ab′)2 in NRG mice with HNSCC patient-derived tumour xenografts based on [64Cu]Cu-DOTA-panitumumab F(ab′)2 – implications for a PET theranostic strategy. EJNMMI radiopharm chem. 2021 Dec;6(1):25.

171. Ku A, Chan C, Aghevlian S, Cai Z, Cescon D, Bratman SV, et al. MicroSPECT/CT Imaging of Cell-Line and Patient-Derived EGFR-Positive Tumor Xenografts in Mice with Panitumumab Fab Modified with Hexahistidine Peptides To Enable Labeling with ^{99m} Tc(I) Tricarbonyl Complex. Mol Pharmaceutics. 2019 Aug 5;16(8):3559–68.

172. Garmestani K, Milenic DE, Brady ED, Plascjak PS, Brechbiel MW. Purification of cyclotron-produced 203Pb for labeling Herceptin. Nuclear Medicine and Biology. 2005 Apr;32(3):301–5.

173. Miao Y, Figueroa SD, Fisher DR, Moore HA, Testa RF, Hoffman TJ, et al. ^{203} Pb-Labeled α-Melanocyte–Stimulating Hormone Peptide as an Imaging Probe for Melanoma Detection. J Nucl Med. 2008 May;49(5):823–9.

174. Banerjee SR, Minn I, Kumar V, Josefsson A, Lisok A, Brummet M, et al. Preclinical Evaluation of $^{203/212}$ Pb-Labeled Low-Molecular-Weight Compounds for Targeted Radiopharmaceutical Therapy of Prostate Cancer. J Nucl Med. 2020 Jan;61(1):80–8.

175. Ray G, Baidoo K, Wong K, Williams M, Garmestani K, Brechbiel M, et al. Preclinical evaluation of a monoclonal antibody targeting the epidermal growth factor receptor as a radioimmunodiagnostic and radioimmunotherapeutic agent. British J Pharmacology. 2009 Aug;157(8):1541–8.

176. Nayak TK, Garmestani K, Milenic DE, Brechbiel MW. PET and MRI of Metastatic Peritoneal and Pulmonary Colorectal Cancer in Mice with Human Epidermal Growth Factor Receptor 1–Targeted ^{89} Zr-Labeled Panitumumab. J Nucl Med. 2012 Jan;53(1):113–20.

177. Liu Z, Ma T, Liu H, Jin Z, Sun X, Zhao H, et al. ^{177} Lu-Labeled Antibodies for EGFR-Targeted SPECT/CT Imaging and Radioimmunotherapy in a Preclinical Head and Neck Carcinoma Model. Mol Pharmaceutics. 2014 Mar 3;11(3):800–7.

178. Nayak TK, Garmestani K, Baidoo KE, Milenic DE, Brechbiel MW. Preparation, Biological Evaluation, and Pharmacokinetics of the Human Anti- *HER1* Monoclonal Antibody Panitumumab Labeled with ^{86} Y for Quantitative PET of Carcinoma. J Nucl Med. 2010 Jun;51(6):942–50.

179. Ho FKS. Development of 197Hg-Labelled Panitumumab for Auger Electron Radioimmunotherapy of Triple-Negative Breast Cancer [Internet] [M.Sc.]. ProQuest Dissertations and Theses. [Canada -- Ontario, CA]: University of Toronto (Canada); 2023. Available from: https://login.ezproxy.library.ualberta.ca/login?url=https://www.proquest.com/dissertations-theses/development-sup-197-hg-labelled-panitumumab-auger/docview/2889518073/se-2?accountid=14474

180. Chopra A. 111In-Labeled panitumumab, a fully human monoclonal antibody directed against the extracellular domain III of the epidermal growth factor receptor. In: Molecular Imaging and Contrast Agent Database (MICAD) [Internet]. Bethesda (MD): National Center for Biotechnology Information (US); 2004 [cited 2024 Jan 17]. Available from: http://www.ncbi.nlm.nih.gov/books/NBK97967/

181. Sharma SK, Wuest M, Wang M, Glubrecht D, Andrais B, Lapi SE, et al. Immuno-PET of epithelial ovarian cancer: harnessing the potential of CA125 for non-invasive imaging. EJNMMI Res. 2014 Dec;4(1):60.

182. Nelson BJB, Wilson J, Andersson JD, Wuest F. Theranostic Imaging Surrogates for Targeted Alpha Therapy: Progress in Production, Purification, and Applications. Pharmaceuticals (Basel). 2023 Nov 17;16(11):1622.

183. Rao L, Xu JH, Cai B, Liu H, Li M, Jia Y, et al. Synthetic nanoparticles camouflaged with biomimetic erythrocyte membranes for reduced reticuloendothelial system uptake. Nanotechnology. 2016 Feb 26;27(8):085106.

184. Sindhwani S, Syed AM, Ngai J, Kingston BR, Maiorino L, Rothschild J, et al. The entry of nanoparticles into solid tumours. Nat Mater. 2020 May;19(5):566–75.

185. Xie J, Lee S, Chen X. Nanoparticle-based theranostic agents. Advanced Drug Delivery Reviews. 2010 Aug;62(11):1064–79.

186. Zarepour A, Zarrabi A, Khosravi A. SPIONs as Nano-Theranostics Agents. In: SPIONs as Nano-Theranostics Agents [Internet]. Singapore: Springer Singapore; 2017 [cited 2024 Jul

4]. p. 1–44. (SpringerBriefs in Applied Sciences and Technology). Available from: http://link.springer.com/10.1007/978-981-10-3563-0_1

187. Muhamad N, Plengsuriyakarn T, Na-Bangchang K. Application of active targeting nanoparticle delivery system for chemotherapeutic drugs and traditional/herbal medicines in cancer therapy: a systematic review. IJN. 2018 Jul;Volume 13:3921–35.

188. Ahmad A, Khan F, Mishra RK, Khan R. Precision Cancer Nanotherapy: Evolving Role of Multifunctional Nanoparticles for Cancer Active Targeting. J Med Chem. 2019 Dec 12;62(23):10475–96.

189. Goddard ZR, Marín MJ, Russell DA, Searcey M. Active targeting of gold nanoparticles as cancer therapeutics. Chem Soc Rev. 2020;49(23):8774–89.

190. Bazak R, Houri M, El Achy S, Kamel S, Refaat T. Cancer active targeting by nanoparticles: a comprehensive review of literature. J Cancer Res Clin Oncol. 2015 May;141(5):769–84.

191. Archontakis E, Woythe L, Van Hoof B, Albertazzi L. Mapping the relationship between total and functional antibodies conjugated to nanoparticles with spectrally-resolved direct stochastic optical reconstruction microscopy (SR-dSTORM). Nanoscale Adv. 2022;4(20):4402–9.

192. Yong KW, Yuen D, Chen MZ, Porter CJH, Johnston APR. Pointing in the Right Direction: Controlling the Orientation of Proteins on Nanoparticles Improves Targeting Efficiency. Nano Lett. 2019 Mar 13;19(3):1827–31.

193. Byrne JD, Betancourt T, Brannon-Peppas L. Active targeting schemes for nanoparticle systems in cancer therapeutics. Advanced Drug Delivery Reviews. 2008 Dec;60(15):1615–26.

194. Marbiah M, Kotidis P, Donini R, Gómez IA, Jimenez Del Val I, Haslam SM, et al. Rapid Antibody Glycoengineering in Chinese Hamster Ovary Cells. JoVE. 2022 Jun 2;(184):63872.

195. Wijdeven MA, Van Geel R, Hoogenboom JH, Verkade JMM, Janssen BMG, Hurkmans I, et al. Enzymatic glycan remodeling–metal free click (GlycoConnect^{TM}) provides homogenous antibody-drug conjugates with improved stability and therapeutic index without sequence engineering. mAbs. 2022 Dec 31;14(1):2078466.

196. Li X, Fang T, Boons G. Preparation of Well-Defined Antibody–Drug Conjugates through Glycan Remodeling and Strain-Promoted Azide–Alkyne Cycloadditions. Angewandte Chemie. 2014 Jul 7;126(28):7307–10.

197. Hodoniczky J, Zheng YZ, James DC. Control of Recombinant Monoclonal Antibody Effector Functions by Fc *N* -Glycan Remodeling in Vitro. Biotechnology Progress. 2005 Jan;21(6):1644–52.

198. Manabe S, Yamaguchi Y, Matsumoto K, Fuchigami H, Kawase T, Hirose K, et al. Characterization of Antibody Products Obtained through Enzymatic and Nonenzymatic Glycosylation Reactions with a Glycan Oxazoline and Preparation of a Homogeneous Antibody–Drug Conjugate via Fc *N* -Glycan. Bioconjugate Chem. 2019 May 15;30(5):1343–55.

199. Qasba PK. Glycans of Antibodies as a Specific Site for Drug Conjugation Using Glycosyltransferases. Bioconjugate Chem. 2015 Nov 18;26(11):2170–5.

200. Tron GC, Pirali T, Billington RA, Canonico PL, Sorba G, Genazzani AA. Click chemistry reactions in medicinal chemistry: Applications of the 1,3-dipolar cycloaddition between azides and alkynes. Medicinal Research Reviews. 2008 Mar;28(2):278–308.

201. Zhang X, Zhang Y. Applications of Azide-Based Bioorthogonal Click Chemistry in Glycobiology. Molecules. 2013 Jun 19;18(6):7145–59.

202. Van Geel R, Wijdeven MA, Heesbeen R, Verkade JMM, Wasiel AA, Van Berkel SS, et al. Chemoenzymatic Conjugation of Toxic Payloads to the Globally Conserved N-Glycan of Native mAbs Provides Homogeneous and Highly Efficacious Antibody–Drug Conjugates. Bioconjugate Chem. 2015 Nov 18;26(11):2233–42.

203. Rastin F, Javid H, Oryani MA, Rezagholinejad N, Afshari AR, Karimi-Shahri M. Immunotherapy for colorectal cancer: Rational strategies and novel therapeutic progress. International Immunopharmacology. 2024 Jan;126:111055.

204. Aliabadi HM, Mahmud A, Sharifabadi AD, Lavasanifar A. Micelles of methoxy poly(ethylene oxide)-b-poly(ε-caprolactone) as vehicles for the solubilization and controlled delivery of cyclosporine A. Journal of Controlled Release. 2005 May;104(2):301–11.

205. Sudol ASL, Butler J, Ivory DP, Tews I, Crispin M. Extensive substrate recognition by the streptococcal antibody-degrading enzymes IdeS and EndoS. Nat Commun. 2022 Dec 17;13(1):7801.

206. Barkat MdA, Rahman MA, Ansari MA, Ahmad FJ. Introduction to Nanofabrication for Theranostics Application. In: Barkat MdA, Ahmad FJ, Rahman MA, Ansari MA, editors. Nanotheranostics for Diagnosis and Therapy [Internet]. Singapore: Springer Nature Singapore; 2024 [cited 2024 Jul 31]. p. 1–13. Available from: https://link.springer.com/10.1007/978-981-97-3115-2_1

207. Zaytseva OO, Seeling M, Krištić J, Lauc G, Pezer M, Nimmerjahn F. Fc-Linked IgG N-Glycosylation in FcγR Knock-Out Mice. Front Cell Dev Biol. 2020 Mar 3;8:67.

208. Johansson BP, Shannon O, Björck L. IdeS: a bacterial proteolytic enzyme with therapeutic potential. PLoS One. 2008 Feb 27;3(2):e1692.

209. Wong K, Baidoo K, Nayak T, Garmestani K, Brechbiel M, Milenic D. In Vitro and In Vivo Pre-Clinical Analysis of a F(ab')(2) Fragment of Panitumumab for Molecular Imaging and Therapy of HER1 Positive Cancers. EJNMMI research. 2011 Jun 7;1.

210. Yoon HY, Lee D, Lim D, Koo H, Kim K. Copper-Free Click Chemistry: Applications in Drug Delivery, Cell Tracking, and Tissue Engineering. Advanced Materials. 2022 Mar;34(10):2107192.

211. Yameen B, Choi WI, Vilos C, Swami A, Shi J, Farokhzad OC. Insight into nanoparticle cellular uptake and intracellular targeting. Journal of Controlled Release. 2014 Sep;190:485–99.

212. Shukla VN, Vikas, Mehata AK, Setia A, Kumari P, Mahto SK, et al. EGFR targeted albumin nanoparticles of oleanolic acid: In silico screening of nanocarrier, cytotoxicity and

pharmacokinetics for lung cancer therapy. International Journal of Biological Macromolecules. 2023 Aug;246:125719.

213. Fang F, Zhang X, Tang J, Wang Y, Xu J, Sun Y. EGFR-targeted hybrid lipid nanoparticles for chemo-photothermal therapy against colorectal cancer cells. Chemistry and Physics of Lipids. 2023 Mar;251:105280.

214. Bhattacharya S, Parihar VK, Singh N, Hatware K, Page A, Sharma M, et al. Targeted Delivery of Panitumumab-Scaffold Bosutinib-Encapsulated Polycaprolactone Nanoparticles for EGFR-Overexpressed Colorectal Cancer. Nanomedicine (Lond). 2023 Apr;18(9):713–41.

215. Du L, Xu Y, Han B, Wang Y, Zeng Q, Shao M, et al. EGFR-targeting peptide conjugated polymer–lipid hybrid nanoparticles for delivery of salinomycin to osteosarcoma. Journal of Cancer Research and Therapeutics. 2023 Dec;19(6):1544–51.

216. Chomet M, Schreurs M, Vos R, Verlaan M, Kooijman EJ, Poot AJ, et al. Performance of nanoScan PET/CT and PET/MR for quantitative imaging of 18F and 89Zr as compared with ex vivo biodistribution in tumor-bearing mice. EJNMMI Res. 2021 Jun 12;11(1):57.

217. Kießling F, Pichler B, editors. Small animal imaging: basics and practical guide. 1. ed. Berlin Heidelberg: Springer; 2011. 597 p.

218. Chen WC, Zhang AX, Li SD. Limitations and niches of the active targeting approach for nanoparticle drug delivery. European Journal of Nanomedicine. 2012 Dec 1;4(2–4):89–93.

219. Cheng WWK, Allen TM. Targeted delivery of anti-CD19 liposomal doxorubicin in B-cell lymphoma: A comparison of whole monoclonal antibody, Fab′ fragments and single chain Fv. Journal of Controlled Release. 2008 Feb;126(1):50–8.

220. Kappel C, Seidl C, Medina-Montano C, Schinnerer M, Alberg I, Leps C, et al. Density of Conjugated Antibody Determines the Extent of Fc Receptor Dependent Capture of Nanoparticles by Liver Sinusoidal Endothelial Cells. ACS Nano. 2021 Sep 28;15(9):15191–209.

221. Li SD, Huang L. Pharmacokinetics and Biodistribution of Nanoparticles. Mol Pharmaceutics. 2008 Aug 1;5(4):496–504.

222. Luo WC, O'Reilly Beringhs A, Kim R, Zhang W, Patel SM, Bogner RH, et al. Impact of formulation on the quality and stability of freeze-dried nanoparticles. European Journal of Pharmaceutics and Biopharmaceutics. 2021 Dec;169:256–67.

223. Choi MJ, Briançon S, Andrieu J, Min SG, Fessi H. Effect of Freeze-Drying Process Conditions on the Stability of Nanoparticles. Drying Technology. 2004 Dec 31;22(1–2):335–46.

224. Trenkenschuh E, Friess W. Freeze-drying of nanoparticles: How to overcome colloidal instability by formulation and process optimization. European Journal of Pharmaceutics and Biopharmaceutics. 2021 Aug;165:345–60.

225. Umerska A, Paluch KJ, Santos-Martinez MJ, Corrigan OI, Medina C, Tajber L. Freeze drying of polyelectrolyte complex nanoparticles: Effect of nanoparticle composition and cryoprotectant selection. International Journal of Pharmaceutics. 2018 Dec;552(1–2):27–38.

226. Abla KK, Mehanna MM. Freeze-drying: A flourishing strategy to fabricate stable pharmaceutical and biological products. International Journal of Pharmaceutics. 2022 Nov;628:122233.

227. Chen G, Wang W. Role of Freeze Drying in Nanotechnology. Drying Technology. 2007 Feb 12;25(1):29–35.

228. Lee MK, Kim MY, Kim S, Lee J. Cryoprotectants for freeze drying of drug nano-suspensions: Effect of freezing rate. Journal of Pharmaceutical Sciences. 2009 Dec;98(12):4808–17.

229. Date PV, Samad A, Devarajan PV. Freeze Thaw: A Simple Approach for Prediction of Optimal Cryoprotectant for Freeze Drying. AAPS PharmSciTech. 2010 Mar;11(1):304–13.

230. Andreana I, Bincoletto V, Manzoli M, Rodà F, Giarraputo V, Milla P, et al. Freeze Drying of Polymer Nanoparticles and Liposomes Exploiting Different Saccharide-Based Approaches. Materials. 2023 Jan 31;16(3):1212.

231. Abdelwahed W, Degobert G, Stainmesse S, Fessi H. Freeze-drying of nanoparticles: Formulation, process and storage considerations☆. Advanced Drug Delivery Reviews. 2006 Dec 30;58(15):1688–713.

232. Schwarz C, Mehnert W. Freeze-drying of drug-free and drug-loaded solid lipid nanoparticles (SLN). Int J Pharm. 1997 Nov 28;157(2):171–9.

233. Fonte P, Soares S, Sousa F, Costa A, Seabra V, Reis S, et al. Stability Study Perspective of the Effect of Freeze-Drying Using Cryoprotectants on the Structure of Insulin Loaded into PLGA Nanoparticles. Biomacromolecules. 2014 Oct 13;15(10):3753–65.

234. Amis TM, Renukuntla J, Bolla PK, Clark BA. Selection of Cryoprotectant in Lyophilization of Progesterone-Loaded Stearic Acid Solid Lipid Nanoparticles. Pharmaceutics. 2020 Sep 19;12(9):892.

235. Hassankhani Rad A, Asiaee F, Jafari S, Shayanfar A, Lavasanifar A, Molavi O. Poly(ethylene glycol)-poly(ε-caprolactone)-based micelles for solubilization and tumor-targeted delivery of silibinin. Bioimpacts. 2019 Nov 2;10(2):87–95.

236. Oliyapour Y, Dabiri S, Molavi O, Hejazi MS, Davaran S, Jafari S, et al. Chrysin and chrysin-loaded nanocarriers induced immunogenic cell death on B16 melanoma cells. Med Oncol. 2023 Aug 25;40(10):278.

237. Shire Z, Vakili MR, Morgan TDR, Hall DG, Lavasanifar A, Weinfeld M. Nanoencapsulation of Novel Inhibitors of PNKP for Selective Sensitization to Ionizing Radiation and Irinotecan and Induction of Synthetic Lethality. Mol Pharmaceutics. 2018 Jun 4;15(6):2316–26.

238. Elmenoufy AH, Gentile F, Jay D, Karimi-Busheri F, Yang X, Soueidan OM, et al. Targeting DNA Repair in Tumor Cells via Inhibition of ERCC1–XPF. J Med Chem. 2019 Sep 12;62(17):7684–96.

239. Moura Paiva I. Development of active tumor targeting systems for delivery of siRNA and drugs into breast and colorectal cancer. 2020 [cited 2024 Jun 20]; Available from: https://era.library.ualberta.ca/items/9895a0bf-ac23-40fd-9ea5-a2687d9b4bc8

240. Mehinrad, Parnian. Nanodelivery of Novel Inhibitors of ERCC1/XPF for sensitizing colorectal cancer cell to platinum drugs. [cited 2024 Jun 19]; Available from: https://era.library.ualberta.ca/items/63b187d3-7905-479b-995b-a3d1b05cd18b

241. Leardi R. Experimental design in chemistry: A tutorial. Analytica Chimica Acta. 2009 Oct;652(1–2):161–72.

242. Gatto MS, Najahi-Missaoui W. Lyophilization of Nanoparticles, Does It Really Work? Overview of the Current Status and Challenges. Int J Mol Sci. 2023 Sep 13;24(18):14041.

243. Fonte P, Soares S, Costa A, Andrade JC, Seabra V, Reis S, et al. Effect of cryoprotectants on the porosity and stability of insulin-loaded PLGA nanoparticles after freeze-drying. Biomatter. 2012 Oct;2(4):329–39.

244. Degobert G, Aydin D. Lyophilization of Nanocapsules: Instability Sources, Formulation and Process Parameters. Pharmaceutics. 2021 Jul 21;13(8):1112.

245. Luo WC, Zhang W, Kim R, Chong H, Patel SM, Bogner RH, et al. Impact of controlled ice nucleation and lyoprotectants on nanoparticle stability during Freeze-drying and upon storage. International Journal of Pharmaceutics. 2023 Jun;641:123084.

246. Jeong YI, Shim YH, Kim C, Lim GT, Choi KC, Yoon C. Effect of cryoprotectants on the reconstitution of surfactant-free nanoparticles of poly(DL-lactide-co-glycolide). Journal of Microencapsulation. 2005 Sep;22(6):593–601.

247. Almalik A, Alradwan I, Kalam MA, Alshamsan A. Effect of cryoprotection on particle size stability and preservation of chitosan nanoparticles with and without hyaluronate or alginate coating. Saudi Pharmaceutical Journal. 2017 Sep;25(6):861–7.

248. Yang ZL, Li XR, Yang KW, Liu Y. Amphotericin B-loaded poly(ethylene glycol)–poly(lactide) micelles: Preparation, freeze-drying, and *in vitro* release. J Biomedical Materials Res. 2008 May;85A(2):539–46.

249. Ramos Yacasi GR, Calpena Campmany AC, Egea Gras MA, Espina García M, García López ML. Freeze drying optimization of polymeric nanoparticles for ocular flurbiprofen delivery: effect of protectant agents and critical process parameters on long-term stability. Drug Development and Industrial Pharmacy. 2017 Apr 3;43(4):637–51.

250. Abdelwahed W, Degobert G, Fessi H. A pilot study of freeze drying of poly(epsilon-caprolactone) nanocapsules stabilized by poly(vinyl alcohol): Formulation and process optimization. International Journal of Pharmaceutics. 2006 Feb;309(1–2):178–88.

251. Sun J, He C, Zhuang X, Jing X, Chen X. The crystallization behavior of poly(ethylene glycol)-poly(ε-caprolactone) diblock copolymers with asymmetric block compositions. J Polym Res. 2011 Nov;18(6):2161–8.

252. He C, Sun J, Deng C, Zhao T, Deng M, Chen X, et al. Study of the Synthesis, Crystallization, and Morphology of Poly(ethylene glycol)−Poly(ε-caprolactone) Diblock Copolymers. Biomacromolecules. 2004 Sep 1;5(5):2042–7.

253. Neal RD, Tharmanathan P, France B, Din NU, Cotton S, Fallon-Ferguson J, et al. Is increased time to diagnosis and treatment in symptomatic cancer associated with poorer outcomes? Systematic review. Br J Cancer. 2015 Mar 31;112(S1):S92–107.

254. Hanna TP, King WD, Thibodeau S, Jalink M, Paulin GA, Harvey-Jones E, et al. Mortality due to cancer treatment delay: systematic review and meta-analysis. BMJ. 2020 Nov 4;m4087.

255. Lammers T, Aime S, Hennink WE, Storm G, Kiessling F. Theranostic Nanomedicine. Acc Chem Res. 2011 Oct 18;44(10):1029–38.

256. Céspedes MV, Casanova I, Parreño M, Mangues R. Mouse models in oncogenesis and cancer therapy. Clin Transl Oncol. 2006 May;8(5):318–29.

257. Matsumura Y. Cancer stromal targeting therapy to overcome the pitfall of EPR effect. Advanced Drug Delivery Reviews. 2020;154–155:142–50.

258. Riihimäki M, Hemminki A, Fallah M, Thomsen H, Sundquist K, Sundquist J, et al. Metastatic sites and survival in lung cancer. Lung Cancer. 2014 Oct;86(1):78–84.

259. Peck M, Pollack HA, Friesen A, Muzi M, Shoner SC, Shankland EG, et al. Applications of PET imaging with the proliferation marker [18F]-FLT. Q J Nucl Med Mol Imaging. 2015 Mar;59(1):95–104.

260. Keinänen O, Fung K, Brennan JM, Zia N, Harris M, Van Dam E, et al. Harnessing ^{64}Cu/^{67}Cu for a theranostic approach to pretargeted radioimmunotherapy. Proc Natl Acad Sci USA. 2020 Nov 10;117(45):28316–27.

261. Huynh TT, Van Dam EM, Sreekumar S, Mpoy C, Blyth BJ, Muntz F, et al. Copper-67-Labeled Bombesin Peptide for Targeted Radionuclide Therapy of Prostate Cancer. Pharmaceuticals. 2022 Jun 8;15(6):728.

262. Kokov KV, Egorova BV, German MN, Klabukov ID, Krasheninnikov ME, Larkin-Kondrov AA, et al. 212Pb: Production Approaches and Targeted Therapy Applications. Pharmaceutics. 2022 Jan 13;14(1):189.

263. DEMPKE WCM, EDVARDSEN K, LU S, REINMUTH N, RECK M, INOUE A. Brain Metastases in NSCLC – are TKIs Changing the Treatment Strategy? Anticancer Res. 2015 Nov 1;35(11):5797.

264. Burgess AW. EGFR family: Structure physiology signalling and therapeutic targets †. Growth Factors. 2008 Jan;26(5):263–74.